International Journal of Aerospace Engineering

Dynamics and Control of Large Space Systems

Lead Guest Editor: Shunan Wu
Guest Editors: Jiafu Liu and Gangqiang Li

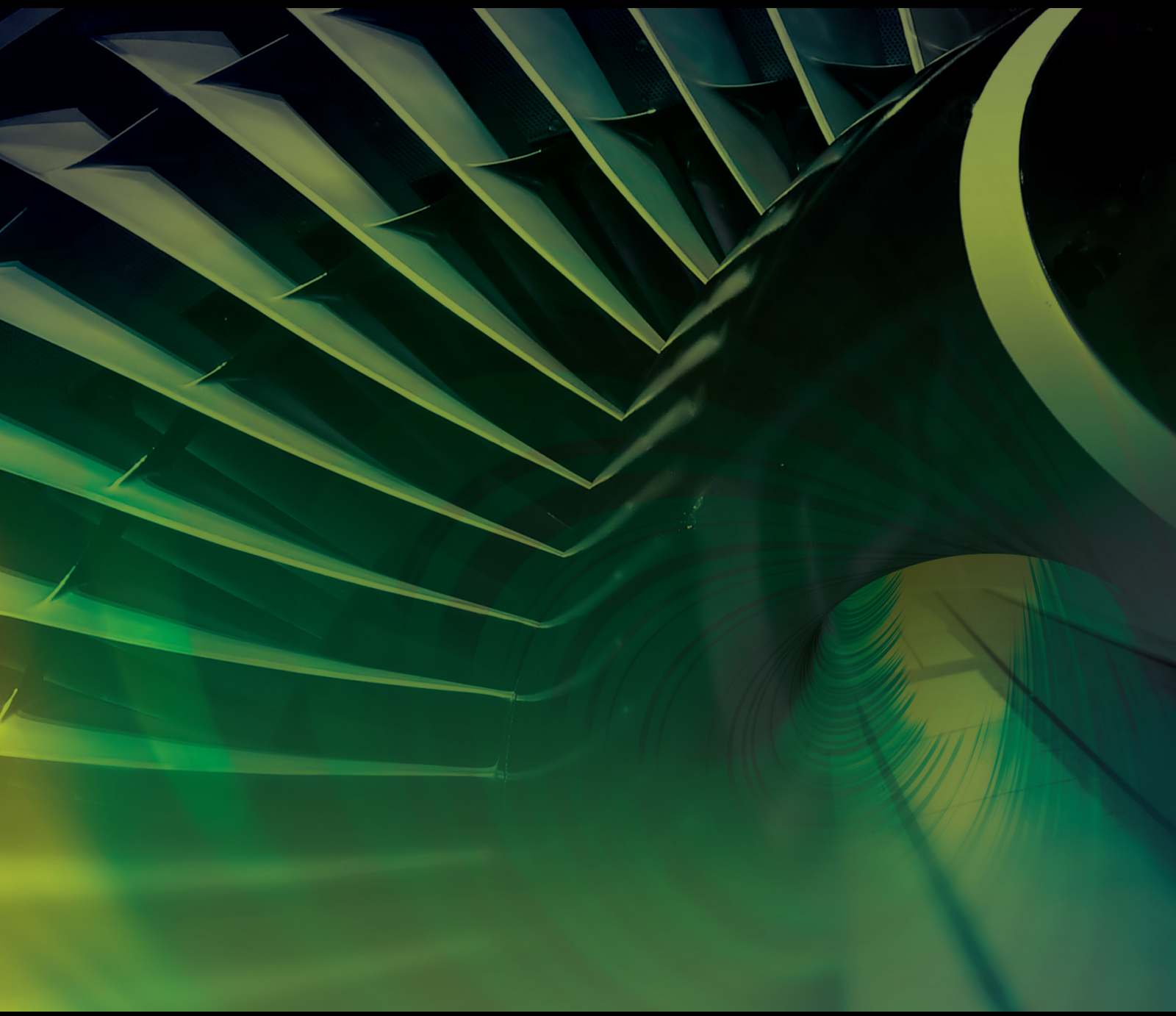

Dynamics and Control of Large Space Systems

International Journal of Aerospace Engineering

Dynamics and Control of Large Space Systems

Lead Guest Editor: Shunan Wu
Guest Editors: Jiafu Liu and Gangqiang Li

Contents

Hindawi
International Journal of Aerospace Engineering
Volume 2022, Article ID 9307837, 14 pages
https://doi.org/10.1155/2022/9307837

Research Article

Self-Organizing Method on Mission-Level Task Allocation of Large-Scale Remote Sensing Satellite Swarm

Yang Jiang[1], **Yuan Gao**[2], **Longjiang Yu**[1], **Jing Yu**[1], **Yuting Li**[1] and **Hongtao Gao**[1]

[1]*Institute of Remote Sensing Satellite, China Academy of Space Technology, Beijing 100094, China*
[2]*Shanghai Electro-Mechanical Engineering Institute, Shanghai Academy of Spaceflight Technology, Shanghai 201109, China*

Correspondence should be addressed to Longjiang Yu; likeherod@163.com

Received 11 August 2021; Revised 18 June 2022; Accepted 15 July 2022; Published 1 September 2022

Academic Editor: Shaoming He

Distributed self-organization and self-management is an ideal way to achieve an autonomous and efficient operation of large-scale remote sensing satellite swarm. A distributed task allocation method based on the improved contract network algorithm is designed, orienting typical mission-level tasks. And the satellite swarm task allocation and planning model of potential target searching, moving target tracking, and sensitive target feature confirmation is given. The model is composed of observation requirement generation, observing area decomposition, and task allocation between different satellites. Simulation results confirm that the improved contract network algorithm can optimally solve the problem of mission-level task allocation autonomously in distributed swarm. This paper verifies that the self-organization method has the potential for engineering applications with simple realization theory and high calculation efficiency.

1. Introduction

Space-based earth observing system is developing from a small number of high-cost satellites to a large scale of swarm-satellites [1], with continuous cost reduction of satellite manufacture and launching. A satellite swarm refers to a decentralized control system of satellites that consists of multiple satellites with different orbit types, payloads, onboard resources, and platform capabilities [2]. The swarm members have to exchange information in accordance with standard communication protocols. The observing tasks are collected onboard or on the ground, exchanged through intersatellites and satellite-ground communication link, and finally executed by a group of satellites in the swarm.

The increasing number of satellites on orbit can enhance the overall application capabilities of the swarm system [3], while it also brings new obstacles in the operation of the system, such as

(i) ground system's operating difficulties caused by the large number of satellites

(ii) satellites' cooperation difficulties caused by the complexity of information exchanging in a dynamic environment

(iii) task allocation and planning difficulties caused by the complexity of diverse mission-level tasks

Hence, mission-level task allocation of large-scale satellite swarm remains to be researched. There are many researches on multisatellite task planning and management and on satellite data processing, and great progress has also been made in engineering. Aiming at the issues of swarm task allocation, the early research mainly focused on the centralized planning method on the ground. Considering multisatellite cooperation planning under emergency conditions, Chuan et al. proposed a multisatellite cooperative planning algorithm based on particle swarm optimization (PSO) algorithm combined with a heuristic algorithm [4]. Yingwu et al. proposed an evolutionary learning ant colony algorithm for multisatellite task planning [5]. Chao et al. established a multisatellite and multiobjective mission planning model

for agile satellites and proposed a hybrid parallel algorithm of generic and simulated annealing algorithm based on similarity and aggregation [6, 7]. Xiaolu et al. proposed an adaptive large neighborhood search algorithm for coordinated planning of multiple agile satellites [8]. Chuanqi et al. proposed an algorithm based on the improved genetic algorithm with elitist retention strategy that is used for mission planning of small satellite constellation [9]. These methods solved the task assignment issues of a constellation with small number of satellites and improved the response ability of satellite to unexpected observation tasks. But these studies are still difficult to apply to large-scale, heterogeneous satellite swarm.

To meet the requirements of heterogeneous satellite swarm task planning, distributed allocation methods were proposed. Huicheng et al. proposed a dynamic task allocation method for agile satellite constellation based on multiagent theory and introduced the contract network mechanism into the algorithm process [10]. Yitao et al. further developed an autonomous task planning method based on the bidding mechanism [11]. Longjiang et al. established a distributed collaborative task allocation model for agile satellite constellation [12]. The studies mentioned above improve the contract network algorithm; proposed task interaction strategies such as buying, selling, exchanging, and replacement; and improved the efficiency of constellation task allocation. However, most of the existing research does not model and simulate typical task scenarios; hence, there is still a gap between practical engineering applications.

Compared to a single-satellite task, swarm-oriented tasks are more abstract, macroscopic, and complex, which can be seen from potential target searching task, moving target tracking task, and sensitive target feature confirmation task [13–16]. The planning process of these mission-level tasks is mainly manifested as the autonomous mission transferring, negotiation, and assignment process among satellites, which can be defined as "self-organizing assignment of swarm missions." We further improve the distributed task allocation method of swarm based on the contract network algorithm, apply it to the complex task planning, and explore the method in the task allocation efficiency and task execution effect. The task allocation and planning are mainly discussed, and there remains further works to be done for engineering practice of remote sensing. For instance, image processing in diverse weather conditions [17, 18].

This paper is divided into five sections. A description of the remote sensing satellite swarm missions is given in Section 2. The distributed self-organizing method based on the improved contract network and the task allocation models orienting three typical mission-level tasks are presented in Section 3. The numerical simulations that demonstrate the feasibility of the designed method in three scenarios are performed in Section 4. And Section 5 gives a conclusion of the work.

2. Typical Mission-Level Task Description

For large-scale remote sensing satellite swarm, its structural characteristics are heterogeneous, distributed, and self-organized. The swarm (including its subgroups) can complete tasks that a single satellite cannot, especially some complex tasks.

Compared to a single satellite, the observation tasks faced by the remote sensing satellite swarm are more macroscopic, requiring multiple types of satellites to execute in time sequence, which can be defined as "mission-level" tasks. The swarm can decompose and allocate mission-level tasks as a whole, adjust tasks dynamically as the swarm status evolves, and finally form a task sequence executed by multiple satellites in an orderly manner in time. Three typical mission-level tasks are discussed as follows:

(1) Potential target searching task

Potential target searching task is proposed to search for certain targets in a specific area and find qualified targets as quickly as possible or find as many targets as possible within the specified time, as shown in Figure 1. The specific imaging tasks are planned and executed according to the strategy which based on the terrain, target characteristics, and other information of the area.

(2) Moving target tracking task

The moving target tracking task is proposed to continuously track the whole process of the movement of target from the start point to the end point, to ensure that the target position is always within the observable range and to prevent the target from being lost and restarting the target searching task, as shown in Figure 2. Predict next position range of the target from certain start position and then plan and execute the follow-up observations. The satellite needs to constantly adjust the parameters in the tracking process according to the actual target position and the predicted target position to ensure that the target is always in the detectable area.

(3) Sensitive target task

A sensitive target task is proposed to obtain multidimensional feature information of the target within a specific time window to improve the accuracy of target recognition. The constellation enables the target to be observed multiple times by multiple types of payloads within a period of time, through task planning and allocating, until observation elements of the target are all obtained, and its characteristic attributes are confirmed with a high degree of certainty, as shown in Figure 3. The task completion time is usually an important constraint to ensure the effectiveness of the information obtained. Moreover, the closer the imaging time of multiple types of payloads is, the higher the time correlation and the higher the value of the fusion image can get.

3. Distributed Task Self-Organizing Method of Remote Sensing Swarm

3.1. Swarm Distributed Task Allocation Scheme Architecture. From a principle point of view, the essence of swarm task allocation is the process of gradual decomposition and

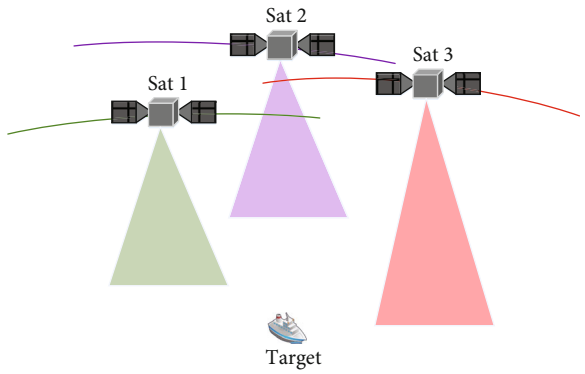

Figure 1: Potential target searching task mode scheme.

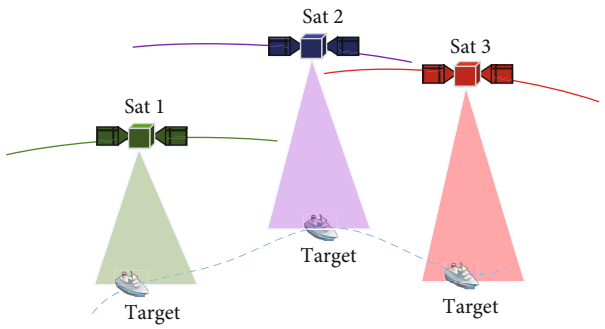

Figure 2: Moving target tracking task mode scheme.

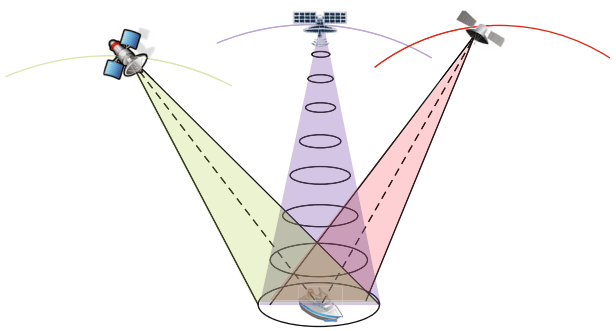

Figure 3: Sensitive target feature confirmation task mode scheme.

mapping of observation requirements among requirement space, task space, and execution space, as shown in Figure 4. The swarm task planning system receives multisource and multicategory observation requirements, forming a requirement space. The mission-level tasks can be classified into different types according to different kinds of targets, observation purposes, and so on, mentioned in Section 2. The ground or single satellite decomposes the requirements according to specific rules (target location, target acquisition period, observation elements, etc.) to generate tasks to be planned with more specific requirements to form a task space. By performing the arrangement of tasks to be planned to the satellites in space (that is, allocation and planning algorithms), the reasonable allocation of multitasks to multisatellites is completed, and the metatask sequence of each satellite is generated.

The distributed task negotiation mechanism is a core mechanism for realizing the mapping of swarm tasks from task space to execution space, and its foundation is the theory of the multiagent system. The remote sensing satellite in the swarm is a typical type of agent, which has the characteristics of high autonomy, strong dynamic, and concurrent behavior. Considering a centralized planner on the ground is used to perform global planning, the search space will be greatly expanded and difficult to solve. The distributed structure is a more ideal structure for agent organizations.

3.2. Intersatellite Task Allocation Algorithm Based on Improved Contract Network. The distributed task allocation method based on the improved contract network algorithm is adopted to realize the optimal allocation of intersatellite tasks, that is, to realize the mapping of swarm tasks from task space to execution space.

After a certain master satellite is determined in a certain event, for satellites with communication conditions between the satellites, the master satellite can initiate the process of intersatellite task negotiation and allocation and iteratively complete task allocation according to the process of bidding, bid evaluation, bid winning, and confirmation [19, 20]. For different observation events, each satellite can act as the master satellite of a certain event, thereby initiating the negotiation and allocation process. Therefore, a single satellite can serve as both the master and slave at a specific moment.

The traditional contract network algorithm adopts the method of "sales contract," which has the limitation that the distribution result is easy to fall into the local optimum, and a single sales contract has insufficient processing capacity for the complex dynamic environment. In order to reinforce the solution processing capabilities of the contract network algorithm, three contract interaction methods, namely, sales contracts, exchange contracts, and replacement contracts, are used for task allocation to achieve better application effects. The negotiation of contract among swarm members is shown in Figure 5, and the contract is proceeded by members is shown in Figure 6.

(1) Contract sale

It is assumed that all tasks to be planned in the initial state are executed by the master satellite S_i in the process of allocating tasks. Contract sale means that the master satellite S_i assigns a task to be planned T_k^i to a slave satellite S_j through negotiation, so as to achieve a higher overall efficiency after allocation. The detailed steps are as follows:

(i) Step 1: the master satellite (auctioneer) S_i announces a task T_k^i from its task sequences to the market, using intersatellite communication to broadcast a tender invitation of the task

(ii) Step 2: after S_j received the auction information of the task T_k^i, self-efficiency variance produced in task execution can be calculated by

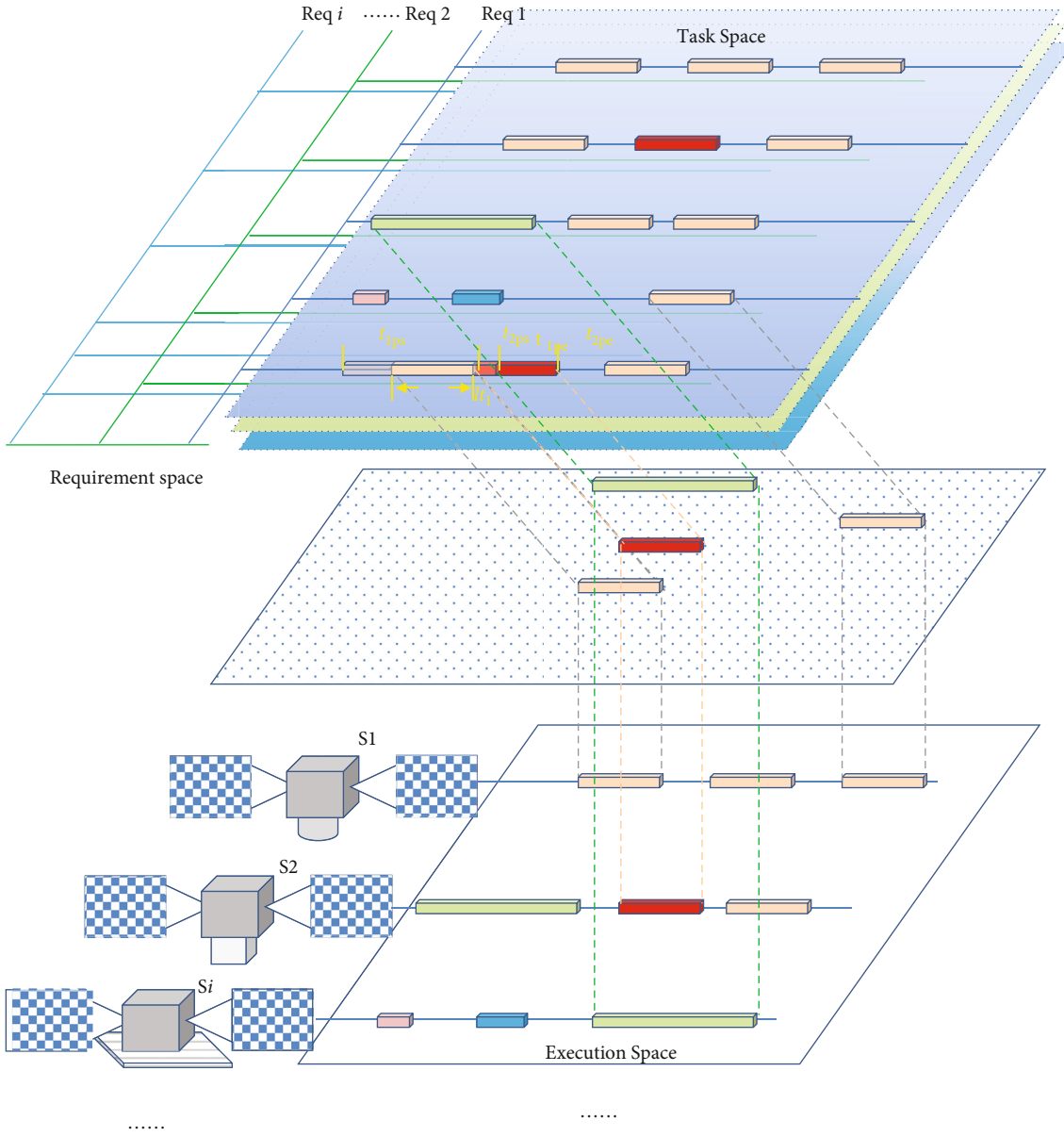

Figure 4: Swarm task allocation process model diagram.

$$\Delta I_j^+\left(T_k^i\right) = I_j\left(S_j \cup \left\{T_k^i\right\}\right) - I_j\left(S_j\right) \quad (1)$$

(i) Step 3: a bidding intention is sent to the auctioneer S_i from S_j when $\Delta I_j^+(T_k^i) > 0$

(ii) Step 4: after receiving the tender information, S_i starts calculating the change in overall efficiency $\Delta I_{i,j}^{\text{sale}}(T_k^i)$ of the system after accepting the biding, which can be obtained by

$$\Delta I_{i,j}^{\text{sale}}\left(T_k^i\right) = \Delta I_j^+\left(T_k^i\right) \quad (2)$$

(i) Step 5: the contract is signed and the task is transmitted to S_j for execution, if S_j can maximize the overall efficiency (has the greatest variation value $\Delta I_{i,j}^{\text{sale}}(T_k^i)_{\max}$)

(2) Contract exchange

Contract exchange means that after the slave satellite S_j gets a task to be planned T_k^i; it replaces its original task T_l^j to be executed and gives T_l^j to the master satellite S_i for execution, so as to obtain a higher overall efficiency. The detailed steps are as follows:

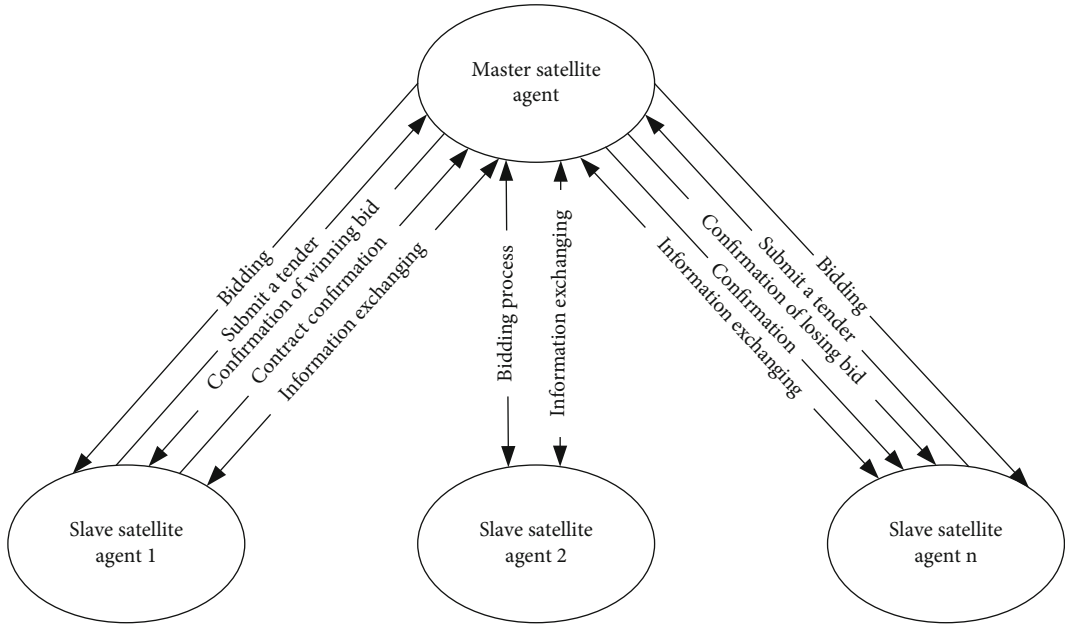

Figure 5: Task negotiation and allocation process based on contract net algorithm.

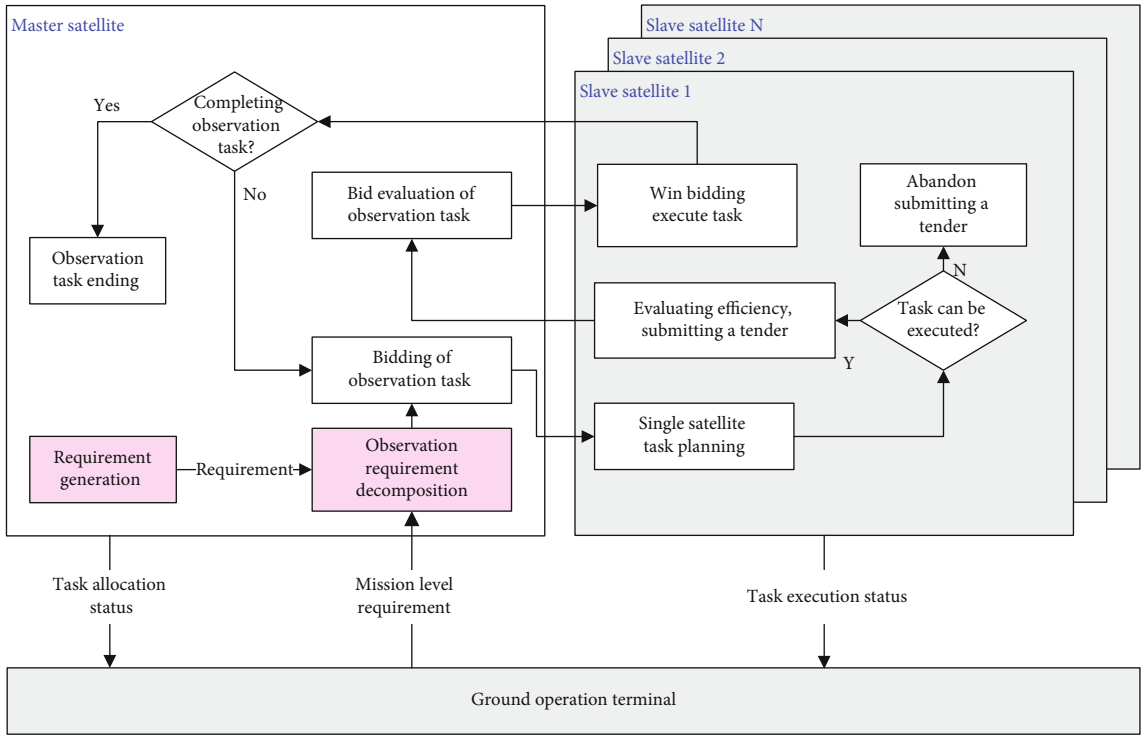

Figure 6: Swarm collaborative task allocation and planning process.

(i) Step 1: contract exchange starts when S_j cannot propose a valid bidding intention, after receiving the bidding announcement of task T_k^i from S_i

(ii) Step 2: S_i proposes to exchange its task T_l^j with task T_k^i, meanwhile, calculates the self-efficiency variance produced in task exchange by

$$\Delta I_j^{\text{swap}}\left(T_k^i, T_l^j\right) = I_j\left(S_j \cup \left\{T_k^i\right\}\right) \setminus \left\{T_l^j\right\} - I_j\left(S_j\right) \quad (3)$$

(i) Step 3: obtain the variance of self-efficiency and overall efficiency by the following equations after the exchange is realized, if S_i accepts the tender:

$$\Delta I_i^{\text{swap}}\left(T_k^i, T_l^j\right) = I_i\left(S_i \cup \left\{T_l^j\right\}\right) - I_i(S_i),$$
$$\Delta I_{i,j}^{\text{swap}}\left(T_k^i, T_l^j\right) = \Delta I_i^{\text{swap}}\left(T_k^i, T_l^j\right) + \Delta I_j^{\text{swap}}\left(T_k^i, T_l^j\right) \tag{4}$$

(i) Step 4: the contract exchange is established if $\Delta I_{i,j}^{\text{swap}}(T_k^i, T_l^j) > 0$, and the overall efficiency can be maximized among all bids in this round

(3) Contract replacement

Contract replacement means that after the slave satellite S_j gets a task to be planned T_k^i, it replaces its original task to be executed T_l^j and directly obtains a higher overall efficiency; the slave satellite S_j can initiate a negotiated allocation mechanism and allocate this task to other slave satellites such as S_k for execution, thereby further increasing the overall revenue. The detailed steps are as follows:

(i) Step 1: contract replacement is only selected when S_j cannot propose a contract of sale, and the proposed contract of exchange is not accepted

(ii) Step 2: the variance of self-efficiency and overall efficiency after replacement is calculated by

$$\Delta I_j^{\text{replace}}\left(T_k^i, T_l^j\right) = I_j\left(\left(S_j \cup \left\{T_k^i\right\}\right) \setminus \left\{T_l^j\right\} - I_j(S_j),$$
$$\Delta I_{i,j}^{\text{replace}}\left(T_k^i, T_l^j\right) = \Delta I_j^{\text{replace}}\left(T_k^i, T_l^j\right) \tag{5}$$

(i) Step 3: the contract replacement is established if $\Delta I_{i,j}^{\text{replace}}(T_k^i, T_l^j) > 0$, and the overall efficiency can be maximized among all bids in this round

Using this algorithm framework, a mission-level task collaborative allocation and planning process is designed, including potential target searching, moving target tracking, and sensitive target feature confirmation. The contract network allocation part of the three types of algorithm processes is exactly the same. The difference lies in the observation requirement generation and the observation task decomposition part, that is, the task-level observation requirement is generated according to specific rules for the task to be planned.

3.3. Fundamental Algorithms in Task Allocation Model

3.3.1. Constraint Model. There are various constraints in multisatellite task allocation, and setting constraints reasonably can reduce the solution complexity with high model practicability. The variable notations are divided into satellite space and task space which are integrated in Table 1.

Assume tasks is $T_i \in T, 0 < i < N_T$ (N_T is the number of tasks to be planned in the collection), satellite $S_j \in S, 0 < i < N_S$ (N_S is the number of satellites in allocation system), the constrains in two aspect is as follows:

(1) Satellite part

(i) Resource constraint: the real-time S_j energy needs to be higher than the minimum allowable energy $E_{S-\min}$ during complete task collection T_{Sj} process, and lower than nominal energy $E_{S-\max}$; the amount of data should not exceed storage

$$E_{S-\min} < E_{Sj} < E_{S-\max},$$
$$G_{Sj} < G_{S-\max} \tag{6}$$

(ii) Attitude range constraint: satellite attitude in anytime At_i must be within the possible attitude of the satellite and meet the requirement of incidence angle:

$$|\text{At}_i| \le |\text{At}| \tag{7}$$

(iii) Attitude maneuvering time constraint: Figure 7 is the schematic diagram of attitude maneuver between neighbor tasks. The attitude maneuver must not exceed the maneuverable limit between tasks, during S_j complete task collection T_{Sj} process:

$$(t_{Ac})_{i-1}^i \ge (t_{Ac-\min})_{i-1}^i, i-1>0,$$
$$(t_{Ac})_i^{i+1} \ge (t_{Ac-\min})_i^{i+1}, \tag{8}$$

where $(t_{Ac})_{i-1}^i$ is the maneuvering time from task T_{Sj}^{i-1} to $T_{Sj}^i$and$t_{Ac-\min}$is the maneuvering time correspond to maximum maneuvering power between neighbor tasks

(iv) Camera working time constraint: the time for S_j to complete task collection T_{Sj} must not exceed the limit imaging time

$$\sum_{i=1}^{N_T} \Delta t_i \le t_{w-\max} \cdot n_o, \tag{9}$$

where Δt_i is the imaging time for task T_i and n_o denotes the number of orbits which the task collection T_{Sj} distribute

Table 1: Variable names and representation notations.

Satellite part		Task part	
Variable name	Representation notation	Variable name	Representation notation
The collection of satellites	$S = \{S_1, S_2, \cdots, S_{N_S}\}$	The collection of tasks to be planned	$T = \{T_1, T_2, \cdots, T_{N_T}\}$
The collection of sorted tasks	$T_S = \{T_S^1, T_S^2, \cdots, T_S^n\}$	Geographic information	$\langle lla \rangle$
Image type of payload	H	Priority level	ω
Image spatial resolution	F	The collection of visible time periods	$W = \{[\text{sw}, \text{ew}]\}$
Energy	E	The earliest start and the latest end of imaging moment	est, let
The amount of stored data	G	Scheduled imaging periods	$\langle \text{set} \rangle = [\text{st}, \text{et}]$
Attitude maneuverability	Ac	Scheduled playback period	$\langle \text{seht} \rangle = [\text{sht}, \text{eht}]$
Attitude range	At	Image type requirements	h
Maximum imaging duration for one orbit	$t_{w-\max}$	Image resolution requirements	f
Replay period collection	$W' = \{[W'_s, W'_e]\}$	Minimum solar altitude angle	$\gamma_{\min}$

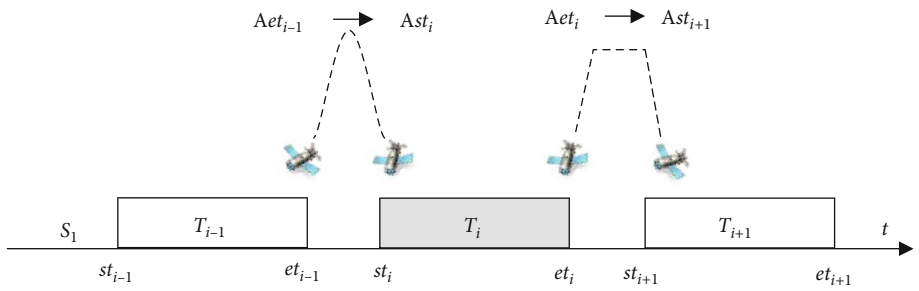

Figure 7: Attitude adjust between neighbor tasks.

(2) Task part

(i) Time constraint: the image task for S_j to T_i must be scheduled during the expected imaging time period and in the visible time collection W_{ij}. Playback activities should occur in the available playback part and does not precede the imaging action

$$\begin{aligned} &\langle \text{elt} \rangle = [\text{est}, \text{let}], \\ &\text{set}_i \subset W_{ij}, \text{set}_i \subset \text{elt}_i, \\ &\text{seht}_i \subset W'_{ij}, \text{sht}_i \leq \text{st}_i \end{aligned} \tag{10}$$

(ii) Imaging request constraint: the satellite payload type needs to match the image type and the resolution requirements of the task

$$H = h, F \geq f \tag{11}$$

(iii) Task revisit constraint: except multiple revisits request, the execution of tasks is unique

$$T_{Sj} \cap T_{Sl} = \varnothing \tag{12}$$

(iv) Solar altitude angle constraint: a typical optical task specifies the sun elevation angle γ range of the imaging to guarantee image quality

$$\gamma > \gamma_{\min} \tag{13}$$

3.3.2. Task Allocation Purpose. The multisatellite Earth observation mission planning process should meet the imaging constraints mentioned in Section 3.3.1; meanwhile, different planning schemes may be generated from different

Table 2: Main initial orbital elements of the satellite in simulation.

UTC time: 2018-06-01 10:30:00				
Orbital plane number	1	2	3	4
Satellite number	1 ~ 6	7 ~ 12	13~18	19~24
Semi-major axis (km)	7024.0	7124.0	7174.0	7224.0
RAAN (°)	256.5	346.5	166.5	76.5
True anomaly (°)		{0.0, 60.0, 120.0, 180.0, 240.0, 300.0}		

optimization angles, and the optimization target is usually given by the ground station. In order to simplify the solution complexity and highlight the task benefits in the dynamic environment, this work take the overall task efficiency of the system as the optimization goal of the algorithm as follows:

$$\max \sum_{j=1}^{N_S} \sum_{i=1}^{n_j'} \frac{1}{\omega_i}, \tag{14}$$

where ω_i is the priority of task T_i in I, which reflects the task importance, and n' is the number of payload task after planning the dynamic task T. The state of dynamic tasks changes rapidly over time, and the earlier the imaging, the greater the probability of high yield, so the yield probability function $P(rt_i)$ is introduced.

$$\begin{aligned} \mathrm{rt}_i &= \mathrm{et}_i - \mathrm{est}, \\ P(\mathrm{rt}_i) &= 1 - \frac{\mathrm{rt}_i}{\mathrm{let} - \mathrm{est}} = \frac{\mathrm{let} - \mathrm{et}_i}{\mathrm{let} - \mathrm{est}}, \end{aligned} \tag{15}$$

where rt_i is the task respond time, which reflects the response system speed to the task. The online earnings indicator after the introduction of $P(\mathrm{rt}_i)$ is as follows:

$$I : \max \sum_{j=1}^{N_S} \sum_{i=1}^{n_j'} \left(\frac{1}{\omega_i} \cdot \frac{\mathrm{let} - \mathrm{et}_i}{\mathrm{let} - \mathrm{est}} \right). \tag{16}$$

3.3.3. Optimization Model in Moving Target Allocation Method. Moving target online task planning problems can be seen as a type of online decision-making problem with real-time rolling updates of tasks, which need to be considered from the stage and the whole. The optimization is as follows:

(1) Overall purpose: in a fixed period of time, the higher the observation frequency of a moving target, the smaller the probability of tracking lost, and the higher the theoretical observation efficiency. Therefore, for the whole process of observation, the overall optimization goal is best time resolution RT

$$\begin{aligned} &I : \min \mathrm{RT} \longrightarrow \min \sim p, \\ &\mathrm{RT} = \frac{1}{n-1} \sum_{i=1}^{n-1} (\mathrm{et}_{i+1} - \mathrm{et}_i),\ 0 < i \le n, \end{aligned} \tag{17}$$

Table 3: Remote sensor simulation parameters.

Remote sensor parameters	Parameter settings
SAR incidence angle	10°~60°
$\gamma_{\min}$	20°
Optical remote sensor width/spatial resolution	100 km/15 m
SAR remote sensor width/spatial resolution	130 km/20 m
Hyperspectral remote sensor width/spatial resolution	50 km/20 m
Hyperspectral remote sensor spectral resolution	10 nm

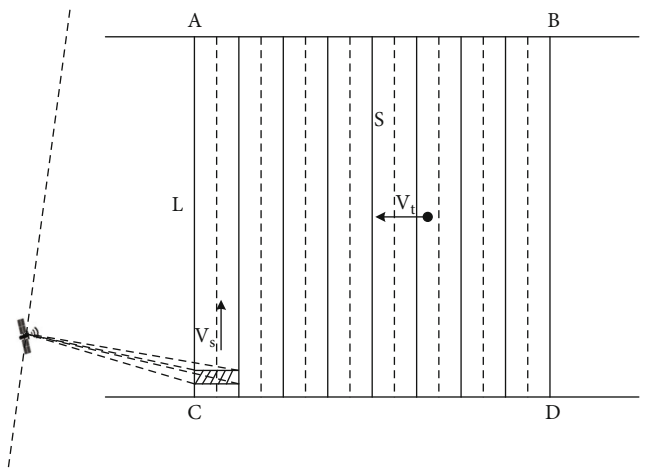

Figure 8: Observation model of swarm potential target search mission.

where n is the subtask executing times and $\sim p$ is the disappearance probability

(2) Single subtask stage objective: since the moving target has the highest priority, the observational benefit of the moving target subtask T_i is expressed as the best system's response speed rt to the subtask

$$\begin{aligned} &I' : \min \mathrm{rt} \longrightarrow \min A_i \longrightarrow \max p_i, \\ &rt = \mathrm{et}_i - \mathrm{est}_i,\ 0 < i \le n, \end{aligned} \tag{18}$$

where I' is the response of the overall goal in the subtask stage; the earlier the subtask time corresponds to the smaller the target potential area A_i, the greater the target discovering

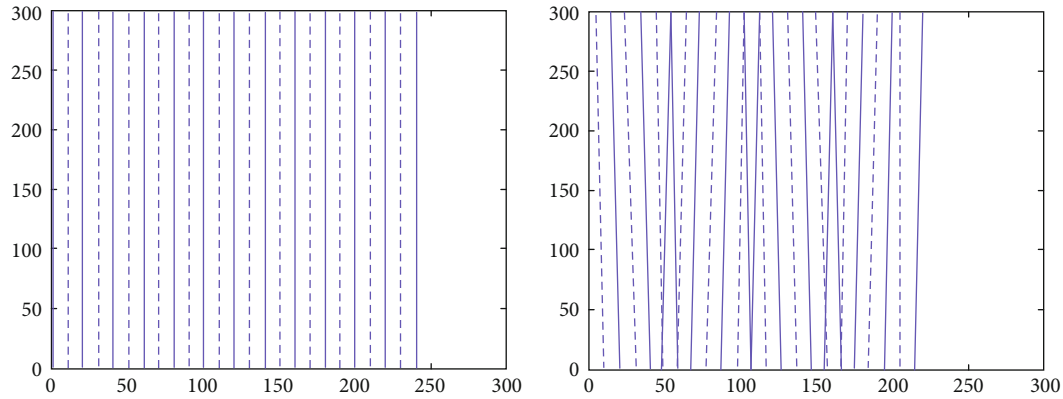

Figure 9: Different search strategies scheme.

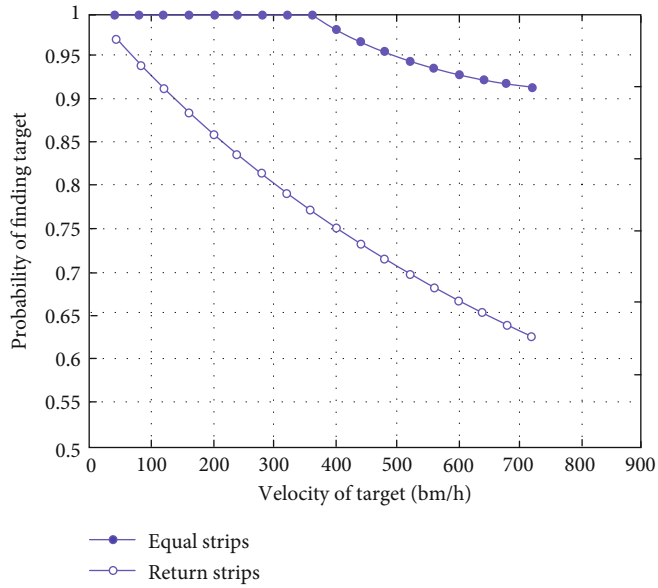

Figure 10: Probability of target discovery based-on different search strategies.

probability p_i. At the same time, the task is guaranteed to be executed as early as possible in the allocation process of each subtask, which will help reduce the time interval between tasks and is beneficial for improving the time resolution of the task, $I' \propto I$.

3.3.4. Optimization Model in Sensitive Target Allocation Method. Sensitive target task planning problems can be seen as an allocation problem combined with a specified time period and resource type. Besides the constraints given in Section 3.1, since the sensitive target must be observed multiple types of remote sensors $\{h\}$, the absence of an image type will let the task being unable to execute, the constraint is expressed as follows, where n denotes the total number of task performed for each type of satellite:

$$s.t.\{h\} = \bigcup_{i=1}^{n} H_i. \tag{19}$$

Time correlation needs to be considered during multitype image fusion, and the more similar the multisatellite imaging time, the higher the time correlation of the plan, and the higher the fusion images yield. Thus, the total execution efficiency for sensitive targets can be defined as the time similarity degree R of various images as follows:

$$\begin{aligned} R &= \max\ d(T_i, T_j), i, j \le n, i \ne j, \\ d(T_i, T_j) &= \left| \frac{\mathrm{st}_i + \mathrm{et}_i}{2} - \frac{\mathrm{st}_j + \mathrm{et}_j}{2} \right|, \end{aligned} \tag{20}$$

where d denotes the time period of any two different types of satellite missions, which is defined as the absolute value of the difference between the two imaging times due to the short execution time of the point target. R is the maximum of d, which represents the maximum time interval in times of imaging. Therefore, the smaller the R, the higher the

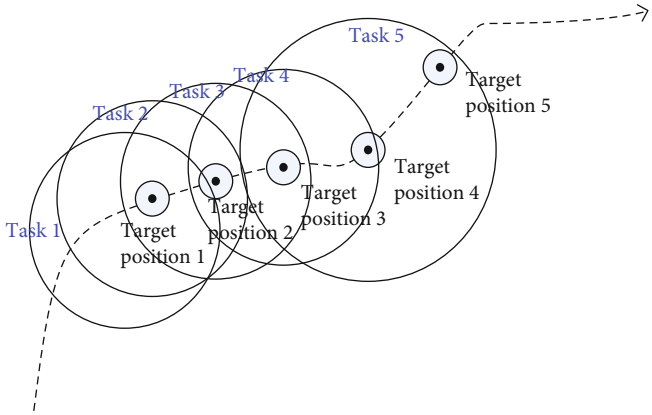

Figure 11: Observation model of swarm moving target tracking task.

image correlation degree is. Thus, the goal of the sensitive target task planning is the highest time correlation, and the purpose of the planning is to select a satellite with a similar imaging time for observation.

$$I = \min R = \min d\left(T_i, T_j\right). \tag{21}$$

4. Simulation of Self-Organizing and Assignment Process of Mission-Level Tasks

4.1. Simulation Environment. The simulation experiments are carried out on a computer with 4 G RAM. The designed satellite swarm earth observation system in this simulation includes 24 satellites: 4 orbital planes, and each orbital plane is distributed with 6 satellites, their orbital parameters are included in Table 2. Satellites are numbered as $6 \times O - 5 \sim 6 \times O$ (1 ~24), O is the orbital plane number. The even-numbered satellites carry SAR payloads, and the odd-numbered satellites carry optical payloads, with a ratio of 1 : 1. In Section 4.4, 8 satellites $(6 \times O - 2, 6 \times O - 4)$ are replaced with hyperspectral payload. The initial orbital elements and remote sensor simulation parameters are shown in Tables 2 and 3.

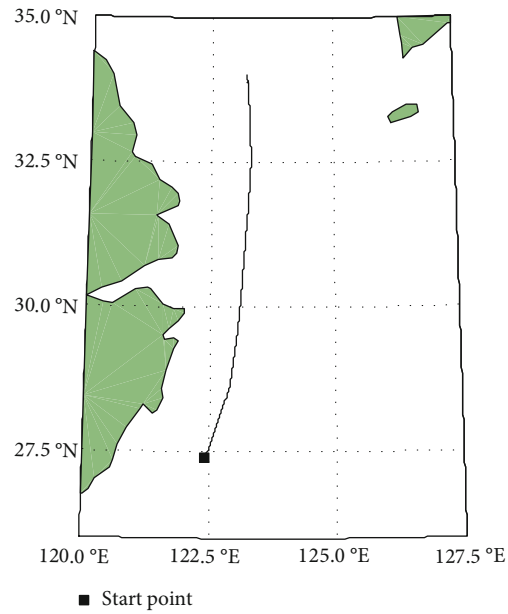

Figure 12: Ship's 24-hour trajectory setting.

4.2. Simulation of Task Allocation Process for Swarm Potential Target Searching. For the potential target searching task, a brief observation task model can be established, as shown in Figure 8. Suppose the area of concern is S, the satellite push-broom imaging direction length is L, the push-broom speed is V_s, and the maximum possible target moving speed is V_t. Considering that different types of satellites have different working modes, the push-broom direction of the satellite may be the direction shown in the figure or its reverse. At the same time, some satellites have agile imaging capabilities, that is, images of multiple strips can be acquired in one orbit, depending on the agile mobility of the satellite and the strip length L.

Since the initial position of the target in the area is unknown and the movement is unknown, the area must be searched in a full-coverage manner. But just covering the entire area is not enough. Since the coverage process is completed by multi-satellites, there is discontinuity. Between two observations, the target may move from an uncovered area to a covered area, causing the search to fail.

In response to the above problems, after the master satellite completes the strip segmentation and launches the task bidding, it needs to constantly repropose the time-constrained observation task requirements based on the completed coverage area and the worst estimation of the target motion, and the covered area entered need to be covered again. For example, as shown in Figure 9, assuming that the initial task bidding starts from the leftmost strip in the figure, the worst movement of the target is to move to the left. Therefore, the stripe range of the next bidding task should be considered to have a certain overlap with the previous one.

This self-organizing target search process is tested by simulation. Assuming that the target area has a length of 300 km in the east-west direction and 300 km in the north-south direction, several agile satellites are distributed in orbit, and there are different imaging directions. Assuming

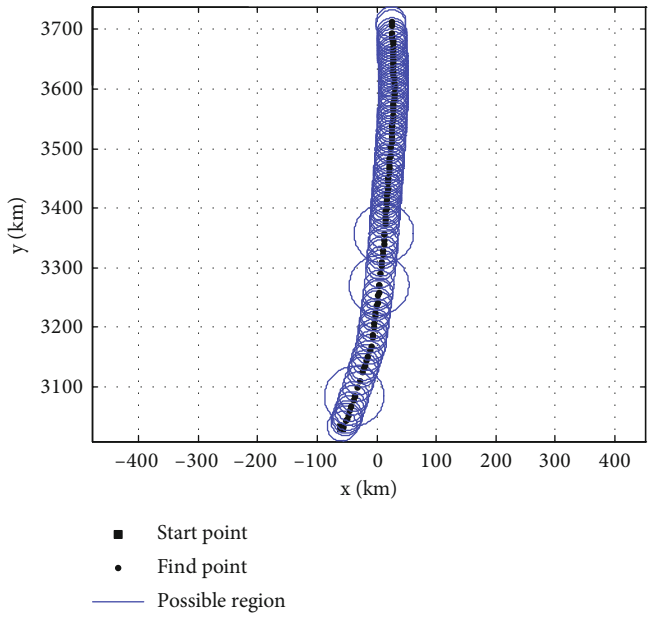

Figure 13: Simulation result of ship's 24-hour voyage tracking process.

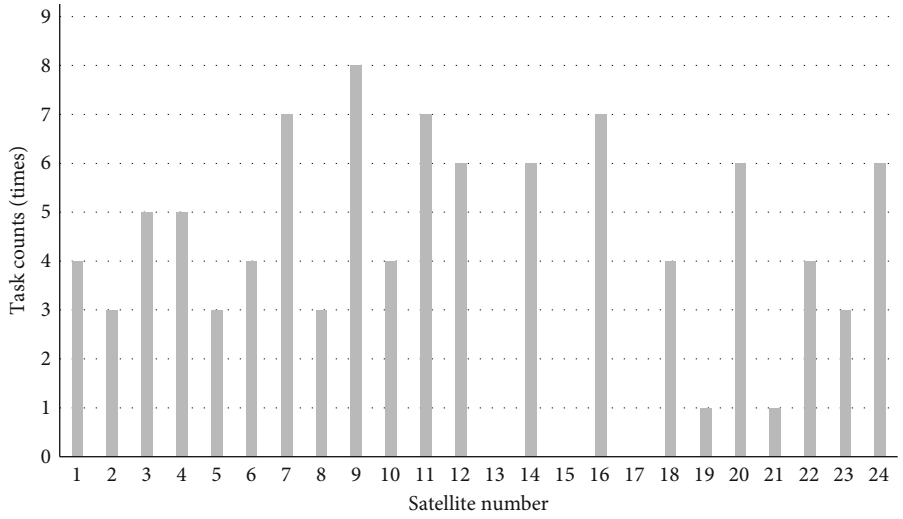

Figure 14: The result of the imaging task allocation of each satellite.

that the satellite has strong agility, it can complete 3 strips in one pass. At the same time, there are many satellites. After one satellite completes the imaging task, the next satellite can be immediately scheduled for imaging. Compare and analyze the effectiveness of two strategies: stripe equipartition search and stripe return search. The stripe equipartition search is shown in Figure 9(a), and the target area is divided into several stripes according to the satellite imaging width; the stripe return search is shown in Figure 9(b), and after the imaging is completed on the previous satellite, the next satellite is completely adjacent to the covered area at its push-broom starting point, and a horizontal search speed is added during the push-broom to form a certain overlap with the covered area.

This article assumes that the push-broom speed is 6 km/s, and the lateral search speed is 0.12 km/s. A large number of simulations are performed by randomly generating target positions to obtain the discovery probability of targets with different moving speeds, as shown in Figure 10.

It can be seen in Figure 10 that with the increase of target speed, the search strategy of stripe equalization reduces the probability of target discovery rapidly, while the stripe return search strategy can better maintain the ability to find the target. Combining the estimation of the target speed in orbit, by adjusting the return speed, the target can be fully discovered.

4.3. Simulation of Task Assignment Process for Moving Target Tracking. For moving target tracking tasks, limited

by the orbiting of satellites, it can only be achieved through intermittent, high-frequency imaging of different satellites. During each imaging time, what the satellite knows is only the potential area of the moving target. The potential area will become larger as the observation interval increases and is also affected by geographic conditions. These factors need to be considered when the master satellite is planning to track and imaging missions in orbit.

After the swarm receives the task of tracking and observing the moving target, the master satellite analyzes the potential area of the moving target and completes task assignment and planning through intersatellite negotiation. According to the task execution result, the recursive trajectory is used to predict the potential location range of the target, and new observation tasks are planned and assigned until the tracking task ends. The observation model of swarm moving target tracking task is represented in Figure 11.

Select the moving target as the ship for simulation test. Assuming that the maximum speed of the ship is 50 km/h, the swarm is configured with 4 orbital planes, and 6 satellites are distributed on each orbital plane, respectively, carrying visible optical or SAR payloads. The ship is found to be active in the sea at (27.4N, 122.4E) at 10:30:00 in the morning. Figure 12 contains the trajectory of the target 24 hours later.

After the tracking task is placed, the master satellite plans and initiates the tracking task. The simulation result of the tracking process is represented in Figure 13.

The task assignment and execution results of each satellite are in Figure 14.

The simulation results in Figure 14 show that imaging tasks are generated and auctioned 100 times; of which 97 tasks are executed with a potential area radius of 25 km; there are no satellite bids for the 3 tasks, and the potential area radius is expanded to 50 km. The cooperation of 24 satellites can complete a continuous day's tracking task, and the imaging quality is high.

The simulation analyzes the swarm of different scales and configurations and the continuous tracking ability of the target. Taking the moving target as above, under the same simulation conditions, adjust the number of orbital surfaces and the number of satellites on the orbital surface, and perform continuous tracking time simulation. The result is shown in Figure 15.

It can be seen in Figure 15 that when the number of orbital surfaces and the number of satellites is small, continuous tracking and observation throughout the day cannot be achieved. When the number of orbital surfaces is not less than 4, the average orbiting satellite is not less than 6, and at least 3 SAR satellites are included, continuous tracking and observation can be achieved throughout the day.

4.4. Simulation of Task Assignment for Sensitive Target Feature Confirmation. After the sensitive target is discovered by ground or earth observing system, it is uploaded to the swarm, and it is expected that the target characteristics can be identified and confirmed through the arrangement of serialized payload imaging tasks. For example, suppose that three types of payloads of A, B, and C are required to detect

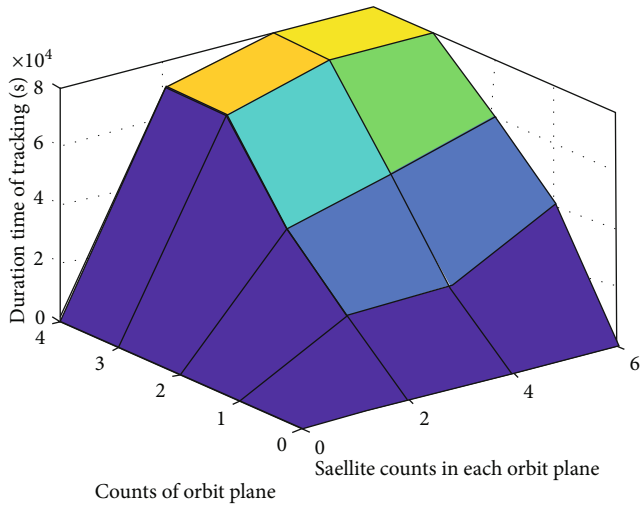

Figure 15: Simulation result of continuous tracking capabilities of swarms of different scales.

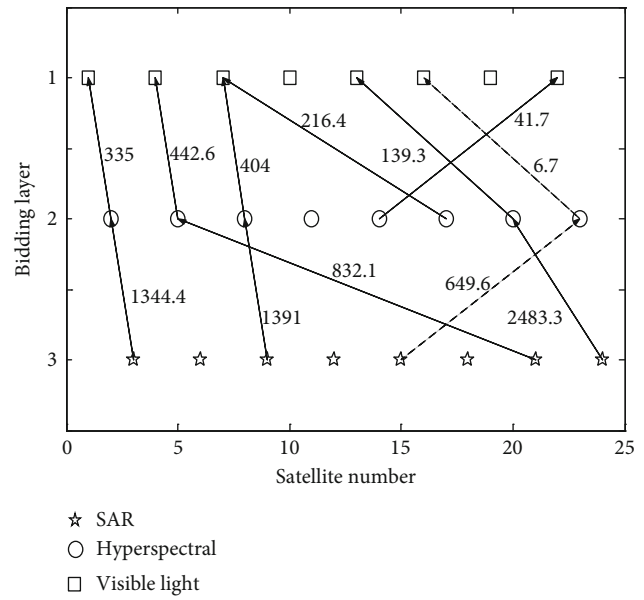

Figure 16: Group bidding model for sensitive target feature confirmation task.

and image the target in sequence, and the constraint condition is that the time interval between the three imaging operations is as short as possible to obtain the observation information of the target at the same time. Therefore, the task bidding process of the sensitive target feature confirmation task is multilayered and comprehensively optimized.

Multilayer, in accordance with the order of load types, the first layer of the A load is first tendered to form multiple bidding results. After that, in accordance with the principle of the closest time to the first-tier results, the bidding obtains the second-tier bidding results for the B-type load and forms several groups of team bidding results with directions. After analogy, the third-tier bidding result for the C-type load is obtained. Finally, the master satellite will evaluate the

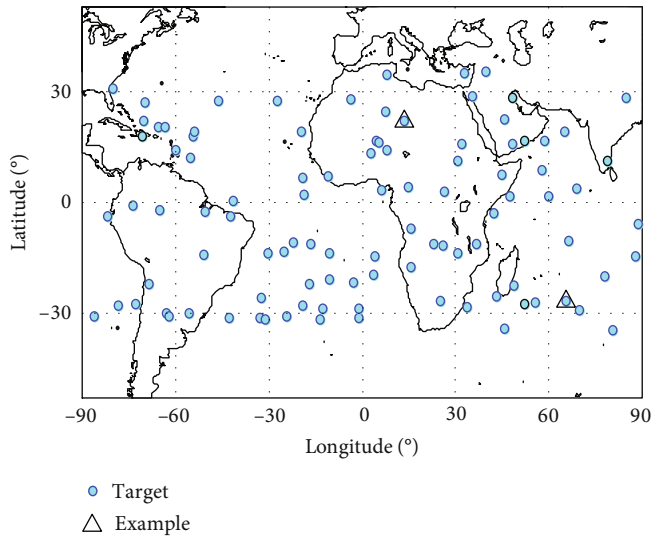

Figure 17: 100 groups of sensitive target distribution settings.

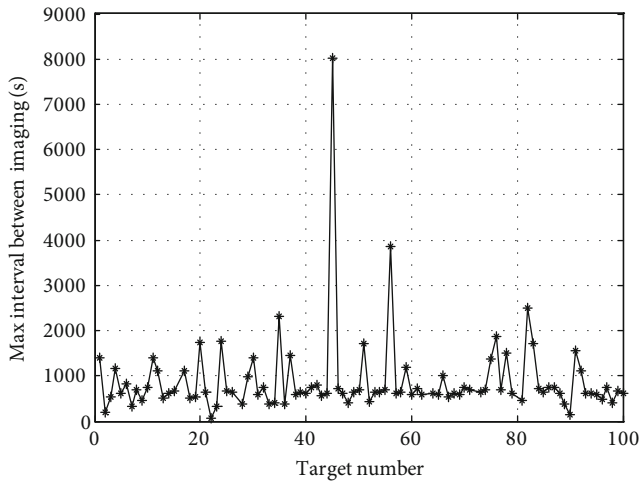

Figure 18: Simulation result of 100 groups of sensitive target observation.

effectiveness of all team bidding results. The evaluation criteria are the shortest task response time and the shortest team imaging process time. After three times of bidding, the bid-link result is represented in Figure 16.

The arrows in Figure 16 represent the bidding direction, and the marked numbers are time costs between the bidding plan and the directing plan. There are 5 complete bid link paths for this sensitive task. Using the bid evaluation method, iterate these paths from the third-tier back to select the optimal path $15 \longrightarrow 23 \longrightarrow 16$, which represented as the dotted line.

100-point targets are randomly generated on the map as sensitive targets, and 100 sets of experiments are performed, as shown in Figure 17. It is assumed that the designated bidding order of the target is visible light, hyperspectral, and SAR, and the team imaging time interval R is defined as the time interval between the first imaging and the last imaging, which represents the worst correlation of different types of images.

It can be seen from the Figure 18 that 5 targets are located in umbra during the planning period, and there is no visible optical satellite bidding, and the mission is directly abandoned. Therefore, the mission completion rate is 95%. Three targets are approaching the umbra during the planning period, and also affected by the scheduled high-level tasks, so that the team imaging time interval R is relatively large. The team imaging time interval R of most targets is below 1800s, with an average of 788.5 s. It can be concluded that, under suitable observation conditions, different targets can find a team of satellites within a closed imaging time through multisatellite negotiation to perform sequence observation tasks.

5. Conclusion

Large-scale swarm is the development trend of space-based earth observation system in the future. For swarm, mission-level task self-organization and collaboration techniques are important research topics, including potential target searching, moving target tracking, and target feature confirmation. This paper adopts the distributed task allocation method based on the improved contract network algorithm to realize the optimal allocation of inter-satellite tasks, that is, the mapping of swarm tasks from task space to execution space. Based on this, a mission-level task swarm coordination task allocation and planning process is designed, including some algorithms for the generation of observation requirements and the decomposition of observation tasks for different task types, as well as a common contract network allocation algorithm. Simulations are carried out on typical mission scenarios, focusing on the performance of different methods of potential target searching strategies, the effectiveness of tracking moving targets of different swarm scales, and the ability of multisatellite team bidding to complete sensitive target feature observation

tasks. Results verify that the improved contract network algorithm can solve the problem of optimizing the assignment of swarm mission-level observation tasks well and has potential in engineering application.

Data Availability

The data used to support the findings of this study are included within this paper.

Conflicts of Interest

The authors declare that there is no conflict of interest regarding the publication of this paper.

Acknowledgments

This work is supported in part by the project D020214, the Fundamental Research Funds for the Central Universities (No. 3072022JC0202).

References

[1] X. Yang, H. Mingren, S. Jiang, and L. Delin, "Attitude antagonistic consensus control of satellite swarm system based on MRPs," *Systems Engineering and Electronics*, vol. 43, no. 7, pp. 1904–1911, 2021.

[2] D. Izzo and L. Pettazzi, "Autonomous and distributed motion planning for satellite swarm," *Journal of Guidance, Control, and Dynamics*, vol. 30, no. 2, p. 449, 2007.

[3] A. Farrag, S. Othman, T. Mahmoud, and A. Y. ELRaffiei, "Satellite swarm survey and new conceptual design for Earth observation applications," *The Egyptian Journal of Remote Sensing and Space Science*, vol. 24, no. 1, pp. 47–54, 2021.

[4] H. Chuan, Z. Xiaomin, and Q. Dishan, "Cooperative scheduling method of multi-satellites for imaging reconnaissance in emergency condition," *Systems Engineering and Electronics*, vol. 34, no. 4, pp. 726–731, 2012.

[5] C. Yingwu, Y. Feng, and L. Jufang, "A learnable ant colony optimization to the mission planning of multiple satellites," *Systems Engineering - Theory & Practice*, vol. 33, no. 3, pp. 791–801, 2013.

[6] Z. Chao and L. Yanbin, "Planning and scheduling method for multi agile satellite coordinated mission," *Science Technology and Engineering*, vol. 17, no. 22, pp. 271–277, 2017.

[7] Z. Chao, L. Yuqing, F. Xiaoen et al., "A ground-onboard joint operation mechanism for the autonomous mission planning of imaging satellite cluster," *Journal of Harbin Institute of Technology*, vol. 50, no. 4, pp. 56–61, 2018.

[8] L. Xiaolu, H. Lei, C. Yingwu, and C. Yinguo, "An adaptive large neighborhood search algorithm for multiple agile satellites coordination and scheduling," *The Fourth China High Resolution Earth Observation Conference, Wuhan, September*, vol. 17, 2017.

[9] H. Chuanqi, L. Yurong, and L. Hu, "Mission planning for small satellite constellations based on improved genetic algorithm," *Chinese Journal of Space Science*, vol. 39, no. 1, pp. 129–134, 2019.

[10] H. Huicheng, J. Wei, L. Yijun, and Z. Yuan, "Research on agile satellite dynamic mission planning based on multi-agent," *Journal of National University of Defense Technology*, vol. 35, no. 1, pp. 53–59, 2013.

[11] C. Taoyi, F. Xiaoen, C. Jinyong, and L. Yuqing, "A multi-satellite autonomous coordination task planning method based on bidding mechanism," *Journal of Harbin Institute of Technology*, vol. 51, no. 4, pp. 138–145, 2019.

[12] Y. Longjiang, W. Xiande, M. Yilan, H. Gao, and Y. Hao, "Task allocation for distributed remote sensing satellites based on contract network algorithm," *Journal of Harbin Engineering University*, vol. 41, no. 7, pp. 1059–1065, 2020.

[13] W. Xiande, W. Bai, Y. Xie, X. Sun, C. Deng, and H. Cui, "A hybrid algorithm of particle swarm optimization, metropolis criterion and RTS smoother for path planning of UAVs," *Applied Soft Computing Journal*, vol. 73, no. 12, pp. 735–747, 2018.

[14] X. Sun, W. Xiande, W. Chen, Y. Hao, K. A. Mantey, and H. Zhao, "Dual quaternion based dynamics modeling for electromagnetic collocated satellites of diffraction imaging on geostationary orbit," *Acta Astronautica*, vol. 166, pp. 52–58, 2020.

[15] X. Wu, H. Zhao, B. Huang, J. Li, S. Song, and R. Liu, "Minimum-learning-parameter-based anti-unwinding attitude tracking control for spacecraft with unknown inertia parameters," *ACTA Astronautica*, vol. 179, pp. 498–508, 2021.

[16] X. Zhang, W. Zhu, X. Wu, T. Song, Y. Xie, and H. Zhao, "Dynamics and control for in-space assembly robots with large translational and rotational maneuvers," *Acta Astronautica*, vol. 174, pp. 166–179, 2020.

[17] Z. Zhu, Y. Luo, H. Wei et al., "Atmospheric light estimation based remote sensing image dehazing," *Remote Sensing*, vol. 13, no. 13, p. 2432, 2021.

[18] Z. Zhu, Y. Luo, G. Qi, J. Meng, Y. Li, and N. Mazur, "Remote sensing image defogging networks based on dual self-attention boost residual octave convolution," *Remote Sensing*, vol. 13, no. 16, p. 3104, 2021.

[19] H. Zhao, X. Wu, Y. Xie, Y. Du, Z. Zhang, and Y. Li, "Rotation matrix-based finite-time attitude synchronization control for flexible spacecrafts with unknown inertial parameters and actuator faults," in *ISA Transactions*, Elsevier, 2021.

[20] W. Zhou, Z. Xing, B. Wenbin, D. Chengchen, Y. Xie, and X. Wu, "Route planning algorithm for autonomous underwater vehicles based on the hybrid of particle swarm optimization algorithm and radial basis function," *Transactions of the Institute of Measurement and Control*, vol. 41, no. 4, pp. 942–953, 2019.

Hindawi
International Journal of Aerospace Engineering
Volume 2022, Article ID 3451171, 16 pages
https://doi.org/10.1155/2022/3451171

Research Article

A Convex Approach for Trajectory Optimization of Super-Synchronous-Transfer-Orbit Large Launch Systems with Time-Position Constraints

Yuan Li,[1] **Ruisheng Sun**,[1] **Wei Chen**,[1] **and Nan Yang**[2]

[1]*Nanjing University of Science and Technology, Nanjing 210094, China*
[2]*Shanghai Institute of Aerospace System Engineering, Shanghai 200000, China*

Correspondence should be addressed to Ruisheng Sun; rs.sun@njust.edu.cn

Received 12 January 2022; Accepted 8 June 2022; Published 10 August 2022

Academic Editor: Shunan Wu

This paper presents a trajectory optimization algorithm for super-synchronous-transfer-orbit (SSTO) large launch systems by convex optimization. The payload of SSTO launch systems is typically a geostationary equatorial orbit (GEO) satellite, and the time and position of orbital injection are constrained, which is quite different from the case of general satellites. In this paper, the optimal control problem of SSTO large launch systems is formulated considering the terminal constraints including orbital elements and the time-position equation. To improve the computational performance of the algorithm, the terminal orbital element constraints are expressed in the perifocal coordinate system with second-order equations. And then, several convexification techniques and their modified strategies are applied to transform the original trajectory optimization problem into a series of convex optimization problems, which can be solved iteratively with high accuracy and computational efficiency. Considering the time-position constraint of the payload, the flight time updater design method is proposed to correct the error of time during the flight, which lays solid foundation for the subsequent flight phase, guaranteeing that the GEO satellite settles into the required position. Finally, simulation results indicate the high efficiency and accuracy and strong robustness of the proposed algorithm in different special situations including engine failure and time delay. The algorithm proposed in this paper has great development potential and application prospect in onboard trajectory optimization of SSTO launch missions and similar situations.

1. Introduction

Geostationary equatorial orbit (GEO) is a special circular earth orbit, in which satellites remain relatively stationary with the earth, and the ground stations do not have to track the satellites [1]. The GEO attitude is 35786 kilometers, where the visible portion of the earth's surface is very large. Because of these meaningful properties, the satellites for communication, global weather, radio, etc. are always placed in GEO [1]. However, in order to avoid interference with other satellites in GEO, and achieve predetermined functions, the satellites should stay above the predetermined point on the earth's equator. In other words, the time and position of orbital injection for GEO satellites are strictly constrained, which is different from the case of general satellites [2, 3]. Because of the high attitude of the GEO, the scale of the launch system is always very large, and the special situations such as engine failure of large launch systems should be considered.

In general, there are three flight phases from the satellite launching to the satellite settling into the GEO. Firstly, the launch system put the satellite and upper stage into a low earth orbit (LEO), which is a circular orbit locating 200 km~400 km away from the surface of the earth. After that, the launch system will park in the LEO for a few minutes before turning on the engine of the upper stage and sending the satellite into a geostationary transfer orbit (GTO). GTO is a highly eccentric orbit, of which the perigee is near the parking LEO, and the apogee is near the GEO. Finally, the satellites transfer into the target GEO. In this

paper, super-synchronous-transfer-orbit (SSTO) [4] is adopted to transfer the satellites from LEO to GEO instead of GTO. SSTO has a higher apogee and eccentricity, and the speed increment required by transferring from SSTO to GEO is greater than that required by transferring from GTO to GEO, which is beneficial for saving the propellant in the process of transferring orbit plane to GEO. The mission of launch systems for GEO satellites is to put the payload into the predetermined SSTO accurately, during which the guidance algorithm plays an important role.

As for the ascent phase of launch systems, the iterative guidance method has been widely and successfully used in the past few decades [5, 6]. However, for most rocket engines, the thrust magnitude is uncontrollable, and the time and position of orbital injection cannot be constrained based on the iterative guidance method. When the deviation of the flight time is large, the iterative guidance method cannot correct the error, which will cause more propellant consumption for orbit transfer, or even lead to the failure of settling into the predetermined point of GEO.

In recent years, with the development of computational technologies, the online trajectory optimization method has been developed rapidly, which provides new ideas for solving the optimal guidance and control problems in aerospace applications [7]. Various optimization theories and algorithms have been developed for online or onboard trajectory optimization of different vehicles [8]. There are three important performance indexes for online trajectory algorithms: accuracy, computational efficiency, and robustness [7]. For guidance algorithms, accuracy is certainly the most important index. Considering the limited onboard computing resources, the computation amount and memory occupation of the algorithm should be reduced. The algorithm should also be robust enough to handle the deviation or other situations when the real trajectory is quite different from the nominal one.

Among the trajectory optimization algorithms developed in recent years, including indirect methods and direct methods [9–14], convex optimization algorithms have great advantages in onboard aerospace applications because the convex optimization problem can be solved in polynomial time with no need for initial guesses supplied by the user [15]. However, most of the original trajectory optimization problems are infinite and nonconvex, which cannot be solved by convex optimization methods directly [16]. Thus, the convexification techniques for trajectory optimization problems are widely studied. In general, lossless convexification and successive convexification are two effective methods to convexify the nonconvex term of the trajectory optimization problem. Lossless convexification was proposed to solve general optimal control problems [17–19]. For aerospace applications, lossless relaxation and convexification are always applied to convexify the thrust magnitude constraints [20]. Lossless convexification has been successfully applied to solve the optimization problem of landing vehicles [21], launch vehicles [20], missiles [22], etc. Successive convexification has a broader range of applications. With successive linearization, all the nonlinear and nonconvex terms can be converted into linear ones based on a known solution, which is very simple and of practical significance [16]. On this basis, the original optimization problem can be transformed into a series of convex optimization subproblems, which can be solved iteratively until the solution converges. The convex optimization has been successfully and widely applied to launch vehicles [23], unmanned aerial vehicles [24], hypersonic glide vehicles [25], etc. [26–30].

To solve the trajectory optimization problem of SSTO launch systems accurately and rapidly, a convex-optimization-based algorithm is applied in this work. In general, the terminal constraints of launch missions are expressed as six orbital elements [1], including the semimajor axis, eccentricity, inclination, longitude of the ascending node, argument perigee, and true anomaly. However, the calculating formulas of these elements are very complex and strongly nonlinear, which negatively affects the computational efficiency and convergence of the algorithm during the iteration. To improve the computational performance, the trajectory optimization problem, the terminal constraints are given in the perifocal coordinate system. The perifocal coordinate system is defined in the target orbital plane based on the geometric feature of the elliptical orbit, and the terminal constraints of orbital elements can be formulated simply as linear or second-order equations. After that, several convexification techniques are applied to transform the original trajectory optimization problem into a series of second-order cone programming (SOCP) problems, which can be solved by the primal-dual interior-point method (IPM). IPM is a typical and widely used algorithm for SOCP. For any given initial guess and accuracy, a globally optimal solution can be found by IPM within the predetermined upper bound of iteration times on condition that the feasible solution exists [10]. To ensure the problem can be solved by IPM, the flip-Radau pseudospectral discretization method is adopted to convert the continuous and infinite problem into a finite one, and the thrust magnitude constraint is relaxed based on lossless convexification. Other nonconvexity of the problem is handled by successive convexification. The main procedure of successive convexification is described as follows: linearize the nonlinear part of the solution obtained by the initial guess or the previous iteration and then solve the linearized (convexified) problem iteratively. If the initial guess is not accurate, the solution cannot be found at the beginning of the iteration. To avoid this, the relaxation method is applied [31], but the computational efficiency declines seriously with the additional relaxation variables. In this paper, the successive convexification is modified to improve both the robustness and computational efficiency of the algorithm. Considering the accuracy of linearization and equality constraints, the parameters of optimization and relaxation variables are changed or removed adaptively with the convergence of the solution during the iteration. In this way, the trajectory optimization problem can be solved based on convex optimization with satisfactory computational performance.

Another research focus of this paper is the terminal time and position constraints. As for the GEO satellites, the position of the subastral point is stationary and strictly constrained. In general, the low-thrust stage is often applied to transfer the satellite from SSTO to GTO [32], and the ability of the stage to correct the deviation is weak. Therefore, the

launch mission of SSTO must ensure that the satellite arrives at the point of orbit transfer at a predetermined time, which lays the foundation for orbit transfer and the subsequent on-orbit missions. In other words, the trajectory optimization algorithm should concentrate on the orbital elements and the time/position of orbital injection. In this paper, the terminal constraint of the orbital injection point is formulated as a function of time and eccentric anomaly equivalently. However, as the thrust magnitude of a rocket engine is uncontrollable, it is difficult to constrain the time and position of orbital injection during the flight from LEO to SSTO. To this end, the flight time of parking in the LEO updater design algorithm is studied in this paper. With the adjustment of the time parking in LEO, the time-position of orbital injection can meet the requirement. The algorithm proposed in this paper has strong robustness and can solve the online trajectory optimization problem even under partial engine failure or launch time delay.

This paper is organized as follows. In Section 2, the trajectory optimization problem of SSTO launch systems is formulated. In Section 3, the original trajectory optimization problem is transformed into SOCP subproblems by several modified convexification techniques. In Section 4, the flight time of parking in the LEO updater design algorithm is studied. In Section 5, simulation is carried out to compare the proposed optimization method with the traditional optimization method under different conditions. In Section 6, some conclusions are given.

2. Problem Formulation

Firstly, we formulate the dimensionless equations of motion of SSTO launch systems in the Earth Center Inertial Coordinate System [1] as follows:

$$\begin{aligned} \dot{r} &= V, \\ \dot{V} &= -\frac{1}{\|r\|^3} r + \frac{1}{m g_0} u, \\ \dot{m} &= -\frac{\|u\|}{g_0 I_{\mathrm{sp}}} \cdot \sqrt{\frac{R_0}{g_0}}, \end{aligned} \tag{1}$$

where r and $V \in R^3$ are the dimensionless inertial position and velocity vectors, respectively; m is the mass of the system. u is the thrust vector and also represents the attitude angle of the system. g_0 is the gravitational acceleration magnitude on the surface of the Earth. I_{sp} is the specific impulse of the engine. The distance is normalized by the radius of the Earth at the equator R_0, the time by $\sqrt{R_0/g_0}$, and the velocity by $\sqrt{R_0 g_0}$ [33].

When the payload is boosted into an LEO, the rocket engine turns off and the thrust magnitude $T = 0$. After a few minutes of unpowered flight, the rocket engine of the upper stage turns on, and the payload is boosted into an SSTO. For SSTO launch systems, the thrust magnitude of a rocket engine T is uncontrollable, and the magnitude of the thrust vector is constrained:

$$\|u\| = T. \tag{2}$$

Considering the strict constraints of the terminal position and velocity in the noninertial coordinate system for GEO satellites, the terminal constraints for SSTO launch systems are also important. Traditionally, the terminal constraints of launch systems are expressed as orbital elements: the semimajor axis, eccentricity, inclination, longitude of the ascending node, argument perigee, and true anomaly $[a, e, i, \Omega, \omega, f]$ [1]. As for GEO satellite launch missions, the position of the subastral point is strictly constrained; so, the time and position of the SSTO injection also need to be considered. In other words, the payload should settle into the nominal SSTO, and the position as a function of time should be the same as the nominal one.

For convenience, the terminal constraints of SSTO launch systems can be expressed in the perifocal coordinate system [34]. O is the center of the earth, the 4-axis X_p points towards the perigee, and the Z-axis Z_p is parallel to the normal of the orbital plane (along the positive direction of the normal). The Y-axis Y_p completes the right-hand coordinate system. And then the terminal constraints of SSTO launch systems can be expressed in the perifocal coordinate system as follows:

Considering the accuracy of the semimajor axis, eccentricity, inclination, longitude of the ascending node, and argument perigee, the following five terminal equality constraints must be satisfied:

$$\begin{aligned} \frac{\left(r_{fx} + c\right)^2}{a^2} + \frac{r_{fy}^2}{b^2} - 1 &= 0, \\ \frac{\left(r_{fx} + c\right) V_{fx}}{a^2} + \frac{r_{fy} V_{fy}}{a^2 (1 - e^2)} &= 0, \\ r_{fx} V_{fy} - r_{fy} V_{fx} - h &= 0, \\ r_{fz} &= 0, \\ V_{fz} &= 0, \end{aligned} \tag{3}$$

where b is the semiminor axis and $b^2 = a^2(1 - e^2)$; c is the distance from the center of earth to the center of ellipse orbit and $c = ae$. $h = \sqrt{a(1 - e^2)}$ is the required magnitude of angular momentum. The subscript "f" represents the final value of the parameters.

In addition, the system must settle into SSTO at a certain time and position. As an equivalent transformation, the time and position of injection should satisfy the following condition:

As shown in Figure 1, t_1 and r_1 are the expected time and position of injection, and t_f and r_f are the actual time and position of injection. Δt is the unpowered flight time from r_1 to r_f. ϕ is the eccentric anomaly. If Δt satisfies, then

$$\Delta t = t_f - t_1. \tag{4}$$

The payload can be considered to settle into SSTO at the expected time and position equivalently. According to the

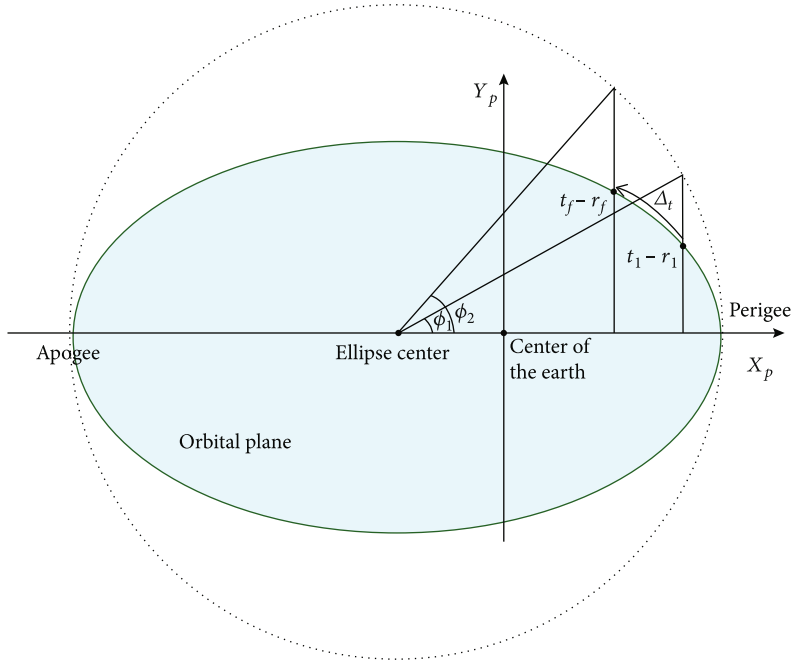

Figure 1: Time-position constraint of SSTO.

Kepler's equation, Δt can be calculated by

$$\Delta t = M_e\left[\phi_f\left(r_f\right)\right] - M_e[\phi_1(r_1)], \tag{5}$$

where M_e is the flight time starting at the apogee, which can be calculated as a function of eccentric anomaly ϕ [1]:

$$M_e = \phi - e\sin\phi. \tag{6}$$

And eccentric anomaly ϕ can be calculated simply in the perifocal coordinate system as follows:

$$\phi = \begin{cases} \arccos\dfrac{r_{xf}+c}{a} & r_{xf} \geq 0, \\ 2\pi - \arccos\dfrac{r_{xf}+c}{a} & r_{xf} < 0. \end{cases} \tag{7}$$

Considering Eqs. (4) and (7), the error of time E_t can be defined as

$$E_t = t_1 - t_f + \left(\phi_f - \phi_1 + e\sin\phi_1 - e\sin\phi_f\right). \tag{8}$$

In conclusion, the terminal constraints of SSTO launch systems are Eqs. (3)–(8). As for most launch systems, because the thrust magnitude is uncontrollable, only five terminal constraints can be guaranteed; so, the time and position of the injection are uncontrollable. In Section 4, the strategy to decrease the error of time E_t is proposed in detail.

Considering the following mission of orbit transfer, the trajectory optimization problem of SSTO launch systems is defined as an optimal control problem to achieve the minimum fuel consumption:

$$\min J = -m\left(t_f\right), \tag{9}$$

subject to

$$\text{Eq.}(1), \text{Eq.}(2), \text{Eq.}(3), \text{Eq.}(8) \quad m_f \geq m_{\text{dry}}, \tag{10}$$

$$x(t_0) = x_0, \tag{11}$$

where the variable $x = [r, V]$, m_{dry}, is the dry mass of the launch system. Equation Eq. (11) is inertial constraints. It is obvious that the original trajectory optimization problem (Eqs. (9) and (11)) is nonconvex. In the next section, the trajectory optimization problem is transformed into a series of SOCP subproblems, which can be solved directly by the primal-dual interior point method rapidly with good accuracy.

3. Convexification

In this section, the original trajectory optimization in Section 2 is transformed into a series of discrete SOCP subproblems by pseudospectral discretization, lossless convexification, and successive convexification. For better computational efficiency, a second-order correction algorithm and an improved relaxation method for successive convexification are proposed.

3.1. Pseudospectral Discretization and Lossless Convexification. To meet the requirement of the convex optimization method, the continuous infinite dynamical constraints are always converted into a finite set of equality constraints by discretization. Considering the accuracy of the terminal constraints in different phases, the flip-Radau pseudospectral discretization method, by which the collocation points discreted within the

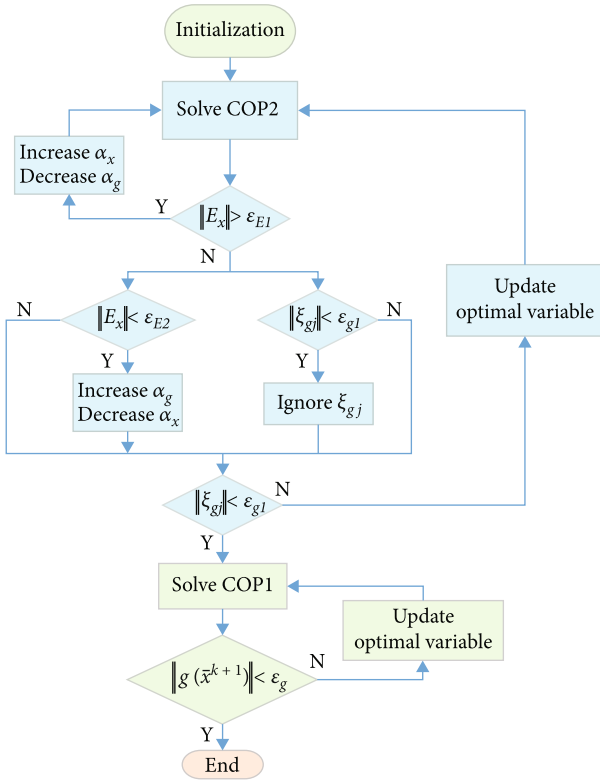

Figure 2: Trajectory optimization algorithm.

domain $(-1, 1]$, is adopted in this paper:

$$\sum_{j=0}^{N} D_{ij} x(\tau_j) - \frac{t_f - t_0}{2} f[x(\tau_j)] = 0, (i = 1, \cdots, N), \tag{12}$$

where D is the flip-Radau pseudospectral differentiation matrix [35], f is the right side of the differential dynamic equations Eq. (1), and $\tau_i, (i = 1, \cdots, N)$ is the collocation points within the domain $(-1, 1]$. N is the number of collocation points. $\mathbf{x}$ is state variables including r, V, and m.

On the other hand, the constraint of the thrust magnitude in Eq. (2) is a nonconvex equality constraint. For launch systems, the most commonly used method to handle the nonconvexity of the thrust magnitude constraint is feasible domain relaxation. The feasible domain can be relaxed from a spherical-shell region to a solid sphere, and the relaxed constraint of the thrust magnitude is

$$\|u\| \le T. \tag{13}$$

The relaxed optimization problem has the same optimal solution as the original one, which means the transformation is equivalent, and the convexification technique is called lossless convexification [17–19]. The equivalence of the transformation can be proved based on optimal control theory. The detailed proof can be found in [20].

After discretization and lossless convexification, the original trajectory optimization problem formulated in Section 2 can be expressed as

$$\min J = -m(t_f), \tag{14}$$

subject to

$$\text{Eq.}(3), \text{Eq.}(8), \tag{15}$$

$$\begin{aligned} x(t_0) &= x_0, \\ \|u\| &\le T, \\ \sum_{j=0}^{N} D_{ij} x(\tau_j) - \frac{t_f - t_0}{2} f[x(\tau_j)] &= 0, (i = 1, \cdots, N). \end{aligned} \tag{16}$$

The equality constraints of terminal conditions and discretized dynamical equations are still nonlinear (nonaffine), which is not suitable for the SCOP-based method. This problem can be handled by successive convexification in the next subsection.

3.2. Improved Successive Convexification. By linearization and the successive solution procedure, successive convexification has been successfully applied to converting the nonlinear equality constraints into affine ones. It is a popular and simple technique to handle the residual nonconvexity of the optimization problem in Section 4.1. In this paper, the nonlinear equality constraints Eq. (12) and the terminal constraints Eq. (3) are linearized repeatedly at the previous iteration with a known solution. For convenience, all nonlinear equality constraints are expressed as $g(\bar{x})$, and they can be linearized by first-order Taylor series expansion [16]:

$$g(\bar{x}^k) + \nabla g(\bar{x}^k) \Delta \bar{x} = 0, \tag{17}$$

where $\bar{x} = [x, u, t_f]$.

Considering the accuracy of linearization, the update variable Δx in Eq. (21) is added as a penalty term in the performance index function. And the convex optimization problem is formulated as COP1:

$$\min J = -m(t_f) + \alpha_x \|\Delta \bar{x}\|, \tag{18}$$

subject to

$$g(\bar{x}^k) + \nabla g(\bar{x}^k) \Delta \bar{x} = 0, \tag{19}$$

$$\begin{aligned} x(t_0) &= x_0, \\ \|u + \Delta u\| &\le T, \end{aligned} \tag{20}$$

where α_x is the penalty coefficient of $\|\Delta \bar{\mathbf{x}}\|$.

In this way, the trajectory optimization problem of the SSTO launch system is converted into a series of SOCP subproblems, which can be solved by IPM iteratively. COP1 has $10N + 1$ optimal variables, including r, V, m, u at every discrete point. It should be noted that the error of time E_t is ignored in this section because it is hard to control the position and time of the injection when the thrust magnitude is

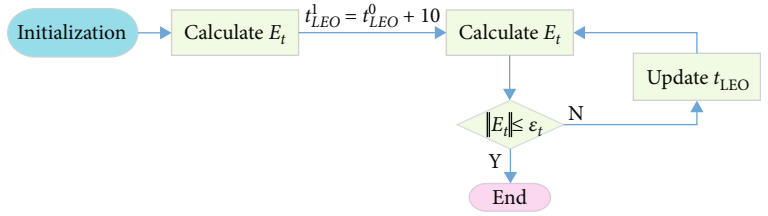

Figure 3: Flight time in LEO updater design.

Table 1: Parameters of the launch system.

Initial mass, t	35.38
Dry mass, t	16.00
Exhaust velocity, m/s	4340
Thrust magnitude, N	208320

Table 2: Parameters of the mission.

Initial condition	V_{x0}, m/s	-4841.51
	V_{y0}, m/s	-5032.27
	V_{z0}, m/s	-3439.57
	X_0, m	-4.994e+06
	Y_0, m	4.185e+06
	Z_0, m	9.065e+05
	Flight time in LEO, s	1000
Orbital injection	Semimajor axis, m	40478140
	Eccentricity	0.837489
	Attitude of the perigee, km	200
	Attitude of the apogee, km	68000
	Inclination, deg	27.59
	Longitude of ascending node, deg	335.41
	Argument perigee, deg	226.49
	True anomaly, deg	33.54
	Nominal time of injection, s	1410

uncontrollable. The terminal constraint E_t is considered in Section 4.

However, because of the error of the initial guess, the feasible solution considering the strict constraint Eq. (17) may not exist at the beginning of the iteration, even if the solution to the original problem can be found. This phenomenon is called "artificial infeasibility," and the detailed analysis can be found in [31]. This problem is solved by relaxation and the penalty strategy. Firstly, the constraint Eq. (17) is replaced by

$$g\left(\bar{x}^k\right) + \nabla g\left(\bar{x}^k\right) \Delta\bar{x} = \xi_g, \tag{21}$$

where ξ_g is the relaxation variable for equality constraints. The dimension of ξ_g is the same as the number of equality constraints.

And the relaxation variable is added as a penalty term in the performance index function. The relaxed convex optimization problem is called COP2:

$$\min J = -m\left(t_f\right) + \alpha_g \left\|\boldsymbol{\xi}_g\right\| + \alpha_x \|\Delta\bar{\mathbf{x}}\|, \tag{22}$$

subject to

$$g\left(\bar{x}^k\right) + \nabla g\left(\bar{x}^k\right) \Delta\bar{x} = 0, \tag{23}$$

$$\begin{aligned} x(t_0) &= x_0, \\ \|u + \Delta u\| &\leq T, \end{aligned} \tag{24}$$

where α_g is the penalty coefficient of $\|\boldsymbol{\xi}_g\|$.

In the performance index function of COP2, there are two intercoupling penalty coefficients α_g and α_x. The accuracy of the equality constraints increases as α_g increases and α_x decreases, and at the same time, the accuracy of linearization decreases. However, if the error of linearization is too large, the high accuracy of the equality constraints becomes insignificance. The error of linearization E_x can be defined as

$$E_{xj} = \frac{\left\| g_j\left(\bar{x}^k + \Delta\bar{x}^k\right) - \xi_{gj} \right\|}{\left\| g_j\left(\bar{x}^k + \Delta\bar{x}^k\right) \right\|} \quad j = 1, 2, \cdots, p, \tag{25}$$

where p is the number of equality constraints, $E_{xj} \in [0, 1]$. If $\|E_x\|$ is larger than ε_{E1}, the accuracy of linearization is unacceptable, the penalty coefficient α_x needs to be increased ,and the solution of this iteration should be given up. If $\|E_x\|$ is smaller than ε_{E2}, α_g can be increased to improve the accuracy of equality constraints and the rate of convergence.

By comparing COP2 with COP1, it can be found that considering the relaxation variable ξ_g, the number of optimal variables increases to $17N + 6$. It is well known that as the number of optimal variables grows, the computational time of the optimization problem grows exponentially. That is, the computational efficiency of COP2 is much worse than that of COP1. Actually, when the accuracy of equality constraints reaches a certain degree ε_{g1}, artificial infeasibility will not happen, and the relaxation variable and penalty terms in the performance index can be ignored.

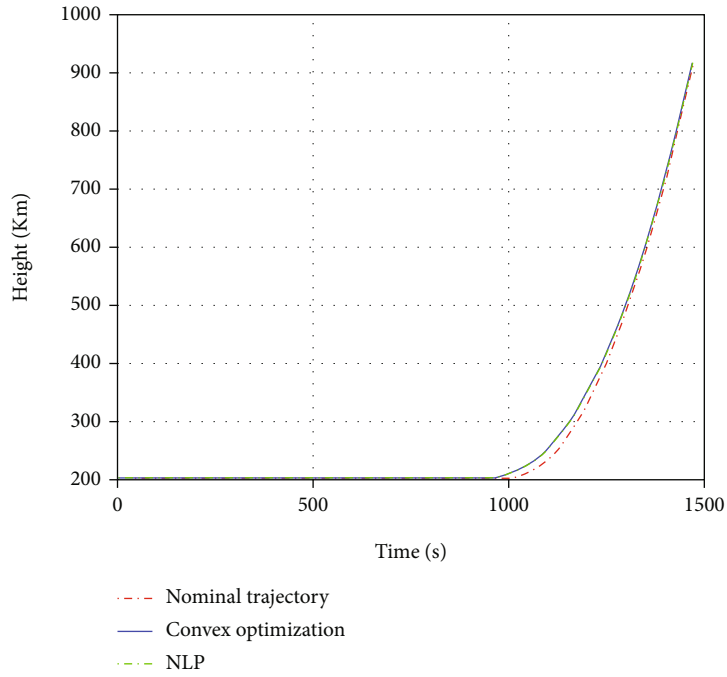

Figure 4: Curve of height.

In conclusion, considering both accuracy and computational efficiency of the algorithm, the trajectory optimization problem can be solved iteratively by the following steps (as shown in Figure 2):

(1) Initialization: input the initial variables including $\bar{x}^0$,α_g,α_x, ε_{E1}, ε_{E2}, and ε_{g1}, the permitted range of penalty coefficients $[\alpha_{g\ \min}, \alpha_{g\ \max}]$ and $[\alpha_{x\ \min}, \alpha_{x\ \max}]$, and the accuracy requirement ε_g

(2) Set $k = 0$

(3) Solve the problem COP2 by IPM, obtain the optimal solution $\Delta\bar{x}$, and calculate E_x by Eq. (25)

(4) If $\|E_x\| > \varepsilon_{E1}$, set $\alpha_x = \max\{\alpha_x \times 2, \alpha_{x\ \max}\}$, $\alpha_g = \min\{\alpha_g \div 2, \alpha_{g\ \min}\}$ and give up the solution $\Delta\bar{x}$. Otherwise, update the optimal variable $\bar{x}^{k+1} = \bar{x}^k + \Delta\bar{x}$ and set $k = k + 1$

(5) If $\|E_x\| < \varepsilon_{E2}$, set $\alpha_g = \max\{\alpha_g \times 2, \alpha_{g\ \max}\}$ and $\alpha_x = \min\{\alpha_x \div 2, \alpha_{x\ \min}\}$. If $\|\xi_{gj}\| < \varepsilon_{g1}, j = 1, 2, \cdots, p$, ignore the relaxation variable $\boldsymbol{\xi}_{gj}$ and the corresponding penalty term

(6) If $\|\xi_{gj}\| < \varepsilon_{g1}$, solve the problem COP1 iteratively. Otherwise, return to step 3

(7) Check the convergence condition:

$$\left\| g\left(\bar{x}^k + \Delta\bar{x}\right) \right\| < \varepsilon_g. \tag{26}$$

If Eq. (26) is satisfied, the trajectory optimization problem is solved, and the optimal solution is $\bar{x}^k + \Delta\bar{x}$.

In this way, the trajectory optimization problem is solved without considering the error of time E_t in Eq. (8). In the next section, to ensure the injection accuracy of GEO satellites, the flight time in LEO for launch systems is calculated to meet the accuracy requirement of E_t.

4. Flight Time Updater Design

As for the launch mission of GEO satellites, the systems always settle into a circular LEO, and then, SSTO is used to transfer satellites from LEO to GEO. Between these two flight phases, the launch systems have a few minutes of unpowered flight, and then the rocket engine turns on to settle the payload into SSTO. In Section 3, the trajectory optimization algorithm is proposed, but the error of time E_t is ignored. In this section, the strategy of LEO flight time updater design is proposed, and the terminal constraint E_t in Eq. (8) is considered.

By the analysis of the trajectory optimization problem of SSTO launch systems in Section 3, when an initial condition $x(t_0)$ is given, the error of time E_t can be calculated by Eq. (8) based on the optimal solution. In other words, the error of time E_t can be treated as a function of the initial condition $x(t_0)$. As for the unpowered flight phase in LEO, the initial condition of the powered phase from LEO to SSTO $x(t_0)$ can be easily calculated when the orbital elements of LEO are given. When the LEO is circular and the radius of the orbit is a_{LEO}, the initial true anomaly is f_0,the flight time in LEO is t_{LEO}, and the true anomaly at t_{LEO} is

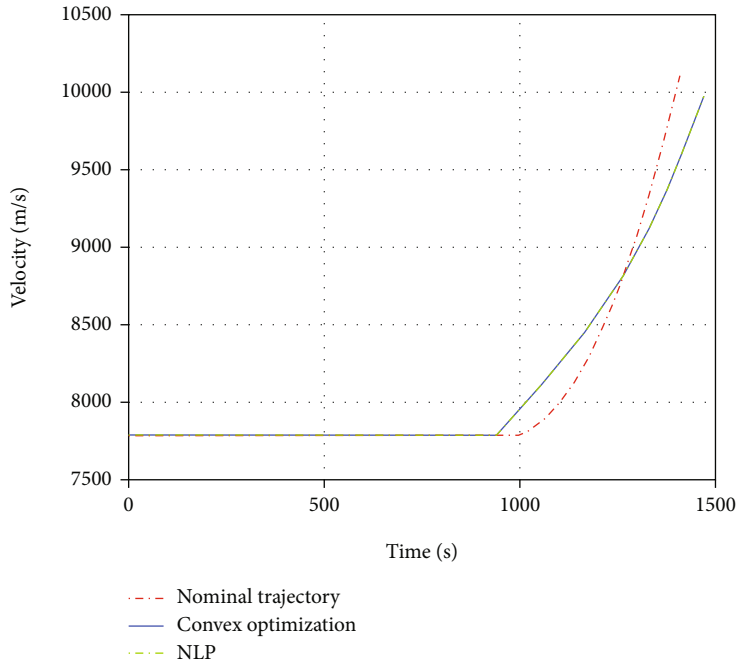

Figure 5: Curve of velocity.

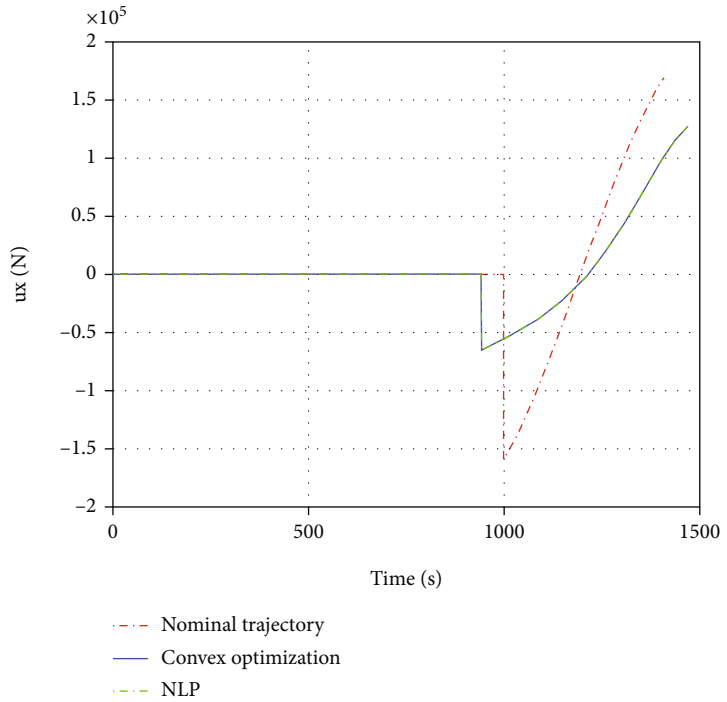

Figure 6: Curve of u_x.

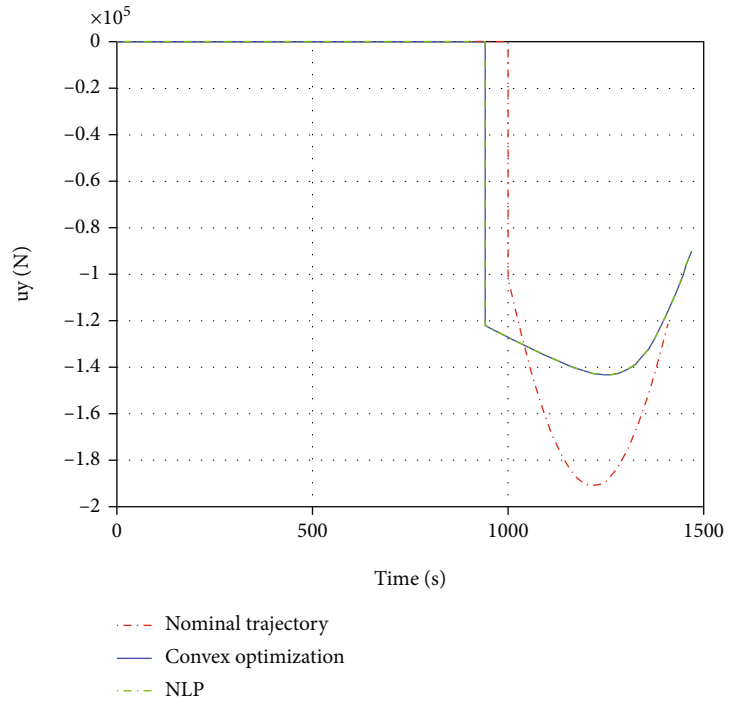

Figure 7: Curve of u_y.

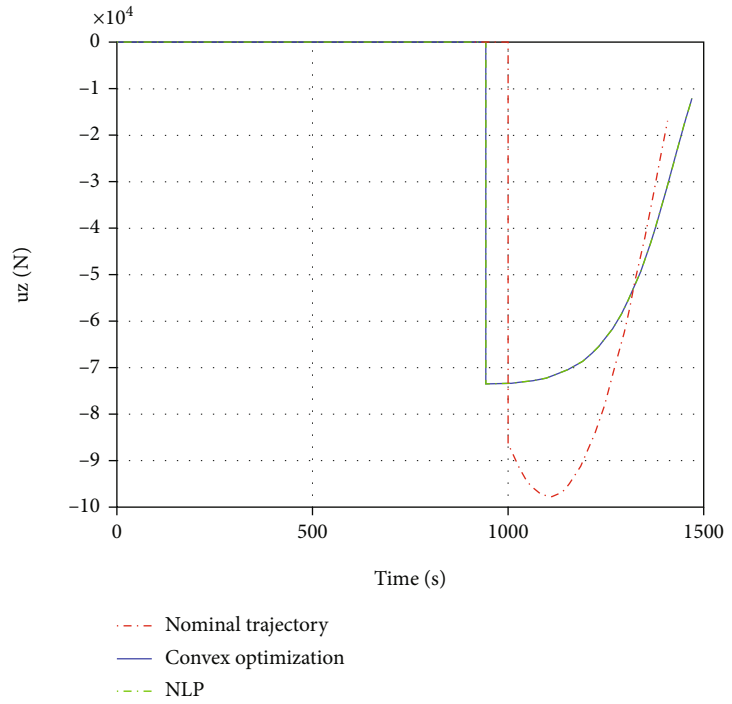

Figure 8: Curve of u_z.

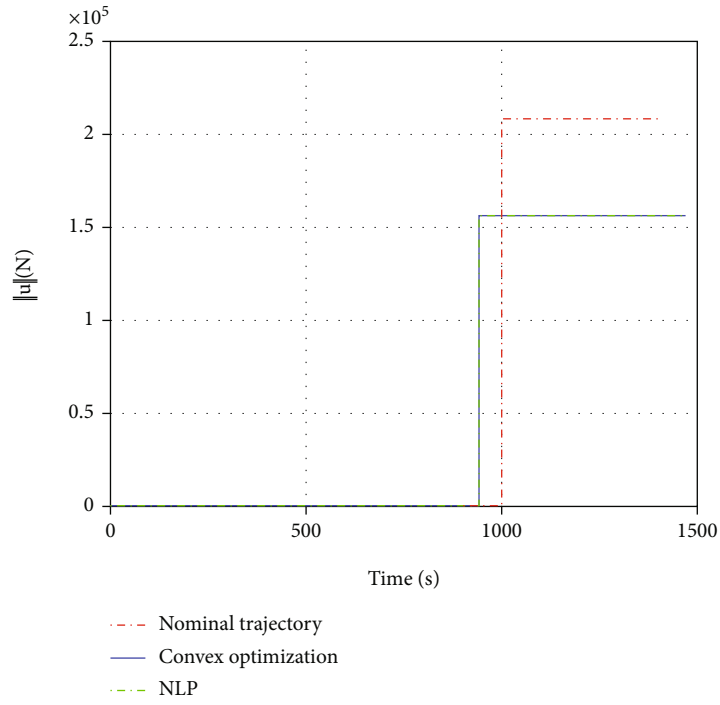

Figure 9: Curve of thrust magnitude.

Table 3: Comparison of simulation results.

	Convex optimization	NLP
Flight time in LEO, s	942.2	942.3
Flight time from LEO to SSTO, s	527.8	527.6
CPU time, s	2.23	38.34

$$f_{\mathrm{LEO}} = f_0 + t_{\mathrm{LEO}} \sqrt{\frac{\mu}{a_{\mathrm{LEO}}^3}}, \tag{27}$$

where μ is the gravitational parameter of the Earth.

And then the initial condition $x(t_0)$ can be easily calculated in the perifocal coordinate system as follows:

$$\begin{aligned} r_x(t_0) &= a_{\mathrm{LEO}}^3 \cos f_{\mathrm{LEO}}, \\ r_y(t_0) &= a_{\mathrm{LEO}}^3 \sin f_{\mathrm{LEO}}, \\ r_z(t_0) &= 0, \\ V_x(t_0) &= \sqrt{\frac{\mu}{a_{\mathrm{LEO}}}} \cos f_{\mathrm{LEO}}, \\ V_y(t_0) &= \sqrt{\frac{\mu}{a_{\mathrm{LEO}}}} \sin f_{\mathrm{LEO}}, \\ V_z(t_0) &= 0. \end{aligned} \tag{28}$$

It should be noted that all variables in Eqs. (27) and (28) are dimensional to facilitate understanding, which is different from that in Section 3. When they are given as the initial condition of the trajectory optimization problem, all variables must be nondimensional.

Based on Eqs. (27) and (28), and the trajectory optimization algorithm in Section 3, the error of time E_t can be calculated when the flight time in LEO t_{LEO} is given. And t_{LEO} can be calculated iteratively by the Newton method to solve the equation:

$$E_t(t_{\mathrm{LEO}}) = 0. \tag{29}$$

However, E_t is calculated based on a complex optimization procedure, and the partial derivative $\partial E_t / \partial t_{\mathrm{LEO}}$ is hard to calculate accurately by the numerical method when Δt_{LEO} is too small. So, a modified Newton method is given, and the detailed calculation procedure is as follows (as shown in Figure 3):

(1) According to the nominal trajectory, initialize the flight time in LEO t_{LEO}^0. Set $k = 0$

(2) Calculate the initial condition $x(t_0)$ by Eqs.(27) and (28) and solve the trajectory optimization problem by the algorithm proposed in Section 3, and then the error of time E_t^0 can be calculated by Eq.(8) based on the optimal solution

(3) Set $t_{LEO}^1 = t_{LEO}^0 + 10$, $k = 1$

(4) Calculate E_t^k in the same way as step 2

(5) If $\|E_t^k\| \le \varepsilon_t$ (ε_t is the accuracy requirement of E_t), the flight time in LEO is $t_{\mathrm{LEO}} = t_{\mathrm{LEO}}^k$; else, go to step 6

(6) Update t_{LEO} by

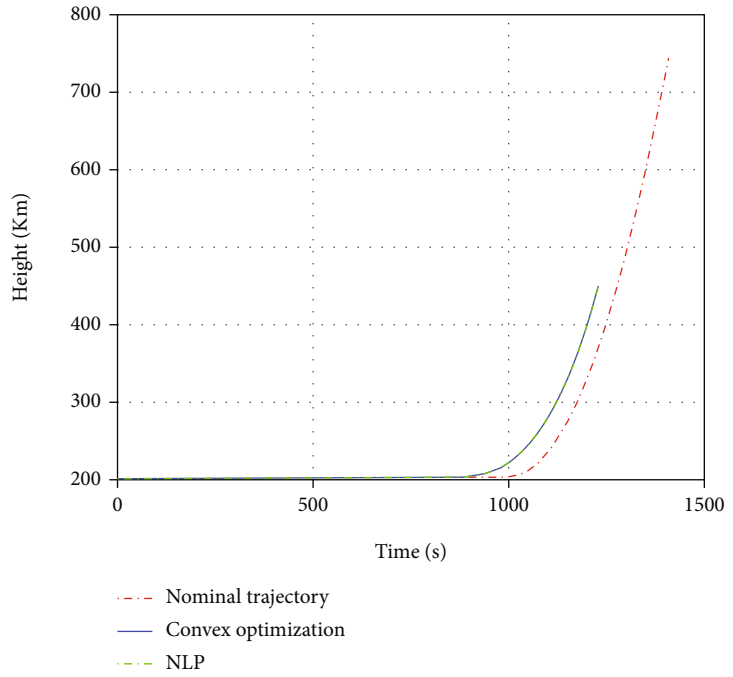

Figure 10: Curve of height.

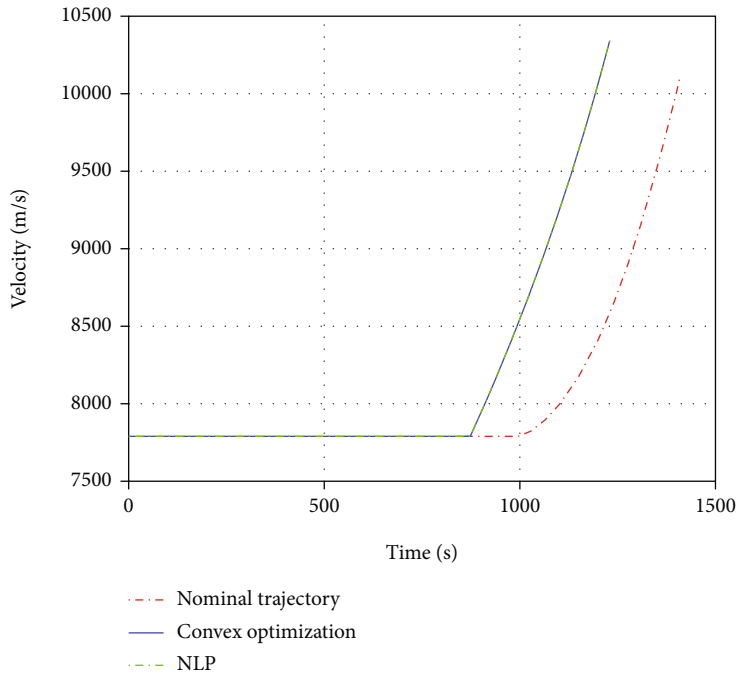

Figure 11: Curve of velocity.

$$t_{\mathrm{LEO}}^{k+1} = t_{\mathrm{LEO}}^{k} - \frac{E_t^k\left(t_{\mathrm{LEO}}^{k} - t_{\mathrm{LEO}}^{k-1}\right)}{E_t^k - E_t^{k-1}}. \tag{30}$$

(7) Set $k = k + 1$, and go to step 4

5. Simulation and Analysis

In this section, simulation experiments are carried out by taking the whole flight from LEO to SSTO. To verify the robustness of the algorithm proposed in this paper, two kinds of special conditions are considered:

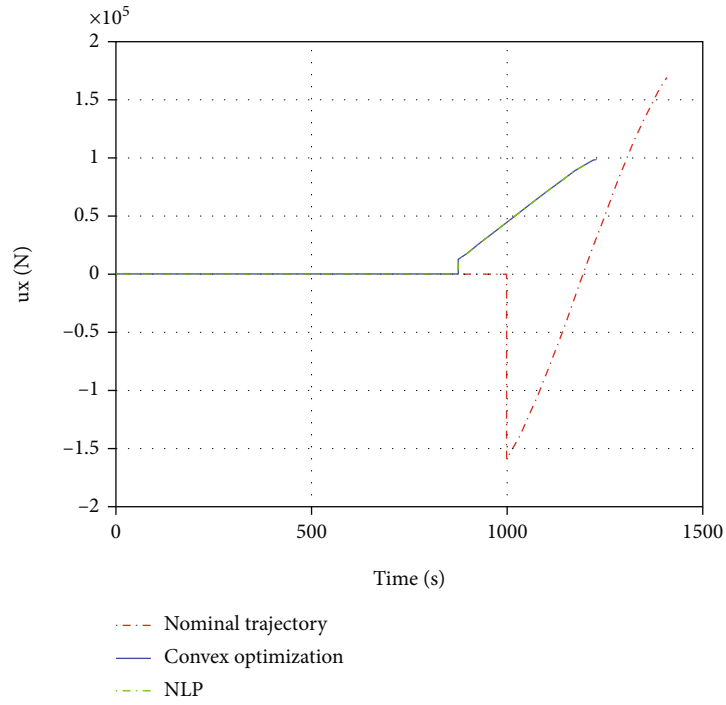

Figure 12: Curve of u_x.

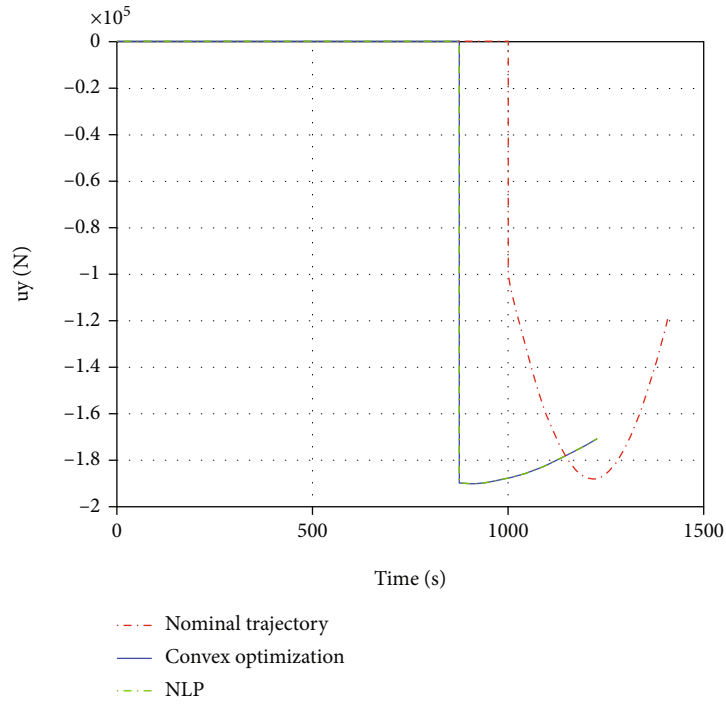

Figure 13: Curve of u_y.

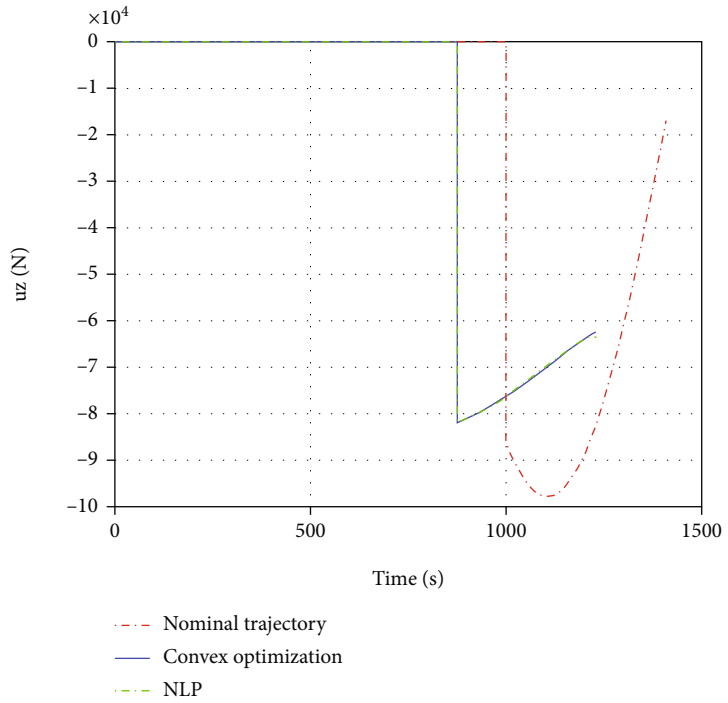

Figure 14: Curve of u_z.

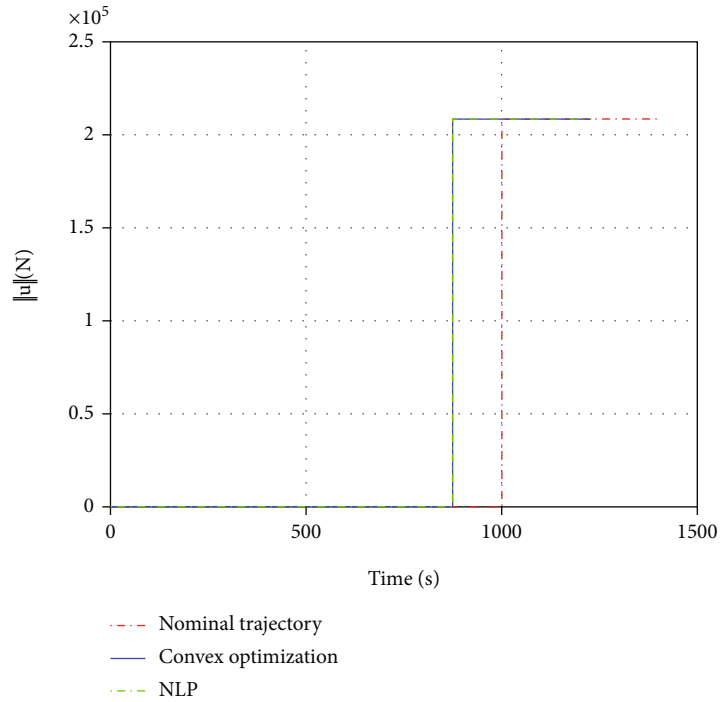

Figure 15: Curve of thrust magnitude.

Table 4: Comparison of simulation results.

	Convex optimization	NLP
Flight time in LEO, s	874.4	874.2
Flight time from LEO to SSTO, s	355.6	355.4
CPU time, s	2.48	43.27

Table 5: Deviations of terminal orbital elements.

Parameters	Deviations
Semimajor axis, m	1.56
Eccentricity	0.0000001
Inclination, deg	0.0001
Longitude of ascending node, deg	-0.0002
Argument perigee, deg	0.0001
E_t, s	0.07

Table 6: Deviations of terminal orbital elements.

Parameters	Deviations
Semimajor axis, m	1.26
Eccentricity	0.0000001
Inclination, deg	-0.0001
Longitude of ascending node, deg	-0.0001
Argument perigee, deg	-0.0002
E_t, s	0.06

(1) One of the four engines breaks down and cannot work, which means the thrust magnitude and the rate of mass flow both decrease by 25%

(2) Flight time delay caused by a fault in the previous flight phase, such as the launch delay, system fault, and flight deviation

In this paper, the convex optimization problems are solved by the MOSEK software [36], and the simulation results are compared with the solutions obtained by a traditional optimization method, which employs the hp-adaptive Radau pseudospectral method and the general NLP methods [31]. All numerical simulations in this paper are performed on a laptop with Intel Core i7 CPU 2.80GHz.

Parameters of the SSTO launch system are listed in Table 1. Parameters of the initial condition and target orbit (SSTO) are listed in Table 2. The variables contained in this section's figures and tables are with respect to the Earth Centered Inertial Coordinate System.

5.1. Engine Failure. In this subsection, we assume that the thrust magnitude and the rate of mass flow both decrease by 25% at the same time. The number of the collocation points is $N = 50$, the penalty parameter is $\alpha_g = \alpha_x = 1000$, and the permitted range of penalty coefficients is $\alpha_{g\ \min} = \alpha_{x\ \min} = 100$, $\alpha_{g\ \max} = \alpha_{\mathrm{x\ max}} = 10000$. $\varepsilon_{E1} = 0.5$, $\varepsilon_{E2} = 0.05$, $\varepsilon_{g1} = 10^{-3}$, and the accuracy requirements $\varepsilon_g = 10^{-7}$, $\varepsilon_t = 0.1$.

As shown in Figures 4–9 and Table 3, the optimal solutions to the trajectory optimization problem obtained by both methods are very similar, and they are quite different from the nominal trajectory because of the failure of the engine. In other words, the algorithm proposed in this paper can solve the trajectory optimization problem without good initial guesses in case of engine failures. Moreover, the accuracy and optimality of the optimal solution are proved by comparison with the traditional optimization method. In Figure 9, the constraint of the thrust magnitude is active during the whole flight, which demonstrates the validity of the lossless convexification in Section 3.1. As shown in Table 3, the average CPU time is 2.23 s for the algorithm presented in Section 3.2, which is only 5.8% of the average CPU time for the traditional method. It takes 7 iterations and 15.61 s' CPU time to calculate the flight time in LEO by the algorithm in Section 4. Due to the long time parking in the LEO, there is enough time to solve the trajectory optimization problem.

5.2. Time Delay. In this subsection, we assume that the flight time delays by 50 s because of the fault in the previous flight phase. All the parameters of the optimization algorithm are the same as those in Section 5.1. The simulation results are as follows:

Compared with the work in Section 5.1, similar simulation results (shown in Figures 10–15, Table 4) and research conclusions can be obtained. Another significant research result is that with the same optimization parameters, the trajectory optimization problem can be solved in different situations, which further proves the robustness of the algorithm. Similar experiment results can also be obtained based on different launch systems and missions. As for the time delay, the average CPU time is 2.48 s for the algorithm presented in Section 3.2, which is 5.7% of the average CPU time for the traditional method. It takes 8 iterations and 19.84 s' CPU time to calculate the flight time in LEO by the algorithm in Section 4. The deviations of terminal orbital elements shown in Tables 5 and 6 verify the accuracy of the equation of terminal constraints Eq. (3) and the flight time updater design algorithm in Section 4.

The above simulation results demonstrate that the algorithm proposed in this paper has good robustness, accuracy, and computational efficiency, which indicates great development potential and application prospect in onboard trajectory optimization.

6. Conclusion

This paper presents a convex optimization algorithm for SSTO launch systems considering the orbital elements and time-position constraints. For convenience and better computational performance, the optimal control problem including the terminal constraints is given in the perifocal coordinate system. And then the flip-Radau pseudospectral method is adopted to convert the trajectory optimization

problem into a finite problem. Lossless convexification is also utilized to convexify the constraint of the thrust magnitude. To improve the robustness and computational efficiency of the algorithm, successive convexification and its modified method are proposed. In this way, the trajectory optimization problem is transformed into a convex one, which can be solved by IPM accurately and rapidly. To correct the flight time deviation of SSTO launch systems, the LEO flight time updater design algorithm is proposed. Finally, the algorithm proposed in this paper is tested under two special conditions: engine failure and time delay. Compared with the traditional optimization method, the proposed algorithm demonstrates stronger robustness, higher accuracy, and higher computational efficiency. The improved convex approach and flight time design method proposed in this paper have great application potential in onboard trajectory optimization of SSTO launch systems and other similar systems, especially under nonnominal conditions. In our follow-up work, we will modify the proposed algorithm for the flight from SSTO to GEO and concentrate on the improvement of injection accuracy and robustness of the algorithm.

Data Availability

The numerical simulation data used to support the findings of this study are included within the article.

Conflicts of Interest

The authors declare that there is no conflict of interest regarding the publication of this paper.

Acknowledgments

This work was supported by the National Natural Science Foundation of China under Grant 51809138 and China Postdoctoral Science Foundation under Grant 2019M651837.

References

[1] H. D. Curtis, *Orbital Mechanics for Engineering Students, Butterworth-Heinemann*, Butterworth-Heinemann, United Kingdom, 2013.

[2] L. Li, J. Zhang, S. Zhao, R. Qi, and Y. Li, "Autonomous onboard estimation of mean orbital elements for geostationary electric-propulsion satellites," *Aerospace Science and Technology*, vol. 94, article 105369, 2019.

[3] Y. Liu, J. Heiligers, and M. Ceriotti, "Loosely-displaced geostationary orbits with hybrid sail propulsion," *Aerospace Science and Technology*, vol. 79, pp. 105–117, 2018.

[4] M. J. Kelchner and C. A. Kluever, "Rapid evaluation of low-thrust transfers from elliptical orbits to geostationary orbit," *Journal of Spacecraft and Rockets*, vol. 57, no. 5, pp. 898–906, 2020.

[5] H. J. Horn, D. C. Chandler, and V. L. Buckelew, "Iterative guidance applied to generalized missions," *Journal Of Spacecraft and Rockets*, vol. 6, no. 1, pp. 4–8, 1969.

[6] Z. Xu and Q. Zhang, "Multi-constrained ascent guidance for solid propellant launch vehicles," *Aerospace Science and Technology*, vol. 76, pp. 260–271, 2018.

[7] P. Lu, "Introducing computational guidance and control," *Journal of Guidance, Control, and Dynamics*, vol. 40, no. 2, pp. 193–193, 2017.

[8] C. H. A. I. Runqi, A. Tsourdos, A. Savvaris, C. H. A. I. Senchun, and X. I. A. Yuanqing, "High-fidelity trajectory optimization for aeroassisted vehicles using variable order pseudospectral method," *Chinese Journal of Aeronautics*, vol. 34, no. 1, pp. 237–251, 2021.

[9] W. A. N. G. Shaoqi, M. A. Dongli, Y. A. N. G. Muqing, L. Zhang, and L. I. Guanxiong, "Flight strategy optimization for high-altitude long-endurance solar-powered aircraft based on Gauss pseudo-spectral method," *Chinese Journal of Aeronautics*, vol. 32, no. 10, pp. 2286–2298, 2019.

[10] J. Roshanian, A. A. Bataleblu, and M. Ebrahimi, "Robust ascent trajectory design and optimization of a typical launch vehicle," *Proceedings of the Institution of Mechanical Engineers, Part C: Journal of Mechanical Engineering Science*, vol. 232, no. 24, pp. 4601–4614, 2018.

[11] C. A. Kluever, "Terminal guidance for an unpowered reusable launch vehicle with bank constraints," *Journal of Guidance, Control, and Dynamics*, vol. 30, no. 1, pp. 162–168, 2007.

[12] P. Lu, B. J. Griffin, G. A. Dukeman, and F. R. Chavez, "Rapid optimal multiburn ascent planning and guidance," *Journal of Guidance, Control, and Dynamics*, vol. 31, no. 6, pp. 1656–1664, 2008.

[13] L. Wang, R. Chen, and X. Yan, "Trajectory optimization of aerial slung load release for piloted helicopters," *Chinese Journal of Aeronautics*, vol. 34, no. 2, pp. 229–239, 2021.

[14] W. A. N. G. Mingkai, S. Zhang, J. Diepolder, and F. Holzapfel, "Battery package design optimization for small electric aircraft," *Chinese Journal of Aeronautics*, vol. 33, no. 11, pp. 2864–2876, 2020.

[15] J. Wang, N. Cui, and C. Wei, "Optimal rocket landing guidance using convex optimization and model predictive control," *Journal of Guidance, Control, and Dynamics*, vol. 42, no. 5, pp. 1078–1092, 2019.

[16] X. Liu, P. Lu, and B. Pan, "Survey of convex optimization for aerospace applications," *Astrodynamics.*, vol. 1, no. 1, pp. 23–40, 2017.

[17] B. Açıkmeşe and L. Blackmore, "Lossless convexification of a class of optimal control problems with non- convex control constraints," *Automatica*, vol. 47, no. 2, pp. 341–347, 2011.

[18] L. Blackmore, B. Açıkmeşe, and J. M. Carson III, "Lossless convexification of control constraints for a class of nonlinear optimal control problems," *Systems & Control Letters*, vol. 61, no. 8, pp. 863–870, 2012.

[19] M. W. Harris and B. Açıkmeşe, "Lossless convexification of non-convex optimal control problems for state constrained linear systems," *Automatica*, vol. 50, no. 9, pp. 2304–2311, 2014.

[20] Y. Li, B. Pang, C. Wei, N. Cui, and Y. Liu, "Online trajectory optimization for power system fault of launch vehicles via convex programming," *Aerospace Science and Technology*, vol. 98, article 105682, 2020.

[21] B. Acikmese and S. R. Ploen, "convex programming approach to powered descent guidance for mars landing," *Journal of Guidance, Control, and Dynamics*, vol. 30, no. 5, pp. 1353–1366, 2007.

[22] Y. Li, Y. Guan, C. Wei, and R. Hu, "Optimal control of ascent trajectory for launch vehicles: a convex approach," *IEEE Access*, vol. 7, pp. 186491–186498, 2019.

[23] D. C. Chandler and I. E. Smith, "Development of the iterative guidance mode with its application to various vehicles and missions," *Journal of Spacecraft and Rockets*, vol. 4, no. 7, pp. 898–903, 1967.

[24] Z. Wang and S. T. McDonald, "Convex relaxation for optimal rendezvous of unmanned aerial and ground vehicles," *Aerospace Science and Technology*, vol. 99, article 105756, 2020.

[25] Z. Wang, "Optimal trajectories and normal load analysis of hypersonic glide vehicles via convex optimization," *Aerospace Science and Technology*, vol. 87, pp. 357–368, 2019.

[26] X. Cheng, H. Li, and R. Zhang, "Efficient ascent trajectory optimization using convex models based on the Newton-Kantorovich/Pseudospectral approach," *Aerospace Science and Technology*, vol. 66, pp. 140–151, 2017.

[27] D. Zhou, Y. Zhang, and S. Li, "Receding horizon guidance and control using sequential convex programming for spacecraft 6-DoF close proximity," *Aerospace Science and Technology*, vol. 87, pp. 459–477, 2019.

[28] M. Sagliano, "Pseudospectral convex optimization for powered descent and landing," *Journal of Guidance, Control, and Dynamics*, vol. 41, pp. 320–334, 2017.

[29] H. Han, D. Qiao, H. Chen, and X. Li, "Rapid planning for aerocapture trajectory via convex optimization," *Aerospace Science and Technology*, vol. 84, pp. 763–775, 2019.

[30] X. Liu and Z. Shen, "Rapid smooth entry trajectory planning for high lift/drag hypersonic glide vehicles," *Journal of Optimization Theory and Applications*, vol. 168, no. 3, pp. 917–943, 2016.

[31] J. Wang and N. Cui, "A pseudospectral-convex optimization algorithm for rocket landing guidance," in *2018 AIAA Guidance, Navigation, and Control Conference*, Kissimmee, Florida, January 2018.

[32] V. Coverstone-Carroll, J. W. Hartmann, and W. J. Mason, "Optimal multi-objective low-thrust spacecraft trajectories," *Computer Methods in Applied Mechanics and Engineering*, vol. 186, no. 2-4, pp. 387–402, 2000.

[33] H. Sun, *Closed-Loop Endo-Atmospheric Ascent Guidance for Reusable Launch Vehicle*, Iowa State University, United States, 2005.

[34] X. Liu, *Autonomous Trajectory Planning by Convex Optimization, [Ph.D. thesis]*, Iowa State University, United States, 2013.

[35] D. Garg, *Advances in Global Pseudospectral Methods for Optimal Control*, University of Florida, United States, 2011.

[36] E. D. Andersen, C. Roos, and T. Terlaky, "On implementing a primal-dual interior-point method for conic quadratic optimization," *Mathematical Programming*, vol. 95, no. 2, pp. 249–277, 2003.

Hindawi
International Journal of Aerospace Engineering
Volume 2022, Article ID 6055819, 14 pages
https://doi.org/10.1155/2022/6055819

Research Article

Envelope-Based Variable-Gain Control Strategy for Vibration Suppression of Solar Array Using Reaction Wheel Actuator

Song Wu,[1,2] Guoan Tang,[1] and Bifa Chen[3]

[1]*Department of Aeronautics and Astronautics, Fudan University, Shanghai 200433, China*
[2]*Shanghai Key Laboratory of Spacecraft Mechanism/Shanghai Institute of Aerospace System Engineering, Shanghai 201109, China*
[3]*School of Aerospace Engineering, Xiamen University, Xiamen, Fujian 361102, China*

Correspondence should be addressed to Bifa Chen; bfchen@xmu.edu.cn

Received 10 January 2022; Revised 12 April 2022; Accepted 15 April 2022; Published 20 May 2022

Academic Editor: Jiafu Liu

The orbital operation of spacecraft can excite the long-drawn and low-frequency vibration of the solar array, which is prone to affecting the task execution of the system. To address this issue, an envelope-based variable-gain control strategy is proposed to suppress vibration of the solar array using the reaction wheel (RW) actuator. The RW actuator is individually mounted on the solar array to provide reaction torque through the speed change of its rotor. The governing equation of motion of the solar array actuated by a RW actuator is deduced with the state space representation. The control relation between the measured bending moment and the rotational speed of the RW actuator with the constant-gain coefficient is firstly developed and demonstrated in numerical simulation. Changing the gain coefficient to be inversely proportional to the envelope function of vibration, a variable-gain control strategy is proposed to improve the damping effect of the RW actuator. Simulation results show that the vibration suppression performance of the RW actuator is improved compared to the constant-gain control. As the actual on-orbit natural frequency of the solar array is not always exactly known, the robustness of the control system is analyzed for the deviation between the estimated and the actual natural frequency values. The proposed variable-gain control is also experimentally verified using a simplified elastic plate model. Experimental results indicate that the vibration attenuation time is decreased to 29.1% and 50.22% compared to the uncontrolled and the constant-gain controlled states, respectively.

1. Introduction

With the trend of larger expansion in dimensions, the deployable appendages of the spacecraft, such as the solar array, the antenna, and the manipulator, possess remarkable flexibility in a fully deployed state [1, 2]. The ultralow natural frequency of the large-scale flexible appendage f_n is the main reason for slow vibration attenuation. The vibration can result from various on-orbit excitations, e.g., the spacecraft's attitude adjusting, the payload pointing, and the spacecraft docking [3–5]. Besides, due to the absence of air resistance and weak friction between mechanisms under low gravity, the inherent modal damping ratio ζ_n of the appendage is quite small. According to the exponential law of vibration attenuation, for vibration amplitude decaying by ς times, the required time is estimated by $-\ln \varsigma/(2\pi f_n \zeta_n)$. If the empirical values of f_n and ζ_n are taken as 0.05 Hz and 0.005, respectively, and the required $\varsigma = 5\%$, then the required time is 1907.1 s. In such cases, it takes a long time to sufficiently attenuate the excited vibration, which is unfavorable for the spacecraft attitude control and payload accurate pointing. In addition, the longtime vibration may accumulate mechanical damage to the flexible appendages.

Various methods have been developed to suppress the vibration of the spacecraft's flexible appendages in the last decades. These methods can mainly be divided into the feedforward control such as the input shaping technique, the passive vibration control (PVC), and the active vibration control (AVC). The input shaping technique was applied to reduce the vibration of the appendages during spacecraft orbital maneuvering, solar array sun pointing, or manipulator transporting [6, 7]. For example, Na et al. [4] used the built-in actuator at the array base to control the vibration of a solar array. However, the input shaping technique does

not work when the structural vibration direction is different from the actuating direction of the built-in actuator. Moreover, it is not suitable for accelerating the residual vibration attenuation of the structure.

Adopting the passive or active control method satisfied the needs of accelerating vibration attenuation [8–11]. By applying damping materials or passive dampers to the structures, the passive control methods were implemented and demonstrated to be highly stable and efficient [12–14]. However, for the large-scale flexible appendages, the partially covered damping materials or passive dampers are not able to efficiently improve the low-order modal damping of the whole system. The active control methods perform well by combining a network of sensor-controller-actuator and provide a significant vibration suppression effect [15–17]. The actuator selection for different application situations is one of the issues in AVC. Piezoelectric material is a type of widely used actuator [18–20]. It is also employed as the sensor in active control [21–24]. However, the suppression effect is not obvious when the piezoelectric actuator is applied to large-scale flexible space structures. To solve this issue, Casella et al. [25] combined both the piezoelectric material and the on–off air jet thrusters as the actuators, but the compensation of the air jet working medium of the thrusters is an obstacle in space application. Sun et al. [26] proposed a novel vibration suppression scheme for solar arrays by using the cable-driven parallel robot actuators, which achieved a remarkable vibration suppression effect. Whereas for the deployable space structures, the involved cables cause issues in deploying process design. Meanwhile, its robustness is also an issue in practical application. Hu et al. [27] used a stiffness-variable joint mechanism for two hinged flexible plates. Both simulation and experimental results demonstrated the significant damping effect induced by the innovative joint mechanism. However, the actuator is only suitable for the sort of flexible structures embedded with joint mechanisms.

The reaction wheel (RW) is usually implemented in spacecraft attitude control, which has the benefits of light weight and high efficiency with consumption of renewable electricity [28–32]. An active control method to suppress the vibration of the solar array through the RW actuator was studied in [33]. Numerical simulations of a solar array showed that, by using a RW actuator with approximately 2% of the structural mass, the vibration attenuation time was reduced to one-third of that from the uncontrolled state. However, for aerospace applications, the requirements of the RW actuator, such as the volume and weight, are very strict. Therefore, it is desirable to maximize the actuator's vibration suppression capability. The sliding mode control [34, 35], the fuzzy logic [36], and the artificial algorithm [37] were investigated and integrated into the vibration control strategy design for the space flexible appendages. Bonding the piezoelectric actuator to the flexible panel, Liu et al. [38] developed a hybrid control scheme for the attitude stabilization and vibration suppression of the flexible spacecraft by considering model parameter uncertainty, measurement error, actuator faults, and other factors. It is worth pointing out that finding the optimal gains for the controller is very crucial and challenging for achieving the best performance of vibration suppression in the control system, which is still an open research problem. The variable gain control methods have been developed by other researchers in various engineering applications previously [39–43]. Combining the variable gain control into the design of a vibration suppression strategy has the potential in improving the damping performance of the actuators. Due to the fact that the gain adjustment rules require complex procedures and the calculations of the relevant parameters usually depend on experience [44–46], it is challenging to construct a feasible variable-gain control strategy for AVC in actual implementation.

In this paper, we focus on developing a variable gain control strategy for the RW actuator to maximize its capability in suppressing vibration of the solar array. The main contribution of this paper is the variable-gain control strategy through the envelope function of vibration to improve the damping performance of the RW actuator for vibration suppression of the solar array. The numerical models of a full-scale solar array with variable-gain control and constant-gain control are developed to evaluate and validate the proposed algorithm. An elastic plate model is used in the laboratory for feasibility investigation. The design, implementation, and verification of the proposed strategy are presented to highlight the significant vibration suppression performance of the RW actuator. The control relation between the measured bending moment and the rotational speed of the RW actuator with the constant gain is firstly applied to the solar array. It is figured out from the simulation results that a larger amplitude of the rotational speed of the RW actuator implies a larger output reaction torque in the control, which leads to a better damping effect. In our work, adjusting the control gain to be linear to the inverse of the vibration envelope is the strategy to increase the output reaction torque of the RW actuator. The proposed variable-gain control strategy is proved to be able to improve the damping performance of the RW actuator compared to the constant-gain control.

The rest of the paper is organized as follows. In Section 2, dynamic modelling for vibration suppression of the solar array by utilizing the RW actuator is deduced, and the damping effect of the RW actuator is demonstrated through a full-scale flexible solar array with numerical simulation. The design, numerical verification, and robustness analysis of the envelope-based variable-gain control strategy are discussed in Section 3. Experimental results are presented in Section 4 to illustrate the effectiveness and feasibility of the presented method. Conclusions are drawn in Section 5.

2. Dynamic Modelling and Effect of Vibration Suppression for Solar Array

2.1. Vibration Suppression for Solar Array Utilizing RW Actuator. For vibrating structures dominated by the first-order mode, the physical quantities describing the structural motion state can be approximately expressed by the modal coordinate ξ_1 and its corresponding modal shape function φ, in which ξ_1 is a temporal function and φ is a spatial function. For example, as shown in Figure 1, the solar array has

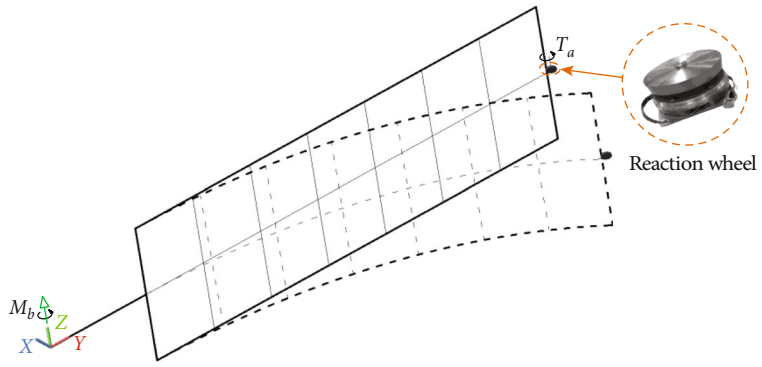

Figure 1: Structural diagram of the solar array with a RW actuator.

the geometric characteristic of a large length-to-width ratio. The root of the solar array connecting to the spacecraft body is fixed based on the assumption that the mass and moment of inertia of the spacecraft body are much larger than that of the solar array [47]. For the sake of illustration, a Cartesian coordinate system is established on the solar array. The X-axis is parallel to the normal direction of the panel surface. The Y-axis is parallel to the extension direction. The Z-axis follows the right-hand rule. In this paper, the first-order out-of-plane bending mode of the solar array along the X-axis is assumed to be dominant.

To suppress the first-order out-of-plane bending vibration, a RW actuator is mounted at the midspan of the free side of the solar array, as shown in Figure 1. The reaction torque induced by the speed change of the RW actuator is applied as the active force. The angular displacement around the Z-axis at the RW mounted position is designated as θ. The root bending moment M_b is defined as the moment around the Z-axis at the connected position between the root of the flexible solar array and the spacecraft body. Both M_b and θ can be expressed as linear functions of the modal coordinate ξ_1.

Denoting the linear proportionality coefficients as φ_M and φ_θ, M_b and θ can be written as

$$\begin{aligned} M_b &= \varphi_M \xi_1, \\ \theta &= \varphi_\theta \xi_1, \end{aligned} \tag{1}$$

respectively. Such that

$$M_b = \frac{\varphi_M}{\varphi_\theta}\theta. \tag{2}$$

The control law for the rotational speed of RW Ω is designed to be proportional to the root bending moment M_b:

$$\Omega = \eta M_b = \eta \varphi_M \xi_1. \tag{3}$$

The rotating axis of Ω is parallel to the Z-axis. The control gain η can be given by

$$\eta = \frac{\Omega_{\max}}{M_{b,\max}} = \frac{\Omega_{\max}}{\theta_{\max}} \frac{\varphi_\theta}{\varphi_M}. \tag{4}$$

Here, $\Omega_{\max}$ denotes the permitted maximum rotational speed of the RW actuator; the peak values of θ, M_b during vibration are $\theta_{\max}, M_{b,\max}$, respectively. Specifying η by Equation (4) results that the RW actuator rotates at $\Omega_{\max}$ when the structural vibration reaches the peak with no overload.

Denoting the rotational acceleration of the RW as $\dot{\Omega}$, according to the moment of momentum theorem, the induced reaction torque applied to the solar array is $T_a = -I\dot{\Omega}$. Considering Equation (3), the reaction torque T_a can be written as

$$T_a = -I\eta \dot{M}_b, \tag{5}$$

in which I is the rotating moment of inertia of the RW about its rotational axis. Controlling the rotational speed Ω by the designed algorithm, the induced torque T_a can be used to suppress the vibration of the solar array.

Performing a first-order time derivative on both sides of Equation (2) and substituting the result into Equation (5) by considering Equation (4) gives

$$T_a = -I \frac{\Omega_{\max}}{\theta_{\max}} \dot{\theta}. \tag{6}$$

The minus sign "−" guarantees the direction of the reaction torque T_a always opposite to the direction of the angular velocity $\dot{\theta}$. As a result, the RW actuator can always do negative work to the solar array. That is, T_a plays a role of consuming the vibration mechanical energy of the solar array, so it can be regarded as artificial damping.

The motion equation of the flexible solar array with a RW actuator can be expressed in the first-order modal coordinate as

$$\ddot{\xi}_1 + 2\omega_1 \zeta_1 \dot{\xi}_1 + \omega_1^2 \xi_1 = \varphi_\theta T_a. \tag{7}$$

Here, ω_1 and ζ_1 are the first-order natural frequency (rad/s) and modal damping ratio, respectively. The detailed

derivation of Equation (7) can be consulted from [33]. Rewriting Equation (7) in a state-space representation:

$$\dot{\mathbf{x}} = \mathbf{A}\mathbf{x} + \mathbf{B}\mathbf{u}, \tag{8}$$

where

$$\begin{aligned} \mathbf{x} &= \left[\dot{\xi}_1 \; \xi_1\right]^T, \\ \mathbf{u} &= [T_a], \\ \mathbf{A} &= -\begin{bmatrix} 2\omega_1\zeta_1 & \omega_1^2 \\ -1 & 0 \end{bmatrix}, \\ \mathbf{B} &= [\varphi_\theta \quad 0]^T. \end{aligned} \tag{9}$$

They can be referred to as the state vector ($\mathbf{x}$), the input vector ($\mathbf{u}$), the state matrix ($\mathbf{A}$), and the input matrix ($\mathbf{B}$), respectively.

On the other hand, Equation (1) can be equivalently written as

$$\mathbf{y} = \mathbf{C}\mathbf{x}, \tag{10}$$

where

$$\begin{aligned} \mathbf{y} &= [M_b], \\ \mathbf{C} &= [0 \quad \varphi_M]. \end{aligned} \tag{11}$$

Here, $\mathbf{y}$ and $\mathbf{C}$ are the output vector and the output matrix, respectively.

Equation groups (8) and (10) are the typical state-space form of a dynamic system [48]. The abovementioned modal parameters can be obtained by numerical approach, e.g., finite element method.

2.2. Numerical Simulations and Analysis. The solar array with a deployed area of 6.2 m × 25 m utilized in the Tianhe core module of the Chinese Space Station is adopted to validate the effectiveness of the vibration control method. The corresponding finite element model with a full scale is constructed using MSC/PATRAN, and it is shown in Figure 2.

The flexible panels are meshed by shell elements. The driving mechanisms, the deployable structures, and the storing tubes and boxes are modelled using beam elements with measured physical parameters. Interested readers can consult Reference [49] for more detailed information. A torsional spring element with a modulus of 10^6 N · m/rad is employed to connect the root of the solar array and the spacecraft body. The end of the spring element with connection to the spacecraft body is fixed. The finite element mesh (blue grid) and its first-order out-of-plane bending vibration mode are shown in Figure 2. The modal analysis is performed with MSC/NASTRAN. The total mass of the solar array model is 594.2 kg. The RW actuator selected in the simulation weighed 1 kg, which accounted for about 0.17% of the model in this study case. The moment of inertia of

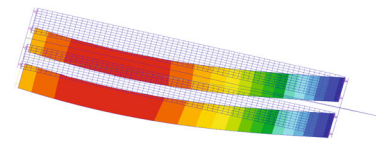

Figure 2: The finite element mesh of the flexible solar array and its first-order bending mode.

the current RW is 0.005 kg · m^2. The maximum rotational speed is 6000 RPM, i.e., $\Omega_{\max} = 628.3$ rad/s.

The modal parameters of the full-size flexible solar array model utilized in the numerical simulation are listed as follows. The first-order natural frequency of the model is $\omega_1 = 0.2746$ rad/s. The modal parameters mentioned in Equation (1) are $\varphi_M = 29.15$ N · m and $\varphi_\theta = 0.003$ rad, respectively. Considering the testing experiences for similar structures, the modal damping ratio of the model is taken as $\zeta_1 = 0.005$ (very small as suggested by the aerospace agency).

To make the simulation more realistic, a band-pass filter is adopted for the sensor signal to eliminate the DC (direct current) drift and high-frequency noise. The band-pass filter is a 2$^{\text{nd}}$-order Butterworth filter with a high cut-off frequency of 0.06118 Hz and a low cut-off frequency of 0.02622 Hz. Namely, the band width of the filter is determined through taking the first-order bending natural frequency of the solar array as the central frequency and floating up and down by 40%. The constant-gain control law expressed in Equation (3) is firstly employed to verify the vibration suppression effect. The simulation process is executed with a fixed-step size of 0.01 s. The peak value of the root bending moment is approximately 150 N · m once disturbed. Thus, the initial conditions of the model are given by

$$\xi_1(0) = 0, \dot{\xi}_1(0) = 1.5 \text{ s}^{-1}. \tag{12}$$

As shown in Figure 3, the controller realized by Equation (3) is involved to obtain the speed signal for the RW actuator. The control gain is 3.76 N · m · s/rad given by Equation (4). If the gain coefficient is 0, the reaction torque T_a equals to 0 during the whole simulation process, which can be regarded as the state without control.

The simulation results of the bending moment M_b with and without control are plotted as the solid and the dashed lines in Figure 4, respectively. Compared to the dashed line (without control), the attenuation of the solid line (with control) is accelerated. The comparison demonstrates that the reaction torque T_a can be used to suppress the vibration of the solar array through designing the rotational speed Ω according to the control law given by Equation (3).

The rotational speed Ω is shown in Figure 5. It is much larger and close to its permitted maximum value $\Omega_{\max}$ in the early stage. However, according to Equations (3) and (5), the peak values of Ω and the reaction torque T_a decrease with the attenuation of vibration. For example, the rotational speed of the RW decays to 267.4 rad/s at 384.3 s, which is

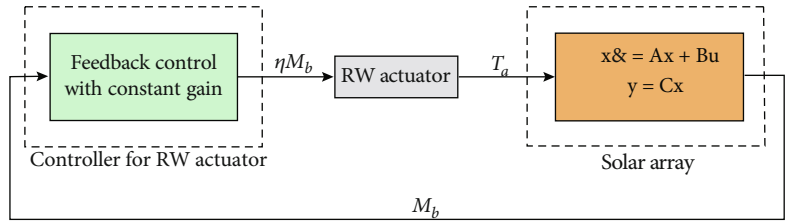

Figure 3: Diagram of the feedback control with constant gain.

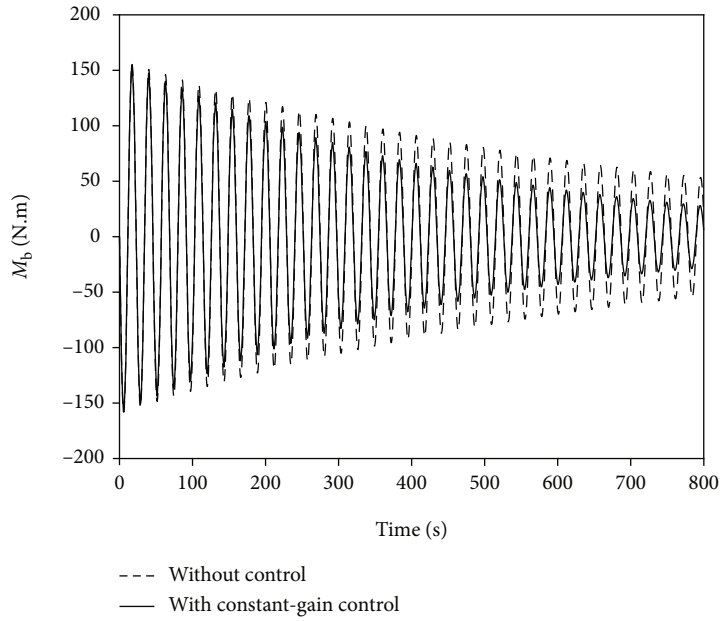

Figure 4: Response curve of the root bending moment with constant-gain control.

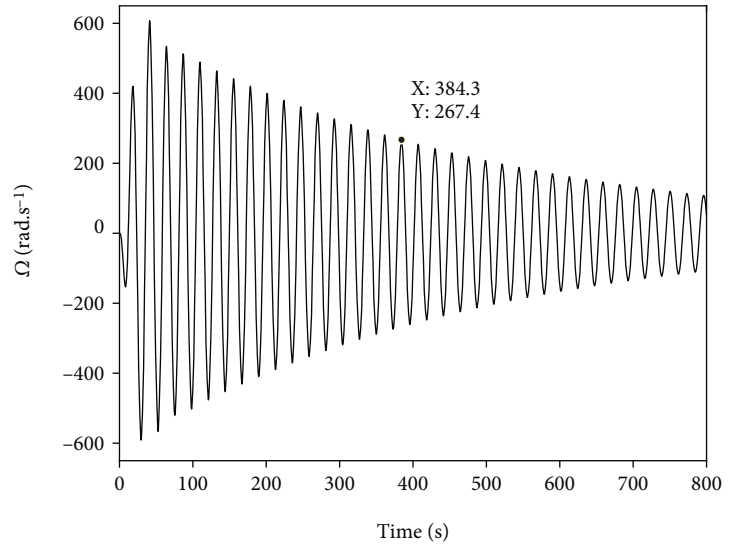

Figure 5: Rotational speed of the RW actuator with constant-gain control.

less than half of Ω_{max}. In this paper, the amplitude of the rotational speed is defined as a measure of the capability of the RW actuator utilized for vibration suppression. A larger amplitude of the rotational speed, which is closer to Ω_{max}, is preferred, for which the capability of the RW actuator is more sufficiently utilized to provide a better control effect.

Hence, it indicates that the capability of the RW actuator has the potential to be improved for providing a better control effect.

3. Design, Simulation, and Analysis of Envelope-Based Variable-Gain Control

To overcome the issue that the amplitude of the rotational speed decreases with the attenuation of vibration, it is proposed to involve a variable-gain control algorithm based on the envelope function of vibration in the feedback control law. The controller design, as well as the numerical verification and the robustness analysis of the control system, is going to be discussed in this section.

3.1. Controller Design. With the action of the damping force (i.e., the inherent structural damping and the reaction torque), vibration amplitude of the solar array decreases over time with a given initial condition. The envelope of the root bending moment M_b gradually converges to 0 from $M_{b,\max}$. Hence, determining the gain coefficient η according to Equation (4) guarantees Ω not exceed its permitted limit in the beginning of the control. Whereas the structure vibration amplitude decreases, amplifying the gain coefficient also makes the RW operate in the permitted operating range. For example, the relationship of M_b and Ω can be redesigned as

$$\Omega = \gamma \eta M_b. \tag{13}$$

Here, γ is the design factor to amplify the gain coefficient appropriately.

The control effect of the RW decreases with the vibration attenuation by adopting the constant-gain control. Inspired by that, the gain amplifying coefficient γ can be designed to be linear to the inverse of the envelope function of vibration. The response of the bending moment $M_b(t)$ in the time domain presents the characteristics of periodic vibration and relatively slow attenuation. The slow attenuation part is the so-called envelope function in mathematics, and it can be denoted as $\mathscr{E}[M_b(t)]$. During the free vibration attenuation, the ideal envelope function of the root bending moment $\mathscr{E}[M_b(t)]$ is a monotonically decreasing function with a maximum value $M_{b,\max}$. The reciprocal of $\mathscr{E}[M_b(t)]$ is a monotonically increasing function. Therefore, the amplifying coefficient γ is accordingly designed as

$$\gamma = \frac{M_{b,\max}}{\mathscr{E}[M_b(t)]}. \tag{14}$$

Considering Equation (4), Equation (14) can be described as

$$\gamma = \frac{\Omega_{\max}}{\eta \mathscr{E}[M_b(t)]} = \frac{\Omega_{\max}}{\mathscr{E}[\eta M_b(t)]}. \tag{15}$$

To avoid the exception that the denominator (i.e., $\mathscr{E}[M_b(t)]$) is zero in the numerical calculations, the maximum value of γ should be limited. A simple way is to apply a hard-bound $\gamma_{\max}$ to the computation of γ. Substituting Equation (15) into Equation (13), M_b and Ω are linked via

$$\Omega = \min\left(\frac{\Omega_{\max}}{\mathscr{E}[\eta M_b(t)]}, \gamma_{\max}\right) \times \eta M_b(t). \tag{16}$$

In the digital signal process, the envelope function can be computed by various methods, such as Hilbert transform [50, 51] or squaring and low-pass filtering [52, 53]. In this research, the envelope of the measured response signal is solved by using the squaring and low-pass filtering method. Designate the envelope function $\mathscr{E}[M_b(t)] = \bar{M}$. If the low-pass filter is taken as a 2nd-order Butterworth low-pass filter with a cutoff frequency Ω_p(rad/s), the squaring of $\bar{M}$ in the Laplace domain satisfies [54]

$$\mathrm{L}[N] = G(s)\mathrm{L}\left[2M_b^2\right] = \frac{2\Omega_p^2}{s^2 + \sqrt{2}\Omega_p s + \Omega_p^2}\mathrm{L}\left[M_b^2\right], \tag{17}$$

in which $\mathrm{L}[\cdot]$ denotes the Laplace transformation, $G(s)$ is the transfer function of the filter, and s is the Laplace variable,

$$N = \bar{M}^2. \tag{18}$$

Rewriting Equation (17) in the time domain:

$$\ddot{N} + \sqrt{2}\Omega_p \dot{N} + \Omega_p^2 N = 2\Omega_p^2 M_b^2. \tag{19}$$

Performing the first- and second-order time derivatives on both sides of Equation (18), respectively, we have

$$\dot{N} = 2\bar{M}\dot{\bar{M}}, \ddot{N} = 2\bar{M}\ddot{\bar{M}} + 2\dot{\bar{M}}^2. \tag{20}$$

Substituting Equations (18) and (20) into Equation (19), the relation of $\bar{M}$ and M_b can be constructed:

$$2\bar{M}\ddot{\bar{M}} + 2\dot{\bar{M}}^2 + \sqrt{2}\Omega_p 2\bar{M}\dot{\bar{M}} + \Omega_p^2\bar{M}^2 = 2\Omega_p^2 M_b^2. \tag{21}$$

Unit Equations (13) and (14) to eliminate γ:

$$M_b = \frac{\Omega\bar{M}}{\eta\Omega_{\max}}. \tag{22}$$

Substituting Equation (22) into Equation (21) and moving the item on the right-hand side of the equation to the left-hand side lead to

$$\ddot{\bar{M}} + \frac{1}{\bar{M}}\dot{\bar{M}}^2 + \sqrt{2}\Omega_p\dot{\bar{M}} + \frac{\Omega_p^2}{2}\bar{M} - \frac{\Omega_p^2\Omega^2\bar{M}}{\eta^2\Omega_{\max}^2} = 0. \tag{23}$$

Then, substituting the first equation of Equation (1) into Equation (22),

$$\frac{\Omega\bar{M}}{\eta\Omega_{\max}} = \varphi_M\xi_1. \tag{24}$$

Recalling Equation (24), one can get

$$\Omega = \eta\Omega_{\max}\varphi_M \frac{\xi_1}{\bar{M}}, \dot{\Omega} = \eta\Omega_{\max}\varphi_M \left(\frac{\dot{\xi}_1}{\bar{M}} - \frac{\xi_1\dot{\bar{M}}}{\bar{M}^2}\right). \tag{25}$$

Simultaneous formulas (5), (7), (23), and (25), the equation group of the closed-loop system is constituted by ξ_1 and $\bar{M}$:

$$\begin{cases} \ddot{\xi}_1 + 2\omega_1\zeta_1\dot{\xi}_1 + \omega_1^2\xi_1 = a\left(\dfrac{\xi_1\dot{\bar{M}}}{\bar{M}^2} - \dfrac{\dot{\xi}_1}{\bar{M}}\right), \\ \ddot{\bar{M}} + \sqrt{2}\Omega_p\dot{\bar{M}} + \dfrac{\Omega_p^2}{2}\bar{M} = \dfrac{b}{\bar{M}}\xi_1^2 - \dfrac{1}{\bar{M}}\dot{\bar{M}}^2, \end{cases} \tag{26}$$

where $a = I\Omega_{\max}^2\varphi_\theta^2/\theta_{\max}$, $b = \Omega_p^2\varphi_M^2$, and $a, b > 0$.

Designating $\{y_1 \quad y_2 \quad y_3 \quad y_4\}^T = \left\{\dot{\xi}_1 \quad \xi_1 \quad \dot{\bar{M}} \quad \bar{M}\right\}^T$, the equation group (26) can be written equivalently as follows:

$$\begin{cases} \dot{y}_1 = -2\omega_1\zeta_1 y_1 - \omega_1^2 y_2 + a\dfrac{y_2 y_3}{y_4^2} - a\dfrac{y_1}{y_4}, \\ \dot{y}_3 = -\sqrt{2}\Omega_p y_3 - \dfrac{\Omega_p^2}{2}y_4 + \dfrac{b}{y_4}y_2^2 - \dfrac{1}{y_4}y_3^2. \end{cases} \tag{27}$$

Perform a Taylor expansion of function y_4 at time t_0, and denote $y_4 = y_{40} + \Delta y_4$ $(y_{40} > 0)$, where Δy_4 is the corresponding small increment. Then,

$$\begin{aligned} \dot{y}_4 &= \Delta\dot{y}_4, \\ \frac{1}{y_4} &= \frac{1}{y_{40} + \Delta y_4} = \frac{1}{y_{40}}\frac{1}{1 + \Delta y_4/y_{40}} \approx \frac{1}{y_{40}}\left(1 - \frac{\Delta y_4}{y_{40}}\right), \\ \frac{1}{y_4^2} &= \frac{1}{y_{40}^2}\left(1 - \frac{\Delta y_4}{y_{40}}\right)^2 \approx \frac{1}{y_{40}^2}\left(1 - 2\frac{\Delta y_4}{y_{40}}\right). \end{aligned} \tag{28}$$

Substituting Equation (28) into Equation (27), and adding two identical equations $\dot{y}_2 = y_1$ and $\Delta\dot{y}_4 = y_3$, one can obtain

$$\begin{cases} \dot{y}_1 = -2\omega_1\zeta_1 y_1 - \omega_1^2 y_2 + \dfrac{a}{y_{40}^2}y_2 y_3 - \dfrac{a}{y_{40}}y_1 - \dfrac{2a}{y_{40}^3}y_2 y_3\Delta y_4 - \dfrac{a}{y_{40}^2}y_1\Delta y_4, \\ \dot{y}_2 = y_1, \\ \dot{y}_3 = -\sqrt{2}\Omega_p\dot{y}_3 - \dfrac{\Omega_p^2}{2}y_{40} + \dfrac{b}{y_{40}}y_2^2 - \dfrac{1}{y_{40}}y_3^2 + \dfrac{1}{y_{40}^2}y_3^2\Delta y_4 - \dfrac{\Omega_p^2}{2}\Delta y_4 - \dfrac{b}{y_{40}^2}y_2^2\Delta y_4, \\ \Delta\dot{y}_4 = y_3. \end{cases} \tag{29}$$

Considering the assumption of small perturbation and weak damping, y_1, y_2, y_3, and Δy_4 are small quantities. Thus, neglecting the higher-order terms, the corresponding state-space representation of Equation (29) can be built up:

$$\dot{\mathbf{y}}_s = \mathbf{A}_s\mathbf{y}_s + \mathbf{B}_s u_s. \tag{30}$$

Here,

$$\begin{aligned} \mathbf{A}_s &= \begin{bmatrix} -\left(2\omega_1\zeta_1 + \dfrac{a}{y_{40}}\right) & -\omega_1^2 & \mathbf{0} \\ 1 & 0 & \\ & \mathbf{0} & \begin{matrix} -\sqrt{2}\Omega_p & -\dfrac{\Omega_p^2}{2} \\ 1 & 0 \end{matrix} \end{bmatrix}, \\ \mathbf{y}_s &= \begin{bmatrix} y_1 \\ y_2 \\ y_3 \\ \Delta y_4 \end{bmatrix}, \\ \mathbf{B}_s &= \begin{bmatrix} 0 \\ 0 \\ 1 \\ 0 \end{bmatrix}, \\ u_s &= -\frac{\Omega_p^2}{2}y_{40} = \text{constant}, \end{aligned} \tag{31}$$

in which $\mathbf{0}$ is a 2×2 zero matrix.

The characteristic equation of the closed-loop system (30) is

$$\left[\lambda^2 + \left(2\omega_1\zeta_1 + \frac{a}{y_{40}}\right)\lambda + \omega_1^2\right]\left[\lambda^2 + \sqrt{2}\Omega_p\lambda + \frac{\Omega_p^2}{2}\right] = 0. \tag{32}$$

The solutions of Equation (32) are

$$\begin{aligned} \lambda_{1,2} &= \frac{-(2\omega_1\zeta_1 + a/y_{40}) \pm \sqrt{(2\omega_1\zeta_1 + a/y_{40})^2 - 4\omega_1^2}}{2}, \\ \lambda_{3,4} &= -\frac{\sqrt{2}}{2}\Omega_p. \end{aligned} \tag{33}$$

It can be seen from Equation (33) that the real parts of $\lambda_i (i = 1, 2, 3, 4)$ are negative, and it is independent of y_{40}. Or, namely, the system is stable with a local Taylor expansion of y_4 at any time such that the stability in the whole process can be guaranteed. Thus, the closed-loop system is stable in small perturbation.

3.2. Numerical Verification. In this section, to make the different control strategies comparable, the numerical model of the flexible solar array, as shown in Figure 2, is used to examine the effect of the proposed variable-gain control strategy.

The feedback control diagram with envelope-based variable-gain control is updated based on Figure 3, and it is shown in Figure 6. The gain amplifying coefficient γ, which is constructed according to Equation (15), is involved in the controller to improve the reaction torque provided by

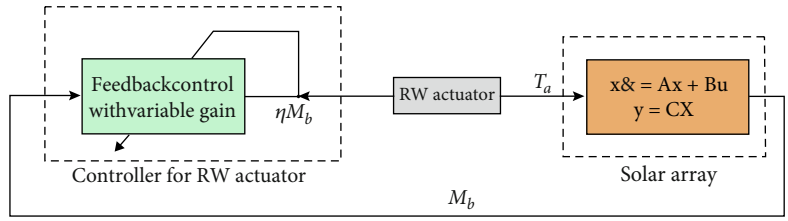

Figure 6: Diagram of the feedback control with variable gain.

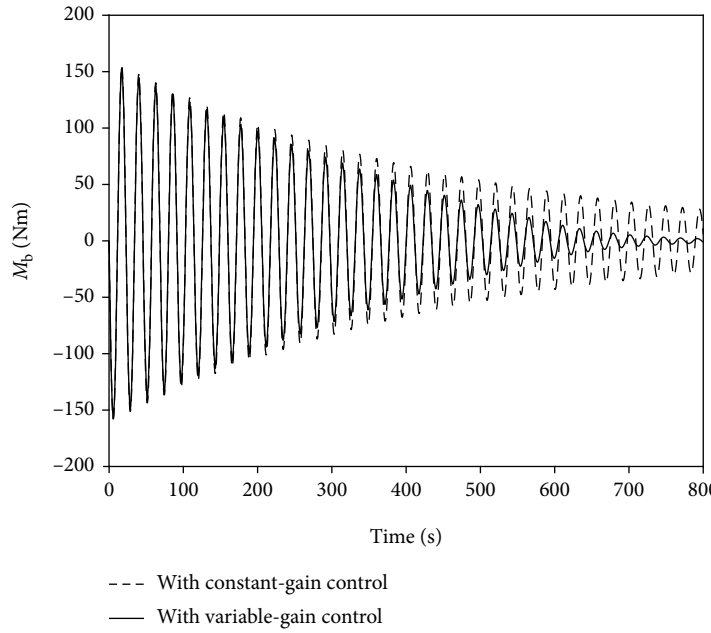

Figure 7: Response curve of the root bending moment with variable-gain control.

the RW actuator. The bound $\gamma_{\max}$ is taken as 10 in this study. There is a delay in calculating the envelope function of the response signal by using the squaring and low-pass filtering method. The correct envelope value of the signal is output at about the second natural period of vibration after the simulation starts. Therefore, the rotational speed Ω should be limited in case exceeding its permitted operating range. To this end, a saturation module is utilized to limit the absolute value of its output within $\Omega_{\max}$, which is also applied to the negative values of Ω.

The transient responses are revisited with the same initial condition, as shown in Equation (12). Figure 7 reveals two response curves of M_b, in which the black bold line and the black dashed line are the responses with envelope-based variable-gain and constant-gain control, respectively. Compared to the response with constant-gain control, the vibration attenuation speed with envelope-based variable-gain control is increased, which verifies the effectiveness of the proposed approach. Taking the threshold as 5% of $M_{b,\max}$, the time required for vibration amplitude damping to the threshold is called vibration attenuation time. The vibration attenuation times in different cases are listed in Table 1.

Table 1: The vibration attenuation times of the simulation model.

	Without control	Constant-gain control	Variable-gain control
Vibration attenuation time (s)	2181.7	1367.6	657.5

As shown, the result with constant-gain control is 1367.6 s, which is reduced to 657.5 s when adopting envelope-based variable-gain control. That is, the vibration attenuation time with variable-gain control is decreased to 48.1% from the state with constant-gain control and to 30.1% from the state without control.

The rotational speed Ω with envelope-based variable-gain control is shown in Figure 8. As seen, in the first 600 s, the RW actuator rotates at a peak value near $\Omega_{\max}$, which implies the output reaction torque is improved. Therefore, involving the variable-gain control algorithm enables us to maximize the capability of the RW actuator and improve its damping effect.

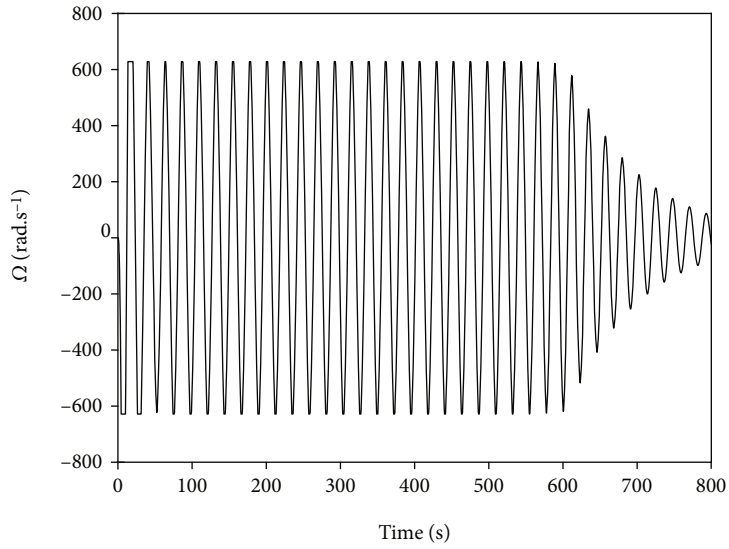

Figure 8: Rotational speed of the RW with variable-gain control.

3.3. Robustness Analysis. The envelope-based variable-gain control strategy is designed and verified for the configuration of the solar array characterized by nominal parameters. However, once the spacecraft is orbiting, some of its structural characteristics can result different from the ones measured during ground tests or derived from a numerical model. Among all the possible uncertainties, the ones that have a major impact on the performance of the vibration suppression of the solar array are associated with the natural frequency. In the following, these uncertainties reflect on the estimated errors of the first-order bending natural frequency, which result in the effect of the capability of the proposed control strategy to reduce the vibrations. Taking $\omega_1 = 0.2746$ rad/s as the benchmark, it is assumed that the predetermined frequency for the control system design exists relative errors of ±5%, ±10%, ±15%, and ± 20%, respectively. Adopting the method mentioned above, the high cut-off and the low cut-off frequencies of the band-pass filter are redesigned under different frequency error settings. The corresponding transient responses of the solar array are revisited with the same model and initial conditions.

Compared to the vibration attenuation time $t_0 = 2181.7$ s without control, the vibration attenuation times with control and their relative ratios to t_0 (i.e., relative attenuation time) under different estimated error settings are listed in Table 2. From Table 2, the vibration suppression still works effectively when the predetermined frequency deviates to a certain extent from the exact frequency (0.2746 rad/s). It reveals that the control system is robust when there are errors in the predetermined frequency. Unfortunately, if the error is too large, for example, an error of -20%, the relative attenuation time is only decreased to 52.16%. Therefore, in order to achieve a better vibration suppression effect, it is advisable to provide the natural frequency of the solar array as accurately as possible.

Table 2: Vibration suppression effect under different relative error conditions.

	Relative error	Vibration attenuation time (s)	Relative attenuation time (%)
1	0	657.5	30.14
2	5%	670.3	30.72
3	-5%	713.4	32.70
4	10%	671.1	30.76
5	-10%	779.4	35.72
6	15%	672.7	30.84
7	-15%	901.8	41.34
8	20%	696.0	31.90
9	-20%	1137.9	52.16

4. Experimental Verification

4.1. Experimental Setup for Vibration Suppression. In this section, a real example is used for feasibility investigation. The test article is an elastic plate with two additional weights. Figure 9 details the experimental setup. The anti-shock sponges with a thickness of 0.5 mm are pasted on both surfaces of the plate. The two additional weights and anti-shock sponges are utilized to adjust the natural frequency and damping of the model, respectively. To reduce the influence of gravity, the plate is laterally placed to ensure that the bending vibration is perpendicular to the gravity direction. One side of the elastic plate is fixed on a sliding table to simulate the disturbance from the spacecraft body. The other side is equipped with a brushed-DC motor (BDCM), which serves as a RW actuator to provide reaction torque.

In this case, the total mass of the DC motor is 5.8 g. Parameters of the experimental apparatus are listed in Table 3. By experimental test and analysis, the natural

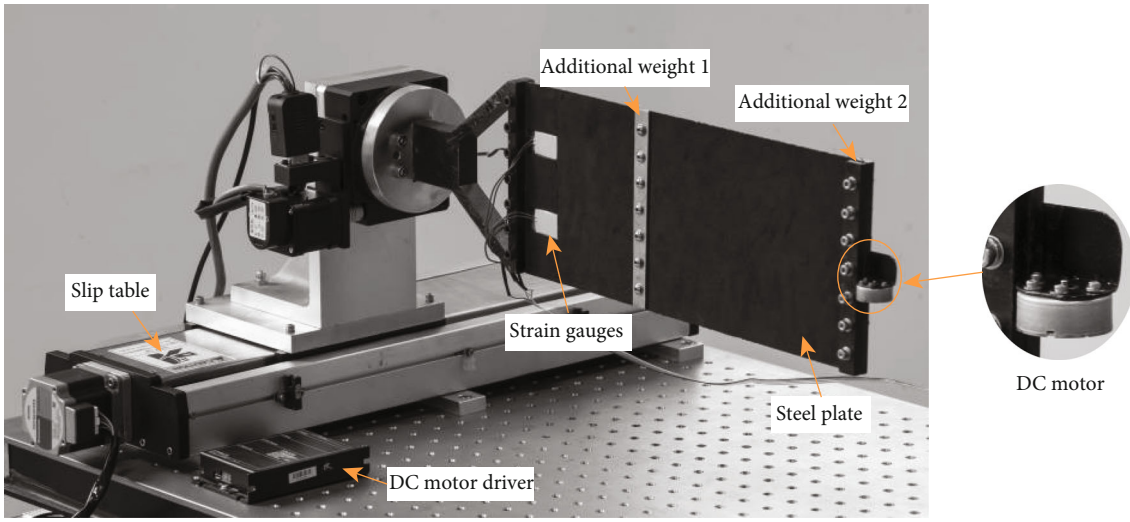

Figure 9: Photograph of the experimental setup for vibration suppression.

Table 3: Parameters of the experimental apparatus.

Length, height, and thickness of elastic plate	370 mm × 150 mm × 0.3 mm
Mass of elastic plate	126 g
Mass of additional weight 1	67 g
Mass of additional weight 2	115 g
Distance from fixed side to additional weight 1	217.5 mm
Distance from fixed side to additional weight 2	362.5 mm
Mass of DC motor	5.8 g

frequency corresponding to the first-order out-of-plane bending mode of the model is 0.805 Hz.

Instead of measuring the bending moment as done in the numerical simulation, in the experiment, the strain signal of the vibrating structure is measured to acquire the input of the control system. To acquire the signal with a larger SNR (signal-to-noise ratio), the measuring point is arranged at a location with higher stresses. Denote the longitudinal strain of the measured position as ε_l, then the modal coordinate can be solved by

$$\xi_1(t) = \frac{\varepsilon_l}{\varphi_\varepsilon}, \tag{34}$$

where φ_ε is the first-order modal coefficient corresponding to ε_l. Meanwhile, Equation (34) indicates that the measured strain signal is proportional to ξ_1. Therefore, according to Equations (3) and (34), the rotational speed and the measured strain signal can be linked via

$$\Omega = \frac{\eta\varphi_M}{\varphi_\varepsilon}\varepsilon_l. \tag{35}$$

Equation (35) states that similar to measuring the root bending moment M_b, the measured strain signal is linear to the speed signal of the RW actuator in the experiment. However, it should be noted that Equation (35) holds, if and only if the linear relationships exist between the modal coordinate and M_b, ε_l, as stated in Equations (1) and (34).

The strain gauges, with a resistance of 350 Ω, are bonded on the elastic plate near the fixed side to acquire the local strain signal ε_l. The input voltage of the full-bridge strain circuit is 1.5 V. The output voltage of the strain bridge circuit is amplified 3000 times linearly by a strain amplifier and sampled by an analog-to-digital (A/D) module. Let V_ε be the strain amplifier's output voltage, which is also called strain voltage. Through the A/D module, the corresponding digital value of V_ε is acquired and regarded as the input of the control system.

When the elastic plate is disturbed, V_ε changes with the vibration of the elastic plate. According to the predesigned algorithm, the driving signal voltage V_d commanding the speed of the DC motor is solved and output to the motor driver through a D/A (digital-to-analog) module. In this paper, the motor driver is ESCON-50/5 produced by MAXON Corporation. The speed signal voltage range is 0 ~ 2.4 V, corresponding to the rotational speed 0~14800 RPM linearly. The direction of the rotational speed is commanded by a logic high or low signal.

The slip table administrated by a stepper motor is adopted to excite the vibration of the elastic plate model. The excitation is performed as follows. The slip table undergoes two periods of sinusoidal motion at 0.8 Hz along the normal direction of the plate surface. The speed function v_e of the excitation table is given in mm/s by

$$v_e = \begin{cases} 15\sin(1.6\pi t), & 0 \le t \le 2.5\text{ s}, \\ 0, & t > 2.5\text{ s}. \end{cases} \tag{36}$$

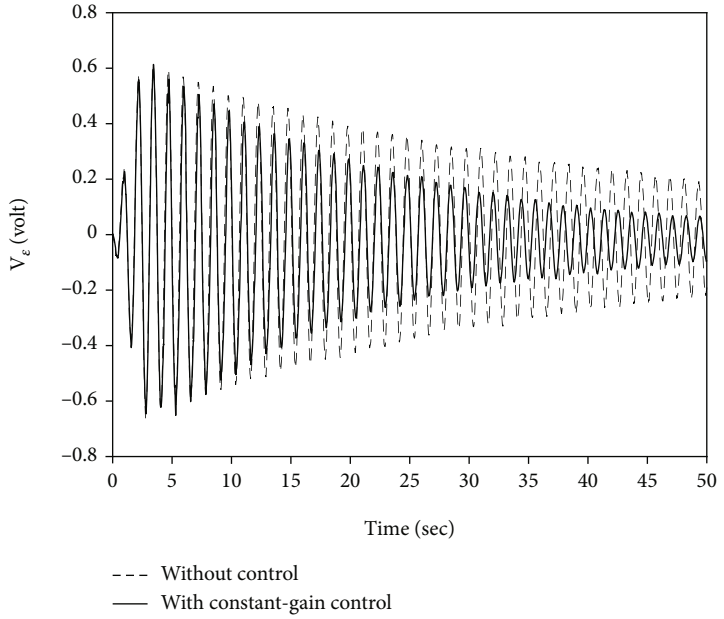

Figure 10: Measured response curve of the strain voltage with constant-gain control.

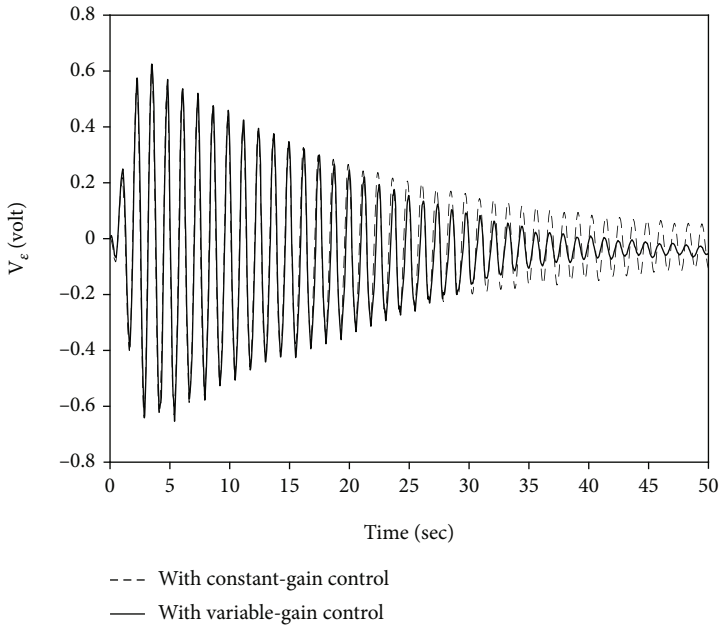

Figure 11: Measured response curve of the strain voltage with variable-gain control.

The vibration response is measured by strain gauges during the entire time period (from the beginning of the excitation to the end of the experiment). In order to verify the suppression effectiveness, the vibration attenuation with and without control is measured.

4.2. Experimental Performance of Vibration Suppression Subjected to Different Control Strategies. As aforementioned, the rotational speed Ω and the strain ε_l are linear to the electric voltage V_d and V_ε, respectively. Recalling Equation (35), the driving signal voltage V_d is proportional to the strain voltage V_ε:

$$V_{\mathrm{d}} = \kappa V_\varepsilon, \tag{37}$$

where κ is the proportional gain coefficient in the experiment. It is required that the motor rotates within the maximum ratings and near the maximum speed when V_ε reaches its peak value. Therefore, the coefficient κ is estimated by $V_d^{\max}/V_\varepsilon^{\max}$, and it is taken as -3.5 in this case, in

Table 4: The vibration attenuation time of the experiment model.

	Without control	Constant-gain control	Variable-gain control
Vibration attenuation time (s)	153.4	89	44.7

which $V_d^{\max}$ is the permitted maximum value of the driving voltage, which equals to 2.4 V in this case.

The response curve of the strain voltage V_ε with constant-gain control is shown as the solid line in Figure 10. Compared to the response without control (the dashed line), the vibration attenuation process is accelerated. The results verify that the vibration attenuation of the elastic plate can be accelerated by applying the reaction torque based on the control relation (37).

The envelope-based variable-gain control strategy is also validated based on the elastic plate model. Recalling Equations (15) and (16), the gain amplifying coefficient γ in the experiment is accordingly designed to be

$$\gamma = \min\left(\frac{V_d^{\max}}{\mathscr{E}[\kappa V_\varepsilon(t)]}, \gamma_{\max}\right). \tag{38}$$

The calculation module for γ is added to the control program according to Equation (38). The envelope-based variable-gain control strategy is employed for vibration suppression of the plate model with the same experimental settings. The response curve of the strain voltage V_ε is plotted as the solid line in Figure 11. Compared to the measured result with constant-gain control (the dashed line), the attenuation speed with the proposed variable-gain control is increased.

The vibration attenuation time is used as a metric to demonstrate the vibration suppression efficiency. The vibration amplitude threshold $V_\varepsilon^* = 0.05\mathscr{E}^{\max}[V_\varepsilon(t)]$. Based on the measured responses, the vibration attenuation times without control, with constant-gain control, and with envelope-based variable-gain control are listed in Table 4, respectively. Compared to 153.4 s and 89 s, the vibration attenuation time with envelope-based variable-gain control is reduced to 29.1% of that from the uncontrolled state and to 50.22% of that from the constant-gain controlled state.

5. Conclusion

In this paper, an envelope-based variable-gain control strategy for the reaction wheel (RW) actuator is proposed to suppress the bending vibration of the solar array. Both numerical simulations and experimental studies are provided to demonstrate the rationality and validity of the proposed variable-gain control in improving the vibration suppression performance of the RW actuator compared to the constant-gain control. Taking the finite element model of a full-scale solar array as the object, the damping effects of the RW actuator subjected to different control strategies are compared by using the vibration attenuation time as a metric. The vibration attenuation time without control and with constant-gain control are 2181.7 s and 1367.6 s, respectively, and it is reduced to 657.5 s when the envelope-based variable-gain control is adopted. The numerical simulations considering deviations between the estimated and the exact natural frequency values are performed to analyze the robustness of the control system. It is concluded that the proposed technique is robust within a deviation range of ±20%. To obtain a better control effect, a more accurate estimation value of the natural frequency is required. Experiments on an elastic plate model further prove that the proposed variable-gain control method is a valid and feasible technology. Compared to 153.4 s and 89 s, the vibration attenuation time with envelope-based variable-gain control is reduced to 29.1% of that from the uncontrolled state and to 50.22% of that from the constant-gain controlled state.

Data Availability

The data used to support the findings of this study are available from the corresponding author upon request.

Conflicts of Interest

The authors declared no potential conflicts of interest with respect to the research, authorship, and/or publication of this article.

Acknowledgments

This research is supported by the Open Project of Shanghai Key Laboratory of Spacecraft Mechanism (Grant No. 18DZ2272200).

References

[1] J. Santiago-Prowald and H. Baier, "Advances in deployable structures and surfaces for large apertures in space," *CEAS Space Journal*, vol. 5, no. 3-4, pp. 89–115, 2013.

[2] E. Wang, S. Wu, G. Xun, Y. Liu, and Z. Wu, "Active vibration suppression for large space structure assembly: a distributed adaptive model predictive control approach," *Journal of Vibration and Control*, vol. 27, pp. 365–377, 2020.

[3] B. A. Albassam, "Fast attitude maneuver of a flexible spacecraft with passive vibration control using shunted piezoelectric transducers," *International Journal of Aerospace Engineering*, vol. 2019, 2019.

[4] S. Na, G.-A. Tang, and L.-F. Chen, "Vibration reduction of flexible solar array during orbital maneuver, aircraft engineering and aerospace technology: an," *International Journal*, vol. 86, pp. 155–164, 2014.

[5] K. Shi, C. Liu, Z. Sun, and X. Yue, "Coupled orbit-attitude dynamics and trajectory tracking control for spacecraft electromagnetic docking," *Applied Mathematical Modelling*, vol. 101, pp. 553–572, 2022.

[6] H. Yavuz, S. Mıstıkoğlu, and S. Kapucu, "Hybrid input shaping to suppress residual vibration of flexible systems," *Journal of Vibration and Control*, vol. 18, no. 1, pp. 132–140, 2012.

[7] H. Ghorbani, K. Alipour, B. Tarvirdizadeh, and A. Hadi, "Comparison of various input shaping methods in rest-to-rest motion of the end- effecter of a rigid-flexible robotic

system with large deformations capability," *Mechanical Systems and Signal Processing*, vol. 118, pp. 584–602, 2019.

[8] Q. Hu and G. Ma, "Spacecraft vibration suppression using variable structure output feedback control and smart materials," *Journal of Vibration and Acoustics*, vol. 128, pp. 221–230, 2005.

[9] X.-Y. Mao, H. Ding, and L.-Q. Chen, "Passive isolation by nonlinear boundaries for flexible structures," *Journal of Vibration and Acoustics*, vol. 141, no. 5, 2019.

[10] L. Zhang, S. Xu, Z. Zhang, and N. Cui, "Active vibration suppression for flexible satellites using a novel component synthesis method," *Advances in Space Research*, vol. 67, pp. 1968–1980, 2020.

[11] P. Tarazaga, D. Inman, and W. Wilkie, "Control of a space rigidizable-inflatable boom using embedded piezoelectric composite actuators," in *47th AIAA/ASME/ASCE/AHS/ASC Structures, Structural Dynamics, and Materials Conference*, p. 1976, Newport, RI, USA, 2006.

[12] T. P. Sales, D. A. Rade, and L. C. G. de Souza, "Passive vibration control of flexible spacecraft using shunted piezoelectric transducers," *Aerospace Science and Technology*, vol. 29, no. 1, pp. 403–412, 2013.

[13] M. Bodaghi, M. Shakeri, and M. Aghdam, "Passive vibration control of plate structures using shape memory alloy ribbons," *Journal of Vibration and Control*, vol. 23, no. 1, pp. 69–88, 2017.

[14] S. Bhattarai, H. Kim, and H.-U. Oh, "CubeSat's deployable solar panel with viscoelastic multilayered stiffener for launch vibration attenuation," *International Journal of Aerospace Engineering*, vol. 2020, Article ID 8820619, 10 pages, 2020.

[15] Y. Xie, H. Shi, F. Bi, and J. Shi, "A MIMO data driven control to suppress structural vibrations," *Aerospace Science and Technology*, vol. 77, pp. 429–438, 2018.

[16] Y. Zhang and X. Guan, "Active damping control of flexible appendages for spacecraft," *Aerospace Science and Technology*, vol. 75, pp. 237–244, 2018.

[17] M. Azimi and G. Sharifi, "A hybrid control scheme for attitude and vibration suppression of a flexible spacecraft using energy-based actuators switching mechanism," *Aerospace Science and Technology*, vol. 82-83, pp. 140–148, 2018.

[18] W. Niu, C. Zou, B. Li, and W. Wang, "Adaptive vibration suppression of time-varying structures with enhanced FxLMS algorithm," *Mechanical Systems and Signal Processing*, vol. 118, pp. 93–107, 2019.

[19] S. Mohanty and S. K. Dwivedy, "Linear and nonlinear analysis of traditional and non-traditional piezoelectric vibration absorber with time delay feedback for simultaneous resonance conditions," *Mechanical Systems and Signal Processing*, vol. 161, article 107980, 2021.

[20] D. Zhang and L. Zheng, "Active vibration control of plate partly treated with ACLD using hybrid control," *International Journal of Aerospace Engineering*, vol. 2014, Article ID 432970, 12 pages, 2014.

[21] A. Bronowicki, "A layered vibration control strategy for space telescopes, smart," *Structures and Materials*, vol. 5056, pp. 487–496, 2003.

[22] R. Jamshidi and A. A. Jafari, "Nonlinear vibration of conical shell with a piezoelectric sensor patch and a piezoelectric actuator patch," *Journal of Vibration and Control*, 2021.

[23] J. Yao, "Intelligent plate vibration control using pizeoelectric sensors and actuators," *Proceedings of SPIE*, vol. 5253, pp. 624–629, 2003.

[24] Z.-C. Qiu, C. Li, and X.-M. Zhang, "Experimental study on active vibration control for a kind of two-link flexible manipulator," *Mechanical Systems and Signal Processing*, vol. 118, pp. 623–644, 2019.

[25] F. Casella, A. Locatelli, and N. Schiavoni, "Modelling and control for vibration suppression in a large flexible structure with jet thrusters and piezoactuators," in *Proceedings of the 39th IEEE Conference on Decision and Control (Cat. No.00CH37187)*, pp. 4491–4499, Sydney, NSW, Australia, 2000.

[26] H. Sun, X. Tang, S. Hou, and X. Wang, "Vibration suppression for large-scale flexible structures based on cable-driven parallel robots," *Journal of Vibration and Control*, vol. 27, no. 21-22, pp. 2536–2547, 2020.

[27] W. Hu, Y. Gao, and B. Yang, "Semi-active vibration control of two flexible plates using an innovative joint mechanism," *Mechanical Systems and Signal Processing*, vol. 130, pp. 565–584, 2019.

[28] G. Shengmin and C. Hao, "A comparative design of satellite attitude control system with reaction wheel," in *First NASA/ESA Conference on Adaptive Hardware and Systems (AHS'06)*, pp. 359–364, Istanbul, Turkey, 2006.

[29] Z. Ismail and R. Varatharajoo, "A study of reaction wheel configurations for a 3-axis satellite attitude control," *Advances in Space Research*, vol. 45, no. 6, pp. 750–759, 2010.

[30] A. M. Si Mohammed, M. Benyettou, Y. Bentoutou, A. Boudjemai, Y. Hashida, and M. N. Sweeting, "Three-axis active control system for gravity gradient stabilised microsatellite," *Acta Astronautica*, vol. 64, no. 7-8, pp. 796–809, 2009.

[31] I. M. da Fonseca, P. M. Bainum, and A. R. da Silva, "Structural control interaction for an LSS attitude control system using thrusters and reaction wheels," *Acta Astronautica*, vol. 60, no. 10-11, pp. 865–872, 2007.

[32] S. Boulouma, S. Labiod, and H. Boubertakh, "Direct adaptive control of a flexible spacecraft with disturbances and uncertain actuator failures," *Mechanical Systems and Signal Processing*, vol. 110, pp. 73–89, 2018.

[33] B. Chen, M. Zhang, G. A. Tang, and G.-A. Tang, "Principle and experimental research on vibration reduction of flexible solar array using reaction flywheel," *Aircraft Engineering and Aerospace Technology*, vol. 90, no. 8, pp. 1282–1287, 2018.

[34] M. Shahravi and M. Azimi, "A hybrid scheme of synthesized sliding mode/strain rate feedback control design for flexible spacecraft attitude maneuver using time scale decomposition," *International Journal of Structural Stability and Dynamics*, vol. 16, article 1450101, 2014.

[35] M. Azimi, M. Shahravi, and K. Malekzadeh Fard, "Modeling and vibration suppression of flexible spacecraft using higher-order Sandwich panel theory," *The International Journal of Acoustics and Vibration*, vol. 22, no. 2, 2017.

[36] G. Ma, M. Xu, J. Tian, and X. Kan, "The vibration suppression of solar panel based on smart structure," *Aeronautical Journal*, vol. 125, no. 1283, pp. 244–255, 2021.

[37] M. Hadi, I. Mat Darus, M. O. Tokhi, and M. Jamid, "Active vibration control of a horizontal flexible plate structure using intelligent proportional-integral-derivative controller tuned by fuzzy logic and artificial bee colony algorithm," *Journal of*

Low Frequency Noise Vibration and Active Control, vol. 39, pp. 1159–1171, 2019.

[38] C. Liu, X. Yue, and Z. Yang, "Are nonfragile controllers always better than fragile controllers in attitude control performance of post-capture flexible spacecraft?," *Aerospace Science and Technology*, vol. 118, article 107053, 2021.

[39] C. L. Nascimento and D. W. McMichael, "Robot control using the feedback-error-learning rule with variable feedback gain," in *1991 Second International Conference on Artificial Neural Networks*, pp. 139–143, Bournemouth, UK, 1991.

[40] S.-J. Tsai, C.-L. Huo, Y.-K. Yang, and T.-Y. Sun, "Variable feedback gain control design based on particle swarm optimizer for automatic fighter tracking problems," *Applied Soft Computing*, vol. 13, no. 1, pp. 58–75, 2013.

[41] J. Wang, C. Yu, Y. Liu, D. Shen, and Y. Chen, "Variable gain feedback PD^{α} -type iterative learning control for fractional nonlinear systems with time-delay," *IEEE Access*, vol. 7, pp. 90106–90114, 2019.

[42] M. Heertjes, B. Hunnekens, N. V. D. Wouw, and H. Nijmeijer, "Learning in the synthesis of data-driven variable-gain controllers," in *2013 American Control Conference*, pp. 6685–6690, Washington, DC, USA, 2013.

[43] D. J. Leith and W. E. Leithead, "Survey of gain-scheduling analysis and design," *International Journal of Control*, vol. 73, no. 11, pp. 1001–1025, 2000.

[44] F. M. Caswara and H. Unbehauen, "A neurofuzzy approach to the control of a flexible-link manipulator," *IEEE Transactions on Robotics and Automation*, vol. 18, no. 6, pp. 932–944, 2002.

[45] V. G. Moudgal, K. M. Passino, and S. Yurkovich, "Rule-based control for a flexible-link robot," *IEEE Transactions on Control Systems Technology*, vol. 2, no. 4, pp. 392–405, 1994.

[46] I. Nagashima and Y. Shinozaki, "Variable gain feedback control technique of active mass damper and its application to hybrid structural control," *Earthquake Engineering and Structural Dynamics*, vol. 26, no. 8, pp. 815–838, 1997.

[47] Q. Guo, S. Wu, F. Liu, and G.-A. Tang, "Analysis of the affect and change rule of spacecraft flexible annex on system natural vibration characteristics (in Chinese)," *Journal of Vibration and Shock*, vol. 35, pp. 187–191, 2016.

[48] J. Bay, "Fundamentals of linear state space systems," *Electrical and Computer Engineering Faculty Scholarship*, vol. 3, 1999.

[49] X. Zang, S. Wu, Q. W. Guo, and G. A. Tang, "Modal analysis and fundamental frequency optimization for a space station's flexible solar panel (in Chinese)," *Journal of Vibration and Shock*, vol. 38, pp. 246–250, 2019.

[50] P. Maragos, J. F. Kaiser, and T. F. Quatieri, "Energy separation in signal modulations with application to speech analysis," *IEEE Transactions on Signal Processing*, vol. 41, no. 10, pp. 3024–3051, 1993.

[51] A. Potamianos and P. Maragos, "A comparison of the energy operator and the Hilbert transform approach to signal and speech demodulation," *Signal Processing*, vol. 37, no. 1, pp. 95–120, 1994.

[52] R. Dillon, "Classifying musical performance by statistical analysis of audio cues," *Journal of New Music Research*, vol. 32, no. 3, pp. 327–332, 2003.

[53] S. Baloch, S. Z. Jamali, K. K. Mehmood et al., "Microgrid protection strategy based on the autocorrelation of current envelopes using the squaring and low-pass filtering method," *Energies*, vol. 13, pp. 1–13, 2020.

[54] T. W. Parks and C. S. Burrus, *Digital Filter Design*, Wiley-Interscience, 1987.

Hindawi
International Journal of Aerospace Engineering
Volume 2022, Article ID 1911820, 11 pages
https://doi.org/10.1155/2022/1911820

Research Article

Finite-Time Orbit Control for Spacecraft Formation with External Disturbances and Limited Data Communication

Lei Xing,[1] **Dechao Ran**,[2] **Jian Zhang**,[3] **and Li Huang**[4]

[1]*Research Center of Satellite Technology, Harbin Institute of Technology, Harbin 150001, China*
[2]*National Innovation Institute of Defense Technology, Chinese Academy of Military Science, Beijing 100000, China*
[3]*Shanghai Institute of Satellite Engineering, Shanghai 200000, China*
[4]*Beijing Aerospace Automatic Control Institute, Beijing 100000, China*

Correspondence should be addressed to Lei Xing; xinglei@hit.edu.cn

Received 25 October 2021; Revised 11 January 2022; Accepted 15 March 2022; Published 9 May 2022

Academic Editor: Angelo Cervone

This work addresses the finite-time orbit control problem for spacecraft formation flying with external disturbances and limited data communication. A hysteretic quantizer is employed for data quantization in the controller-actuator channel to decrease the communication rate and prevent the chattering phenomenon caused by the logarithmic quantizer. Combined with the adding one power integrator method and backstepping technique, a new finite-time tracking control strategy with adaptation law is designed to ensure that the closed-loop system is practical finite-time stable, and that the tracking errors of relative position and velocity are bounded within finite-time despite with limited data communication and external disturbances. Finally, an example is shown to validate the effectiveness of the proposed finite-time tracking controller.

1. Introduction

Spacecraft formation flying (SFF) is a concept that the functionality of traditional large spacecraft is replaced by a group of less-expensive, smaller, and cooperative spacecraft [1, 2]. In recent years, the study of spacecraft formation control has gradually became an active area of research owing to the reason that SFF is a primary technology for modern space missions, such as deep space exploration, spacecraft on-orbit servicing, and deep space imaging [3–6]. So far, a rich body of orbit control strategies for SFF has been presented, and the relative dynamic model of these strategies can be roughly categorized into two types, namely, linear dynamic model and nonlinear dynamic model [7, 8]. Considering the linearizing of relative dynamic model can induce model errors, various control schemes based on the nonlinear relative dynamic model for spacecraft formation flying have been proposed [9–12].

It is to be noticed that all aforementioned control schemes can only guarantee the asymptotical stability of the controlled systems. A fast convergence rate is an essential demand for SFF. In the past few years, the finite-time control method has been widely adopted to design controllers for various nonlinear systems since it can guarantee the controlled systems have better disturbance rejection property, faster convergence rate, and higher precision control performance compared with the asymptotic control [13–16]. To date, the finite-time method has been found successfully applied to handle the spacecraft control problem [17, 18]. The design approaches for finite-time control for spacecraft main include three type approaches, namely, the adding one power integrator technique, the terminal sliding mode method, and the homogeneity theorem. However, the few studies have focused on finite-time orbit control based on the adding one power integrator technique for spacecraft formation.

Despite the fact that the mentioned research results above can ensure the controlled system finite-time stability, most of the existing finite-time control strategies focused on traditional large spacecraft, in which the bandwidth of the communication channel is assumed to be not limited. However, in modern spacecraft formation control system,

data communication between different modules is usually executed by wireless networks, which means that the bandwidth of the communication channel is limited [19, 20]. Although the use of wireless networks brings many advantages, such as lighter weight, implementation, and installation with less cost, some new challenges have inevitably been induced, for example, data missing, communication time delay, and quantization effect [21–24]. It is well known that when the data of the control module is transmitted to the actuator module by limited communication networks, the quantization errors caused by signal quantization have unavoidably emerged. If the effect of quantization errors is not compensated effectively, the control performance may be degraded or even let the system unstable. Therefore, it is desirable to design a new controller considering limited data communication for network-based spacecraft formation control systems. Recently, the attitude control problem with limited data communication for spacecraft has been studied in [25]. Unfortunately, the study concentrated on finite-time control for SFF with limited data communication is scarce.

Motivated by the above discussion, the finite-time orbit control for SFF with limited data communication will be investigated. The main contribution of this work can be summarized as follows: (1) a novel finite-time tracking controller for SFF is proposed such that the tracking errors are bounded within finite time, in which the external disturbances are considered. (2) Compared with some existing finite-time controllers designed based on the terminal sliding mode method [26–28], the advantage of our method is that it can avoid noncontinuous and singular problem by using the backstepping approach and the adding one power integrator technique. (3) The needed communication rate is decreased by employing the hysteresis quantizer to quantify the control data, in which the chattering phenomenon induced by the logarithmic quantizer can be successfully prevented.

The rest of the paper is organized as follows. The modeling and preliminaries are given in Section 2. In Section 3, the main results are presented. In Section 4 and Section 5, the illustrative example and conclusions are presented, respectively.

2. Modeling and Preliminaries

2.1. Spacecraft Formation Flying Dynamic Model. The nonlinear relative motion dynamics of SFF can be described as follows [29]:

$$\begin{cases} \ddot{x} - 2n\dot{y} - \dot{n}y - n^2x = -\dfrac{\mu x}{\|R + q_1(t)\|^3} - \dfrac{u_{l1}}{m_l} + w_1 + \dfrac{u_1}{m_f}, \\ \ddot{y} + 2n\dot{x} + \dot{n}x - n^2y = \dfrac{u_2}{m_f} - \dfrac{\mu(y+r)}{\|R + q_1(t)\|^3} + \dfrac{\mu r}{\|R\|^3} - \dfrac{u_{l2}}{m_l} + w_2, \\ \ddot{z} + \dfrac{\mu z}{\|R + q_1(t)\|^3} + \dfrac{u_{l3}}{m_l} = w_3 + \dfrac{u_3}{m_f}, \end{cases} \tag{1}$$

where $q_1(t) = [x, y, z]^T$ is the relative position from the follower spacecraft to the leader spacecraft in the local coordinate frame, $u(t) = [u_1, u_2, u_3]^T$ and $u_l(t) = [u_{l1}, u_{l2}, u_{l3}]^T$ are the control inputs of the follower spacecraft and leader spacecraft, respectively, m_f and m_l denote the mass of the follower spacecraft and leader spacecraft, respectively, $w(t) = [w_1, w_2, w_3]^T$ denotes the bounded external disturbance, μ denotes the Earth gravitational constant, n denotes the orbit angular velocity of the leader spacecraft, and $R = (0, r, 0)^T$ is the position vector from the inertial coordinate attached to the center of Earth to the leader spacecraft described in the local coordinate frame.

The position tracking error $e_1(t)$ and velocity tracking error $e_2(t)$ are defined as

$$e_1(t) = q_1(t) - q_{1d} = [e_{11}, e_{12}, e_{13}]^T, \quad e_2(t) = q_2(t) - q_{2d} = [e_{21}, e_{22}, e_{23}]^T, \tag{2}$$

where $q_2(t) = [\dot{x}, \dot{y}, \dot{z}]^T$, $q_{1d} = [x_d, y_d, z_d]^T$ m, and $q_{2d} = [\dot{x}_d, \dot{y}_d, \dot{z}_d]^T$ m/s are the relative velocity vector, desired position state, and desired velocity state, respectively.

Then, the error relative motion dynamics of SFF can be described as follows:

$$\begin{cases} \dot{e}_1(t) = e_2(t), \\ \dot{e}_2(t) = f(q_1, q_2, \dot{q}_{2d}) + \dfrac{1}{m}(u(t) + w(t)) \end{cases}, \tag{3}$$

where

$$\begin{aligned} f(q_1, q_2, \dot{q}_{2d}) &= \begin{bmatrix} f_1(q_{11}, q_{21}, \dot{q}_{2d1}) \\ f_2(q_{12}, q_{22}, \dot{q}_{2d2}) \\ f_3(q_{13}, q_{23}, \dot{q}_{2d3}) \end{bmatrix} \\ &= \begin{bmatrix} 2n\dot{y} + \dot{n}y + n^2x - \dfrac{\mu x}{\|R + q_1(t)\|^3} - \dfrac{u_{l1}}{m_l} - \ddot{x}_d \\ -2n\dot{x} - \dot{n}x + n^2y - \dfrac{\mu(y+r)}{\|R + q_1(t)\|^3} + \dfrac{\mu r}{\|R\|^3} - \dfrac{u_{l2}}{m_l} - \ddot{y}_d \\ -\dfrac{\mu z}{\|R + q_1(t)\|^3} - \dfrac{u_{l3}}{m_l} - \ddot{z}_d \end{bmatrix}. \\ f(q_1, q_2, \dot{q}_{2d}) &= [f_1(q_{11}, q_{21}, \dot{q}_{2d1}), f_2(q_{12}, q_{22}, \dot{q}_{2d2}), f_3(q_{13}, q_{23}, \dot{q}_{2d3})]^T. \end{aligned} \tag{4}$$

Assumption 1. The desired states q_{1d} and q_{2d} are assumed to bounded, and their first two-order time derivatives are assumed to be bounded.

Definition 2. The solution of (3) can be regarded as finite-time bounded or practical finite-time stable if for all $e(0) = e_0$, and there exists $\bar{\nu} > 0$ and $T_r(\bar{\nu}, e_0) < \infty$, such that $\|e(t)\| < \bar{\nu}$ for $t \geq T_r$.

Lemma 3 (see [30]). *For $x_i \in R$, $i = 1, \cdots, m$ if $q > 1$, we have*

$$\left(\sum_{i=1}^{m}|x_i|\right)^q \le 2^{q-1}\sum_{i=1}^{m}|x_i|^q,$$
$$\left(\sum_{i=1}^{m}|x_i|\right)^{1/q} \le \sum_{i=1}^{m}|x_i|^{1/q}. \tag{5}$$

Lemma 4 (see [31]). *If α and β be positive constants, then $\varsigma(y, z) > 0$ is a real-valued function. We have*

$$|y|^{\alpha}|z|^{\beta} \le \frac{\alpha\varsigma(y,z)}{\alpha+\beta}|y|^{\alpha+\beta} + \frac{\beta\varsigma(y,z)^{-\alpha/\beta}}{\alpha+\beta}|z|^{\alpha+\beta}. \tag{6}$$

2.2. Fuzzy-Logic Systems. The IF-THEN rules of the FLSs are constructed:

$$R^l: \text{if } x_1 \text{ is } \mathfrak{F}_1^l, x_2 \text{ is } \mathfrak{F}_2^l, \cdots, \text{and } x_n \text{ is } \mathfrak{F}_n^l, \text{then } y \text{ is } \mathfrak{G}^l, \tag{7}$$

where $x = [x_1, \cdots, x_n]^T \in \mathbb{R}^n$ is the input of FLSs, $y \in \mathbb{R}$ is the output of FLSs, and $\mathfrak{F}_i^l$ and $\mathfrak{G}^l$ are the fuzzy sets associate with the membership functions $\mu_{\mathfrak{F}_2^l}(x_i)$ and $\mu_{\mathfrak{G}^l}(y)$, respectively. $m = 1, 2, \cdots, k$ and k are the number of rules. Then, the FLSs can be expressed as

$$y(x) = \frac{\sum_{m=1}^{k}\Lambda_m\prod_{i=1}^{n}\mu_{\mathfrak{F}_i^m}(x_i)}{\sum_{m=1}^{k}\prod_{i=1}^{n}\mu_{\mathfrak{F}_i^m}(x_i)}, \tag{8}$$

where $\Lambda_m = \max_{y\in\mathbb{R}}\mu_{\mathfrak{G}^m}(y)$, and the fuzzy basis functions can be expressed by

$$\xi_m(x) = \frac{\prod_{i=1}^{n}\mu_{\mathfrak{F}_i^m}(x_i)}{\sum_{l=1}^{k}\left[\prod_{i=1}^{n}\mu_{\mathfrak{F}_i^m}(x_i)\right]}. \tag{9}$$

Let $\Lambda^T = [\Lambda_1, \Lambda_2, \cdots, \Lambda_k]$ and $\xi^T(x) = [\xi_1, \xi_2, \cdots, \xi_k]$. Based on (9), we have $\xi^T(x)\xi(x) < 1$. Then, considering (8) and (9), we can obtain

$$y(x) = \Lambda^T\xi(x). \tag{10}$$

Moreover, we can obtain the following property when the membership function is the Gaussian function.

Lemma 5 (see [32]). *If $f(x)$ is a continuous function defined on a compact set Ω, then there exists an FLSs for any given positive constant $\varepsilon^* > 0$ satisfying*

$$\sup_{x\in\Omega}\left|f(x) - \Lambda^{*T}\xi(x)\right| \le \varepsilon^*, \tag{11}$$

where Λ^* is the optimal parameter vector.

It is well known that FLSs have been used to deal with the uncertainties of nonlinear control systems owing to their universal approximation ability. In this paper, the FLSs will be used to approximate $\Omega(\mathfrak{R}_{2i})$.

2.3. Hysteretic Quantizer. In this paper, the hysteresis quantizer $Q(\cdot)$ is introduced to quantify the control signal, which can be expressed as follows [33]:

$$Q(u_i) \triangleq \begin{cases} u_{ik}\ \mathrm{sgn}\ (u_i) & \text{if } \dfrac{u_{ik}}{1+\eta} < |u_i| \le \dfrac{u_{ik}}{1-\eta}, \dot{u}_{ik} < 0, \\ & u_{ik} < |u_i| \le \dfrac{u_{ik}}{1-\eta}, \dot{u}_{ik} > 0, \\ u_{ik}(1+\delta)\ \mathrm{sgn}\ (u_i) & \text{if } u_{ik} < |u_i| \le \dfrac{u_{ik}}{1-\eta}, \dot{u}_{ik} < 0, \\ & \dfrac{u_{ik}}{1-\eta} \le |u_i| \le \dfrac{u_{ik}(1+\eta)}{1-\eta}, \dot{u}_{ik} > 0, \\ 0, & \text{if } 0 \le |u_i| < \dfrac{u_{\min}}{1+\eta}, \dot{u}_{ik} < 0, \\ & \dfrac{u_{\min}}{1+\eta} \le |u_i| \le u_{\min}, \dot{u}_{ik} > 0, \\ Q(u_i)(t^-) & \text{othercase} \end{cases} \tag{12}$$

where

$$u_{ik} = \rho^{(1-k)}u_{\min}, \quad k = 1, 2, \cdots n, \tag{13}$$

and $u_{\min} > 0$, $0 < \rho < 1$, and $\eta = 1 - \rho/1 + \rho$. $Q(u_i)$ is in the set of $U = \{0, \pm u_{ik}, \pm u_{ik}(1+\delta)\}$. The size of the dead-zone for $Q(u_i)$ is determined by $u_{\min}$. The map of the hysteresis quantizer $Q(u_i)$ for $u_i > 0$ is given in Figure 1.

Remark 6. The parameter ρ can be considered as a measure of quantization density. From (13), it is well known that the smaller ρ is, the coarser the quantizer becomes. Furthermore, η approaches 1 while ρ approaches zero, and then $Q(u_i)$ will have fewer quantization levels since u_i ranges over that interval [34]. Thus, the needed communication rate between the actuator module and control module is lower.

Remark 7. Unlike the logarithmic quantizer, additional quantization levels have been added in (12) to prevent oscillations. Besides, the parameter ρ chosen should be based on a principle that the controlled system is stable can be ensured.

To facilitate the next controller design, the hysteretic quantizer $Q(u_i)$ is decomposed into the following form:

$$Q(u_i) = \phi_i(t)u_i + d_i(t), \tag{14}$$

where $\phi_i(t)$ and $d_i(t)$ are nonlinear functions.

Lemma 8. *The nonlinear blue functions $\phi_i(t)$ and $d_i(t)$, respectively, satisfy*

$$1 - \eta \le \phi_i(t) \le 1 + \eta, |d_i(t)| \le u_{\min}. \tag{15}$$

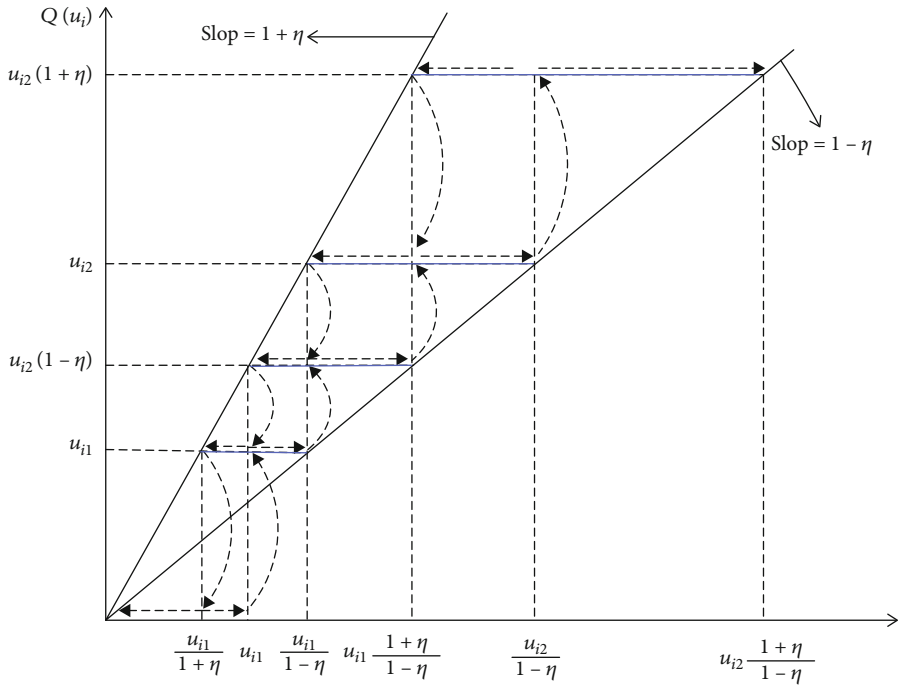

Figure 1: Map of $Q(u_i)$ for $u_i > 0$.

Proof. From Figure 2 and according to the sector-bound properties, for $|u_i| \geq u_{\min}$, we have

$$(1-\eta)u_i \leq Q(u_i) \leq (1+\eta)u_i(t). \tag{16}$$

For $|u_i| \leq u_{\min}$, when $Q(u_i) = 0$, one has

$$0 = \phi_i(t)u_i + d_i(t). \tag{17}$$

□

Define

$$\phi_i(t) = \begin{cases} \dfrac{Q(u_i)}{u_i}, & |u_i| > u_{\min} \\ 1, & |u_i| \leq u_{\min} \end{cases} \quad d_i(t) = \begin{cases} 0 & |u_i| > u_{\min} \\ -u_i(t), & |u_i| \leq u_{\min} \end{cases}. \tag{18}$$

Then, $Q(u_i) = \phi_i(t)u_i + d_i(t)$ holds, where $\phi_i(t)$ and $d_i(t)$ satisfy (15).

2.4. Control Objective. The objective of this paper is to develop a finite-time adaptive tracking controller $u(t)$ such that the position state $q_1(t)$ and velocity state $q_2(t)$ can track the desired state q_{1d} and q_{2d} in finite-time, and that the tracking error states $e_1(t)$ and $e_2(t)$ are finite-time bounded with limited data communication and external disturbances.

3. Main Results

In this section, a novel finite-time orbit tracking control strategy for formation spacecraft will be proposed. To facilitate the control strategy propose, the intermediate variables

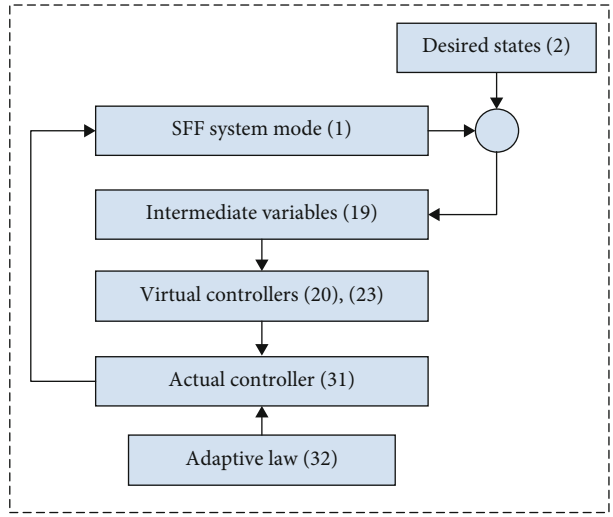

Figure 2: Block diagram of the finite-time control scheme.

$\mathfrak{R}_{1i}$ and $\mathfrak{R}_{2i}$ is defined as follows:

$$\begin{aligned} \mathfrak{R}_{1i} &= e_{1i}^{1/\alpha_1} - \sigma_{1i}^{1/\alpha_1}, \\ \mathfrak{R}_{2i} &= e_{2i}^{1/\alpha_2} - \sigma_{2i}^{1/\alpha_2}, \; i = 1, 2, 3, \end{aligned} \tag{19}$$

where $\alpha_1 = 1$, $0 < \alpha_2 = 1 + \tau < 1$, and $\tau = -m/n < 0$ be the ration of an even integer m and an odd integer n. σ_{1i} and σ_{2i} are the virtual controller. Under the backstepping method framework, the control strategy develop procedure is described as follows:

Step 1. Propose of virtual control law σ_{1i} and σ_{2i}.

Consider a Lyapunov function candidate as $V_1 = \sum_{i=1}^{3} \int_{\sigma_{1i}}^{e_{1i}} \left(s^{1/\alpha_1} - {\sigma_{1i}}^{1/\alpha_1}\right)^{2-\alpha_2} ds$.

Design the virtual controller σ_{1i} as follows:

$$\sigma_{1i} = 0. \tag{20}$$

The derivative of V_1 is obtained as follows:

$$\dot{V}_1 = \sum_{i=1}^{3} {\mathfrak{R}_{1i}}^{2-\alpha_2} \dot{e}_{1i} = \sum_{i=1}^{3} {\mathfrak{R}_{1i}}^{2-\alpha_2} (e_{2i} - \sigma_{2i}) + \sum_{i=1}^{3} {\mathfrak{R}_{1i}}^{2-\alpha_2} \sigma_{2i}, \tag{21}$$

and then applying Lemmas 3 to 5 yields

$$\begin{aligned} {\mathfrak{R}_{1i}}^{2-\alpha_2} (e_{2i} - \sigma_{2i}) &\le \left| {\mathfrak{R}_{1i}}^{2-\alpha_2} (e_{2i} - \sigma_{2i}) \right| \le 2 |\mathfrak{R}_{1i}|^{2-\alpha_2} |\mathfrak{R}_{2i}|^{\alpha_2} \\ &\le |\mathfrak{R}_{1i}|^2 + \varsigma |\mathfrak{R}_{2i}|^2, \end{aligned} \tag{22}$$

where $\varsigma = \alpha_2 (2 - \alpha_2)^{(2-\alpha_2)/\alpha_2} > 0$ is a positive constant. The virtual control scheme is proposed as

$$\sigma_{2i} = -2\mathfrak{R}_{1i}^{\alpha_2}. \tag{23}$$

Then substituting (22) and (23) into above (21)

$$\begin{aligned} \dot{V}_1 &\le \sum_{i=1}^{3} |\mathfrak{R}_{1i}|^2 + \sum_{i=1}^{3} \varsigma |\mathfrak{R}_{2i}|^2 + \sum_{i=1}^{3} \left({\mathfrak{R}_{1i}}^{2-\alpha_2} \right) \sigma_{2i} \le \sum_{i=1}^{3} |\mathfrak{R}_{1i}|^2 \\ &\quad + \sum_{i=1}^{3} \varsigma |\mathfrak{R}_{2i}|^2 - 2 \sum_{i=1}^{3} \mathfrak{R}_{1i}^2 \le \sum_{i=1}^{3} \varsigma |\mathfrak{R}_{2i}|^2 - \sum_{i=1}^{3} \mathfrak{R}_{1i}^2. \end{aligned} \tag{24}$$

Step 2. Propose of controller u_i.

Consider the Lyapunov function as follows:

$$V = V_1 + \varpi + 1/2 \sum_{i=1}^{3} \tilde{\psi}_i^2, \tag{25}$$

where $0 < \alpha_2 + \tau < 1$

$$\varpi = \sum_{i=1}^{3} \int_{\sigma_{2i}}^{e_{2i}} \left(s^{1/\alpha_2} - {\sigma_{2i}}^{1/\alpha_2} \right)^{2-\alpha_3} ds. \tag{26}$$

The time derivative of ϖ is derived as

$$\dot{\varpi} = \sum_{i=1}^{3} \mathfrak{R}_{2i}^{2-\alpha_3} \dot{e}_{2i} + \sum_{i=1}^{3} (2 - \alpha_3) \frac{-d\left({\sigma_{2i}}^{1/\alpha_2}\right)}{dt} \int_{\sigma_{2i}}^{e_{2i}} \left(s^{1/\alpha_2} - {\sigma_{2i}}^{1/\alpha_2} \right)^{1-\alpha_3} ds. \tag{27}$$

Note that

$$\int_{\sigma_{2i}}^{e_{2i}} \left(s^{1/\alpha_2} - {\sigma_{2i}}^{1/\alpha_2} \right)^{1-\alpha_3} ds \le |\mathfrak{R}_{2i}|^{1-\alpha_3} |e_{2i} - \sigma_{2i}| \le 2^{1-\alpha_2} |\mathfrak{R}_{2i}|^{1-\tau} \le 2 |\mathfrak{R}_{2i}|^{1-\tau}. \tag{28}$$

Based on (28), we have

$$\begin{aligned} &(2 - \alpha_3) \frac{-d\left({\sigma_{2i}}^{1/\alpha_2}\right)}{dt} \int_{\sigma_{2i}}^{e_{2i}} \left(s^{1/\alpha_2} - {\sigma_{2i}}^{1/\alpha_2} \right)^{1-\alpha_3} ds \\ &\quad \le (2 - \alpha_3) 2^{1+\alpha_2/\alpha_2} e_{2i} |\mathfrak{R}_{2i}|^{1-\tau} \triangleq \chi(e_{2i}, \sigma_{2i}). \end{aligned} \tag{29}$$

Substituting (29) into the time derivative of V, it yields

$$\begin{aligned} \dot{V} &= \dot{V}_1 + \dot{\varpi} + \sum_{i=1}^{3} \tilde{\psi}_i \tilde{\psi}_i \le \sum_{i=1}^{3} \varsigma |\mathfrak{R}_{2i}|^2 - \sum_{i=1}^{3} \mathfrak{R}_{1i}^2 + \sum_{i=1}^{3} \mathfrak{R}_{2i}^{2-\alpha_3} \dot{e}_{2i} \\ &\quad + \chi(e_{2i}, \sigma_{2i}) + \sum_{i=1}^{3} \tilde{\psi}_i \tilde{\psi}_i \le \sum_{i=1}^{3} \varsigma |\mathfrak{R}_{2i}|^2 - \sum_{i=1}^{3} \mathfrak{R}_{1i}^2 \\ &\quad + \sum_{i=1}^{3} \mathfrak{R}_{2i}^{2-\alpha_3} (\mathfrak{R}_{2i}) \left(f_i(q_{1i}, q_{2i}, \dot{q}_{2di}) + \frac{1}{m} (Q(u_i) + w_i) \right) \\ &\quad + \chi(e_{2i}, \sigma_{2i}) - \sum_{i=1}^{3} \tilde{\psi}_i \dot{\hat{\psi}}_i. \end{aligned} \tag{30}$$

The controller u_i is designed as

$$u_i = -\frac{m}{1 - \eta} \left(\mathfrak{R}_{2i}^{\alpha_3} \left(\ell_i \hat{\psi}_i + 1 \right) + f_i(q_{1i}, q_{2i}, \dot{q}_{2di}) \right). \tag{31}$$

The adaptive law of $\hat{\psi}_i$ is designed as

$$\dot{\hat{\psi}}_i = \ell_i \mathfrak{R}_{2i}^2 - \mu_i \hat{\psi}_i, \tag{32}$$

where $\ell_i > 0$ and $\mu_i > 0$ are designed parameters.

Substituting (31) into (30) yields

$$\begin{aligned} \dot{V} &\le \sum_{i=1}^{3} \varsigma |\mathfrak{R}_{2i}|^2 - \sum_{i=1}^{3} \mathfrak{R}_{1i}^2 + \sum_{i=1}^{3} \mathfrak{R}_{2i}^{2-\alpha_3} \\ &\quad \cdot \left(f_i(q_{1i}, q_{2i}, \dot{q}_{2di}) + \frac{1}{m} (\phi_i(t) u_i + d_i(t) + w_i) \right) \\ &\quad + \sum_{i=1}^{3} \chi(e_{2i}, \sigma_{2i}) - \sum_{i=1}^{3} \tilde{\psi}_i \dot{\hat{\psi}}_i \le \sum_{i=1}^{3} \varsigma |\mathfrak{R}_{2i}|^2 \\ &\quad - \sum_{i=1}^{3} \mathfrak{R}_{1i}^2 + \mathfrak{R}_{2i}^{2-\alpha_3} \left(\frac{1}{m} (d_i(t) + w_i) \right) - \sum_{i=1}^{3} \mathfrak{R}_{2i}^2 \left(\ell_i \hat{\psi}_i + 1 \right) \\ &\quad + \sum_{i=1}^{3} \chi(e_{2i}, \sigma_{2i}) - \sum_{i=1}^{3} \tilde{\psi}_i \dot{\hat{\psi}}_i. \end{aligned} \tag{33}$$

Let $\Omega(\mathfrak{R}_{2i}) = \mathfrak{R}_{2i}^{\tau-1}(\varsigma|\mathfrak{R}_{2i}|^2 + \mathfrak{R}_{2i}^{2-\alpha_3}((1/m)(d_i(t)+w_i)) + \chi(e_{2i},\sigma_{2i}))$. Then, (33) can be rewritten as

$$\dot{V} \le -\sum_{i=1}^{3}\mathfrak{R}_{1i}^2 - \sum_{i=1}^{3}\mathfrak{R}_{2i}^2\left(\ell_i\widehat{\psi}_i + 1\right) - \sum_{i=1}^{3}\tilde{\psi}_i\dot{\widehat{\psi}}_i + \sum_{i=1}^{3}\mathfrak{R}_{2i}^{1-\tau}\Omega(\mathfrak{R}_{2i}). \tag{34}$$

By using the approximation ability of FLSs in Lemma 5, we have

$$\Omega(\mathfrak{R}_{2i}) = \varphi_i(\mathfrak{R}_{2i})^{*T}\xi_i + \varepsilon_1. \tag{35}$$

For convenience, let

$$\Omega = \varphi_i^{*T}\xi_i + \varepsilon_1 \le \bar{\varphi}_i^{*T}\bar{\xi}_i, \tag{36}$$

where φ_i^{*T} is the optimal fuzzy weight vector, $|\varepsilon_1| \le \varepsilon_1^*$, with ε_1^* being a positive constant. $\bar{\varphi}_i^{*T} = [\varphi_i^{*T}, \varepsilon_1^*]$ and $\bar{\xi}_i^T = [\xi_i^T, 1]$. According to Lemmas 3 to 4, and noting that $0 < \xi_i^T\xi_i \le 1$, one has

$$\mathfrak{R}_{2i}^{1-\tau}\Omega \le |\mathfrak{R}_{2i}|^{1-\tau}\psi_i^{1-\tau 2} \le \ell_i\mathfrak{R}_{2i}^2\psi_i + \Gamma_i, \tag{37}$$

where $\tilde{\psi}_i = \psi_i - \widehat{\psi}_i$, $\psi = (\sqrt{2}\|\bar{\varphi}_i^*\|)^{2/(1-\tau)}$, and $\ell_i > 0$ are positive design parameters, $\Gamma_i = (1+\tau/2)((2/1-\tau)\ell_i)^{-1-\tau/1+\tau}$, and $\widehat{\psi}_i$ is the estimate of the parameter ψ_i. Substituting (32) and (37) into (34) yields

$$\begin{aligned}\dot{V} &\le -\sum_{i=1}^{3}\mathfrak{R}_{1i}^2 - \sum_{i=1}^{3}\mathfrak{R}_{2i}^2\left(\ell_i\widehat{\psi}_i + 1\right) - \sum_{i=1}^{3}\tilde{\psi}_i\dot{\widehat{\psi}}_i + \sum_{i=1}^{3}\ell_i\mathfrak{R}_{2i}^2\psi_i \\ &+ \sum_{i=1}^{3}\Gamma_i \le -\sum_{i=1}^{3}\mathfrak{R}_{1i}^2 - \sum_{i=1}^{3}\mathfrak{R}_{2i}^2\left(\ell_i\widehat{\psi}_i + 1\right) \\ &- \sum_{i=1}^{3}\tilde{\psi}_i\left(\ell_i\mathfrak{R}_{2i}^2 - \mu_i\widehat{\psi}_i\right) + \sum_{i=1}^{3}\ell_i\mathfrak{R}_{2i}^2\psi_i + \sum_{i=1}^{3}\Gamma_i \le -\sum_{i=1}^{3}\mathfrak{R}_{1i}^2 \\ &- \sum_{i=1}^{3}\mathfrak{R}_{2i}^2 + \sum_{i=1}^{3}\mu_i\tilde{\psi}_i\widehat{\psi}_i + \sum_{i=1}^{3}\Gamma_i.\end{aligned} \tag{38}$$

The main theorem of this paper is presented as follows.

Theorem 9. *Consider the dynamic model of SFF described by (1) with the hysteretic quantizer given in (14). If the controller is designed as (31), and the adaptation law is given in (32), then the tracking errors e_{1i} and e_{2i}, $i = 1, 2, 3$ will converge into a region of the origin within finite-time.*

Proof. Denoting $\bar{V} = V_1 + \bar{\omega}$, one has

$$\bar{V} = \sum_{j=1}^{2}\sum_{i=1}^{3}\int_{\sigma_{ji}}^{e_{ji}}\left(s^{1/\alpha_j} - \sigma_{ji}^{1/\alpha_j}\right)^{2-\alpha_{j+1}}ds \le 2\sum_{i=1}^{3}|\mathfrak{R}_{1i}|^{2-\tau} + 2\sum_{i=1}^{3}|\mathfrak{R}_{2i}|^{2-\tau}. \tag{39}$$

Choosing $0 < \gamma = 2/2 - \tau < 1$, and according to Lemma 3, one then has

$$\bar{V}^{\gamma} \le \left(2\sum_{i=1}^{3}|\mathfrak{R}_{1i}|^{2-\tau} + 2\sum_{i=1}^{3}|\mathfrak{R}_{2i}|^{2-\tau}\right)^{\gamma} \le 2\sum_{i=1}^{3}\mathfrak{R}_{1i}^2 + 2\sum_{i=1}^{3}\mathfrak{R}_{2i}^2. \tag{40}$$

According to the definition of V and $\bar{V}$, we can obtain

$$V = \bar{V} + \frac{1}{2}\sum_{i=1}^{3}\tilde{\psi}_i^2 \tag{41}$$

According to (38) and (39), one has

$$\begin{aligned}\dot{V} &\le -\frac{1}{2}V^{\gamma} + \frac{1}{2}V^{\gamma} - \sum_{i=1}^{3}\mathfrak{R}_{1i}^2 - \sum_{i=1}^{3}\mathfrak{R}_{2i}^2 + \sum_{i=1}^{3}\mu_i\tilde{\psi}_i\widehat{\psi}_i + \sum_{i=1}^{3}\Gamma_i \\ &\le -\frac{1}{2}V^{\gamma} + \frac{1}{2}\bar{V}^{\gamma} + \frac{1}{2}\left(\frac{1}{2}\sum_{i=1}^{3}\tilde{\psi}_i^2\right)^{\gamma} - \sum_{i=1}^{3}\mathfrak{R}_{1i}^2 - \sum_{i=1}^{3}\mathfrak{R}_{2i}^2 \\ &+ \sum_{i=1}^{3}\mu_i\tilde{\psi}_i\widehat{\psi}_i + \sum_{i=1}^{3}\Gamma_i \le -\frac{1}{2}V^{\gamma} + \left(\frac{1}{2}\sum_{i=1}^{3}\tilde{\psi}_i^2\right)^{\gamma} \\ &+ \sum_{i=1}^{3}\mu_i\tilde{\psi}_i\widehat{\psi}_i + \sum_{i=1}^{3}\Gamma_i.\end{aligned} \tag{42}$$

Moreover, applying Lemma 4

$$\begin{aligned}\mu_i\tilde{\psi}_i\widehat{\psi}_i &\le -\mu_i 2\tilde{\psi}_i^2 + \mu_i 2\psi_i^2, \\ \left(\frac{1}{2}\sum_{i=1}^{3}\tilde{\psi}_i^2\right)^{\gamma} &\le \sum_{i=1}^{3}\frac{\mu_i}{2}\tilde{\psi}_i^2 + \sum_{i=1}^{3}\nu_i,\end{aligned} \tag{43}$$

where $\nu_i = (1-\gamma)(\gamma/\mu_i)^{\gamma/(1-\gamma)}$. □

Then,

$$\begin{aligned}\dot{V} &\le -\frac{1}{2}V^{\gamma} + \sum_{i=1}^{3}\nu_i + \frac{\mu_i}{2}\psi_i^2 + \sum_{i=1}^{3}\Gamma_i \le -\frac{1}{2}\kappa V^{\gamma} - \frac{1}{2}(1-\kappa)V^{\gamma} \\ &+ \sum_{i=1}^{3}\nu_i + \frac{\mu_i}{2}\psi_i^2 + \sum_{i=1}^{3}\Gamma_i \le -\frac{1}{2}\kappa V^{\gamma} - \frac{1}{2}(1-\kappa)V^{\gamma} + \vartheta,\end{aligned} \tag{44}$$

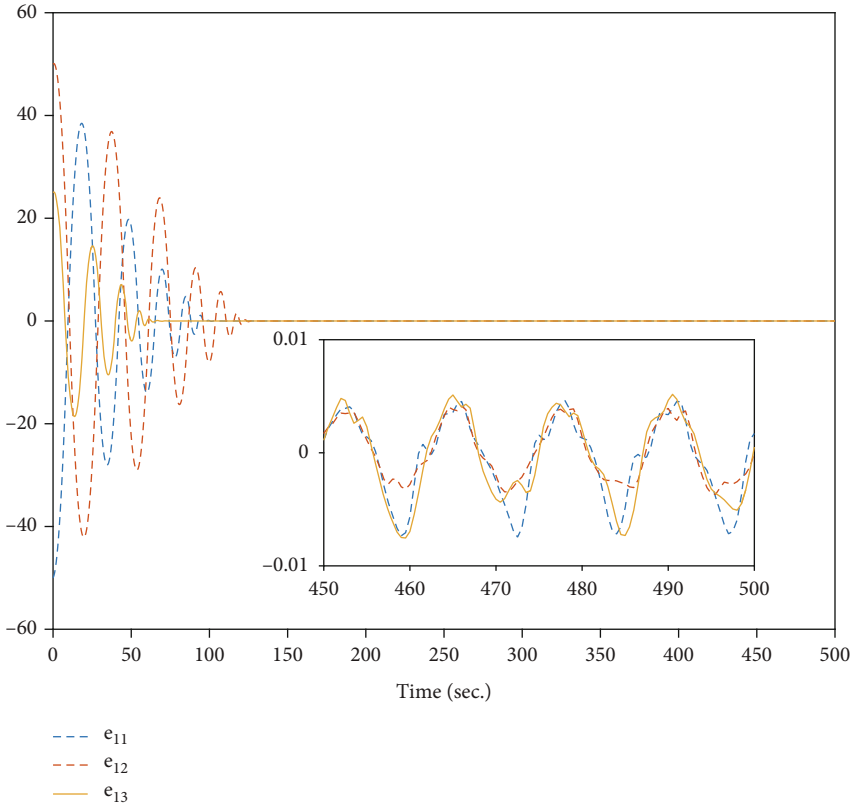

Figure 3: Response curves of position tracking errors.

where $\vartheta = \sum_{i=1}^{3} \nu_i + (\mu_i/2)\psi_i^2 + \sum_{i=1}^{3} \Gamma_i$. From (44), we can obtain that $\dot{V} \leq -12\kappa V^{\gamma}$ if and only if $V^{\gamma} > 2\vartheta/1-\kappa$, which means $V < 0$ out the set $\{V^{\gamma} \leq 2\vartheta/1-\kappa\}$. The required time of reach the bounded set is $T_r \leq 2V^{1-\gamma}(e_0)/\kappa(1-\gamma)$. Thus, as the analysis in [16], we can conclude that V can reach the set within finite time based on Definition 2. Furthermore, we can obtain that the tracking errors e_{1i} and e_{2i}, $i = 1, 2, 3$ converge into a region of the origin with finite-time.

The design procedure of the controller could be visualized from the bloc diagram shown in Figure 2.

Remark 10. By employing the property $0 < \xi_i^T \xi_i \leq 1$ of FLSs [16], only one adaptation law for $\hat{\psi}_i$ is designed to proposed the controller. Furthermore, the effects of quantization errors and external disturbances can be eliminated by the designed adaptation law.

Remark 11. Compared with the finite-time controllers using the terminal sliding mode method, the finite-time controller (31) is proposed by using the adding one power integrator technique and backstepping approach to guarantee the finite-time convergence and overcome the noncontinuous and singular problem.

4. Illustrative Example

In this section, an illustrative example is shown to illustrate the efficiency of the proposed finite-time control scheme. The leader spacecraft and follower spacecraft mass are $m_l = 1$ kg and $m_f = 1$ kg, respectively. For simplicity, the leader spacecraft is assumed in a circular reference orbit of radius 6728 km. The input control force is limited as $u_i \leq u_{\max} = 1$ N, $i = 1, 2, 3$.

The initial relative position and velocity are $q_{10} = [250, -50, 0]^T$ m and $q_{20} = [0, 0, 0]^T$ m/s, respectively. The desired relative position and relative are $q_{1d} = [0, 0, 0]^T$ m and $q_{2d} = [0, 0, 0]^T$ m/s, respectively. The external disturbance is $w(t) = [0.01 \cos(0.5t), 0.01 \cos(0.5t), 0.01 \cos(0.5t)]$. The parameters of the finite time control scheme (31) and the adaptation law (33) are chosen as $\ell_i = 0.001$, $\mu_i = 0.001$, $\hat{\psi}_i(0) = 0.01$, $i = 1, 2, 3\alpha_1 = 1$, $\alpha_2 = 3/5$, and $\alpha_3 = 1/5$, and the quantization parameters are designed as $\rho = 0.4$, $u_{\min} = 0.000001$.

The tracking errors e_{1i} and e_{2i}, $(i = 1, 2, 3)$ of the finite-time controller (31) are shown Figures 3 and 4, respectively. As observed from Figure 2, the position tracking errors can converge to almost zero with 150 s, and the position tracking errors is within $|e_{1i}| < 0.01$ m at 500 s. The control force is given in Figure 5, which force magnitude is limited to 1 N. Figure 6 shows the quantized control force for the finite-time controller (31). The response curves of $\hat{\psi}_i$ are shown in Figure 7. Clearly, the simulation results verify the validity of the hysteresis quantizer and illustrate the efficiency of the proposed finite-time control scheme.

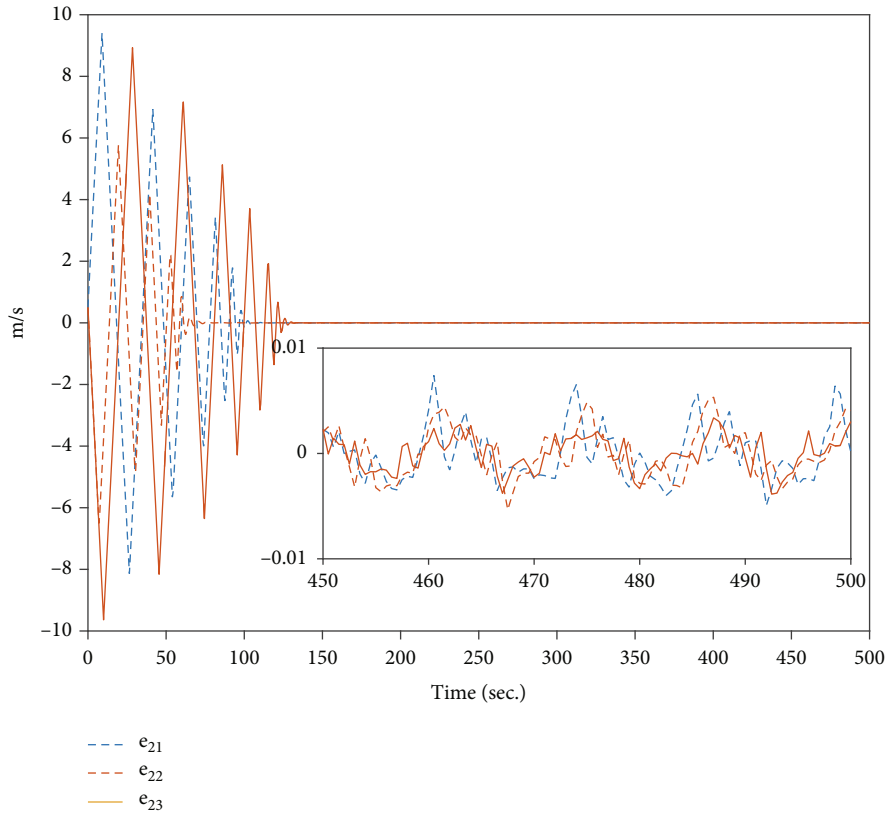

Figure 4: Response curves of velocity tracking errors.

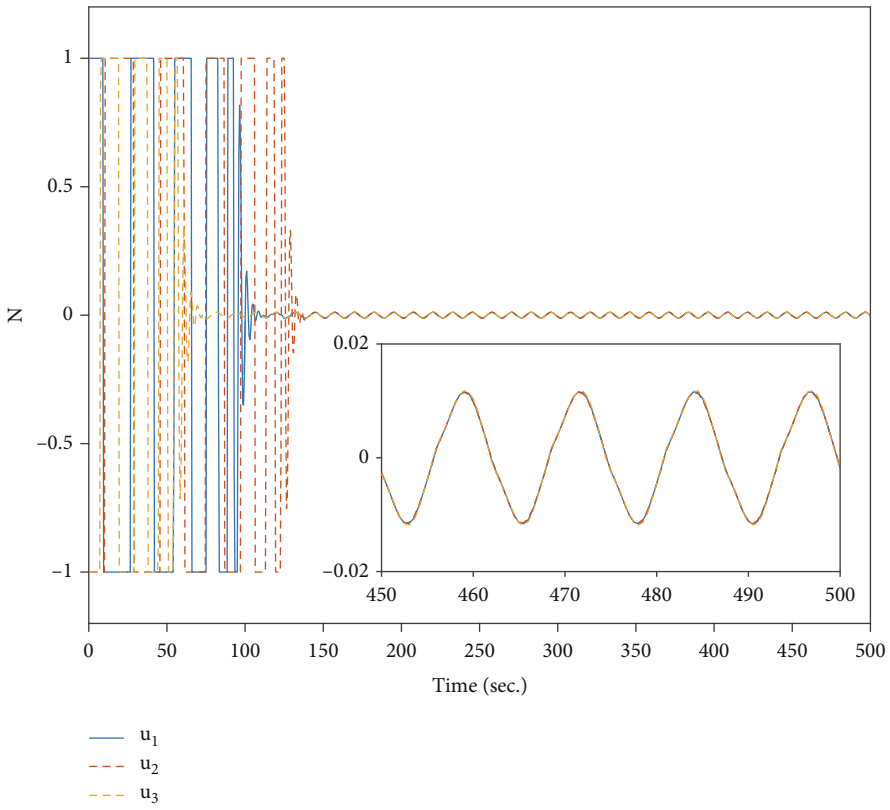

Figure 5: Response curves of control force.

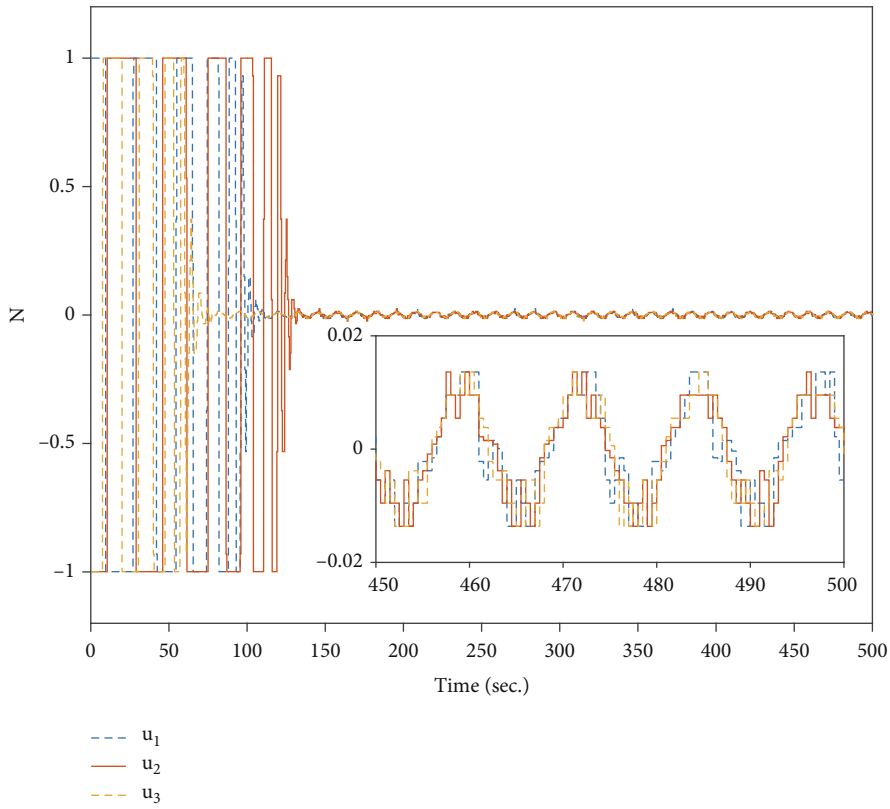

Figure 6: Response curves of quantized control force.

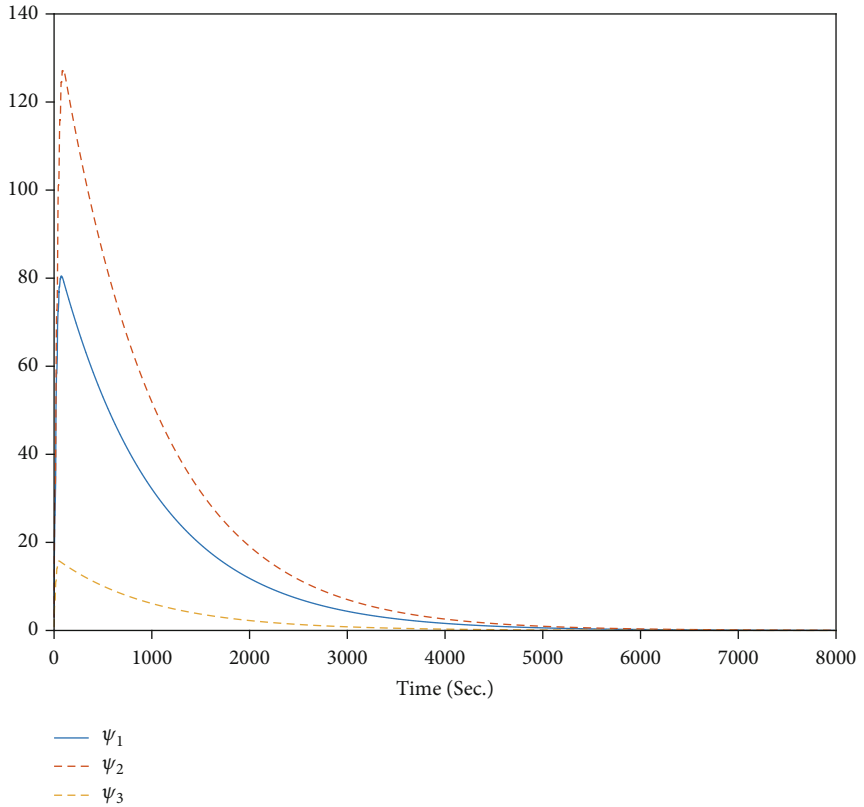

Figure 7: Response curves of the adaptive parameter $\widehat{\psi}_i$, $i = 1, 2, 3$.

5. Conclusion

In this paper, the problem of finite-time orbit control for SFF with limited data communication and external disturbances was studied. We have applied the hysteretic quantizer to quantize the data of the controller-actuator channel to decrease the communication rate. By combining with the adding one power integrator method and the backstepping technique, a finite-time adaptive controller has been developed. Under the proposed control strategy, the effects of quantization errors and external disturbances have been eliminated. Moreover, the finite-time stability of the controlled system and bounded of tracking errors of position and velocity within finite time are guaranteed by the developed controller. Finally, an example has been shown to illustrate the effectiveness of the proposed control strategy. Future work will focus on dealing with the finite-time tracking control problem for SFF with actuator faults.

Data Availability

The data used to support the findings of this study are included within the article.

Conflicts of Interest

The authors declare that they have no conflicts of interest.

References

[1] Y. Xiao, A. De Ruiter, D. Ye, and Z. Sun, "Adaptive fault-tolerant attitude tracking control for flexible spacecraft with guaranteed performance bounds," *IEEE Transactions on Aerospace and Electronic Systems*, p. 1, 2021.

[2] D. Ye, A. Zou, and Z. Sun, "Predefined-time predefined-bounded attitude tracking control for rigid spacecraft," *IEEE Transactions on Aerospace and Electronic Systems*, 2021.

[3] X. Cao, P. Shi, Z. Li, and M. Liu, "Neural-network-based adaptive backstepping control with application to spacecraft attitude regulation," *IEEE Transactions on Neural Networks and Learning Systems*, vol. 29, no. 9, pp. 4303–4313, 2018.

[4] S. M. Esmaeilzadeh, M. Golestani, and S. Mobayen, "Chattering-free fault-tolerant attitude control with fast fixed-time convergence for flexible spacecraft," *International Journal of Control, Automation and Systems*, vol. 19, no. 2, pp. 767–776, 2021.

[5] D. Lee, A. K. Sanyal, and E. A. Butcher, "Asymptotic tracking control for spacecraft formation flying with decentralized collision avoidance," *Journal of Guidance Control and Dynamics*, vol. 38, no. 4, pp. 587–600, 2015.

[6] Q. Ni, Y. Huang, and X. Chen, "Nonlinear control of spacecraft formation flying with disturbance rejection and collision avoidance," *Chinese Physics B*, vol. 26, no. 1, article 014502, 2017.

[7] L. Hui and J. Li, "Terminal sliding mode control for spacecraft formation flying," *IEEE Transactions on Aerospace and Electronic Systems*, vol. 45, no. 3, pp. 835–846, 2009.

[8] A. Zou and K. D. Kumar, "Distributed attitude coordination control for spacecraft formation flying," *IEEE Transactions on Aerospace and Electronic Systems*, vol. 48, no. 2, pp. 1329–1346, 2012.

[9] M. Chen, P. Shi, and C. Lim, "Adaptive neural fault-tolerant control of a 3-DOF model helicopter system," *IEEE Transactions on Systems, Man, and Cybernetics: Systems*, vol. 46, no. 2, pp. 260–270, 2016.

[10] Y. Lv, Q. Hu, G. Ma, and J. Zhou, "6 DOF synchronized control for spacecraft formation flying with input constraint and parameter uncertainties," *ISA Transactions*, vol. 50, no. 4, pp. 573–580, 2011.

[11] J. Shan, "Six-degree-of-freedom synchronised adaptive learning control for spacecraft formation flying," *IET Control Theory & Applications*, vol. 2, no. 10, pp. 930–949, 2008.

[12] B. Shasti, A. Alasty, and N. Assadian, "Robust distributed control of spacecraft formation flying with adaptive network topology," *Acta Astronautica*, vol. 136, pp. 281–296, 2017.

[13] E. Arabi, T. Yucelen, and J. R. Singler, "Finite-time distributed control with time transformation," *International Journal of Robust and Nonlinear Control*, vol. 31, no. 1, pp. 107–130, 2021.

[14] O. Mofid, M. Momeni, S. Mobayen, and A. Fekih, "A disturbance-observer-based sliding mode control for the robust synchronization of uncertain delayed chaotic systems: application to data security," *IEEE Access*, vol. 9, pp. 16546–16555, 2021.

[15] B. Vaseghi, S. Mobayen, S. S. Hashemi, and A. Fekih, "Fast reaching finite time synchronization approach for chaotic systems with application in medical image encryption," *IEEE Access*, vol. 9, pp. 25911–25925, 2021.

[16] A. Wang, L. Liu, J. Qiu, and G. Feng, "Finite-time adaptive fuzzy control for nonstrict-feedback nonlinear systems via an event-triggered strategy," *IEEE Transactions on Fuzzy Systems*, vol. 28, no. 9, pp. 2164–2174, 2020.

[17] D. Ran, X. Chen, and A. K. Misra, "Finite time coordinated formation control for spacecraft formation flying under directed communication topology," *Acta Astronautica*, vol. 136, pp. 125–136, 2017.

[18] A. Zou and K. Kumar, "Adaptive output feedback control of spacecraft formation flying using Chebyshev neural networks," *Journal of Aerospace Engineering*, vol. 24, no. 3, pp. 361–372, 2011.

[19] A. Bagheri, A. Jabbari, and S. Mobayen, "An intelligent ABC-based terminal sliding mode controller for load-frequency control of islanded micro-grids," *Sustainable Cities and Society*, vol. 64, article 102544, 2021.

[20] H. R. Karimi, Y. Niu, J. M. Rossell, and F. Yang, "Analysis and synthesis of control systems over wireless digital channels," *Journal of the Franklin Institute*, vol. 1, pp. 1–4, 2017.

[21] H. R. Karimi, "Robust H-infinity filter design for uncertain linear systems over network with network-induced delays and output quantization," *Modeling, Identification and Control*, vol. 30, no. 1, pp. 27–37, 2009.

[22] H. R. Karimi, M. Zapateiro, and N. Luo, "Stability analysis and control synthesis of neutral systems with time-varying delays and nonlinear uncertainties," *Chaos, Solitons & Fractals*, vol. 42, no. 1, pp. 595–603, 2009.

[23] P. Shi, Y. Zhang, M. Chadli, and R. Agarwal, "Mixed *H-Infinity* and passive filtering for discrete fuzzy neural networks with stochastic jumps and time delays," *IEEE transactions on neural networks and learning systems*, vol. 27, no. 4, pp. 903–909, 2016.

[24] D. Wang, J. Wang, and W. Wang, "Output feedback control of networked control systems with packet dropouts in both channels," *Information Sciences*, vol. 221, pp. 544–554, 2013.

[25] B. Wu, "Spacecraft attitude control with input quantization," *Journal of Guidance, Control, and Dynamics*, vol. 39, no. 1, pp. 176–181, 2016.

[26] K. Eliker and W. Zhang, "Finite-time adaptive integral backstepping fast terminal sliding mode control application on quadrotor UAV," *International Journal of Control, Automation and Systems*, vol. 18, no. 2, pp. 415–430, 2020.

[27] N. Kumar, "Finite time control scheme for robot manipulators using fast terminal sliding mode control and RBFNN," *International Journal of Dynamics and Control*, vol. 7, no. 2, pp. 758–766, 2019.

[28] G. Xia, Y. Zhang, W. Zhang, X. Chen, and H. Yang, "Dual closed-loop robust adaptive fast integral terminal sliding mode formation finite-time control for multi-underactuated AUV system in three dimensional space," *Ocean Engineering*, vol. 233, p. 108903, 2021.

[29] H. Wong, H. Pan, M. S. De Queiroz, and V. Kapila, "Adaptive learning control for spacecraft formation flying," in *Proceedings of the 40th IEEE Conference on Decision and Control (Cat. No.01CH37228),*, pp. 1089–1094, Orlando, FL, USA, 2001.

[30] Y. Li, K. Li, and S. Tong, "Adaptive neural network finite-time control for multi-input and multi-output nonlinear systems with positive powers of odd rational numbers," *IEEE transactions on neural networks and learning systems*, vol. 31, no. 7, pp. 2532–2543, 2020.

[31] C. Qian and W. Lin, "Non-Lipschitz continuous stabilizers for nonlinear systems with uncontrollable unstable linearization," *Systems & Control Letters*, vol. 42, no. 3, pp. 185–200, 2001.

[32] C. Deng and G. Yang, "Distributed adaptive fuzzy control for nonlinear multiagent systems under directed graphs," *IEEE Transactions on Fuzzy Systems*, vol. 26, no. 3, pp. 1–1366, 2017.

[33] F. Wang, Z. Liu, Y. Zhang, and C. Chen, "Adaptive quantized controller design via backstepping and stochastic small-gain approach," *IEEE Transactions on Fuzzy Systems*, vol. 24, no. 2, pp. 330–343, 2016.

[34] J. Zhou and W. Wang, "Adaptive control of quantized uncertain nonlinear systems," *IFAC-PapersOnLine*, vol. 50, no. 1, pp. 10425–10430, 2017.

Hindawi
International Journal of Aerospace Engineering
Volume 2022, Article ID 9787677, 15 pages
https://doi.org/10.1155/2022/9787677

Research Article

Influence of Three-Body Gravitational Perturbation for Drag-Free Spacecraft

Tao Jia,[1] Decheng Jiang,[1] Chenglong Li,[1] Bo Ru,[1] Xiaobin Lian,[2] and Xusheng Zhu[1]

[1]*AVIC Chengdu Aircraft Industrial (Group) Co. Ltd., Chengdu 610092, China*
[2]*Shanghai Institute of Satellite Engineering, Shanghai 201109, China*

Correspondence should be addressed to Xusheng Zhu; zhuxusheng@buaa.edu.cn

Received 8 October 2021; Revised 6 January 2022; Accepted 13 January 2022; Published 11 February 2022

Academic Editor: Chen Pengyun

This paper mainly studies the motion and control of the drag-free spacecraft system for a high-precision mission. In high-precision missions, the influence of three-body gravitational perturbation on a drag-free spacecraft system is still lack of relevant research. To this end, we first established a relative motion model of the test mass and the spacecraft based on multibody dynamics, and the equations of the relative motion of the test mass and the spacecraft cavity were obtained through coordinate transformation. The difference between the sun orbit and the Earth orbit is comparatively analyzed by a numerical solution. The influence of gravitational forces from the Earth, the moon, and the sun on the relative motion is studied in detail. Secondly, a sliding mode controller is designed for the high-precision mission. Finally, the performance of the controller is analyzed from the time domain and the frequency domain. Numerical simulation results show that the controller can meet the requirements of the time domain and the frequency domain.

1. Introduction

The concept of the drag-free spacecraft was first proposed by Pugh in 1959 [1]. It is a method that seals the test mass in a spacecraft cavity, which shields nongravitational interference such as atmospheric resistance and solar radiation pressure, then continuously controls the spacecraft by a microthruster to implement the feed-forward compensation of interference, so that the spacecraft runs in purely gravitational orbit. Because of the high accuracy and high stability of drag-free spacecrafts, they are considered to be used for space science mission.

At present, there are many achievements in the research on the dynamics model of the drag-free spacecraft, but the related research mainly focuses on different mission backgrounds. Lange et al. [2–4] has made great contributions to the development of drag-free spacecrafts. In [2], the motion of the spherical test mass relative to the spacecraft body in low Earth orbit was researched; the relative motion equations of the spacecraft body and the test mass can be obtained by the vector difference between the motion equations. Reference [4] studies the interference cancellation of spin spacecrafts. Wiegand et al. [5] analyzed the stability of the test mass's motion by using Mathieu differential equations and verified the applicability of the method by numerical simulation. Theil et al. [6–8] established a drag-free spacecraft dynamic model from the standpoint of the drag-free control. Reference [6] studied the relative linearization dynamics of the test mass and the spacecraft. By considering the uncertainty of the system, the model can be used to solve a type of drag-free spacecraft mission with nonspherical test mass. Canuto et al. [9–12] studied the dynamics of GOCE spacecrafts in the accelerometer mode based on the embedded model theory. In the LISA Pathfinder mission, the accelerometer mode and displacement mode are adopted simultaneously. Fichter et al.[13–15] and Wu and Fertin [16, 17] studied the dynamics of drag-free spacecrafts with 15 degrees of freedom, respectively.

The interference of drag-free spacecraft is mainly divided into three sources [18]: (1) The interference acts on the spacecraft body, such as sunlight pressure and atmospheric resistance. (2) The interference acts on the test mass,

such as residual gas damping, thermal radiation pressure, and electrostatic force. (3) The coupling interference between the spacecraft body and the test mass, such as gravity gradient from the sun/moon and capacitance gradient. In addition, interference will also be introduced in the TM release process. Lian et al. [19] analyzed the impact of the release process of the test mass and gave a capture controller design method.

Drag-free control is one of the core technologies of drag-free spacecraft. Chapman et al. [20] designed a PID controller for the Spacecraft Test of the Equivalence Principle (STEP) mission and designed the rotation and translation control laws as multiple single-input single-output (SISO) loops. Shi [21] designed a hybrid H_2/H_∞ controller for a drag-free spacecraft in displacement mode and verified the controller's excellent robustness through simulation. Francesco [22] used the quantitative feedback theory to solve the problem of drag-free and attitude control of LISA spacecrafts in his dissertation. Li [23] introduced a nonsmooth optimization tool to handle the parameters of the embedded model controller in his research. Lian et al. [24] proposed a frequency separation control for drag-free spacecraft with frequency domain constraints.

However, the above research mainly focuses on drag-free spacecraft in low Earth orbit, but it is less research on orbit around the sun/high Earth orbit. In addition, current research pays more attention to the influence of nonconservative forces, while less consideration is given to the influence of the three-body gravitational perturbation such as the sun and the moon. In this paper, the kinetic characteristic and high-precision control of the drag-free spacecraft are studied. The main contributions include the following:

(1) The difference between the relative motion of the drag-free spacecraft on the orbit around the sun and the orbit around the Earth is comparatively studied

(2) Considering that there are few studies on the influence characteristics of the sun-moon gravitational perturbation for the drag-free spacecraft of the Earth orbit, this paper analyses in detail the influence of the Earth-sun-moon and designs the controller to overcome the Earth-sun-moon gravitational perturbation

Based on the above analysis, the research on the relative motion of traditional drag-free spacecrafts is mainly focused on low Earth orbit and Solar orbit, while the research on the relative motion of high Earth orbit for gravitational wave detection is lacking. In this paper, the relative motion and control of a drag-free spacecraft system under the gravitational fields of the Earth, moon, and sun are studied with the background of gravitational wave detection in the geocentric very high orbit.

2. The Relative Motion Equation

2.1. Reference Coordinate System. The two test masses are assumed to be mass points; the attitude motion of test masses is not considered in this paper accordingly. To clarify the problems clearly, some reference frames are presented as follows.

(1) Earth-centered inertial (ECI): the origin is located at the Earth's mass center E, the x-axis points to the mean equinox J2000, the z-axis is along the direction the Earth's mass center to the Earth's north pole, and the y-axis forms a right-handed triad as shown in Figure 1

(2) Spacecraft-centered orbit (SCO): the origin is located at the spacecraft's mass center O, the z-axis is along the direction the Earth's mass center to the spacecraft's mass center, the x-axis is perpendicular to the z-axis in the orbit plane and coincides with the direction of the velocity, and the y-axis forms a right-handed triad

(3) The spacecraft cavity coordinate system: the origin is the cavity's center O_i, the x_i-axis is the sensitive axis along the line of sight, the z_i-axis is the vertical sensitive axis in the orbital plane, and the y_i-axis is the normal direction of the orbital plane

2.2. The Relative Motion Dynamics. Merely considering the effect of gravity of the Earth on the motion of the spacecraft, the motion equation of the spacecraft mass center and the test masses in the ECI coordinate system is as follows:

$$\ddot{\mathbf{r}} = -\frac{\mu_e}{r^3}\mathbf{r}, \tag{1}$$

where μ_ϵ is a standard gravitational parameter and $\mathbf{r}$ is the position vectors from the Earth's mass center to the spacecraft mass center.

If the influence of lunar gravity is also considered, the equation of motion of the spacecraft body is

$$\ddot{\mathbf{r}} = -\frac{\mu_e}{r^3}\mathbf{r} - \frac{\mu_{\text{mo}}}{d^3_{\text{mo}-e}}\mathbf{d}_{\mathbf{mo\text{-}e}} - \frac{\mu_{\text{mo}}}{d^3_{\text{mo-sc}}}\mathbf{d}_{\mathbf{mo\text{-}sc}}, \tag{2}$$

where μ_{mo} is a standard gravitational parameter of the moon. $\mathbf{d}_{\mathbf{mo-e}}$ and $\mathbf{d}_{\mathbf{mo-sc}}$ are the position vectors from the moon's mass center to the Earth's mass center and the spacecraft mass center, respectively.

Similarly, the motion equation of the test mass 1 (TM1) and the test mass 2 (TM2) in the *ECI* coordinate system are

$$\ddot{\mathbf{r}}_1 = -\frac{\mu_e}{r_1^3}\mathbf{r}_1 - \frac{\mu_{\text{mo}}}{d^3_{\text{mo}-e}}\mathbf{d}_{\mathbf{mo\text{-}e}} - \frac{\mu_{\text{mo}}}{d^3_{\text{mo-tm1}}}\mathbf{d}_{\mathbf{mo\text{-}tm1}}, \tag{3}$$

$$\ddot{\mathbf{r}}_2 = -\frac{\mu_e}{r_2^3}\mathbf{r}_2 - \frac{\mu_{\text{mo}}}{d^3_{\text{mo}-e}}\mathbf{d}_{\mathbf{mo\text{-}e}} - \frac{\mu_{\text{mo}}}{d^3_{\text{mo-tm2}}}\mathbf{d}_{\mathbf{mo\text{-}tm2}}, \tag{4}$$

where $\mathbf{r_1}$ and $\mathbf{r_2}$ are the position vectors from the Earth's mass center to TM1 and TM2, respectively. $\mathbf{d_{mo-tmi}}$ is the position vectors from the moon's mass center to the ith test mass.

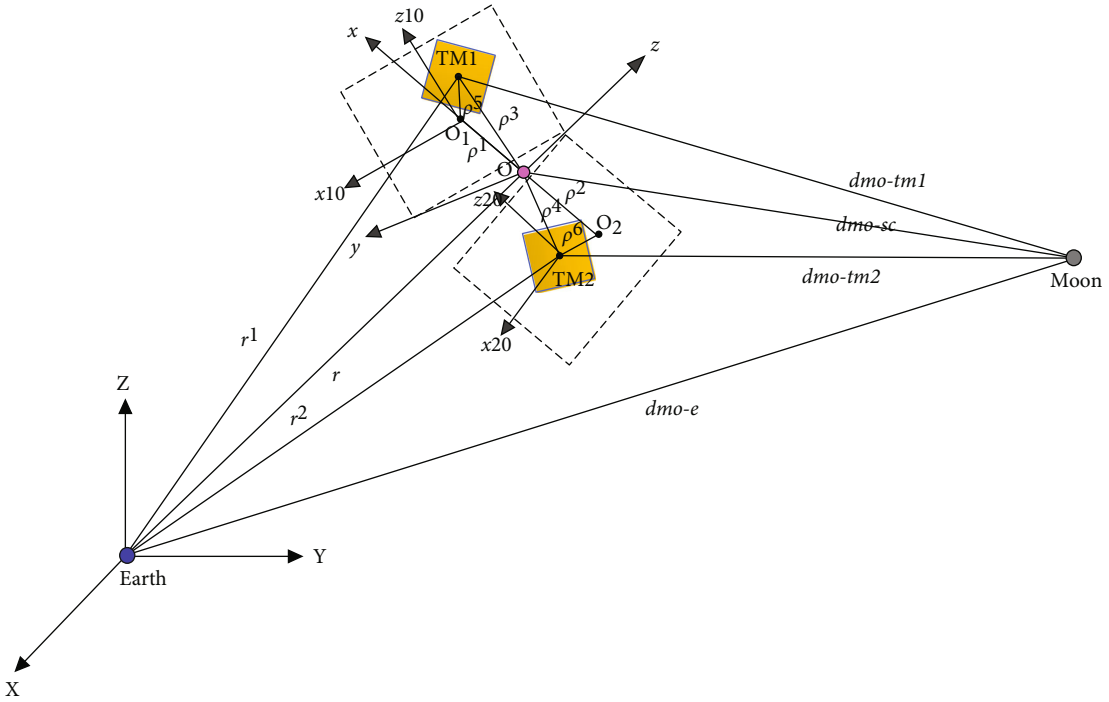

Figure 1: The relative motion between the test masses and the drag-free spacecraft.

The position vectors of TM1 and TM2 relative to spacecraft's mass center O are

$$\boldsymbol{\rho}_3 = \mathbf{r}_1 - \mathbf{r}, \quad \boldsymbol{\rho}_4 = \mathbf{r}_2 - \mathbf{r}. \tag{5}$$

As can be seen from Figure 1, the position vector of the test masses relative to the mass center of the spacecraft cavity can be expressed as

$$\boldsymbol{\rho}_5 = \boldsymbol{\rho}_3 \text{-} \boldsymbol{\rho}_1, \boldsymbol{\rho}_6 = \boldsymbol{\rho}_4 \text{-} \boldsymbol{\rho}_2. \tag{6}$$

Differentiating Equation (5), substituting Equations (3) and (4) into it, and considering the influence of solar gravitation lead to

$$\begin{cases} \ddot{\boldsymbol{\rho}}_3 = -\mu_e\left(\dfrac{\mathbf{r}_1}{r_1^3} - \dfrac{\mathbf{r}}{r^3}\right) - \mu_{\text{mo}}\left(\dfrac{\mathbf{d}_{\text{mo-tm1}}}{d_{\text{mo-tm1}}^3} - \dfrac{\mathbf{d}_{\text{mo-sc}}}{d_{\text{mo-sc}}^3}\right) - \mu_s\left(\dfrac{\mathbf{d}_{\text{s-tm1}}}{d_{\text{s-tm1}}^3} - \dfrac{\mathbf{d}_{\text{s-sc}}}{d_{\text{s-sc}}^3}\right), \\ \ddot{\boldsymbol{\rho}}_4 = -\mu_e\left(\dfrac{\mathbf{r}_2}{r_2^3} - \dfrac{\mathbf{r}}{r^3}\right) - \mu_{\text{mo}}\left(\dfrac{\mathbf{d}_{\text{mo-tm2}}}{d_{\text{mo-tm2}}^3} - \dfrac{\mathbf{d}_{\text{mo-sc}}}{d_{\text{mo-sc}}^3}\right) - \mu_s\left(\dfrac{\mathbf{d}_{\text{s-tm2}}}{d_{\text{s-tm2}}^3} - \dfrac{\mathbf{d}_{\text{s-sc}}}{d_{\text{s-sc}}^3}\right), \end{cases} \tag{7}$$

where μ_s is a standard gravitational parameter of the sun. $\mathbf{d}_{\text{s-sc}}$ and $\mathbf{d}_{\text{s-tmi}}$ are the position vectors from the Solar's mass center to the spacecraft's mass center and the ith test mass, respectively.

According to Equation (7), the influence of the moon and the sun for the relative motion are

$$\boldsymbol{\alpha}_{\text{moon}} = -\mu_{\text{mo}}\left(\frac{\mathbf{d}_{\text{mo-tmi}}}{d_{\text{mo-tmi}}^3} - \frac{\mathbf{d}_{\text{mo-sc}}}{d_{\text{mo-sc}}^3}\right), \mathbf{a}_{\text{sun}} = -\mu_s\left(\frac{\mathbf{d}_{\text{s-tmi}}}{d_{\text{s-tmi}}^3} - \frac{\mathbf{d}_{\text{s-sc}}}{d_{\text{s-sc}}^3}\right). \tag{8}$$

Table 1: The parameters of the sun orbit and Earth orbit [25].

Orbit parameters	Sun orbit	Earth orbit
Semimajor axis a (km)	149597870.700	99995.5723
Eccentricity e	0.009648	0.00043
Orbit inclination i (°)	0.9529	74.5362
RAAN Ω (°)	348.16	211.6003
Argument of perigee w (°)	270	346.5528
True anomaly f (°)	180	61.3296

In *SCO*, we have

$$\begin{aligned} &\mathbf{r} = [00r]^T, \boldsymbol{\rho}_1 = [x_{s1} \quad y_{s1} \quad z_{s1}]^T, \boldsymbol{\rho}_2 = [x_{s2} \quad y_{s2} \quad z_{s2}]^T, \\ &\mathbf{r}_1 = [x_{s1} \quad y_{s1} \quad r + z_{s1}]^T, \mathbf{r}_2 = [x_{s2} \quad y_{s2} \quad r + z_{s2}]^T, \end{aligned} \tag{9}$$

where $r = (1 - e^2)/(1 + e\cos\nu)$, a is the spacecraft's semimajor axes, e is an eccentricity of the orbit, ν is a true anomaly. $\boldsymbol{\rho}_1$ and $\boldsymbol{\rho}_2$ are the position coordinates of TM1 and TM2 in *SCO*, respectively.

The equation of motion for test masses relative to the spacecraft's mass center in *SCO* can be expressed as

$$\begin{aligned} &\frac{\delta^2\boldsymbol{\rho}_i}{\delta t^2} + 2\boldsymbol{\omega}_{\text{SCO}}^{\text{ECI}} \times \frac{\delta\boldsymbol{\rho}_i}{\delta t} + \bar{\boldsymbol{\omega}}_{\text{SCO}}^{\text{ECI}} \times \left(\bar{\boldsymbol{\omega}}_{\text{SCO}}^{\text{ECI}} \times \boldsymbol{\rho}_i\right) + \dot{\bar{\boldsymbol{\omega}}}_{\text{SCO}}^{\text{ECI}} \times \boldsymbol{\rho}_i \\ &\quad = -\mu_e\left(\frac{\mathbf{r}_i}{r_i^3} - \frac{\mathbf{r}}{r^3}\right) - \mu_{\text{mo}}\left(\frac{\mathbf{d}_{\text{mo-tmi}}}{d_{\text{mo-tmi}}^3} - \frac{\mathbf{d}_{\text{mo-sc}}}{d_{\text{mo-sc}}^3}\right) \\ &\quad\quad - \mu_s\left(\frac{\mathbf{d}_{\text{s-tmi}}}{d_{\text{s-tmi}}^3} - \frac{\mathbf{d}_{\text{s-sc}}}{d_{\text{s-sc}}^3}\right), \end{aligned} \tag{10}$$

where $r_i = \sqrt{x_{si}^2 + y_{si}^2 + (r + z_{si})^2}$, $i = 1, 2$. $\boldsymbol{\omega}_{\mathrm{SCO}}^{\mathrm{ECI}}$ and $\boldsymbol{\omega}_{\mathrm{SCO}}^{\mathrm{ECI}}$ are the angular velocity vector and the angular acceleration vector of the *SCO* with respect to the *ECI*, respectively.

And,

$$\boldsymbol{\omega}_{\mathrm{SCO}}^{\mathrm{ECI}} = [0 \quad \omega \quad 0]^T, \dot{\boldsymbol{\omega}}_{\mathrm{SCO}}^{\mathrm{ECI}} = [0 \quad \dot{\omega} \quad 0]^T, \tag{11}$$

where $\omega = \sqrt{(\mu_e(1 + e\cos f))/r^3}$, $\dot{\omega} = -(2\mu_e e \sin f)/r^3$.

Substituting Equations (9) and (11) into Equation (10) leads to

$$\begin{cases} \ddot{x}_{\mathrm{si}} + 2n\dot{z}_{si} - n^2 x_{si} + \dot{n} z_{si} = -\dfrac{\mu_e}{r_i^3} x_{si} - \dfrac{\mu_s}{d_{\mathrm{s\text{-}tmi}}^3}(x_{si} - S_x) - \dfrac{\mu_s}{d_{\mathrm{s\text{-}sc}}^3} S_x - \dfrac{\mu_{\mathrm{mo}}}{d_{\mathrm{mo\text{-}tmi}}^3}(x_{\mathrm{si}} - M_{\mathrm{ox}}) - \dfrac{\mu_{\mathrm{mo}}}{d_{\mathrm{mo\text{-}sc}}^3} M_{\mathrm{ox}}, \\ \ddot{y}_{\mathrm{si}} = -\dfrac{\mu_e}{r_i^3} y_{\mathrm{si}} - \dfrac{\mu_s}{d_{\mathrm{s\text{-}tmi}}^3}(y_{\mathrm{si}} - S_y) - \dfrac{\mu_s}{d_{\mathrm{s\text{-}sc}}^3} S_y - \dfrac{\mu_{\mathrm{mo}}}{d_{\mathrm{mo\text{-}tmi}}^3}(y_{\mathrm{si}} - M_{\mathrm{oy}}) - \dfrac{\mu_{\mathrm{mo}}}{d_{\mathrm{mo\text{-}sc}}^3} M_{\mathrm{oy}}, \\ \ddot{z}_{\mathrm{si}} - 2n\dot{x}_{si} - n^2 z_{\mathrm{si}} - \dot{n} x_{\mathrm{si}} = -\dfrac{\mu_e}{r_i^3}(r + z_{si}) - \dfrac{\mu_s}{d_{\mathrm{s\text{-}tmi}}^3}(z_{si} - S_z) + \dfrac{\mu_s}{d_{\mathrm{s\text{-}sc}}^3}(r - S_z) - \dfrac{\mu_{mo}}{d_{\mathrm{mo\text{-}tmi}}^3}(z_{si} - M_{\mathrm{oz}}) + \dfrac{\mu_{\mathrm{mo}}}{d_{\mathrm{mo\text{-}sc}}^3}(r - M_{\mathrm{oz}}), \end{cases} \tag{12}$$

where $d_{\mathrm{s\text{-}tmi}} = \sqrt{(S_x - x_{\mathrm{si}})^2 + (S_y - y_{\mathrm{si}})^2 + (S_z - z_{\mathrm{si}})^2}$, $i = 1, 2$. $[S_x, S_y, S_z]^T$ and $[M_{ox}, M_{oy}, M_{oz}]^T$ are the position coordinates of sun and moon in *SCO*, respectively. Equation (12) is the equation of motion for the ith test mass relative to the spacecraft's center of mass under the action of the Earth-moon-sun gravitation system.

The relative motion equation of the test mass and the cavity center in the spacecraft cavity coordinate system is as follows:

$$\begin{bmatrix} x_i \\ y_i \\ z_i \end{bmatrix} = \begin{bmatrix} \cos\theta_y & 0 & -\sin\theta_y \\ 0 & 1 & 0 \\ \sin\theta_y & 0 & \cos\theta_y \end{bmatrix} \begin{bmatrix} x_{si} - O_{ix} \\ y_{si} - O_{iy} \\ z_{si} - O_{iz} \end{bmatrix}, \tag{13}$$

where θ_y is the rotation angle of the *SCO* around the y-axis to the spacecraft cavity coordinate system, and $\mathrm{O}_i = [O_{ix}, O_{iy}, O_{iz}]^T$ is the position coordinates from the spacecraft's mass center to the cavity's center.

3. The Relative Motion Analysis

In order to comparative study the relative motion between the spacecraft cavity and test masses in the sun orbit and the Earth orbit, the two orbit parameters are given here, as shown in Table 1.

Since the two test masses' analysis methods are similar, only the relative motion relation of TM1 is considered here. Let the coordinates of the cavity center relative to the center of the spacecraft's mass in the spacecraft orbital coordinate system be (0.3 m, 0, 0). Assuming that the initial motion state of TM1 in the cavity coordinate system is (0, 0, 0, 0, 0, 0), the motion of the TM1 under sun orbit and Earth orbit relative to the center of the cavity is shown in Figure 2. The simulation starts on January 1, 2034.

As can be seen from Figure 2(a), the maximum displacement of the TM1 relative to the center of the cavity in the sensitive axis in sun orbit within a year is about 2.9 mm, and the relative motion in the nonsensitive axis is about 5 mm. In Figure 2(b), the relative motion displacement of the sensitive axis in Earth orbit is about 500 mm (Assuming the cavity size is large enough), while the relative motion displacement of the non-sensitive axis is about 900 mm. According to Figure 2, the test mass in the Earth orbit is significantly affected by the gravitational gradient of celestial bodies, while the motion in the sun orbit is relatively small. Therefore, for gravitational wave detection spacecrafts in Earth orbit, it is necessary to focus on the analysis of the effect of celestial gravity gradient on relative motion, so as to avoid the collision between test mass and cavity.

This study focuses on gravitational wave detectors in the Earth orbit, which are mainly subject to the gravity gradient of the Earth, moon and sun. The influence of the above three celestial bodies on the displacement and acceleration of the test mass relative to the center of the cavity are analyzed in detail, as shown in Figures 3–5.

It can be seen from Figure 3(a) that the relative displacement between the test mass and the center of the cavity in the sensitive axis caused by the gravitational gradient of the Earth-sun system is greater than other systems. The relative displacement caused by the gravitational gradient of the Earth-moon-sun system is smaller than that of the Earth-sun system, which may be due to the damping effect of the moon's gravity. Figure 3(b) shows the relative acceleration effects of the Earth, moon, and sun in the sensitive axis. It can be seen from the figure that the gravity gradient of the Earth is the main influencing factor of the relative motion in the sensitive axis, and its magnitude is 10^{-11} m/s^2. The gravitational gradient of the sun fluctuates greatly, which makes the displacement of relative motion change greatly. The influence magnitude of the moon's gravitational gradient in the sensitive axis is 10^{-14} m/s^2. Figure 5 shows the relative motion effects of the gravitational gradient of the Earth-moon-sun system on the direction of the vertically sensitive axis in the orbital plane. As can be seen from Figure 5, the

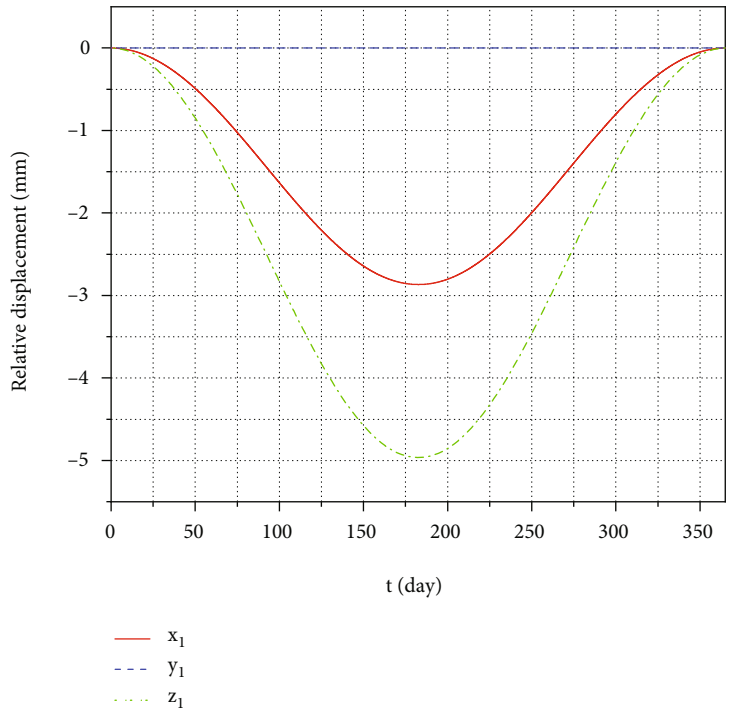

(a) The relative displacement in the sun orbit

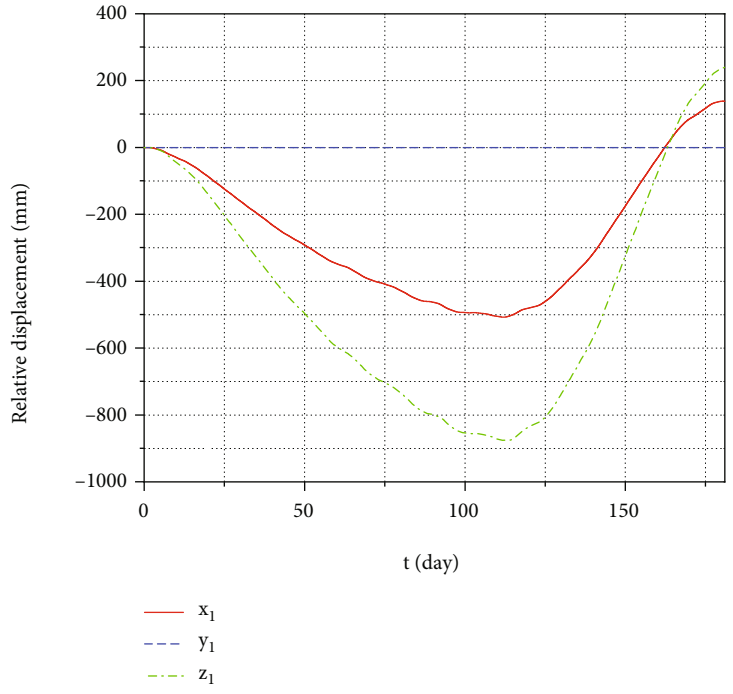

(b) The relative displacement in the Earth orbit

Figure 2: The relative displacement of the sun orbit and Earth orbit.

influence of each system on the relative displacement is similar to the sensitive axis.

In Figure 4(a), the relative displacement caused by the Earth-moon-sun system in the normal direction is greater than that caused by other systems, while the relative displacement of the Earth-moon system in the normal direction is greater than that caused by the Earth-sun system. Figure 4(b) shows that the relative acceleration caused by the Earth's gravitational gradient in the normal direction is 0, which is because the normal direction has no weight in the initial state. And the normal direction is decoupled from the orbital plane, so the relative acceleration in the normal

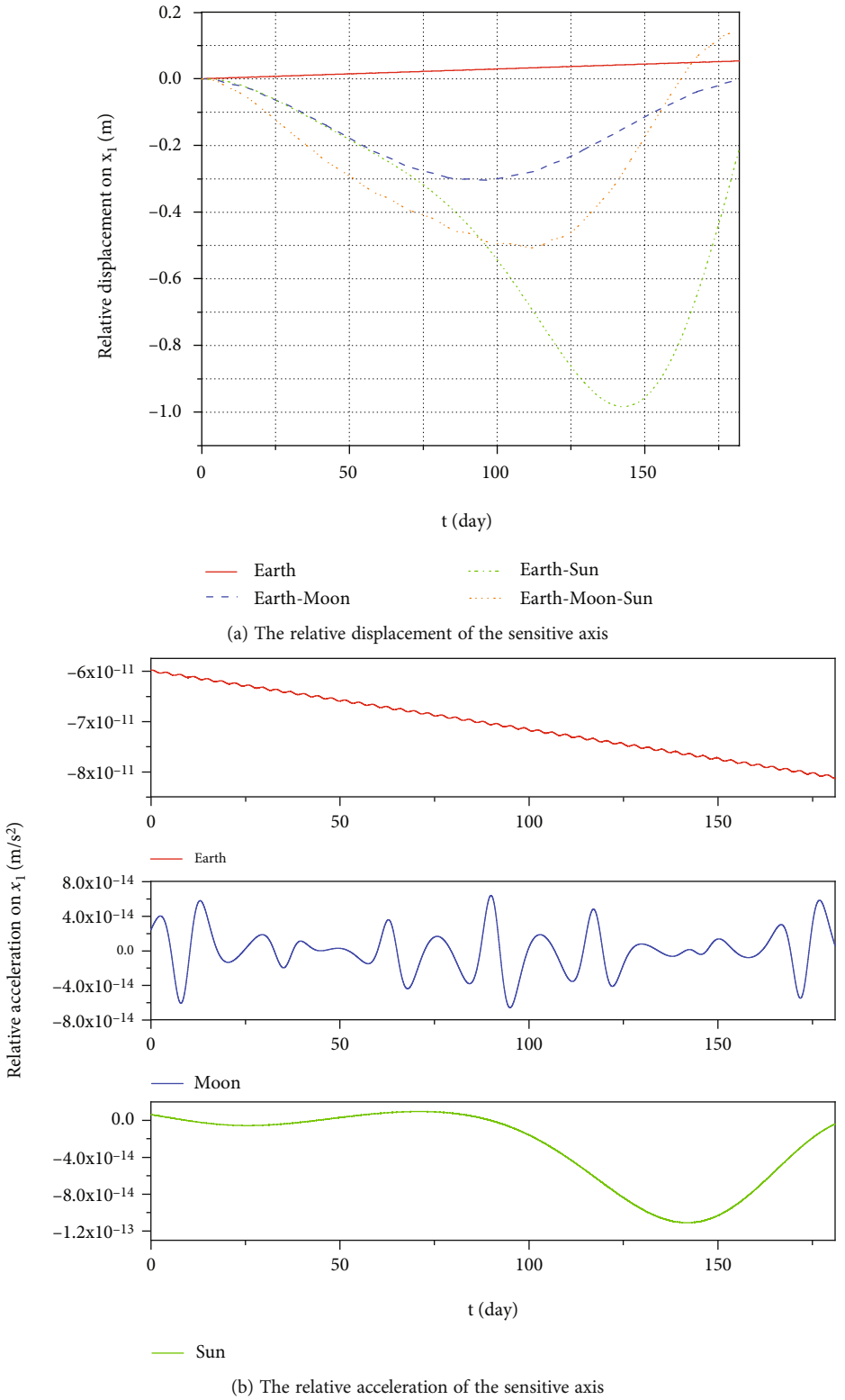

(a) The relative displacement of the sensitive axis

(b) The relative acceleration of the sensitive axis

Figure 3: The effect of the Earth-moon-sun system on the relative motion in the sensitive axis.

direction is 0. In the normal direction, the influence magnitude of the moon's gravitational gradient is 10^{-15} m/s^2, while the sun is 10^{-16} m/s^2. Therefore, the gravitational gradient of the moon dominates in the normal direction, and the influence of the gravitational gradient of the sun still needs to be considered.

A comparative analysis of the gravity gradient of the Earth system, the Earth-moon system, and the Earth-sun

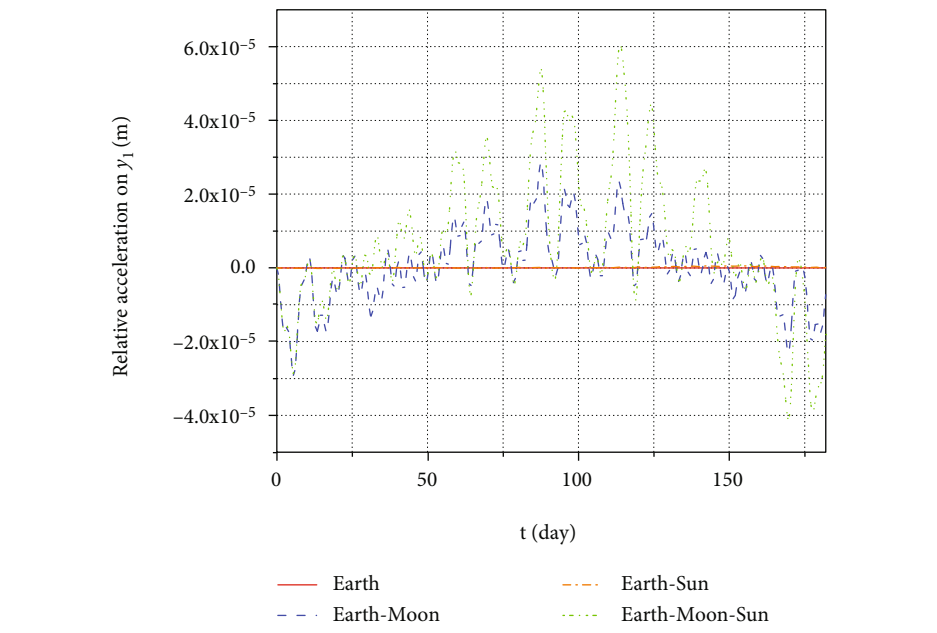

(a) The relative displacement of the normal direction

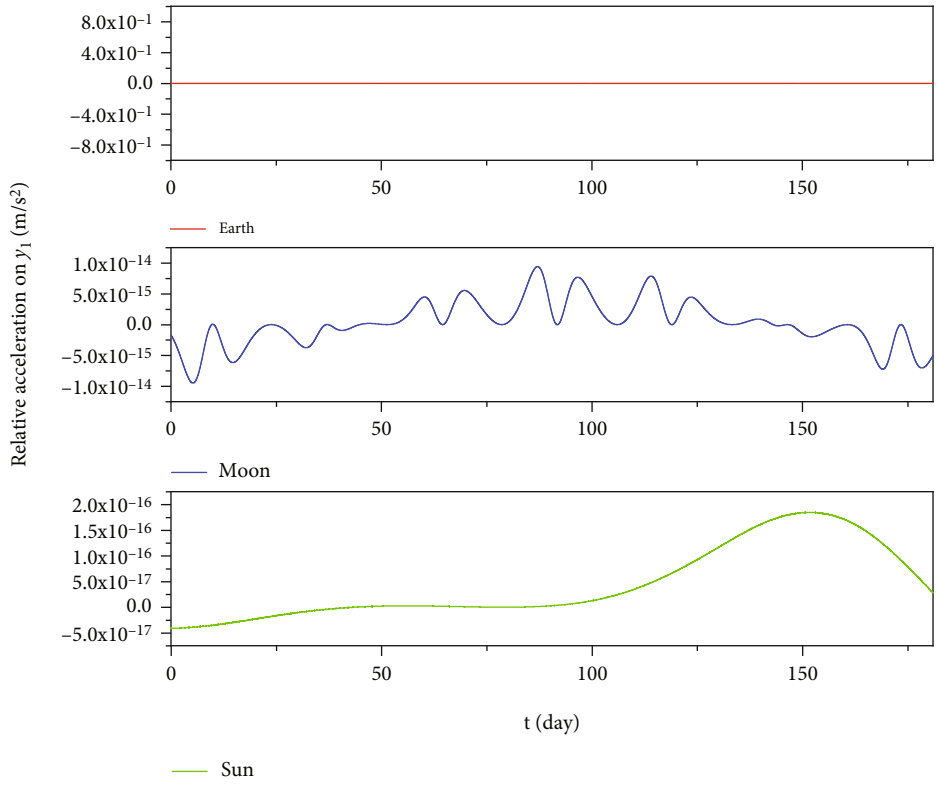

(b) The relative acceleration of the normal direction

Figure 4: The effect of the Earth-moon-sun system on the relative motion in the normal direction.

system shows that in gravitational wave detection spacecrafts of similar heights, the effects of the Earth, the moon, and the sun on the motion of the relative cavity center of the mass need to be considered simultaneously.

Therefore, the influence of the Earth, the moon, and the sun on the relative motion of the test mass and the cavity center should be considered simultaneously in the gravitational wave detection spacecrafts at similar heights.

In the above analysis, it is assumed that the cavity size is large enough, while the actual cavity size is limited. Therefore, the movement of the test mass must be controlled to avoid collision with the cavity. Here, we study the

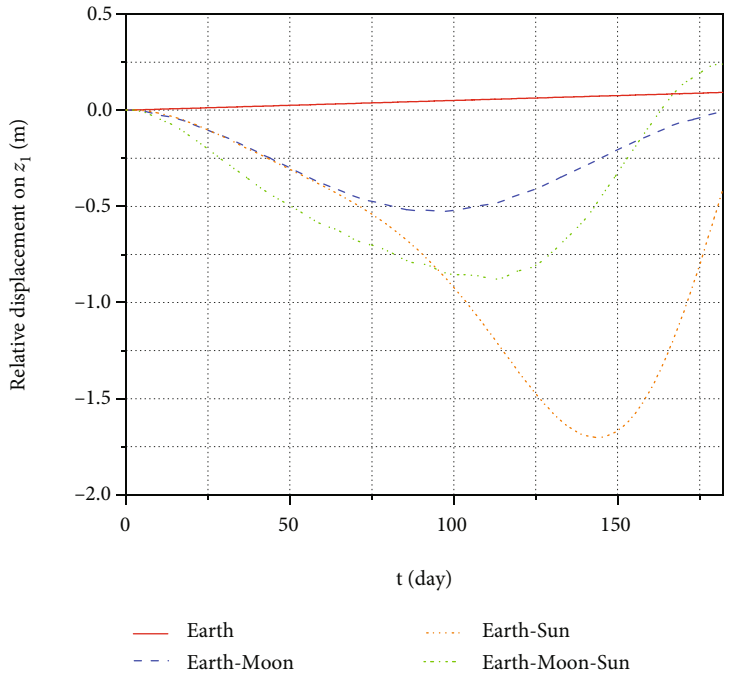

(a) The relative displacement of the vertically sensitive axis direction in the orbital plane

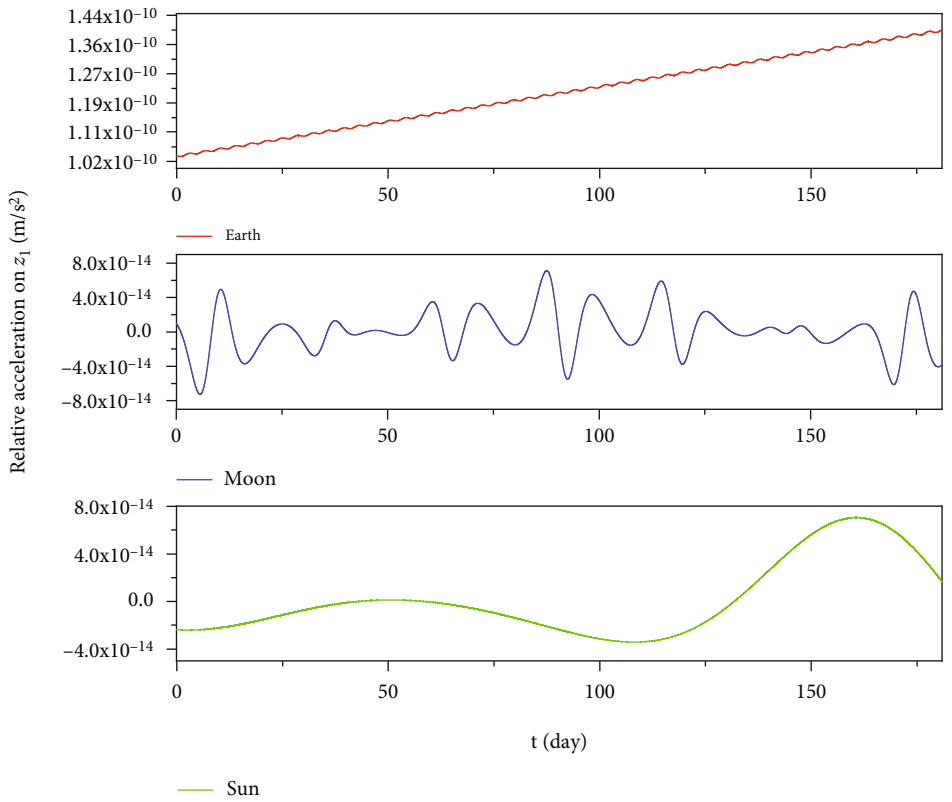

(b) The relative acceleration of the vertically sensitive axis direction in the orbital plane

Figure 5: The effect of the Earth-moon-sun system on the relative motion in the vertically sensitive axis direction.

gravitational wave detector with two test masses, so the movement relationship between the two test masses and the cavity should be considered simultaneously when designing the control strategy. Figure 2(b) shows the relative motion of TM1, and the relative motion of TM2 will be analyzed here. Let the position of the cavity center with TM2 in the SCO be (-0.3 m, 0, 0) and the initial motion state of TM2 in the cavity coordinate system be (0, 0, 0, 0, 0, 0, 0). The

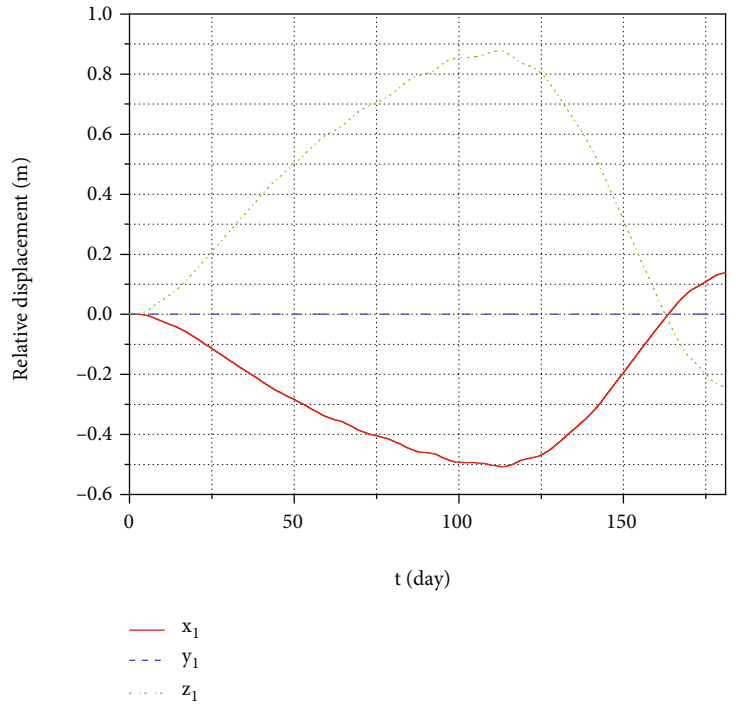

Figure 6: The movement of TM2 relative to the cavity center.

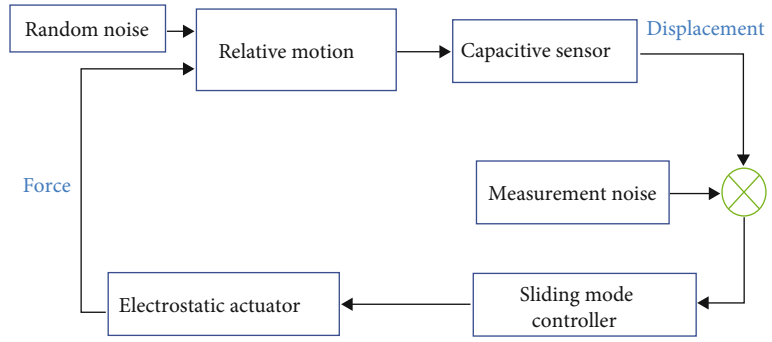

Figure 7: The structure of the control system.

Table 2: The control requirement.

Parameter	Requirement
x_1	10^{-12} mHz$^{-1/2}$@0.1 mHz-1 Hz
y_1, z_1	10^{-9} mHz$^{-1/2}$@0.1 mHz-1 Hz
a_{x1}	10^{-15} ;ms^{-2} Hz$^{-1/2}$@0.1 mHz-1 Hz
a_{y1}, a_{z1}	10^{-13} ms^{-2}·Hz$^{-1/2}$@0.1 mHz-1 Hz
Relative displacement deviation	5 mm

movement of TM2 relative to the cavity center is shown in Figure 6.

In Figures 2(b) and 6, the red line represents the relative motion on the sensitive axis, the blue dotted line represents the relative motion in the normal direction, and the green chain-dotted line represents the relative motion in the direction of the perpendicular sensitive axis in the orbital plane. On the sensitive axis, the relative motion direction of TM1 and TM2 changes from negative to positive with time. On the vertical direction of the sensitive axis, the relative motion direction of TM1 changes from negative to positive with time, while TM2 changes from positive to negative with time.

4. Relative Motion Control

4.1. Sliding Mode Controller Design. In order to avoid the collision between the test mass and the cavity, the following two control strategies can be adopted:

(i) Strategy 1 [24]: displacement mode+acceleration mode: the changes of TM1 and TM2 in the direction of the sensitive axis can first decompose the force to the coordinate axis and then offset by the micro thrusters. The change of nonsensitive axis direction can be controlled by the electrostatic controller alone

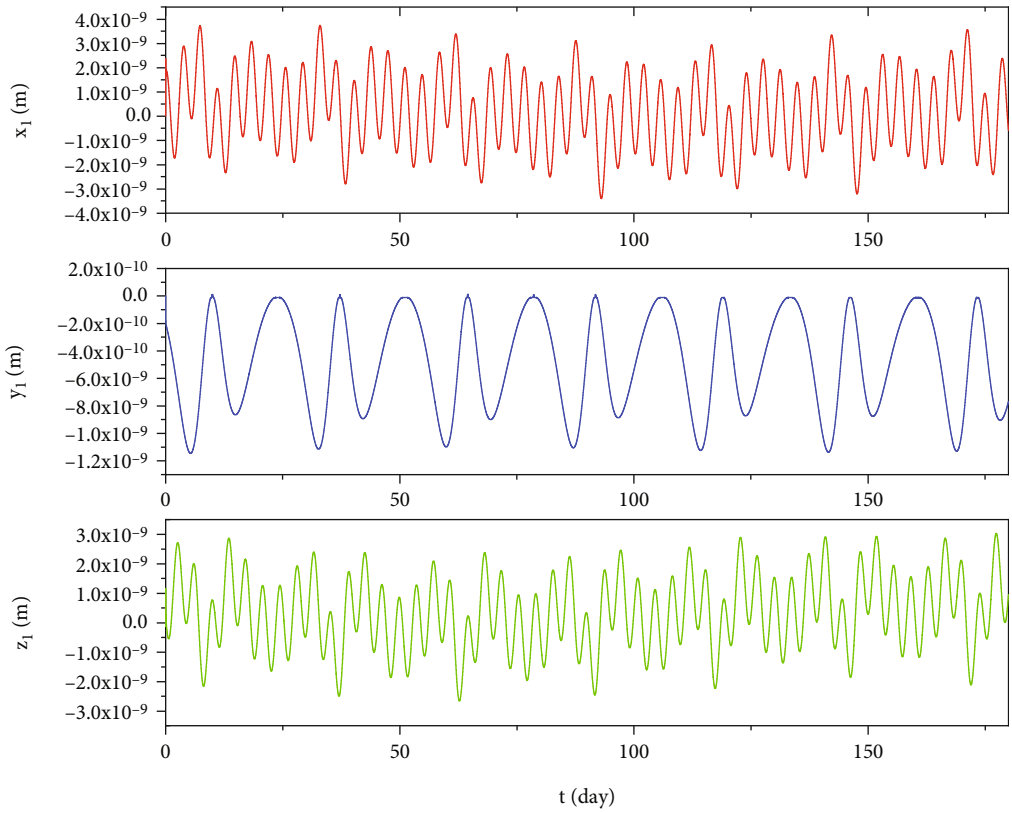

Figure 8: The control effect of relative motion in the time domain.

(ii) Strategy 2: acceleration mode: the change of the sensitive axis and nonsensitive axis directions of TM1 and TM2 are all controlled by the electrostatic controller

In Strategy 1, displacement mode is adopted in the sensitive axis. Compared with Strategy 2, the control accuracy is higher, and the control force can avoid interference of the test mass in the direction of the sensitive axis. However, this method makes TM1 and TM2 mutually coupled, and the control force is relatively complex. In Strategy 2, each axis is controlled by electrostatic force, which can realize the decoupling of TM1 and TM2 controls, but the electrostatic force will introduce the negative stiffness effect. If the interference introduced in Strategy 2 is lower than the requirement, Strategy 2 can still be adopted.

The actuator of Strategy 2 is the capacitive plate, which directly acts on the test mass, so as to realize the decoupling of TM1 and TM2 controls and simplify the controller design process. Therefore, the sliding mode controller is designed for the relative motion control between the test mass and the cavity. Sliding mode control has the characteristics of fast response speed and insensitivity to parameter change and disturbance. The structure of the control system can be seen in Figure 7.

In the design of the controller, Equation (12) is first written as a form of state space, as follows:

$$\begin{cases} \dot{\boldsymbol{x}}(t) = \mathbf{f}(x_i, y_i, z_i, t) + \mathbf{Bu}, \\ \boldsymbol{y}(t) = \mathbf{C}\boldsymbol{x}(t), \end{cases} \tag{14}$$

where $\boldsymbol{x}(t) = [\dot{x}_i, \dot{y}_i, \dot{z}_i]^T$, $\mathtt{f}(x_i, y_i, z_i, t)$ is a nonlinear function, $\mathbf{B}$ and $\mathbf{C}$ are the coefficient matrix, and $\mathbf{u}$ is the control input.

We define the sliding mode function:

$$\mathbf{s}(t) = \mathbf{ce}_\varepsilon + \dot{\mathbf{e}}_\varepsilon, \tag{15}$$

where $\mathbf{c} > 0$ and $\boldsymbol{e}_\varepsilon$ and $\dot{\boldsymbol{e}}_\varepsilon$ are error and error derivative, respectively.

Let

$$\mathbf{e}_\varepsilon(t) = \boldsymbol{x}_d - \boldsymbol{x}, \dot{\mathbf{e}}_\varepsilon = \dot{\boldsymbol{x}}_d - \dot{\boldsymbol{x}}, \tag{16}$$

where $\boldsymbol{x}_d$ is an expected position.

In order to prove the stability of the controller, the Lyapunov function is defined as follows:

$$\mathbf{L}_y = \frac{1}{2}\mathbf{s}^2. \tag{17}$$

Differentiating Equations (15) and (17), we get

$$\dot{\mathbf{s}} = \mathbf{c}\dot{\mathbf{e}}_\varepsilon + \ddot{\boldsymbol{x}}_d - \mathbf{f}(x_i, y_i, z_i, t) - \mathbf{Bu}, \tag{18}$$

$$\dot{\mathbf{L}}_y = \mathbf{s}\dot{\mathbf{s}}. \tag{19}$$

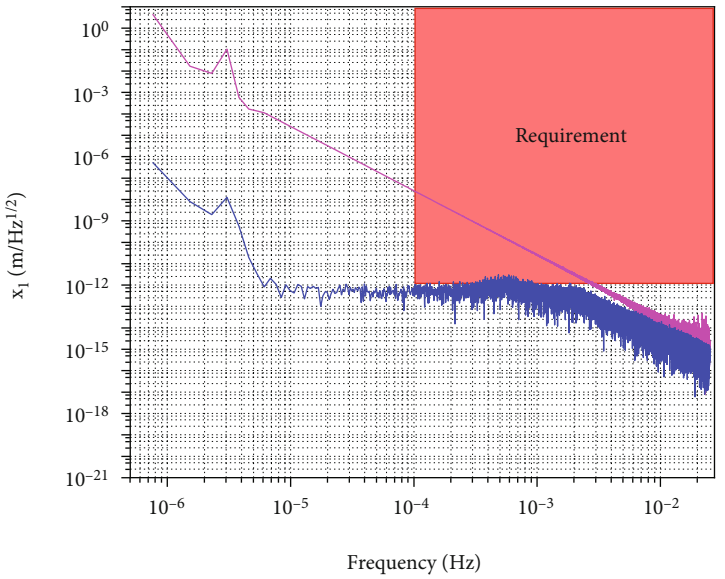

(a) Relative displacement accuracy on x

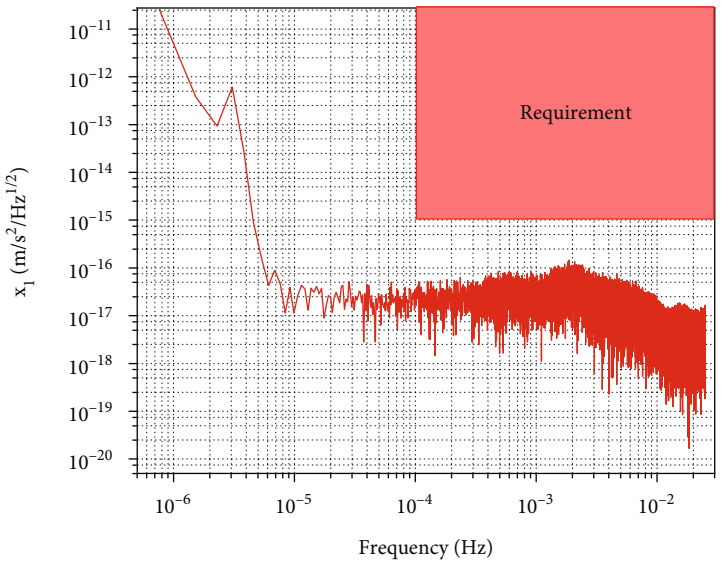

(b) Residual acceleration accuracy on x_1

FIGURE 9: The displacement accuracy and residual acceleration accuracy of the relative motion on x_1.

We use the exponential reaching law; then, the control law is

$$\mathbf{u} = \frac{1}{\mathbf{B}}\left[\mathbf{c}\dot{\mathbf{e}}_\varepsilon + \boldsymbol{x}_d - \mathbf{f}(x_i, y_i, z_i, t) + \mathbf{k}\mathbf{s} + \boldsymbol{\eta}\boldsymbol{sat}(\mathbf{s})\right], \tag{20}$$

where

$$\boldsymbol{sat}(\mathbf{s}) = \begin{cases} \boldsymbol{sgn}(\mathbf{s}), \mathbf{s} \geq \boldsymbol{\phi}, \\ \dfrac{\mathbf{s}}{\mathbf{f}}, \mathbf{s} < \boldsymbol{\phi}. \end{cases} \tag{21}$$

Substituting Equations (18) and (20) in Equation (19) gives

$$\begin{aligned} \dot{\mathbf{L}}_y &= \mathbf{s}(\boldsymbol{c}\dot{\mathbf{e}}_\varepsilon + \ddot{\boldsymbol{x}}_d - \mathbf{f}(x_i, y_i, z_i, t) - \mathbf{c}\dot{\mathbf{e}}_\varepsilon - \ddot{\boldsymbol{x}}_d + \mathbf{f}(x_i, y_i, z_i, t) - \mathbf{k}\mathbf{s} - \boldsymbol{\eta}\boldsymbol{sat}(\mathbf{s})) \\ &= -\mathbf{k}\mathbf{s}^2 - \boldsymbol{\eta}|\mathbf{s}| \leq 0. \end{aligned} \tag{22}$$

According to the LaSalle invariance principle, the closed-loop controller is asymptotically stable.

4.2. Performance Analysis of the Controller. The control analysis of TM1 is given, and the control analysis of TM2 is similar to that of TM1. This section studies the control of test mass relative to the cavity under the gravitational gradient of the Earth-moon-sun system when the geocentric

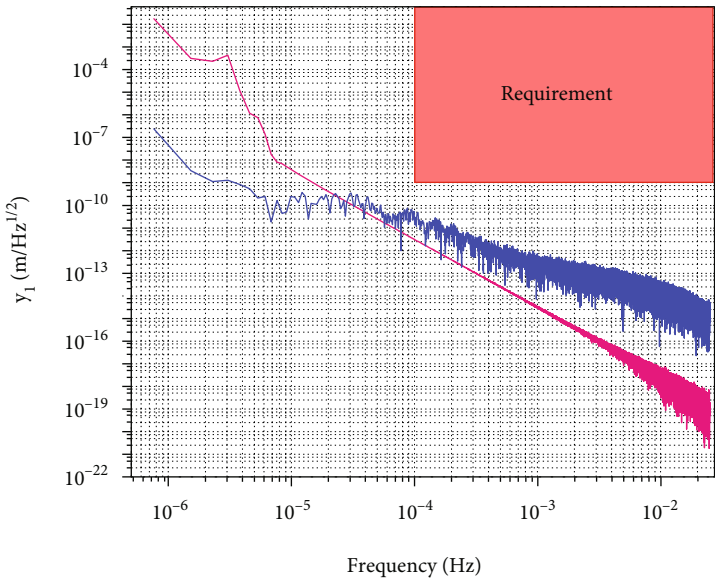

(a) Relative displacement accuracy on y_1

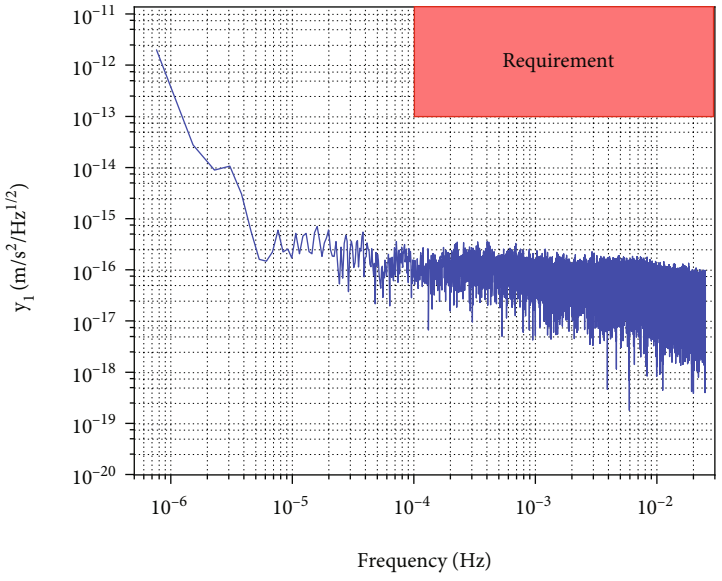

(b) Residual acceleration accuracy on y_1

Figure 10: The displacement accuracy and residual acceleration accuracy of the relative motion on y_1.

gravitational wave detector is operating in scientific mode. The control requirement can be given as shown in Table 2 [26].

In the scientific model, the initial state parameters of TM1 is (0, 0, 0, 0, 0, 0), and the starting time of simulation is January 1, 2034. With the controller designed by Equation (20), the control effect of the relative motion between TM1 and cavity in the time domain can be obtained, as shown in Figure 8.

By comparing Figures 2(b) and 8, it can be seen that the relative motion between the TM1 and the cavity after control is significantly reduced, and the relative displacement of three axes are in the magnitude of 10^{-9} m, 10^{-10} m, and 10^{-9} m, respectively. These results meet the requirements of Table 2 and have the margins of several orders of magnitude. Therefore, the sliding mode controller can realize the high-precision control of drag-free spacecraft and has certain robustness.

In scientific mode, in order to avoid the interference of the controller on sensitive axis and nonsensitive axis to flood the gravitational wave detection signal, the control effect of the controller in the frequency domain is given here. Figures 9–11, respectively, show the displacement accuracy and residual acceleration accuracy of the relative motion in the frequency domain.

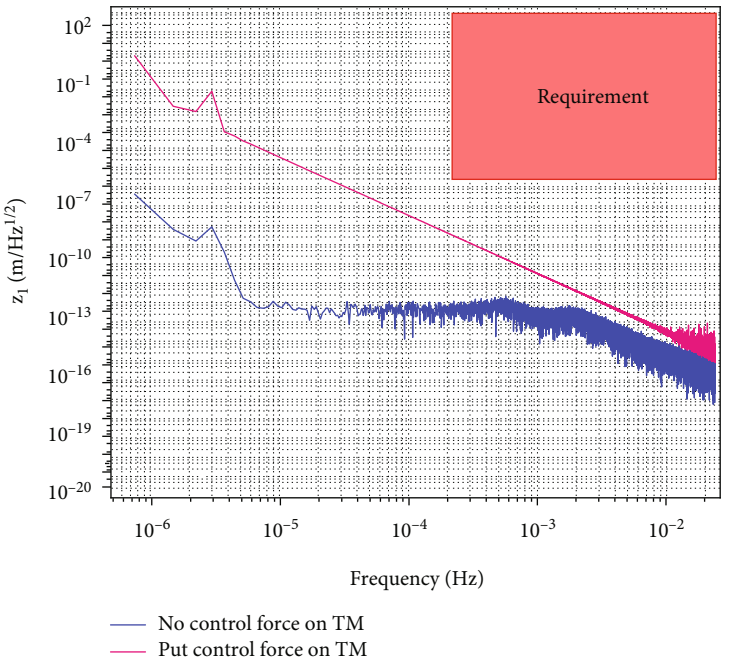

(a) Relative displacement accuracy on z_1

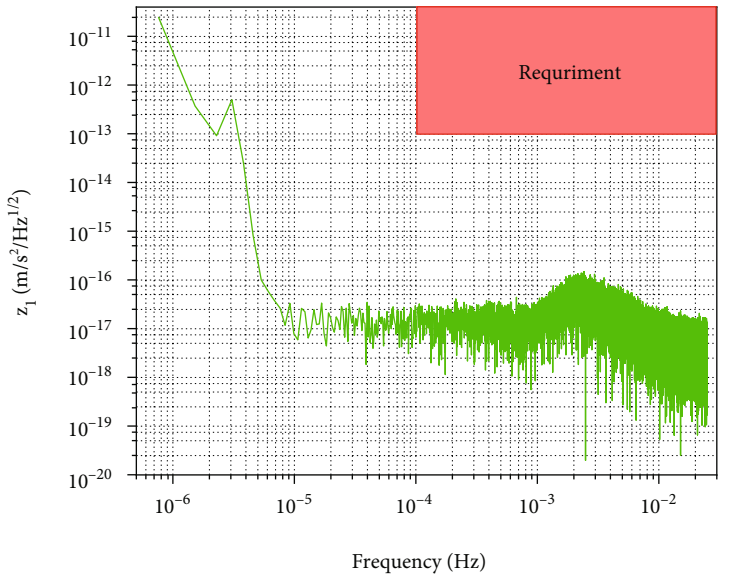

(b) Residual acceleration accuracy on z_1

Figure 11: The displacement accuracy and residual acceleration accuracy of the relative motion on z_1.

In Figures 9–11, Requirement denotes the control index from Table 2. The blue line represents the power spectral density (PSD) of relative displacement when the control force is applied in Figures 9(a)–11(a). It can be seen from Figure 9(a) that the accuracy of the relative displacement between the TM1 and the cavity does not meet the requirements in the detection frequency band when the control force of the sensitive axis is not applied. The slight constraint violation within 0.1 mHz–2 mHz may be caused by the negative stiffness of electrostatic force. In other frequency bands, the requirements are fully met. Considering that 0.1 mHz–2 mHz basically meets the requirements, this violation can be tolerated. The figure in frequency band 0.025 Hz–1 Hz is not shown here, because the large interference is generally reflected in the low-frequency band. In Figure 9(b), the accuracy of residual acceleration in the direction of the sensitive axis is lower than required, and there is a certain margin. This result shows that the sliding mode controller not only achieves robustness in the time domain but also has a robustness to the frequency domain control results.

It can be seen from Figures 10 and 11 that the relative displacement accuracy and residual acceleration accuracy of the nonsensitive axis both meet the requirements and

have a certain margin. Therefore, the controller meets the requirements of the frequency domain. In addition, comparing the frequency domain control results of the relative acceleration on the three axes, it can be seen that the acceleration PSD margin of the sliding mode controller in the z-axis direction is greater than that of the other two axes, which is consistent with the position PSD results.

5. Conclusions

In this paper, the relative motion and control of a drag-free spacecraft system under the gravitational fields of the Earth, moon, and sun are studied for a high-precision mission. The relative motion between the test mass and the spacecraft cavity is analyzed by multibody dynamics, numerical solution, and coordinate transformation. Through the comparative study on the relative motion of the sun orbit and Earth orbit, it was found that under pure gravity, the relative motion of the LISA spacecraft on the sensitive axis was relatively small, and the collision between the test mass and the cavity on the sensitive axis would not occur. However, the relative motion of the Earth orbit drag-free spacecraft on the sensitive axis is relatively large, which will cause a collision if no control is applied. By decomposing the effects of different gravitational fields, the influence of the gravitational gradient of the Earth, moon, and sun in the Earth orbit is studied. It is found that the Earth has the greatest influence on relative motion in the orbital plane, while the moon has the greatest influence on relative motion in the normal direction. Finally, a sliding mode controller is designed to verify one of the control strategies in combination with the background of the high-precision mission. The simulation results show that the controller can meet the requirements of the time domain and frequency domain.

Data Availability

The data used to support the findings of this study are available from the corresponding author upon request.

Conflicts of Interest

The authors declare that they have no conflicts of interest.

References

[1] G. Pugh, "Proposal for a spacecraft test of the coriolis prediction of general relativity," in *Weapons Systems Evaluation Group Research Memorandum*, NASA, USA, 1959.

[2] B. Lange, "The drag-free Satellite," *AIAA Journal*, vol. 2, no. 9, pp. 1590–1606, 1964.

[3] B. Lange, *The Control and Use of Drag-Free Spacecrafts*, Stanford University, Stanford, 1964.

[4] J. D. Powell, B. O. Lange, and P. Jhin, "Mass attraction reduction by integral control in spinning dragfree Satellites," *Journal of Spacecraft and Rockets*, vol. 9, no. 8, pp. 592–596, 1972.

[5] M. Wiegand, S. Scheithauer, and S. Theil, "Step proof mass dynamics," *Acta Astronautica*, vol. 54, no. 9, pp. 631–638, 2004.

[6] S. Theil, *Drag-Free Spacecraft Control. Lasers, Clocks and Drag-Free Control*, Springer, Berlin Heidelberg, 2008.

[7] M. S. Guilherme, W. C. Leite Filho, and S. Theil, "Strategies for in-orbit calibration of drag-free control systems," *Aerospace Science and Technology*, vol. 12, no. 5, pp. 365–375, 2008.

[8] L. Pettazzi, A. Lanzon, S. Theil, and A. E. Finzi, "Design of robust drag-free controllers with given structure," *Journal of Guidance, Control, and Dynamics*, vol. 32, no. 5, pp. 1609–1621, 2009.

[9] E. Canuto, A. Molano, and L. Massotti, "Drag-free control of the GOCE satellite: noise and observer design," *IEEE Transactions on Control Systems Technology*, vol. 18, no. 2, pp. 501–509, 2010.

[10] E. Canuto and L. Massotti, "All-propulsion design of the drag-free and attitude control of the European satellite GOCE," *Acta Astronautica*, vol. 64, no. 2-3, pp. 325–344, 2009.

[11] E. Canuto, "Drag-free and attitude control for the GOCE satellite," *Automatica*, vol. 44, no. 7, pp. 1766–1780, 2008.

[12] E. Canuto, C. Novara, D. Carlucci, C. P. Montenegro, and L. Massotti, *Spacecraft Dynamics and Control: The Embedded Model Control Approach*, Butterworth-Heinemann, 2018.

[13] W. Fichter, P. Gath, S. Vitale, and D. Bortoluzzi, "LISA Pathfinder drag-free control and system implications," *Classical and Quantum Gravity*, vol. 22, no. 10, pp. S139–S148, 2005.

[14] W. Fichter, A. Schleicher, S. Bennani, and S. Wu, "Closed loop performance and limitations of the LISA Pathfinder drag-free control system," in *AIAA Guidance, Navigation and Control Conference and Exhibit*, Hilton Head, South Carolina, 2007.

[15] T. Ziegler and W. Fichter, "Test mass stiffness estimation for the LISA Pathfinder drag-free system," in *Aiaa Guidance, Navigation & Control Conference & Exhibit*, Hilton Head, South Carolina, 2011.

[16] S. F. Wu and D. Fertin, "Spacecraft drag-free attitude control system design with quantitative feedback theory," *Acta Astronautica*, vol. 62, no. 12, pp. 668–682, 2008.

[17] S. F. Wu and D. Fertin, *QFT based drag-free and attitude controller design/tuning*, European Space Agency Space Agency, 2005.

[18] X. Lian, *Relative motion analysis and control strategy for test mass of drag-free spacecraft, [Ph.D. thesis]*, Sun Yat-sen University, 2021.

[19] X. Lian, J. Zhang, L. Chang, J. Song, and J. Sun, "Test mass capture for drag-free satellite based on RBF neural network adaptive sliding mode control," *Advances in Space Research*, vol. 69, no. 2, pp. 1205–1219, 2022.

[20] P. Chapman, P. Zentgraf, and Y. Jafry, "Drag-free control design including attitude transition for the STEP mission," in *Spacecraft Guidance, Navigation and Control Systems*, European Space Agency-Publications-ESA SP, 2003.

[21] L. Shi, *Dynamic Modeling and Control Research of Drag-Free Spacecraft*, Harbin Institute of Technology, Harbin, 2012.

[22] L. Francesco, *Precise Control of LISA with Quantitative Feedback Theory*, Delft University of Technology, 2019.

[23] H. Li, *Research of Drag-Free and Attitude Control System for the Next Generation Gravimetric Spacecraft*, Huazhong University of Science and Technology, Wuhan, 2017.

[24] X. Lian, J. Zhang, L. Lu et al., "Frequency separation control for drag-free satellite with frequency-domain constraints," *IEEE Transactions on Aerospace and Electronic Systems*, vol. 57, no. 6, pp. 4085–4096, 2021.

[25] X. Lian, J. Zhang, J. Yang, Z. Lu, Y. Zhang, and Y. Song, "The determination for ideal release point of test masses in drag-free satellites for the detection of gravitational waves," *Advances in Space Research*, vol. 67, no. 2, pp. 824–833, 2021.

[26] J. Luo, L. S. Chen, H. Z. Duan et al., "TianQin: a space-borne gravitational wave detector," *Classical and Quantum Gravity*, vol. 33, no. 3, pp. 035010–035032, 2016.

Hindawi
International Journal of Aerospace Engineering
Volume 2022, Article ID 2606233, 11 pages
https://doi.org/10.1155/2022/2606233

Research Article

Compound Attitude Maneuver and Collision Avoiding Control for a Novel Noncontact Close-Proximity Formation Satellite Architecture

He Liao,[1] **Jinjin Xie**,[2] **Xiaodong Zhou**,[2] **Chuang Yao**,[2] **Zhongxing Tang**,[2] **Yanbin Zhao**,[2] **and Jirong Qi**[1]

[1]*College of Astronautics, Nanjing University of Aeronautics and Astronautics, Nanjing 210016, China*
[2]*Research Center, Shanghai Academy of Space Technology, Shanghai 201109, China*

Correspondence should be addressed to Jinjin Xie; xiejin1002@163.com

Received 15 September 2021; Revised 20 December 2021; Accepted 31 December 2021; Published 31 January 2022

Academic Editor: Shunan Wu

In order to achieve the attitude maneuver performance of the noncontact close-proximity formation satellite architecture, this paper presents a compound control strategy with variable-parameter sliding mode control and disturbance observer-based feedforward compensation. Firstly, the variable-parameter sliding mode control is proposed to guarantee the attitude maneuver performance of the payload module. Secondly, the collision avoiding control with disturbance observer-based feedforward compensation is proposed to guarantee the synchronization of the two separated modules within the small air clearance constraint of the noncontact Lorentz actuator. Finally, a physical air-floating platform is established to verify the effectiveness of the proposed approach.

1. Introduction

With the development of the space camera technology, high-resolution imaging under attitude maneuver has been focused on recently [1–3]. However, the imaging results could be declined seriously by the huge flexible solar array and the vibration-generating devices [4–6]. For example, the huge flexible solar array could induce pointing overshoot, the high-frequent vibration could induce the imaging blurring, and the low-frequent vibration could induce the imaging warping [7, 8].

The active, passive, and integral active-passive vibration isolations have been proposed to suppress the transmission of the above-mentioned disturbance. Nevertheless, due to their respective limitations, the impact of the above-mentioned disturbance on the control performance cannot fundamentally be rejected [9–12].

A noncontact close-proximity formation satellite concept has been proposed to separate the conventional integrative-contact satellite into an ultraquiet payload module and a service module by noncontact Lorentz actuator [13]. A ground test system with a single rotation degree of freedom (1R-DOF) and two translation degrees of freedom (2T-DOF) by using planar air-bearing technology has been proposed to conduct several experiments, indicating that the isolation performance is improved by two orders of magnitude and not limited by sensor characteristics [14]. However, it is insufficient to verify the multidynamics coupling problem of the noncontact close-proximity formation satellite architecture. The three-axis coupling dynamic model of the noncontact close-proximity formation satellite has been conducted by Newton-Euler approach, indicating that the current driving accuracy of the noncontact Lorentz actuator plays the most important role in the whole architecture

control [15–17]. The optimization approaches based on multiphysical fields have been proposed to resolve the contradiction between the high power and low ripple, leading to a resolution with ppm within its air clearance [18]. By taking the advantages of the noncontact Lorentz actuator, the advanced control algorithms, such as twistor-based synchronous sliding model control, and model predictive control, have been proposed to guarantee a good performance of the stability control. The development of the noncontact close-proximity formation satellite has been greatly promoted through the above-mentioned researches [19–24]. Also, due to the advantage of the noncontact close-proximity formation satellite, the payload module can be considered the conventional satellite and there are many related researches on controller design [25, 26]. It can be easily found that the recent literatures mainly focus on the theory and simulation analysis to improve the stability control performance of the noncontact close-proximity formation satellite.

In view of the application, the noncontact architecture design demonstrates not only the structure separating but also inertia tensor separating, indicating that the attitude maneuver operation can be realized through two-echelon stratification. However, it is more difficult than stability control due to its close-proximity formation characteristics. The whole attitude maneuver control should be designed carefully within small air clearance of the noncontact Lorentz actuator. Otherwise, the separated payload module and service module could be collided. The collision may damage the actuators and the precision instruments of the noncontact close-proximity formation satellite. Therefore, in order to realize the attitude maneuver performance, it is necessary to study the collision avoidance control.

A compound control with variable-parameter sliding mode control and disturbance observer-based feedforward compensation has been proposed to realize both the attitude maneuver performance and the synchronization of the two separated modules in this paper. Meanwhile, a physical air-floating platform with 3R-DOF and 2T-DOF is established to verify the effectiveness of the proposed approach. The main contributions of this paper can be outlined as follows:

(1) Compared with the previous researches on the noncontact close-proximity formation satellite in [19–24], this paper extends its advantage into the attitude maneuver operation by using compound control strategy

(2) Compared with the 1R-DOF ground test system established in [14], the physical air-floating platform with full 3R-DOF can effectively verify the overall performance of the noncontact close-proximity formation satellite with multidynamics

The rest of this article is organized as follows. The dynamic modeling of the noncontact close-proximity formation satellite is given in Section 2. And the compound controller design is introduced in Section 3. Section 4 details the physical air-floating platform and the experimental verification results of the proposed approach. Finally, Section 5 exhibits the conclusions of the whole paper.

2. Dynamic Modeling

In this section, the noncontact close-proximity formation satellite architecture is introduced, and the dynamic modelling is established by using Newton-Euler approach.

2.1. Hierarchical Architecture. The noncontact close-proximity formation satellite is divided the structure into an ultraquiet payload module and a service module by noncontact Lorentz actuator, as shown in Figure 1.

The payload module is used to install the ultraquiet devices, such as the star sensor and the coil component of the noncontact Lorentz actuator. Since the huge flexible solar panel and the vibration-generating devices are not equipped within the payload module, it can be regarded as a rigid body. The service module is used to install the control moment gyroscope, thruster, solar panel, and the permanent magnet component of the noncontact Lorentz actuator. Meanwhile, the wireless communication and the power supply is becoming more mature and reliable gradually, suggesting that the wireless technologies can be adopted to avoid the issues due to the cables [27, 28].

The noncontact Lorentz actuator is a magnetic levitation actuator which is driven by the current with linear force output. Compared with the control moment gyroscope, the accuracy of the noncontact Lorentz actuator is more precise without unbalanced vibration [29].

2.2. Payload Module Dynamics. According to the angular momentum theorem, the attitude dynamics of the payload module has the following expression:

$$\mathbf{J}_p\dot{\boldsymbol{\omega}}_p + \boldsymbol{\omega}_p \times \left(\mathbf{J}_p\boldsymbol{\omega}_p\right) = \mathbf{T}_{cp} + \mathbf{T}_{dp}, \tag{1}$$

where $\boldsymbol{\omega}_p$ represents the angular velocity vector of the payload module; $\mathbf{J}_p$ represents the inertia tensor of the payload module; $\mathbf{T}_{cp}$ represents the control torque by the noncontact Lorentz actuators; and $\mathbf{T}_{cp}$ represents the sum of the external disturbance torque to the payload module.

The attitude kinematics of the payload module is established based on the quaternion method, as shown in the following expression:

$$\dot{\mathbf{q}} = \begin{bmatrix} \dot{q}_0 \\ \dot{q}_1 \\ \dot{q}_2 \\ \dot{q}_3 \end{bmatrix} = \frac{1}{2}\begin{bmatrix} 0 & -\omega_{px} & -\omega_{py} & -\omega_{pz} \\ \omega_{px} & 0 & \omega_{pz} & -\omega_{py} \\ \omega_{py} & -\omega_{pz} & 0 & \omega_{pz} \\ \omega_{pz} & \omega_{py} & -\omega_{px} & 0 \end{bmatrix}\begin{bmatrix} q_0 \\ q_1 \\ q_2 \\ q_3 \end{bmatrix}. \tag{2}$$

In matrix form,

$$\begin{cases} \dot{q}_0 = -\dfrac{1}{2}\mathbf{q}^{\mathrm{T}}\boldsymbol{\omega}_p, \\ \dot{\mathbf{q}} = \dfrac{1}{2}(\mathbf{q}^{\times} + q_0\mathbf{I}_{3\times 3})\boldsymbol{\omega}_p, \end{cases} \tag{3}$$

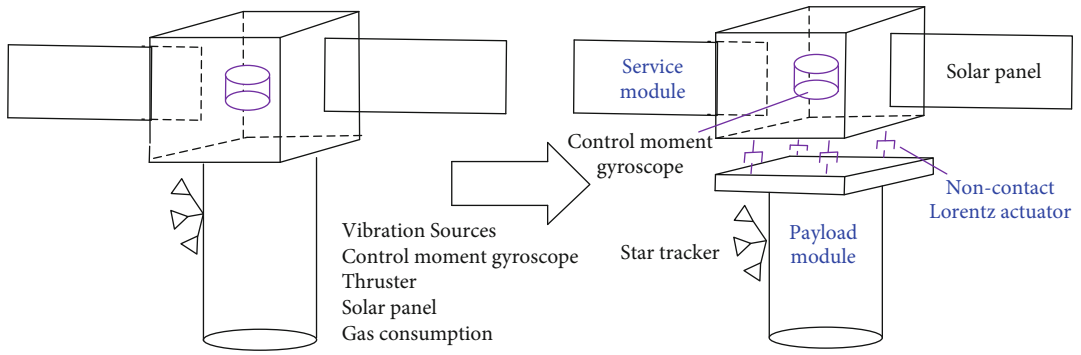

Figure 1: Hierarchical architecture.

where $\mathbf{q}^{\times} \in \mathbb{R}^{3\times 3}$ is the vector cross-product operator of a skew-symmetric matrix:

$$\mathbf{q}^{\times} = \begin{bmatrix} 0 & -q_3 & q_2 \\ q_3 & 0 & -q_1 \\ -q_2 & q_1 & 0 \end{bmatrix}. \tag{4}$$

In this paper, the controller design will be based on the state error. Therefore, defining the desired attitude quaternion $\mathbf{q}_t = [q_{t0}\ \mathbf{q}_t]^{\mathrm{T}} = [q_{t0}\ q_{t1}\ q_{t2}\ q_{t3}]^{\mathrm{T}}$ and the desired attitude angular velocity $\boldsymbol{\omega}_{pt} = [\omega_{ptx}\ \omega_{pty}\ \omega_{ptz}]^{\mathrm{T}}$. The error attitude quaternion $\mathbf{q}_e = [q_{e0}\ \mathbf{q}_e]^{\mathrm{T}} = [q_{e0}\ q_{e1}\ q_{e2}\ q_{e3}]^{\mathrm{T}}$ and the error angular velocity $\boldsymbol{\omega}_{pe} = [\omega_{pex}\ \omega_{pey}\ \omega_{pez}]^{\mathrm{T}}$ can be solved by the following expression:

$$\begin{cases} \mathbf{q_e} = \mathbf{q}_t^{*} \otimes \mathbf{q}, \\ \boldsymbol{\omega}_{pe} = \boldsymbol{\omega}_p - \boldsymbol{\omega}_{pt}, \end{cases} \tag{5}$$

where $\mathbf{q}_t^{*} = [q_{t0}\ -\mathbf{q}_t]^{\mathrm{T}}$ represents the conjugate quaternion and the symbol "$\otimes$" represents the multiplication of quaternions.

2.3. Service Module Dynamics. The control moment gyroscope, flexible solar panel, and other parts with large vibration are installed in the service module; the attitude dynamics of the service module has the following expression:

$$\dot{\mathbf{h}}_s + \boldsymbol{\omega}_s^{\times}\mathbf{h}_s + \mathbf{C}_{a1}\ddot{\mathbf{q}}_{a1} + \mathbf{C}_{a2}\ddot{\mathbf{q}}_{a2} = \mathbf{T}_{cs} + \mathbf{T}_{ds} + \mathbf{T}_{ps}, \tag{6}$$

where $\mathbf{h}_s = \mathbf{J}_s\boldsymbol{\omega}_s + \mathbf{h}_c$ represents the total angular momentum of the service module; $\mathbf{J}_s$ represents the inertia tensor of the service module; $\boldsymbol{\omega}_s$ represents the angular velocity vector of the service module; $\mathbf{h}_c$ represents the angular momentum of the control moment gyroscopes mounted on the service module; $\boldsymbol{\omega}_s$ represents the angular velocity vector; $\mathbf{C}_{ai}$ and $\mathbf{q}_{ai}$ ($i = 1, 2$) represent the coupling matrix and modes of the solar panels, as shown in Equations (7) and (8); $\mathbf{T}_{cs}$ represents the control torque of the control moment gyroscopes; $\mathbf{T}_{ns}$ represents the sum of the external disturbance torque to the service module; and $\mathbf{T}_{ps}$ represents the reaction torque of the noncontact Lorentz actuators to the service module, as shown in Equation (9).

$$\ddot{\mathbf{q}}_{a1} + 2\zeta\boldsymbol{\Lambda}_a\dot{\mathbf{q}}_{a1} + \boldsymbol{\Lambda}_a^2\mathbf{q}_{a1} + \mathbf{C}_{a1}^{T}\dot{\boldsymbol{\omega}}_b = 0, \tag{7}$$

$$\ddot{\mathbf{q}}_{a2} + 2\zeta\boldsymbol{\Lambda}_a\dot{\mathbf{q}}_{a2} + \boldsymbol{\Lambda}_a^2\mathbf{q}_{a2} + \mathbf{C}_{a2}^{T}\dot{\boldsymbol{\omega}}_b = 0, \tag{8}$$

where ζ represents the damping coefficient of the solar panels and $\boldsymbol{\Lambda}_a$ represents the modal frequency of the diagonal matrix.

$$\mathbf{T}_{ps} = -\mathbf{C}_{sp}^{T}\mathbf{T}_{cp}, \tag{9}$$

where $\mathbf{C}_{sp}$ represents the coordinate transformation matrix of the service module relative to the payload module.

Defining the angular velocity of the service module relative to the payload module as $\boldsymbol{\omega}_{sp}$, thus, the following relationship has the following expression:

$$\boldsymbol{\omega}_{sp} = \boldsymbol{\omega}_s - \mathbf{C}_{sp}^{T}\boldsymbol{\omega}_p. \tag{10}$$

According to Equations (1) and (6), the relative attitude dynamics equation of the two modules can be obtained by derivative of the above equation:

$$\begin{aligned} \dot{\boldsymbol{\omega}}_{sp} = {} & \mathbf{J}_s^{-1}\left(\mathbf{T}_{cs} + \mathbf{T}_{ds} + \mathbf{T}_{ps} - \mathbf{C}_{a1}\ddot{\mathbf{q}}_{a1} - \mathbf{C}_{a2}\ddot{\mathbf{q}}_{a2}\right) \\ & - \mathbf{J}_s^{-1}\boldsymbol{\omega}_s^{\times}\left(\mathbf{J}_s\boldsymbol{\omega}_s + \mathbf{h}_c\right) + \boldsymbol{\omega}_{sp} \times \left(\mathbf{C}_{sp}^{T}\boldsymbol{\omega}_p\right) \\ & - \mathbf{C}_{sp}^{T}\mathbf{J}_p^{-1}\left(\mathbf{T}_{cp} + \mathbf{T}_{dp} - \boldsymbol{\omega}_p \times \left(\mathbf{J}_p\boldsymbol{\omega}_p\right)\right). \end{aligned} \tag{11}$$

3. Compound Controller Design

In this section, the attitude maneuver operation of the payload module with variable-parameter sliding mode control and the collision avoiding of the service module with disturbance observer-based feedforward compensation is proposed to realize both the attitude maneuver performance and the synchronization of the two separated modules.

3.1. Block Diagram. The block diagram of the compound attitude maneuver and collision avoiding control for noncontact close-proximity formation satellite control system is shown in Figure 2. There are two control loops, including the active control of the payload module and the cooperative

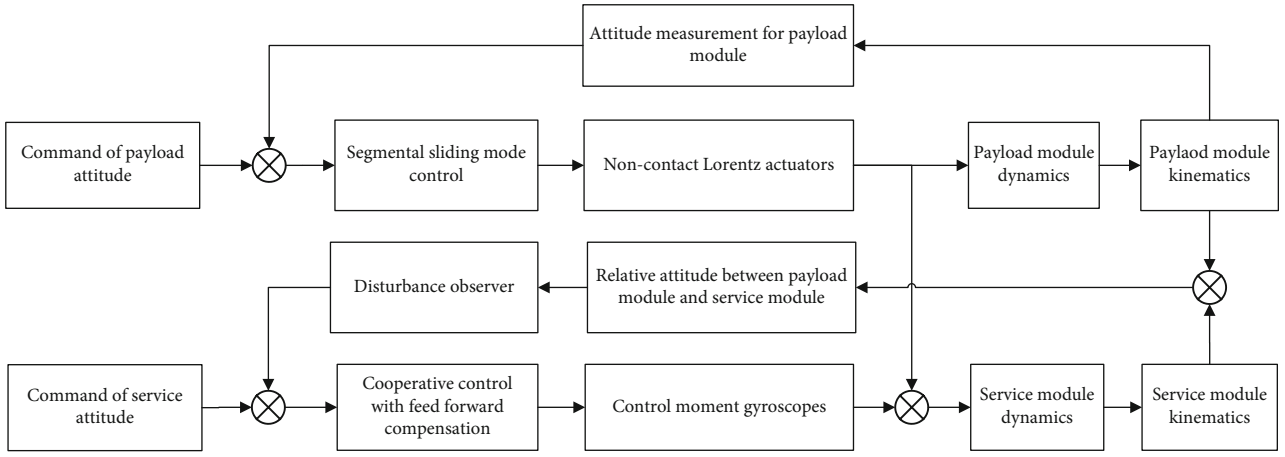

Figure 2: Block diagram of noncontact close-proximity formation satellite control system.

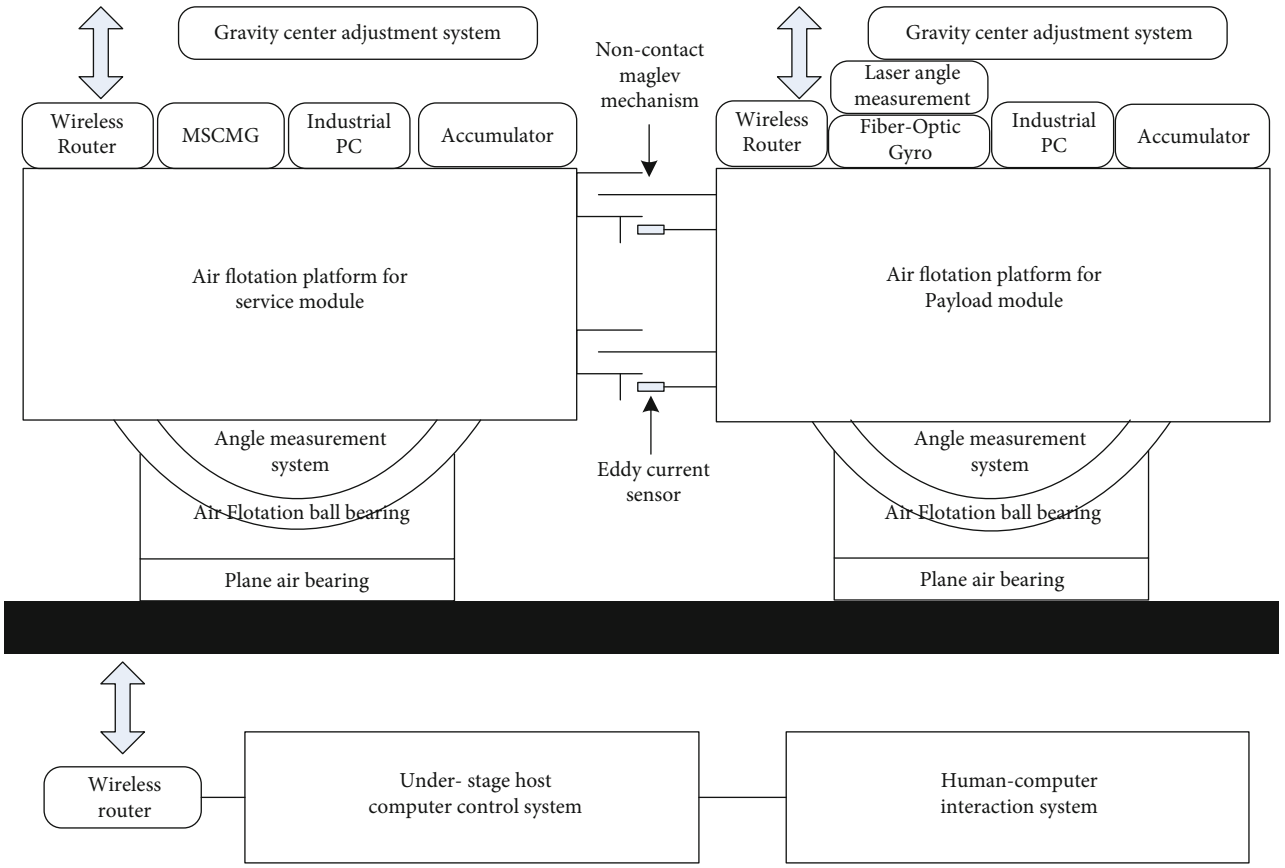

Figure 3: Schematic diagram of test system.

control of the service module. The variable-parameter sliding mode control algorithm is adopted to guarantee the active attitude maneuver control for payload module, while the disturbance observer-based feedforward compensation is adopted to guarantee the cooperative synchronization for service module within the small air clearance constraint.

3.2. Attitude Maneuver Control of Payload Module. The payload module could be affected by external interference. In order to improve the robustness of the system, the article adopts the variable-parameter sliding mode control to design the active attitude maneuver control for payload module. And the sliding mode control is based on the exponential reaching law [28–32].

Defining the sliding surface as follows:

$$\mathbf{s} = \mathbf{k}_p \mathbf{q}_e + \boldsymbol{\omega}_{pe}, \tag{12}$$

where $\mathbf{k}_p$ represents the three-dimensional diagonal matrix and its elements are positive real numbers.

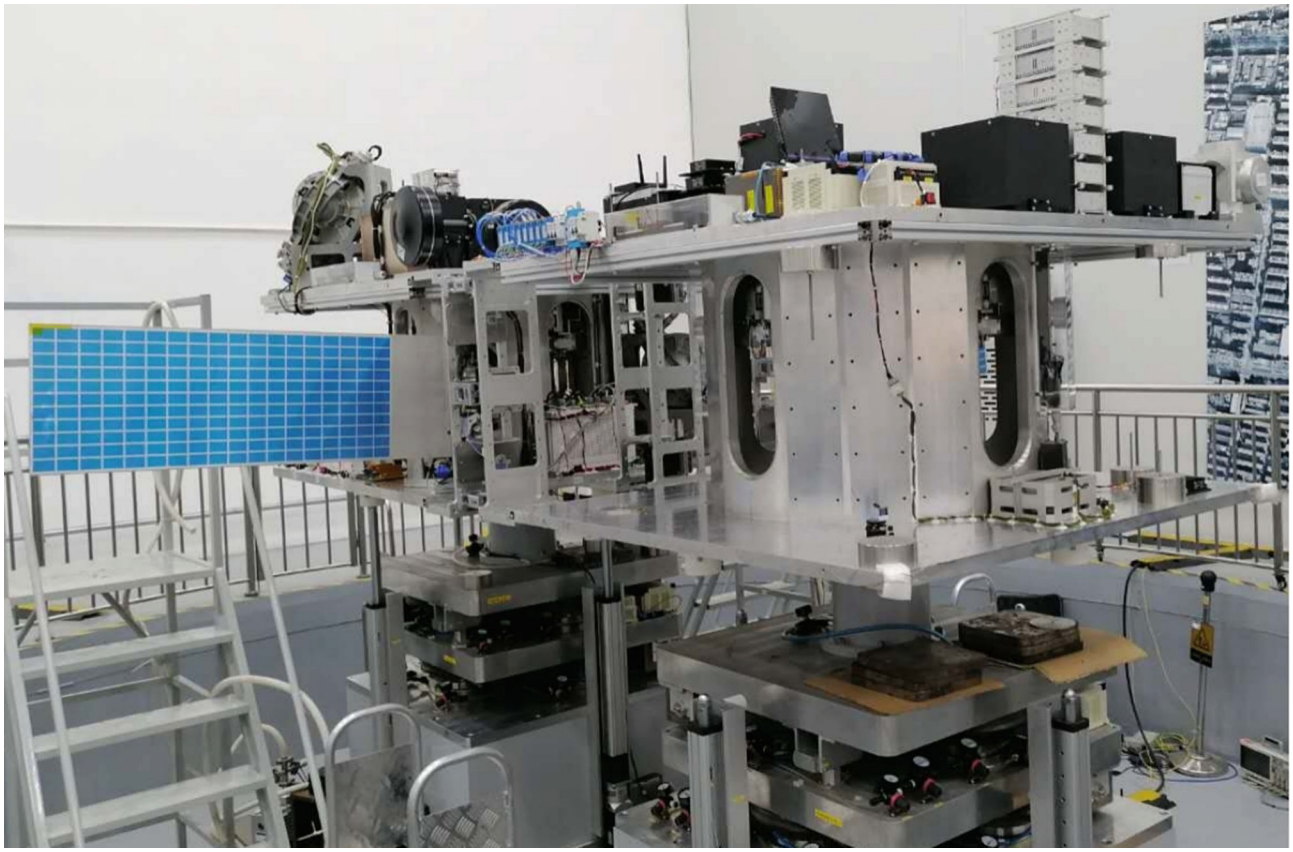

Figure 4: Physical system of the noncontact close-proximity formation satellite.

Table 1: Related parameters of physical system platform.

Parameter	Value
Capacity of air-floating platform	1000-2000 kg
Rotation range of air-floating platform	$\pm 25^{\circ}$ (X-axis)
Centroid fine adjustment error of air-floating platform	≤ 0.2 kgm
Centroid coarse adjustment error of air-floating platform	≤ 5 gcm
System total interference torque of air-floating platform	≤ 0.1 Nm
Dynamic range of wide-range angle measurement	$\pm 30^{\circ}$
Accuracy of wide-range angle measurement	$1''$ (3σ)
Angular momentum of control moment gyroscope	≤ 210 Nms
Output torque of control moment gyroscope	≤ 55 Nm
Frame angular velocity stability of control moment gyroscope	$3.9 \times 10^{-3^{\circ}}$/s
Output force of noncontact Lorentz actuator	≤ 15 N
Air-gap constraint of noncontact Lorentz actuator	$\pm 0.9^{\circ}$

According to the exponential approach law, the following equation has the following expression:

$$\dot{\mathbf{s}} = -\boldsymbol{\varepsilon}\mathbf{s} - \boldsymbol{\lambda}\mathrm{sat}(\mathbf{s}). \tag{13}$$

Both $\boldsymbol{\varepsilon}$ and $\boldsymbol{\lambda}$ are the three-dimensional diagonal matrixes, whose elements are positive real numbers.

Combining the dynamics and kinematics models of the payload module, the attitude maneuver control law of the payload module has the following expression:

$$\mathbf{T}_{cp} = \frac{1}{2}\mathbf{J}_p\mathbf{k}_p(\mathbf{q_e}^{\times} + q_{e0}I)\boldsymbol{\omega}_{pe} + \boldsymbol{\omega}_{pe}{}^{\times}\left(\mathbf{J}_p\boldsymbol{\omega}_{pe}\right) + \boldsymbol{\varepsilon}\mathbf{s} + \boldsymbol{\lambda}\mathrm{sat}(\mathbf{s}). \tag{14}$$

In order to realize the attitude maneuver control of the payload module, the idea of the variable-parameter control is adopted, and different control parameters $\mathbf{k}_p$ and $\boldsymbol{\varepsilon}$ are selected for the different attitude angle errors. As the attitude angle increases, the parameters will increase accordingly to achieve the purpose of quickly tracking large-angle attitude errors during maneuvering. On the other hand, when the angle error is small, the parameters will decrease accordingly to achieve high precision control of the payload module.

3.3. Collision Avoiding Control of Service Module. According to the function of the noncontact close-proximity formation satellite, the service module should be tracked the payload module within the small air clearance of the noncontact Lorentz actuator to avoid collision. Therefore, the service module needs to track the movement of the payload module synchronously.

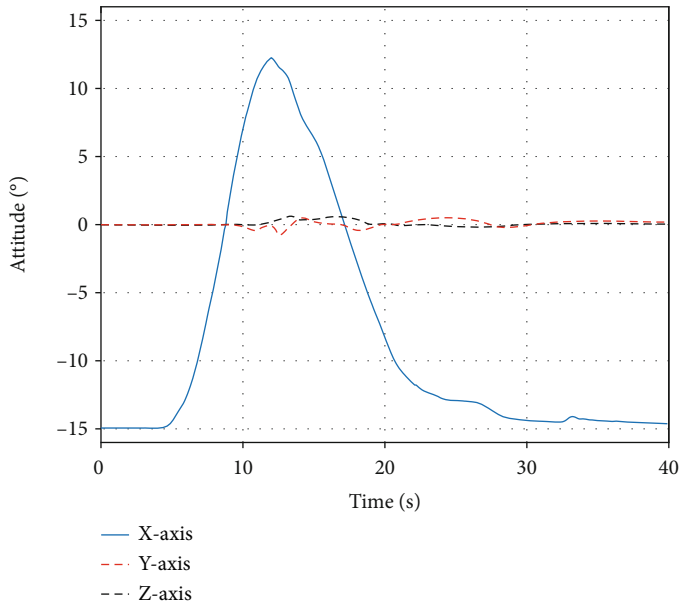

Figure 5: Attitude angle of payload module with PD controller.

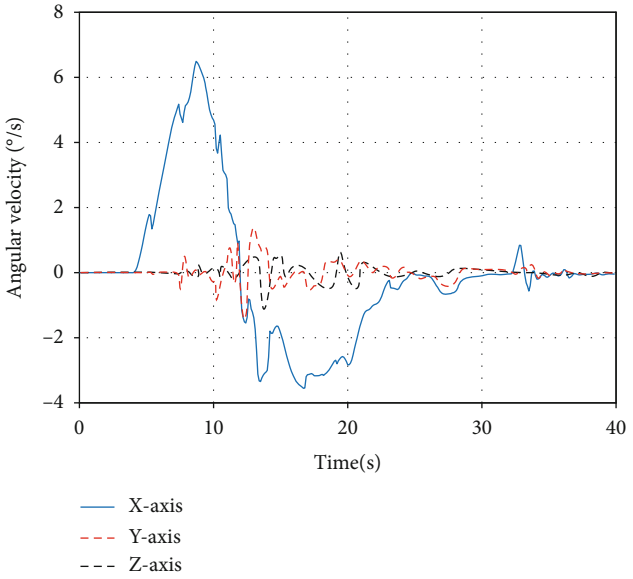

Figure 6: Angular velocity of payload module with PD controller.

According to Equation (6), it can be seen that the control torque by noncontact Lorentz actuators act on the payload module produce reaction torques to the service module at the same time. Since the noncontact Lorentz actuator is a magnetic levitation actuator with active current driving, its reaction torque to the service module can be obtained and compensated by the control law through Equation (9).

Meanwhile, the parameters such as the flexible accessory modal matrix of the solar panel and the coupling coefficient matrix can be precalibrated; the control law thus can be designed to compensate the coupling torques of the flexible accessory. Therefore, the control law has the following expression:

$$\mathbf{T}_{cs} = -\mathbf{K}_p\boldsymbol{\Theta}_{sp} - \mathbf{K}_d\boldsymbol{\omega}_{sp} - \mathbf{T}_{ps} + \mathbf{C}_{a1}\ddot{\mathbf{q}}_{a1} + \mathbf{C}_{a2}\ddot{\mathbf{q}}_{a2}, \tag{15}$$

where $\boldsymbol{\Theta}_{sp} = [\varphi_{sp}, \theta_{sp}, \psi_{sp}]^{\mathrm{T}}$ represents the attitude angle error angle of the service module relative to the three-axis of the payload module.

Substituting Equation (15) into Equation (11), the relative attitude dynamics equation has the following expression:

$$\begin{aligned}\dot{\boldsymbol{\omega}}_{sp} = {} & \mathbf{J}_s^{-1}\left(-\mathbf{K}_p\boldsymbol{\Theta}_{sp} - \mathbf{K}_d\boldsymbol{\omega}_{sp} + \mathbf{T}_{ds} - \boldsymbol{\omega}_s^{\times}\left(\mathbf{J}_s\boldsymbol{\omega}_s + \mathbf{h}_c\right)\right) \\ & + \boldsymbol{\omega}_{sp} \times \left(\mathbf{C}_{sp}^T\boldsymbol{\omega}_p\right) - \mathbf{C}_{sp}^T\mathbf{J}_p^{-1}\left(\mathbf{T}_{cp} + \mathbf{T}_{dp} - \boldsymbol{\omega}_p \times \left(\boldsymbol{B}_p\boldsymbol{\omega}_p\right)\right).\end{aligned} \tag{16}$$

Since the unmeasurable terms, complex high-order terms, and other unknown random disturbance moments could affect the control performance, the disturbance observer is designed to guarantee the synchronicity of the service module relative to the payload module within the small air clearance constraint. Therefore, Equation (16) has the following expression:

$$\begin{cases} \dot{\boldsymbol{\Theta}}_{sp} = \boldsymbol{\omega}_{sp}, \\ \dot{\boldsymbol{\omega}}_{sp} = \mathbf{J}_s^{-1}\left(-\mathbf{K}_p\boldsymbol{\Theta}_{sp} - \mathbf{K}_d\boldsymbol{\omega}_{sp}\right) + \boldsymbol{\omega}_{sp} \times \left(\mathbf{C}_{sp}^T\boldsymbol{\omega}_p\right) - \mathbf{J}_s^{-1}\boldsymbol{\omega}_s^{\times}\left(\mathbf{J}_s\boldsymbol{\omega}_s + \mathbf{h}_c\right) + \mathbf{J}_s^{-1}\mathbf{T}_{ds}. \end{cases} \tag{17}$$

It can also be written as

$$\begin{cases} \mathbf{J}_s\ddot{\boldsymbol{\Theta}}_{sp} + \mathbf{G}\left(\boldsymbol{\Theta}_{sp}, \dot{\boldsymbol{\Theta}}_{sp}\right) + \mathbf{T} = \mathbf{T}_{ds}, \\ \mathbf{G}\left(\boldsymbol{\Theta}_{sp}, \dot{\boldsymbol{\Theta}}_{sp}\right) = \mathbf{K}_p\boldsymbol{\Theta}_{sp} + \mathbf{K}_d\dot{\boldsymbol{\Theta}}_{sp} - \mathbf{J}_s\left(\dot{\boldsymbol{\Theta}}_{sp} \times \left(\mathbf{C}_{sp}^T\boldsymbol{\omega}_p\right)\right), \\ \mathbf{T} = \boldsymbol{\omega}_s^{\times}(\mathbf{J}_s\boldsymbol{\omega}_s + \mathbf{h}_c). \end{cases} \tag{18}$$

The form of the disturbance observer has the following expression:

$$\begin{cases} \dot{\boldsymbol{z}} = -L\left(\boldsymbol{\Theta}_{sp}, \dot{\boldsymbol{\Theta}}_{sp}\right)\boldsymbol{z} + L\left(\boldsymbol{\Theta}_{sp}, \dot{\boldsymbol{\Theta}}_{sp}\right)\left(\mathbf{G}\left(\boldsymbol{\Theta}_{sp}, \dot{\boldsymbol{\Theta}}_{sp}\right) + \mathbf{T} - p\left(\boldsymbol{\Theta}_{sp}, \dot{\boldsymbol{\Theta}}_{sp}\right)\right), \\ \hat{\mathbf{T}}_{ds} = \boldsymbol{z} + p\left(\boldsymbol{\Theta}_{sp}, \dot{\boldsymbol{\Theta}}_{sp}\right), \end{cases} \tag{19}$$

where $\boldsymbol{z}, L(\boldsymbol{\Theta}_{sp}, \dot{\boldsymbol{\Theta}}_{sp}), p(\boldsymbol{\Theta}_{sp}, \dot{\boldsymbol{\Theta}}_{sp})$ represents the internal state variable of the disturbance observer and $L(\boldsymbol{\Theta}_{sp}, \dot{\boldsymbol{\Theta}}_{sp})$ has the following relationship with $p(\boldsymbol{\Theta}_{sp}, \dot{\boldsymbol{\Theta}}_{sp})$:

$$L\left(\boldsymbol{\Theta}_{sp}, \dot{\boldsymbol{\Theta}}_{sp}\right)\mathbf{J}_s\ddot{\boldsymbol{\Theta}}_{sp} = \begin{bmatrix} \dfrac{\partial p\left(\boldsymbol{\Theta}_{sp}, \dot{\boldsymbol{\Theta}}_{sp}\right)}{\partial \boldsymbol{\Theta}_{sp}} & \dfrac{\partial p\left(\boldsymbol{\Theta}_{sp}, \dot{\boldsymbol{\Theta}}_{sp}\right)}{\partial \dot{\boldsymbol{\Theta}}_{sp}} \end{bmatrix} \cdot \begin{bmatrix} \dot{\boldsymbol{\Theta}}_{sp} \\ \ddot{\boldsymbol{\Theta}}_{sp} \end{bmatrix}. \tag{20}$$

The internal state variable $p(\boldsymbol{\Theta}_{sp}, \dot{\boldsymbol{\Theta}}_{sp})$ of the disturbance observer has the following expression:

$$p\left(\boldsymbol{\Theta}_{sp}, \dot{\boldsymbol{\Theta}}_{sp}\right) = c\begin{bmatrix} \dot{\varphi}_{sp} \\ \dot{\varphi}_{sp} + \dot{\theta}_{sp} \\ \dot{\varphi}_{sp} + \dot{\theta}_{sp} + \dot{\psi}_{sp} \end{bmatrix}, \tag{21}$$

where $c \in R^+$ represents the observer gain.

From Equations (20) and (21), we can get

$$L\left(\boldsymbol{\Theta}_{sp}, \dot{\boldsymbol{\Theta}}_{sp}\right)\mathbf{J}_s\ddot{\boldsymbol{\Theta}}_{sp} = \begin{bmatrix} \dfrac{\partial p\left(\boldsymbol{\Theta}_{sp}, \dot{\boldsymbol{\Theta}}_{sp}\right)}{\partial \boldsymbol{\Theta}_{sp}} & \dfrac{\partial p\left(\boldsymbol{\Theta}_{sp}, \dot{\boldsymbol{\Theta}}_{sp}\right)}{\partial \dot{\boldsymbol{\Theta}}_{sp}} \end{bmatrix} \cdot \begin{bmatrix} \dot{\boldsymbol{\Theta}}_{sp} \\ \ddot{\boldsymbol{\Theta}}_{sp} \end{bmatrix} = c\begin{bmatrix} 1 & 0 & 0 \\ 1 & 1 & 0 \\ 1 & 1 & 1 \end{bmatrix}\ddot{\boldsymbol{\Theta}}_{sp}. \tag{22}$$

4. Experimental Verification

In this section, the experimental verification by using the physical air-floating platform is introduced as first. Meanwhile, a PD controller is conducted to demonstrate that the collision avoiding control has to be considered while attitude maneuver operating. Finally, the feasibility and effectiveness of the proposed compound control are successfully verified to guarantee both attitude maneuver performance and collision avoiding performance for noncontact close-proximity formation satellite architecture.

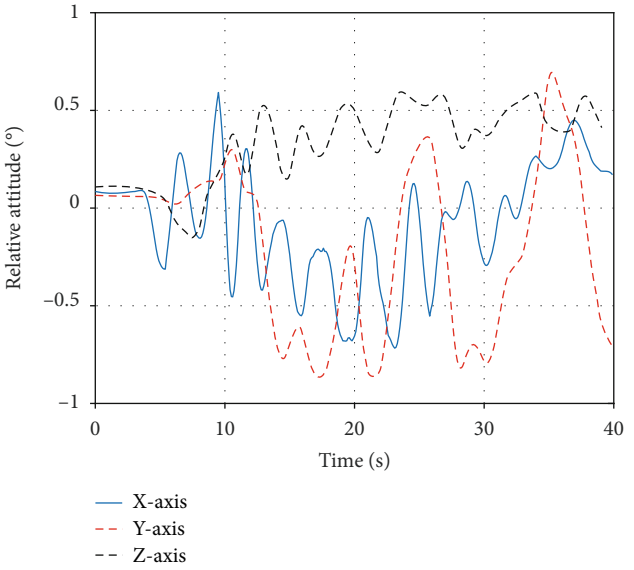

Figure 7: Relative attitude angle between two modules with PD controller.

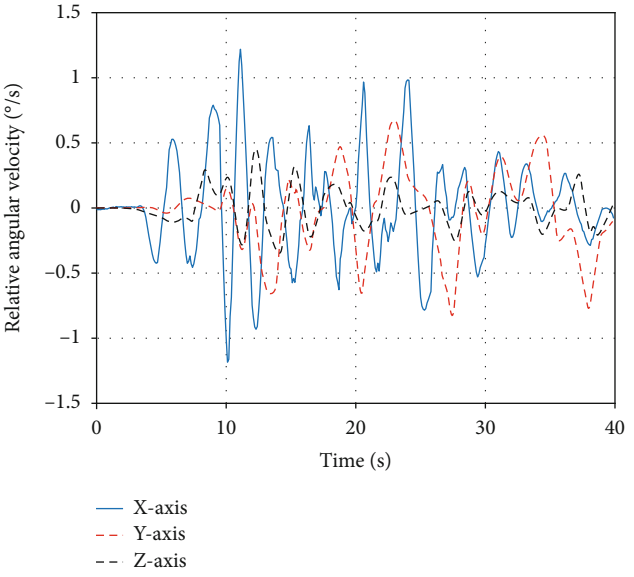

Figure 8: Relative angular velocity between two modules with PD controller.

4.1. Experimental System. In order to verify the proposed compound attitude maneuver and collision avoiding control of the noncontact close-proximity formation satellite, the schematic diagram of the physical air-floating platform with 3R-DOF and 2T-DOF is shown in Figure 3. The system is composed of two air-floating platforms, in which the left air-floating platform is used to simulate the service module, the right air-floating platform is used to simulate the payload

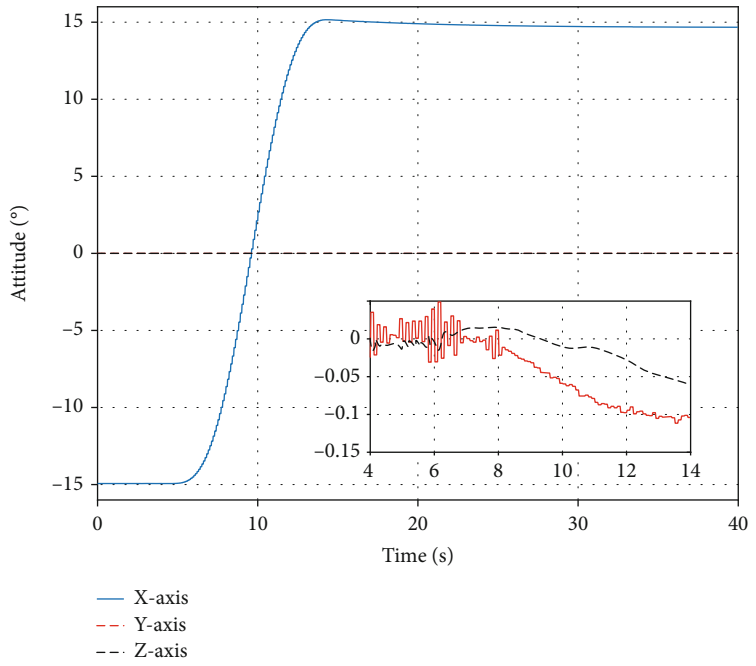

Figure 9: Attitude angle of payload module with compound controller.

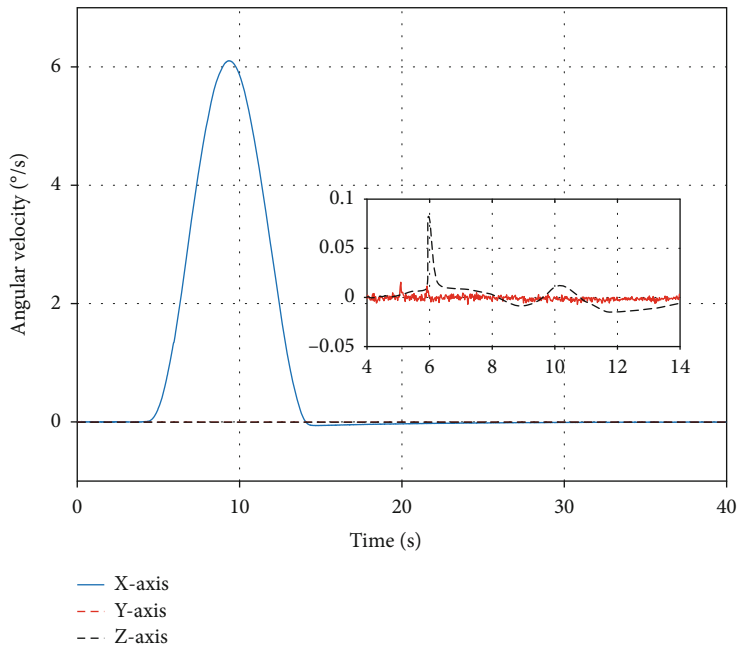

Figure 10: Angular velocity of payload module with compound controller.

module, and eight noncontact Lorentz actuators are installed between the two modules.

The payload module is equipped with the batteries, DC-DC, industrial computer, fiber optic gyros, camera, etc., and the service module is equipped with the batteries, DC-DC, industrial control computer, eddy current sensors, magnetic suspension control moment gyroscopes, and flexible solar panel.

The control system is adopted as the MATLAB/Simulink XPC system. The wide-range angle measurement system and fiber optic gyros are adopted to obtain the current attitude information of the payload module. The relative attitude and position between the service module and payload module are measured and calculated by eight eddy current sensors fixed with the noncontact Lorentz actuators. The attitude information of the experimental system is sent to the industrial computer through RS422 communication. The industrial computer is used to calculate the command input through the attitude control algorithm according to the difference between the current attitude information

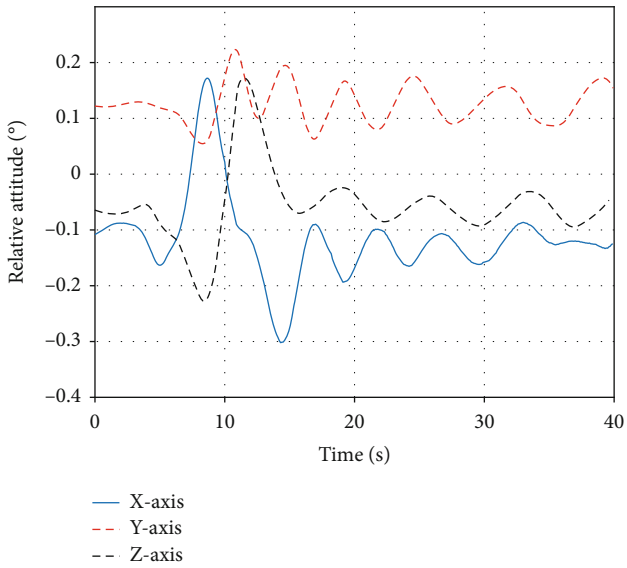

Figure 11: Relative attitude between two modules with compound controller.

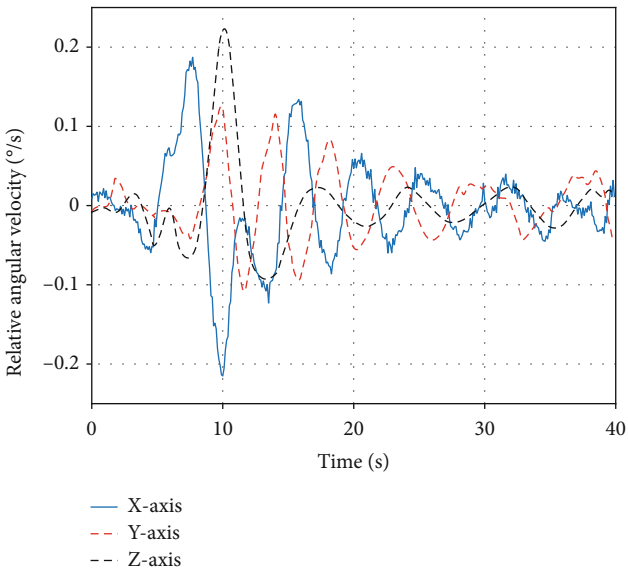

Figure 12: Relative angular velocity between two modules with compound controller.

and the expected attitude and to drive the noncontact Lorentz actuators and control moment gyroscopes to output the command input. The under-stage computer and the on-stage industrial computer are used to upload the control program and to download the telemetry information through the wireless network.

According to the above-mentioned design, the physical air-floating platform of the noncontact close-proximity formation satellite is shown in Figure 4, in which the related parameters are shown in Table 1. Combining with the placement position in the laboratory, the reference coordinate system is established in the east-north-sky direction. Taking the center of mass of the service module as the coordinate origin, the body coordinate system $O_sX_sY_sZ_s$ of the service module is established along the three directions of the inertia axis. In the same way, the payload module body coordinate system $O_pX_pY_pZ_p$ of the payload module is established along the three directions of the inertia axis with the center of mass as the coordinate origin.

Due to the gravity constraint, the physical system of the noncontact close-proximity formation satellite is carried out along X-axis to verify the attitude maneuver control of the payload module and cooperative control of the service module. Setting the initial attitude angle of the two modules as -15°, the desired attitude angle as +15°, and attitude maneuver control as 30°/10s in a sinusoidal manner; therefore, the maneuver angle, angular velocity, and angular acceleration planning command curve can be obtained as follows:

$$\begin{cases} \varphi = 3t - \dfrac{15}{\pi}\sin\left(\dfrac{\pi}{5}\right)t, \\ \omega_x = 3 - 3\cos\left(\dfrac{\pi}{5}\right)t, \quad t \in [t_0, t_0 + 10], \\ \dot{\omega}_x = \dfrac{3}{5}\pi\sin\left(\dfrac{\pi}{5}\right)t. \end{cases} \tag{23}$$

4.2. Test Results with PD Controller. In order to validate the feasibility of the proposed compound controller, the PD controller is carried out firstly in this paper. The control results are shown in Figures 5–8.

Figures 5 and 6 show the attitude angle and angular velocity curves of the payload module while the PD controller is adopted. It can be seen that the attitude angle and angular velocity curves are deformed and the whole attitude maneuver process is not completed.

Figures 7 and 8 show the attitude angle and angular velocity curves of the service module relative to the payload module. It can be seen that the relative attitude angle of the two modules has exceeded the air clearance constraint of the noncontact Lorentz actuator and the relative attitude angular velocity curve of the two modules is greater than 0.5°/s, indicating that the service module could not track the payload module well, and the two modules is colliding in the attitude maneuver process.

4.3. Test Results with Compound Controller. The control results of the proposed compound controller are shown in Figures 9–12. Figures 9 and 10 show the attitude angle and angular velocity curves of the payload module while the compound attitude maneuver and collision avoiding control proposed in this paper are adopted. It can be seen that the X-axis can realize the maneuver control with 30°/10 s. Meanwhile, the angular runout is less than 0.15°, and the angular velocity runout is less than 0.1°/s in the attitude maneuver process.

As shown in Figures 11 and 12, the relative attitude angle between the two modules is less than 0.3°, which is in the range of the small air clearance constraint of the noncontact Lorentz actuator. Meanwhile, the relative attitude angular velocity is less than 0.25°/s. Obviously, the cooperative control of the service module is convergent, suggesting that

Table 2: Controller performance comparison.

Indexes	PD method	Proposed method
Attitude maneuverability	Failed	30°/10s
Collision avoidance ability	Failed	Success
Convergence rate		
Attitude angle of payload module	25 s	10s
Angular velocity of payload module	25 s	10s
Relative attitude	≥35 s	30s
Relative angular velocity	≥35 s	30s
Runout of the other two axes		
Attitude angle of payload module	≥0.7°	≤0.15°
Angular velocity of payload module	≥1°	≤0.1°/s
Relative attitude	≥0.5°	≤0.4°
Relative angular velocity	≥0.5°/s	≤0.35°/s

the service module tracked the payload module very well in the attitude maneuver process without collision.

The above-mentioned experimental results clearly demonstrate that the compound controller with the variable-parameter sliding model control for payload module and disturbance observer-based feedforward compensation for service module can well realize attitude maneuver without collision within the small air clearance constraint of the noncontact Lorentz actuator. The comparison of the control performance of the two methods is shown in Table 2.

5. Conclusion

The noncontact close-proximity formation satellite has been successfully demonstrated for stability control. This paper extends its advantage into the attitude maneuver operation by using a compound control strategy with variable-parameter sliding mode control and disturbance observer-based feedforward compensation. The experimental verification results with the established physical air-floating platform show that the PD controller cannot be used to deform the attitude angle and angular velocity and the collision of the two modules would be occurred. The proposed compound control not only can be used to guarantee the attitude maneuver performance of the payload module but also can be used to guarantee the synchronization of the two separated modules within the small air clearance constraint of the noncontact Lorentz actuator.

Data Availability

No data files are available.

Conflicts of Interest

The author(s) declare(s) that they have no conflicts of interest.

Acknowledgments

This work was supported in part by the Fundamental Research Funds for the Key Program of Chinese Science and Technology Ministry (Grant Nos. 2020YFC2200502 and 2020YFC2200801), National Natural Science Foundation of China (41974034, 12172168, 41971412 and 42171341), Shanghai Rising-Star Program (21QA1408500), and Natural Science Foundation of Shanghai (19ZR1453300).

References

[1] F. Sanfedino, V. Preda, V. Pommier-Budinger, D. Alazard, F. Boquet, and S. Bennani, "Robust active mirror control based on hybrid sensing for spacecraft line-of-sight stabilization," *IEEE Transactions on Control Systems Technology*, vol. 29, no. 1, pp. 220–235, 2021.

[2] W. A. Wahballah, F. Eltohamy, and T. M. Bazan, "Influence of attitude parameters on image quality of very high-resolution satellite telescopes," *IEEE Transactions on Aerospace and Electronic Systems*, vol. 57, no. 2, pp. 1177–1183, 2020.

[3] B. A. Albassam, "Fast attitude maneuver of a flexible spacecraft with passive vibration control using shunted piezoelectric transducers," *International Journal of Aerospace Engineering*, vol. 2019, Article ID 3162105, 18 pages, 2019.

[4] E. M. Wang, S. N. Wu, G. B. Xun, Y. Liu, and Z. Wu, "Active vibration suppression for large space structure assembly: a distributed adaptive model predictive control approach," *Journal of Vibration and Control*, vol. 27, no. 5, pp. 1–13, 2021.

[5] L. Zhang, S. Xu, Z. Zhang, and N. Cui, "Active vibration suppression for flexible satellites using a novel component synthesis method," *Advances in Space Research*, vol. 67, no. 6, pp. 1968–1980, 2021.

[6] L. Li, L. Wang, L. Yuan et al., "Micro-vibration suppression methods and key technologies for high-precision space optical instruments," *Acta Astronautica*, vol. 180, pp. 1968–1980, 2020.

[7] Y. Yu, X. Meng, K. Li, and F. Xiong, "Robust control of flexible spacecraft during large-angle attitude maneuver," *Journal of Guidance, Control, and Dynamics*, vol. 37, no. 3, pp. 1027–1033, 2014.

[8] C. Zhong, Z. Chen, and Y. Guo, "Attitude control for flexible spacecraft with disturbance rejection," *IEEE Transactions on Aerospace and Electronic Systems*, vol. 53, no. 1, pp. 101–110, 2017.

[9] L. Tang and Z. Guo, "Integrated control and magnetic suspension for fast attitude maneuvering and stabilization," *IEEE Transactions on Aerospace and Electronic Systems*, vol. 55, no. 6, pp. 3273–3283, 2019.

[10] S. N. Wu, G. Radice, and Z. W. Sun, "Robust finite-time control for flexible spacecraft attitude maneuver," *Journal of Aerospace Engineering*, vol. 27, no. 1, pp. 185–190, 2014.

[11] Z. Y. Ni, S. N. Wu, Y. W. Zhang, and Z. Wu, "Payload parameter identification of a flexible space manipulator system via complex eigenvalue estimation," *International Journal of Aerospace Engineering*, vol. 2020, Article ID 5142925, 17 pages, 2020.

[12] A. Stabile, G. Aglietti, G. Richardson, and G. Smet, "Design and verification of a negative resistance electromagnetic shunt damper for spacecraft micro-vibration," *Journal of Sound and Vibration*, vol. 386, no. 6, pp. 38–49, 2017.

[13] N. Pedreiro, "Spacecraft architecture for disturbance-free payload," *Journal of Guidance, Control, and Dynamics*, vol. 26, no. 5, pp. 794–804, 2003.

[14] M. Gonzales, N. Pedreiro, K. Brookes, D. Roth, and B. Foster, "Unprecedented vibration isolation demonstration using the disturbance-free payload concept," in *AIAA Guidance, Navigation, and Control Conference and Exhibit*, Providence, Rhodel Island, August 2004.

[15] Y. Kong and H. Huang, "Performance enhancement of disturbance-free payload with a novel design of architecture and control," *Acta Astronautica*, vol. 159, pp. 238–249, 2019.

[16] C. Wu, X. Kong, Y. Liu, and Z. Chen, "Coupling characteristics analysis for the disturbance free payload spacecraft," *Acta Astronautica*, vol. 138, pp. 407–416, 2017.

[17] Y. Chen, H. Wen, and D. Jin, "Design and experiment of a noncontact electromagnetic vibration isolator with controllable stiffness," *Acta Astronautica*, vol. 168, pp. 130–137, 2020.

[18] D. Pan, S. Lin, L. Li et al., "Research on the design method of uniform magnetic field coil based on the MSR," *IEEE Transactions on Industrial Electronic*, vol. 67, no. 2, pp. 1348–1356, 2019.

[19] K. Tajdaran, L. Dewell, E. Eason et al., "Telescope line-of-sight slew control and agility with non-contact vibration isolation for the large ultraviolet/optical/infrared (LUVOIR) surveyor concept," in *Space Telescopes and Instrumentation 2018: Optical, Infrared, and Millimeter Wave*, Austin, Texas, July 2018.

[20] Y. F. Xu, H. Liao, L. Liu, and Y. Wang, "Modeling and robust H-infinite control of a novel non-contact ultra-quiet Stewart spacecraft," *Acta Astronautica*, vol. 107, pp. 274–289, 2015.

[21] H. Yang, L. Liu, H. Yun, and X. Li, "Modeling and collision avoidance control for the disturbance-free payload spacecraft," *Acta Astronautica*, vol. 164, pp. 415–424, 2019.

[22] Q. Li, L. Liu, Y. Deng, S. Tang, and Y. Zhao, "Twistor-based synchronous sliding mode control of spacecraft attitude and position," *Chinese Journal of Aeronautics*, vol. 31, no. 5, pp. 1153–1164, 2018.

[23] C. Sheng, Y. Zhang, Q. Hu, and J. Zhang, "Configuration design and collision avoidance control of an electromagnetic vibration isolation system on satellites considering environmental disturbances," *Acta Astronautica*, vol. 165, pp. 229–241, 2019.

[24] J. Zhou, Z. Wang, W. Li, L. Liu, Y. Deng, and Q. Zhao, "Modeling and pointing performance analysis of disturbance-free-payload system with flexible umbilical connection," *IEEE Access*, vol. 7, pp. 109565–109585, 2019.

[25] B. Farhad, "Model predictive sliding control for finite-time three-axis spacecraft attitude tracking," *IEEE Transactions on Industrial Electronics*, vol. 66, no. 10, pp. 7986–7996, 2019.

[26] C. Lu and X. Bing, "Exponential and resilient control for attitude tracking maneuvering of spacecraft with actuator uncertainties," *IEEE/ASME Transactions on Mechatronics*, vol. 24, no. 6, pp. 2531–2540, 2019.

[27] K. Song, B. Ma, G. Yang et al., "A rotation-lightweight wireless power transfer system for solar wing driving," *IEEE Transactions on Power Electronics*, vol. 34, no. 9, pp. 8816–8830, 2019.

[28] C. Wang, L. Guo, C. Wen, X. Yu, and J. Huang, "Attitude coordination control for spacecraft with disturbances and event-triggered communication," *IEEE Transactions on Aerospace and Electronic Systems*, vol. 57, no. 1, pp. 586–596, 2021.

[29] H. T. Li, S. Q. Zheng, and X. Ning, "Precise control for gimbal system of double gimbal control moment gyro based on cascade extended state observer," *IEEE Transactions on Industrial Electronics*, vol. 64, no. 6, pp. 4653–4661, 2017.

[30] X. Huang, W. Lin, and B. Yang, "Global finite-time stabilization of a class of uncertain nonlinear systems," *Automatica*, vol. 41, no. 5, pp. 881–888, 2005.

[31] R. Hamrah, R. R. Warier, and A. K. Sanyal, "Finite-time stable estimator for attitude motion in the presence of bias in angular velocity measurements," *Automatica*, vol. 132, no. 2, article 109815, 2021.

[32] Z. G. Han, M. H. Wang, X. L. Yan, and H. Qian, "Adaptive fixed-time nonsingular terminal sliding mode attitude tracking control for spacecraft with actuator saturations and faults," *International Journal of Aerospace Engineering*, vol. 2021, Article ID 8838784, 9 pages, 2021.

Hindawi
International Journal of Aerospace Engineering
Volume 2021, Article ID 1305095, 14 pages
https://doi.org/10.1155/2021/1305095

Research Article

Dual Quaternion Based Close Proximity Operation for In-Orbit Assembly via Model Predictive Control

Chuqi Sun, Yan Xiao, Zhaowei Sun, and Dong Ye

Research Center of Satellite Technology, Harbin Institute of Technology, Harbin 150001, China

Correspondence should be addressed to Zhaowei Sun; sunzhaowei@hit.edu.cn

Received 2 September 2021; Revised 15 October 2021; Accepted 20 October 2021; Published 12 November 2021

Academic Editor: Jiafu Liu

This paper studies the problem of guidance and control for autonomous in-orbit assembly. A six-degree-of-freedom (6-DOF) motion control for in-orbit assembly close proximity operation between a service satellite and a target satellite is addressed in detail. The dynamics based on dual quaternion are introduced to dispose the coupling effect between translation and rotation in a succinct frame, in which relevant perturbation and disturbance are involved. With the consideration of economical principle for fuel consume, a generic control system based on model predictive control (MPC) is then designed to generate a suboptimal control sequence for rendezvous trajectory considering actuator output saturation. The stability and robustness issues of the MPC-based control system are analyzed and proved. Numerical simulations are presented to demonstrate the effectiveness and robustness of the proposed control scheme, while additional comparisons for diverse horizons of the MPC are further conducted.

1. Introduction

As the renewal and progress of astronautic science and technology, regular scaled spacecraft could hardly satisfy the increasing demand to explore the universe. Confronting this challenge, on-orbit service was proposed and has been improved to target on constructing large space systems [1]. Lots of space missions such as Intelligent Building Blocks for On-Orbit Satellite Servicing (iBOSS) were investigated consecutively to develop a novel spacecraft structure which can be easily implemented by means of cubic modules in orbit [2], which is illustrated in Figure 1. Hence, the aid of in-orbit assembly, particularly relevant technologies on autonomous rendezvous and docking are crucial to ensure the success of such operations, namely, the guidance and control for proximity operations.

To implement a smooth proximity operation, one of the necessities is to take full consideration of attitude and orbit motions simultaneously, particularly the coupling characters in the 6-DOF dynamics [3]. Besides, orbit perturbation and other disturbances merit weighty attention which could bring barrier to maneuver accuracy. With all these factors taken into consideration, a compact model for controller design is necessary.

Another core of such missions is to design a reliable, economically viable control algorithm. Nowadays, control theories and technologies have been developed with higher potential to incorporate cutting edge algorithms. Engineers in many industrial fields are more inclined to apply robust and transparent control process to target plant with simple controllers, and this is also the main reason that the PID controller can remain the wide popularity compared with the extensive development of other advanced control methodologies [4]. Yet, it is generally acknowledged that PID controller has limitation in performance adjustment and constraint accommodation [5, 6]. From control performance perspective, the method of MPC is superior to the PID method when targeting on optimality, especially when control objective constraints are involved. Besides, practically control instructions may not response to the control instructions immediately. This effect of delay will cause overshoot problem for PID controller design. However, MPC is capable of handling this problem via prediction process. The method of MPC was proposed in 1960s and has been

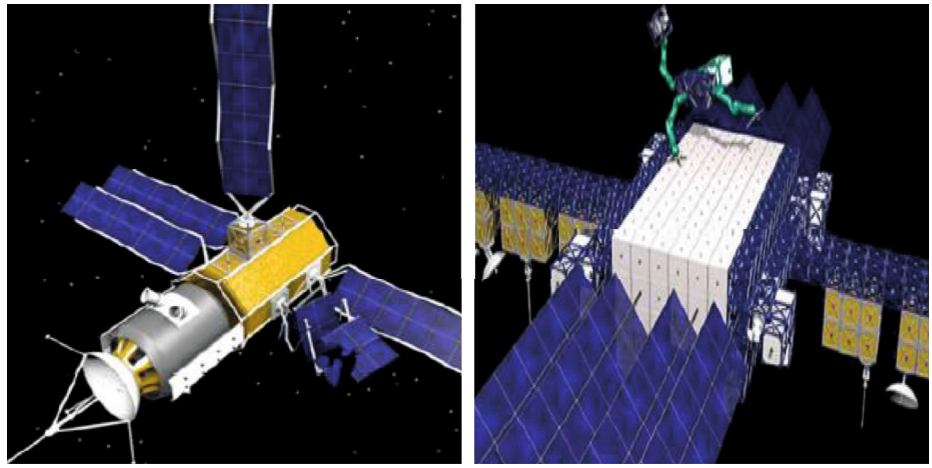

Figure 1: Solar array and platform extension of iBoss through in-orbit assembly.

popularized in various industrial process and products, particularly in autopilot vehicles [7–10]. Inspired by such motivation, this research attempts to design a MPC for spacecraft proximity operation using a compact model, while considering disturbances and maneuver capability during the in-orbit assembly operation.

As for proximity operation, previous works examined the relative motion by isolating the orbit motion and the attitude motion [11, 12]. This technique of "divide and conquer" neglects the coupling influence between the translation and the rotation. Some works established simultaneous equations of translational and rotational motion to fix this deficiency [13]. For instance, Sun et al. designed adaptive robust controllers concerning the coupling effects and model uncertainties based on such nonlinear dynamics [14]. However, this type of dynamics indicates a mathematical representation of the superimposed motion lacking of an explicit physical meaning.

This paper takes advantages of dual quaternion for modeling based on the screw theory [15] associating with a geometric entity by involving combined position and attitude intrinsically to describe a 6-DOF motion in a compact form. Recent evidence has suggested that dual quaternion applied to robotics and satellite sheds new light on 6-DOF motion modeling for state control and estimation [16, 17]. Xza et al. designed an adaptive iterative learning control for flexible spacecraft rendezvous for a noncooperative tumbling target [18]. Sun et al. examined a dual quaternion-based model for electromagnetic collocated satellites for diffraction imaging missions [19]. Furthermore, another similar mathematical representation, Special Euclidean group SE(3), can be also applied to formulate the coupled dynamics. Related works including Zhang et al. investigated a robust adaptive control method with the aid of exponential coordinates on Lie group SE(3) [20]. Peng et al. studied a predictor-based pose stabilization control for unmanned vehicles on SE(3) considering actuator delay and saturation [21]. Wang et al. designed a consensus extended Kalman filter to estimate the motion of a rigid body in a communicate network utilizing SE(3) dynamics [22]. This type of description is essentially the homogeneous matrix of unit dual quaternion [23].

From control theory perspective, massive literature has made achievements for spacecraft pose maneuver. Many works aiming at optimizing pose maneuver trajectory were mostly covered in the frame of optimal control theory. However, most relevant research wanted to find a global optimal solution which is unnecessary in the entire process for practical use [24]. The common solutions for optimal control theory can be approximately inducted by variation method [25], maximum principle [26], and dynamic programming [27]. Under normal circumstances, the variation method and maximum principle are easier to handle linear model without complex constraints. While dynamic programming based on the Bellman optimality principle has become a fundamental core of many intelligent algorithms such as neural network, reinforced learning, and the quadratic programming in the MPC optimization [28, 29]. It should be noted that another optimal control method, linear quadratic regulator (LQR), has the similar structure with MPC. The main difference between LQR and MPC is that the optimized control output is solved in a fixed time window, while MPC calculates the feasible control in a receding time horizon. In other words, LQR is an offline control method whereas MPC is an online control method. The characteristic of MPC has a better performance for a system with external disturbance and constraints. In literature [30], the advantage and disadvantage of MPC have been discussed compared with LQR for a pursuit maneuvering situation. As a state-of-art control method, MPC is designed to solve complex multivariable optimal control problem with constraints. Compared with typical robust control and adaptive control, MPC does not excessively rely on the precision of system model, and MPC can be utilized to dispose various control schemes according to the model dynamics. The proposed work outlines MPC as a general prospective method, which settles for optimal/suboptimal solution in the prediction horizon to balance the optimality and practicability.

Contributions in this paper are threefold. First, the dual quaternion is involved to model the translation and rotation

simultaneously, which can pave the way for the controller. Second, considering actuator output constraints and external disturbance and perturbation, a model predictive controller is designed to track a set-point reference trajectory. Additionally, we discuss the influences of different horizons of the prediction and control for the controller performance through numerical simulation. The rest of the paper is organized as follows. Section 2 devotes mathematical preliminaries of quaternion and dual quaternion. Section 3 establishes the dynamics in the framework of dual quaternion for the proximity operation. Section 4 gives detailed MPC design process and then address the stability proof and robustness analysis. Section 5 presents the simulation results to verify the effectiveness of the proposed control scheme, followed by the conclusion of this work in Section 6.

2. Mathematical Preliminaries

As a preliminary of this work, we concisely present relevant physical concepts and mathematical rules of quaternion and dual quaternion. Readers can also refer to literature [31] for more details.

2.1. Quaternion. Quaternion is a hypercomplex number to space $\mathbb{R}^4$.which is defined as the following:

$$q = q_0 + q_1 i + q_2 j + q_3 k, \tag{1}$$

where the imaginary units follow:

$$ij = -ji = k, jk = -kj = i, ki = -ik = j, i^2 = j^2 = k^2 = -1. \tag{2}$$

Such description also indicates as a combination of scalar and vector components, which can be expressed as $q = [q_0\ q_1\ q_2\ q_3]^T = [\,q_s \quad q_v\,]^T$. From physical perspective, the quaternion is used to define a spatial rotation transformation of a coordinate frame in three dimensions constructed as:

$$\begin{aligned} q &= \left[\cos\left(\frac{\theta}{2}\right) \quad n\sin\left(\frac{\theta}{2}\right)\right]^T \\ &= \left[\cos\left(\frac{\theta}{2}\right) \quad n_x\sin\left(\frac{\theta}{2}\right) \quad n_y\sin\left(\frac{\theta}{2}\right) \quad n_z\sin\left(\frac{\theta}{2}\right)\right]^T, \end{aligned} \tag{3}$$

with θ being the Euler angle and n being the unit Euler axis. This definition denotes a unit quaternion as well, which has the following conjugation and norm properties:

$$\begin{aligned} q^* &= [\,q_s \quad -q_v\,]^T, \\ q^{-1} &= q^*, \\ \|q\| &= \sqrt{q\cdot q} = \sqrt{q\circ q^*} = \sqrt{q^*\circ q} = 1. \end{aligned} \tag{4}$$

Specially, the identity quaternion is addressed as $q_I = [1, 0, 0, 0]^T$, which is a significant denotation for error attitude.

The basic quaternion operations are implemented as follows:

Addition:

$$q_1 + q_2 = \left[\,q_{s_1} + q_{s_2} \quad q_{v_1} + q_{v_2}\,\right]^T. \tag{5}$$

Multiplication:

$$q_1 \circ q_2 = \left[q_{s_1}q_{s_2} - q_{v_1}\cdot q_{v_2}, q_{s_1}q_{v_2} + q_{s_2}q_{v_1} + q_{v_1}\times q_{v_2}\right]^T. \tag{6}$$

It can also be represented in matrix form as:

$$q_1 \circ q_2 = \begin{bmatrix} q_{s_1} & -q_{v_1} \\ {q_{v_1}}^T & \left[q_{v_1}\right]^{\otimes} + q_{s_1}I_3 \end{bmatrix}\begin{bmatrix} q_{s_2} \\ q_{v_2} \end{bmatrix} = q_1^{[\circ]}q_2, \tag{7}$$

where $[\cdot]^{[\otimes]}$ denotes the cross product operator defined as:

$$a^{\otimes} = \begin{bmatrix} 0 & -a_3 & a_2 \\ a_3 & 0 & -a_1 \\ -a_2 & a_1 & 0 \end{bmatrix}. \tag{8}$$

Quaternion cross products:

$$q_1 \times q_2 = \left[0, q_{s_1}q_{v_2} + q_{v_1}q_{s_2} + q_{v_1}\times q_{v_2}\right]^T. \tag{9}$$

Similar, can also be represented in matrix form as:

$$q_1 \times q_2 = \begin{bmatrix} 0 & 0_{1\times 3} \\ {q_{v_1}}^T & \left[q_{v_1}\right]^{\otimes} + q_{s_1}I_3 \end{bmatrix}\begin{bmatrix} q_{s_2} \\ q_{v_2} \end{bmatrix} = q_1^{[\times]}q_2. \tag{10}$$

2.2. Dual Quaternion. Before defining dual quaternion, it is necessary to introduce dual number. Similar to complex numbers, dual numbers consist of real and dual parts denoted as:

$$z = a + \varepsilon b, \text{ where } \quad \varepsilon^2 = 0, \varepsilon \neq 0. \tag{11}$$

In terms of Clifford algebra, dual quaternion fills the real and dual part with two quaternions denoted as:

$$\hat{q} = q_1 + \varepsilon q_2 = \left[\,{q_r}^T \quad {q_d}^T\,\right]^T. \tag{12}$$

Dual quaternion has a physical interpretation according to Chasles' theorem [32], and a rigid body displacement can be seen as a screw motion containing both translation and rotation in the hereunder description:

$$\hat{q} = \left[\cos\left(\frac{\theta\wedge}{2}\right) \quad \sin\left(\frac{\theta\wedge}{2}\right)n\wedge\right]^T, \tag{13}$$

in which $\hat{n} = n + \varepsilon(p\times n)$ is the screw axis, p is a vector

vertical to n. $\widehat{\theta} = \theta + \varepsilon(d)$ is the dual angle, where d is the pitch representing translation, θ representing rotation.

Referring back to quaternion, dual quaternion has similar properties to quaternion. First, we briefly address the dual quaternion basic operation.

Addition:

$$\widehat{q}_1 + \widehat{q}_2 = \left[{q_{r_1}}^T + {q_{r_2}}^T, {q_{d_1}}^T + {q_{d_2}}^T \right]^T. \tag{14}$$

Multiplication:

$$\widehat{q}_1 \odot \widehat{q}_2 = \left[q_{r_1} \circ q_{r_2}, q_{r_1} \circ q_{d_2} + q_{d_2} \circ q_{r_2} \right]^T. \tag{15}$$

It can be represented in matrix multiplication in conformance with quaternion multiplication:

$$\widehat{q}_1 \odot \widehat{q}_2 = \begin{bmatrix} q_{r_1}^{[\circ]} & 0_{4\times4} \\ q_{r_2}^{[\circ]} & q_{r_1}^{[\circ]} \end{bmatrix} \begin{bmatrix} q_{r_2} \\ q_{d_2} \end{bmatrix} = \widehat{q}_1^{[\odot]} \widehat{q}_2. \tag{16}$$

Cross product:

$$\widehat{q}_1 \otimes \widehat{q}_2 = \left[q_{r_1} \times q_{r_2}, q_{r_1} \times q_{d_2} + q_{d_2} \times q_{r_2} \right]^T. \tag{17}$$

Similar,

$$\widehat{q}_1 \otimes \widehat{q}_2 = \begin{bmatrix} q_{r_1}^{[\times]} & 0_{4\times4} \\ q_{r_2}^{[\times]} & q_{r_1}^{[\times]} \end{bmatrix} \begin{bmatrix} q_{r_2} \\ q_{d_2} \end{bmatrix} = \widehat{q}_1^{[\otimes]} \widehat{q}_2. \tag{18}$$

The conjugation and norm of a dual quaternion denote as:

$$\begin{aligned} q\wedge^* &= \begin{bmatrix} q_r^{*T} & q_d^{*T} \end{bmatrix}^T, \\ \|\widehat{q}\| &= \sqrt{\widehat{q} \odot q\wedge^*}, \end{aligned} \tag{19}$$

when $\|\widehat{q}\| = 1$, it is defined as unit dual quaternion which usually denotes as $\widehat{q}_I = \begin{bmatrix} q_I^T & 0_{1\times4} \end{bmatrix}^T$.

3. System Kinematics and Dynamics

In the first place, it is necessary to introduce the operation to be implemented and the necessary coordinate frames. The mission is assumed that the service spacecraft will maneuver to the target spacecraft in a set pose. Throughout this paper, 2 coordinate frames are shown in Figure 2 defined as:

Earth Centered Inertial (ECI) frame $O - X_I Y_I Z_I$: this frame is a nonaccelerating frame originated at the center of the Earth. Its X_I axis points to the vernal, and the Z_I axis points to the north parallel to the Earth rotation axis. Y_I is given by the right-hand rule.

Spacecraft Body Frame for service and target spacecraft $O - X_S Y_S Z_S$ and $O - X_T Y_T Z_T$: the center is located at the center of the mass. The other 3 axes of the frame are fixed

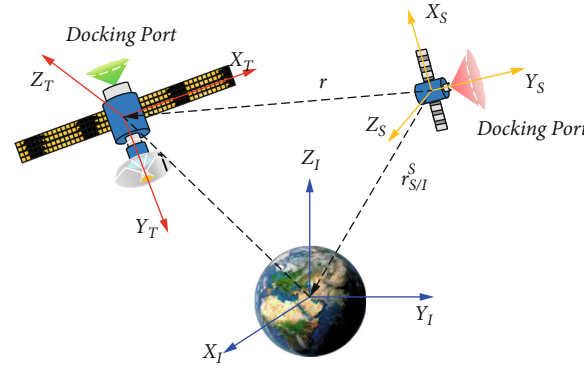

Figure 2: Depiction of in-orbit assembly and coordinate frames.

to the body and aligned to the principle axes of the spacecraft.

Suppose the service spacecraft implements a pose maneuver to the target spacecraft between frame $O - X_S Y_S Z_S$ and frame $O - X_T Y_T Z_T$. The aftermentioned subscripts indicate the frames, respectively. It can be represented by a dual quaternion containing a rotation q and a translation r as follows:

$$\widehat{q} = \begin{bmatrix} q \\ \dfrac{1}{2} q \circ r \end{bmatrix}. \tag{20}$$

The translation vector r represented in two frames has the coordinate transformation relation $r_T = q^* \circ r_S \circ q$, where the 3D translation vector r_S extends to a quaternion form as $r_S = [0, r_{S_x}, r_{S_y}, r_{S_z}]^T$. Particularly, this transformation is applied in the latter definition of dual velocity twist and dual force for dual quaternion dynamic modeling.

The kinematic equation is given as:

$$\dot{\widehat{q}} = \frac{1}{2} \widehat{q} \odot \widehat{\omega}, \tag{21}$$

in which $\widehat{\omega} = [\omega_T, v_T]^T$ is the dual velocity twist defined by angular velocity and translational velocity in the target frame.

As for the dynamic equation, it is given as:

$$\widehat{J} \odot \dot{\widehat{\omega}} + \widehat{\omega} \otimes \widehat{J} \widehat{\omega} = \widehat{F}, \tag{22}$$

in which the dual force $\widehat{F} = [f, \tau]^T$ represents the external forces f and torques τ. The dual inertia matrix is denoted as:

$$\widehat{J} = \begin{bmatrix} 0_{3\times3} & 0 & 1 & 0 \\ 0 & 0 & 0 & mI_3 \\ 0 & 1 & 0 & 0 \\ J & 0 & 0_{3\times3} & 0 \end{bmatrix}. \tag{23}$$

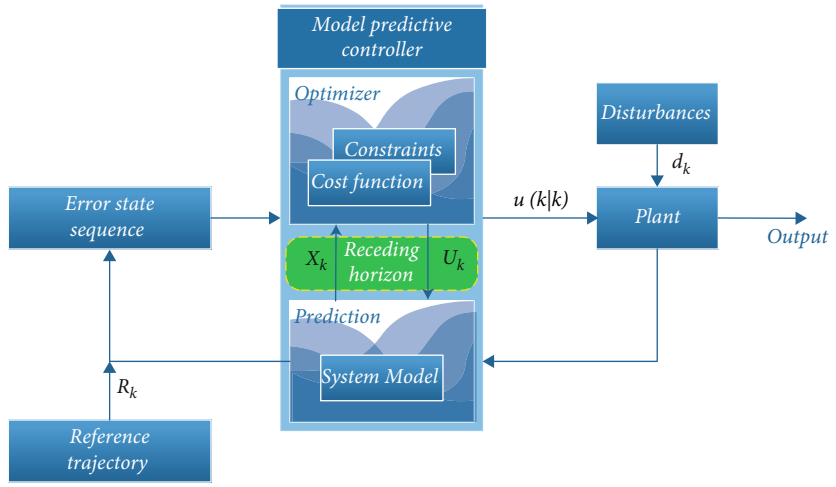

Figure 3: Basic framework of MPC.

In this dynamic equation, the total dual force includes dual control force, dual force J_2 by spherical harmonic perturbation, two-body gravity, gravity gradient torque, and disturbance described as:

$$\hat{F} = \hat{f}_u + \hat{f}_{J_2} + \hat{f}_g + \hat{f}_{\nabla g} + \hat{f}_d, \tag{24}$$

where the dual forces due to spherical harmonic perturbation, two-body gravitation, and gravity gradient are obtained by:

$$\hat{f}_g = \begin{bmatrix} -\dfrac{\mu m r^S_{S/I}}{\left\| r^S_{S/I} \right\|^3} & 0_{1\times 4} \end{bmatrix}^T,$$

$$\hat{f}_{\nabla g} = \begin{bmatrix} 0_{1\times 4} & 3\mu \dfrac{r^S_{S/I} \times J r^S_{S/I}}{\left\| r^S_{S/I} \right\|^5} \end{bmatrix}^T,$$

$$\hat{f}_{J_2} = \frac{3\mu J_2 R_e^2}{2\left\| r^S_{S/I} \right\|^5} \begin{bmatrix} 0 \\ \left(1 - 5\left(\dfrac{r^S_{S_z/I}}{\left\| r^S_{S/I} \right\|}\right)^2\right) r^S_{S_x/I} \\ \left(1 - 5\left(\dfrac{r^S_{S_z/I}}{\left\| r^S_{S/I} \right\|}\right)^2\right) r^S_{S_y/I} \\ \left(3 - 5\left(\dfrac{r^S_{S_z/I}}{\left\| r^S_{S/I} \right\|}\right)^2\right) r^S_{S_z/I} \\ 0_{1\times 4} \end{bmatrix}, \tag{25}$$

where the $r^S_{S/I}$ is the position vector represented in the ECI. R_e is the radius of the Earth. J_2 is the index of harmonic terms.

Remark 1. Other additional forces and torques such as atmospheric drag, solar drag disturbances are not included owing to the short operation period of time. Besides, according to the previous work in literature [33–36], the gravitation and J_2 perturbation have minimal impacts on orbit maneuver. Hence, the aforementioned disturbances can be approximatively taken as a sum of bounded disturbances exerted on the state in terms of a proper magnitude order, and this setting is also convenient for latter controller design.

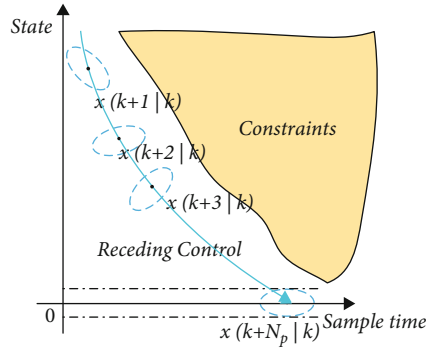

Figure 4: Illustration of receding control approach.

4. Model Predictive Controller Design

In this section, based on the spacecraft dual quaternion dynamics indicated previously, we take advantage of the relevant matrix operator of dual quaternion and forward Euler method to represent a time-varying state space model for MPC design. The structure of model predictive controller for dual quaternion nonlinear system comprises discretization, prediction, and optimization. The schematic is depicted in Figure 3.

Due to the strong nonlinearity of dual quaternion dynamics, it is common to make an approximate linearization by first order Taylor expansion in a sampling period Δt to obtain a discrete state space model as:

$$\begin{aligned} \frac{\hat{\omega}(t+1) - \hat{\omega}(t)}{\Delta t} &= J\Lambda^{-1}\left(-\hat{\omega}(t)^{[\otimes]} J \hat{\omega}(t)\right) + \hat{F}(t), \\ \frac{\hat{q}(t+1) - \hat{q}(t)}{\Delta t} &= \frac{1}{2}\hat{q}(t)^{[\odot]}\hat{\omega}(t+1). \end{aligned} \tag{26}$$

Table 1: Orbit parameters of chaser satellite.

Parameters	Major semi-axis	Eccentricity	Inclination	RAAN	Argument of perigee	True anomaly
Values	6998455 (m)	0.02	45 (deg)	0	0	30 (deg)

To guarantee the controllability, choose the state variable as $x = [\omega\wedge, q\wedge]^T$ and control input as $u(t) = \widehat{F}(t)$. Thus, we can get a concise discrete formula as:

$$x(k+1) = A_t x(k) + B_t u(k), \tag{27}$$

where

$$A = \begin{bmatrix} I_{8\times 8} - J\wedge^{-1}\Delta t\omega\wedge^{[\otimes]}\widehat{J} & 0_{8\times 8} \\ \frac{1}{2}\Delta t q\wedge^{[\odot]} & I_{8\times 8} \end{bmatrix}, B = \begin{bmatrix} \Delta t I_{8\times 8} \\ 0_{8\times 8} \end{bmatrix}. \tag{28}$$

Next, according to the initial state and control, the state information in p sampling instants for prediction can be recurred due to the discrete model as:

$$x(k+p \mid k) = A_t^p x(k) + \sum_{i=0}^{p-1} A_t^{p-1-i} B_t u(k+i \mid k). \tag{29}$$

Given the convenience for latter optimization, denote the state and control input as:

$$\begin{aligned} X_k &= \left[x(k+1 \mid k)^T \quad x(k+2 \mid k)^T \quad \cdots \quad x(k+p \mid k)^T \right]^T, \\ U_k &= \left[u(k \mid k)^T \quad u(k+1 \mid k)^T \quad \cdots \quad u(k+p-1 \mid k)^T \right]^T. \end{aligned} \tag{30}$$

We can obtain a new matrix form for prediction:

$$X_k = \Psi x(k) + \Theta U_k, \tag{31}$$

where Q, R are positive constant diagonal matrices. The cost function can be deduced into a quadratic form for optimization as

$$\begin{aligned} \min J(U_k) &= (X_k - R_k)^T Q(X_k - R_k) + U_k^T R U_k \\ &= (\Psi x(k) - R_k + \Theta U_k)^T Q(\Psi x(k) - R_k + \Theta U_k) \\ &\quad + U_k^T R U_k = (E + \Theta U_k)^T Q(E + \Theta U_k) + U_k^T R U_k \\ &= U_k^T \left(\Theta^T Q\Theta + R\right) U_k + 2E^T Q\Theta U_k + E^T QE. \end{aligned} \tag{32}$$

Hence, the close-loop system converts to a quadratic programming problem

$$\min_{U_k} J\left(x_{(t|0)}, u(t)\right). \tag{33}$$

Table 2: Initial values in simulation.

Parameters	Values
Mass	100kg
Moment of inertia	diag $(19.2, 17, 20)\mathrm{kg}\cdot\mathrm{m}^2$
Initial error attitude	$[0.3772, -0.4329, 0.6645, 0.4783]^T$
Initial error position	$[0, -100, 0]^T (m)$
Initial error velocity	$[0, 0, 0]^T (m/s)$
Initial error angular velocity	$[0, 0, 0]^T (\mathrm{rad}/s)$

Table 3: MPC system set.

Parameters	Values
Sampling period	$0.1s$
Predicting horizon	$6 * Ts$
Control horizon	$1 * Ts$
Thrust bound	$\lvert F_x\rvert, \lvert F_y\rvert, \lvert F_z\rvert \le 10(N)$
Torque bound	$\lvert\tau_x\rvert, \lvert\tau_y\rvert, \lvert\tau_z\rvert \le 0.1(N\cdot m)$
Q	diag $(1, 1, 1, 1, 1, 1, 1, 1, 1, 1, 1, 1, 1, 1, 1, 1)$
R	diag $(1, 1, 1, 1, 1, 1)$

Subject to:

$$\begin{aligned} \widehat{J}\odot\dot{\widehat{\omega}} + \widehat{\omega}\otimes\widehat{J}\widehat{\omega} &= \widehat{F}, \\ \dot{\widehat{q}} &= \frac{1}{2}\widehat{q}\odot\widehat{\omega}, \\ \|\tau_i\| &\le \tau_{\max}, i = 1, 2, 3, \\ \|f_i\| &\le f_{\max}, i = 1, 2, 3, \\ x_{(t|0)} &= [q\wedge(0), \omega\wedge(0)]^T = [q\wedge_0, \omega\wedge_0]^T. \end{aligned} \tag{34}$$

4.1. Stability Analysis. Model predictive control is established using the principle of receding horizon control [37], in which the future control trajectory is optimized at each sample time by minimizing cost function subject to constraints. In this section, we elaborate the stability and robustness in two parts. First, we have to address necessary assumption for the proof.

Assumption 2. The terminal state of the receding horizon optimization can be seen as an additional constraint of $x(k + N_p \mid k) = 0$ resulting from the control sequence$\Delta u(k+m), m = 0, 1, 2, \cdots, N_p$.

Assumption 3. There exists an optimal solution to the cost function for each sampling instant in which the cost function is minimized subject to the constraints.

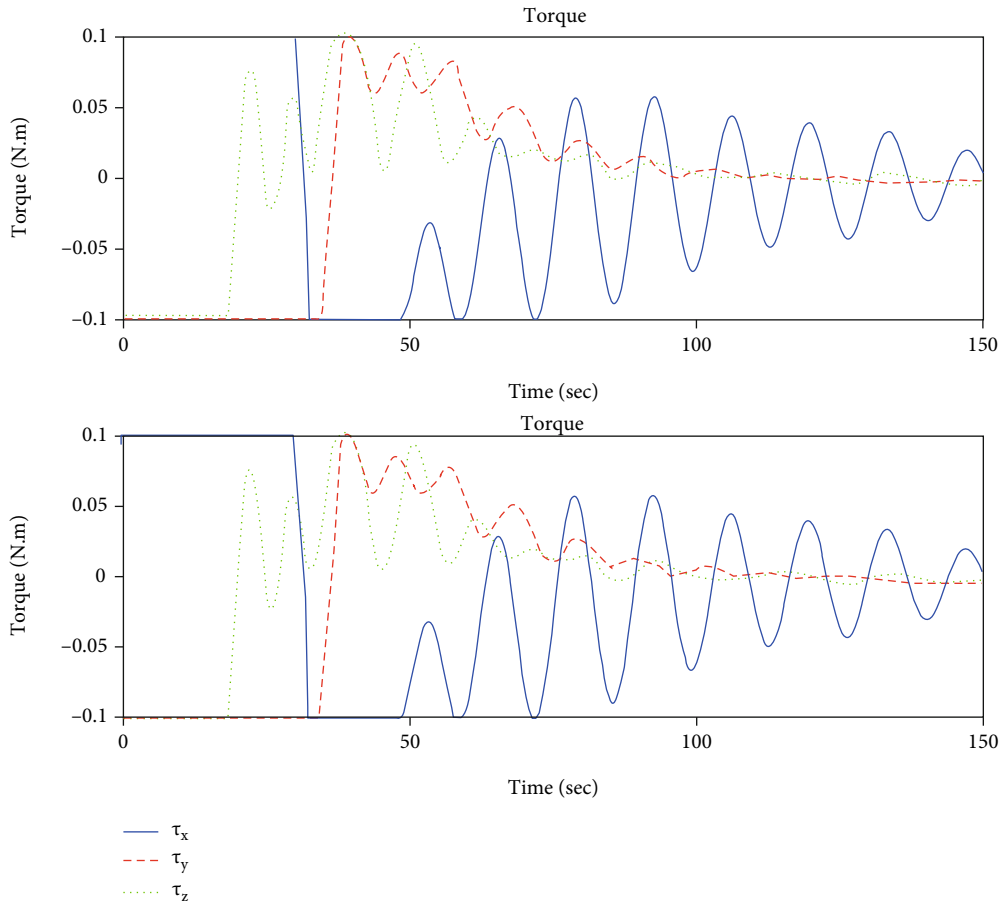

Figure 5: Time histories of control forces and torques expressed in the body-fixed frame.

Strictly based on the assumptions, the closed loop MPC system is asymptotically stable.

Proof. Consider the system without disturbance and perturbation. Unlike continuous system, the Lyapunov function for discrete system herein can be chosen as the minimum of the finite horizon cost function at each sampling instant. At time k, it can be denoted as:

$$V(x(k),k) = \sum_{m=1}^{N_p} x(k+m\mid k)^T Q x(k+m\mid k) + \sum_{m=0}^{N_p-1} \Delta u(k+m)^T R \Delta u(k+m). \tag{35}$$

Namely, $V(X(k),k) = J_{\min}$. It is obvious that $V(x(k),k)$ tends to infinity when $x(k)$ tends to infinity. Similar, at time $k+1$, the Lyapunov function becomes

$$V(x(k+1),k+1) = \sum_{m=1}^{N_p} x(k+m+1\mid k+1)^T Q x(k+m+1\mid k+1) + \sum_{m=0}^{N_p-1} \Delta u(k+m+1)^T R \Delta u(k+m+1). \tag{36}$$

Recall the relationship between the state on time k and $k+1$

$$x(k+1) = Ax(k) + B\Delta u(k), \tag{37}$$

which means the state of time $k+1$ is driven by the previous recursive relation. Particularly, according to Assumption 3 and the Lyapunov function designed, the optimality is guaranteed by the optimization at every single instant. Hence, we have

$$V(x(k+1),k+1) \le \bar{V}(x(k+1),k+1), \tag{38}$$

where the $\bar{V}(X(k+1),k+1)$ uses the feasible control sequence $\Delta u(k)$ for state update for the sample time $k+1$, $k+2,\cdots,k+N_p-1$. It is noticeable the $\bar{V}(x(k+1),k+1)$ and $V(x(k),k)$ share the same state sequence as well. Thus, we have

$$V(x(k+1),k+1) - V(x(k),k) \le \bar{V}(x(k+1),k+1) - V(x(k),k). \tag{39}$$

The right hand part of the unequal sign can be expanded as:

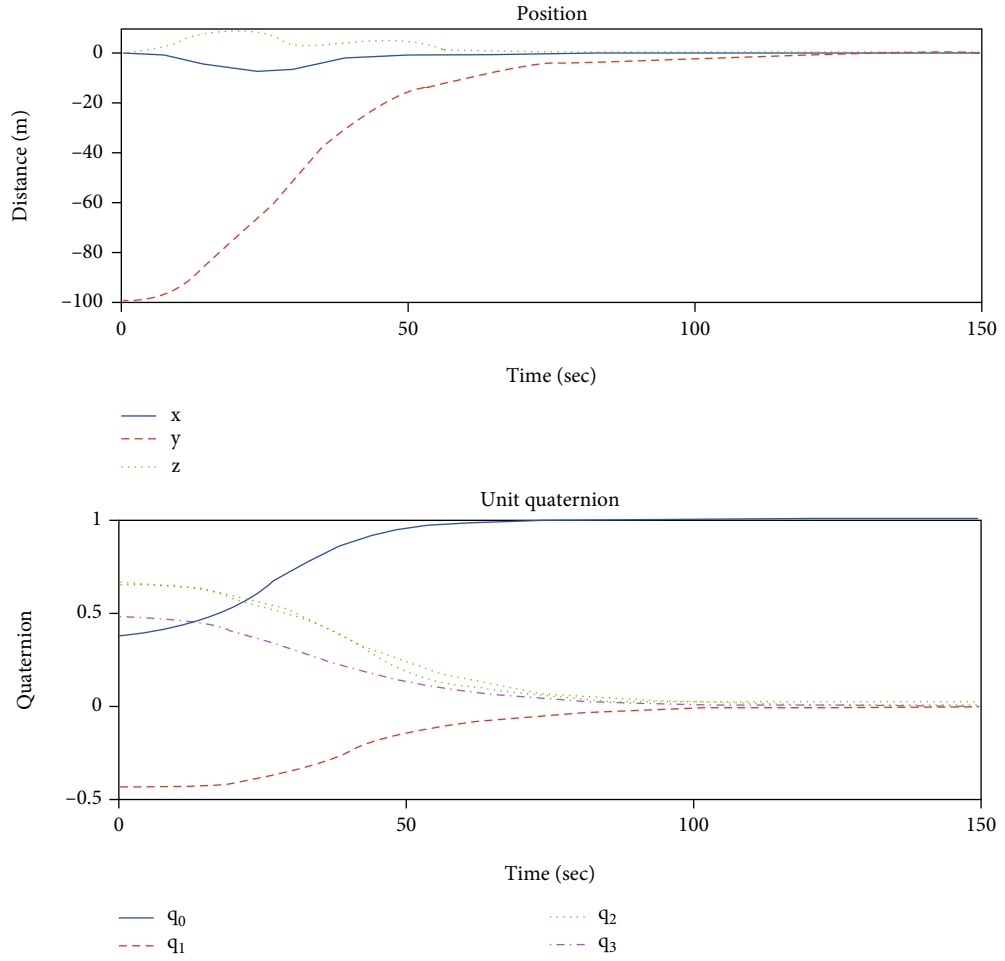

Figure 6: Time histories for the position and attitude of chaser satellite in target body fixed frame.

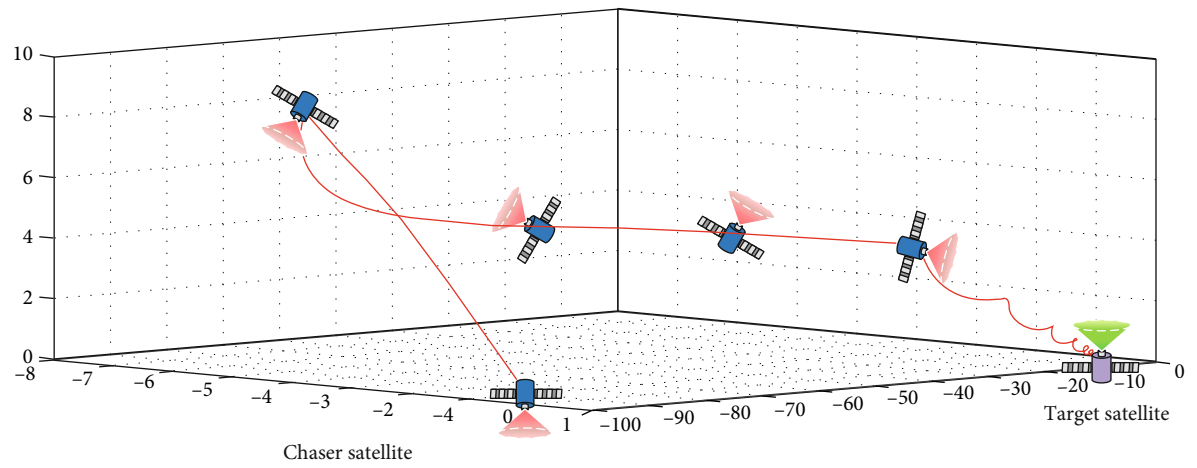

Figure 7: 3-D overall trajectory of close proximity maneuver via MPC.

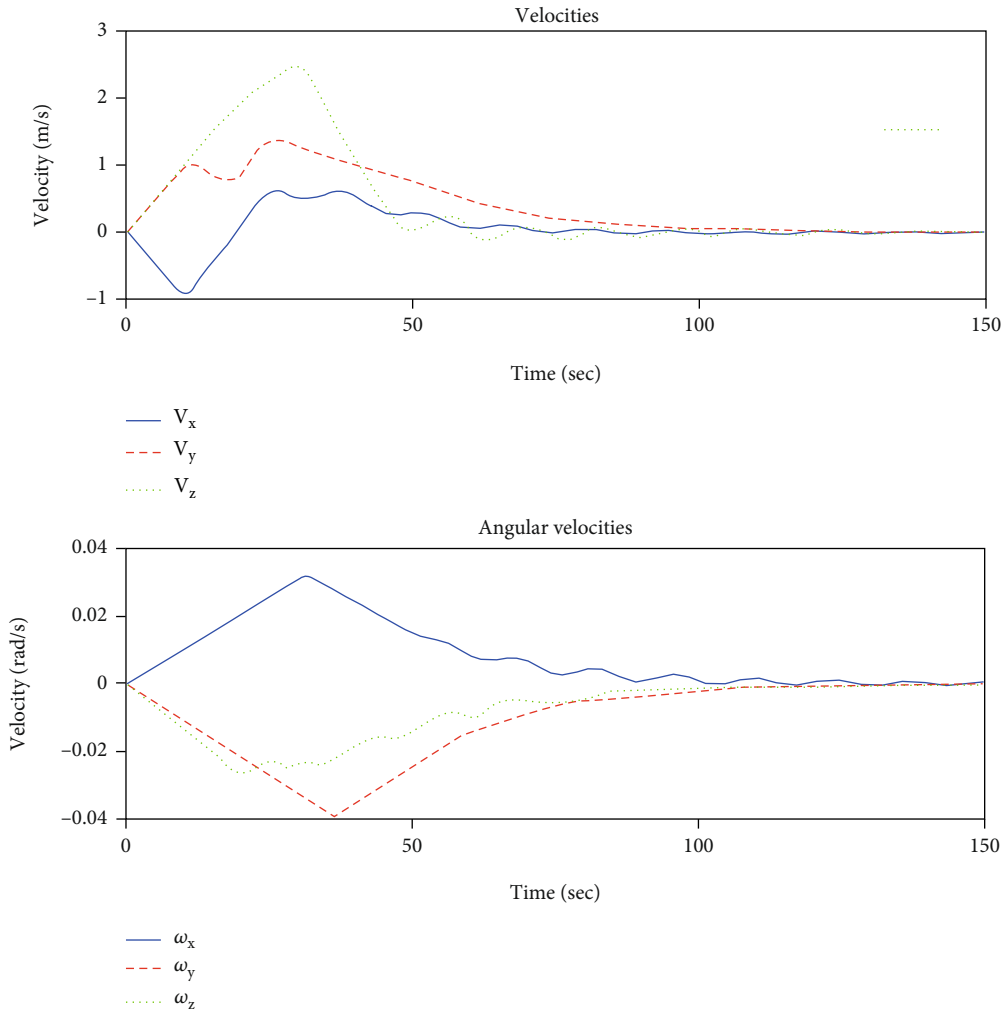

Figure 8: Time histories for the translational and rotational velocities in the body fixed frame.

$$\bar{V}(x(k+1),k+1) - V(x(k),k) = x(k+N_p \mid k)^T Q x(k+N_p \mid k) - x(k+1)^T Q x(k+1) - \Delta u(k)^T R \Delta u(k). \tag{40}$$

In terms of Assumption 2, it can be easily obtained:

$$\bar{V}(x(k+1),k+1) - V(x(k),k) = -x(k+1)^T Q x(k+1) - \Delta u(k)^T R \Delta u(k) < 0. \tag{41}$$

Hence, the asymptotic stability of the MPC is proved.□ □

Remark 4. The attitude part in the set point of reference state denotes as $[1 \quad 0 \quad 0 \quad 0]^T$, which is not a strictly mathematical defined "zero." From physical perspective, this definition has the physical meaning of zero error Euler angle, which will not disobey Assumption 2 mentioned above.

Table 4: Cost comparison according to the prediction horizons.

Prediction horizons	Translational cost	Rotational cost	Convergence time
$6 * Ts$	949.9	12.34	129
$7 * Ts$	886.8	11.7	125
$8 * Ts$	875.4	13.61	137
$9 * Ts$	904.4	15.29	143
$10 * Ts$	967.9	16.85	148
$11 * Ts$	1045	18.21	152
$12 * Ts$	1107	20.81	158
$15 * Ts$	1225	30.65	214

Remark 5. Assumption 3, this precondition holds water if and only if the optimal problem of solving the cost function can be described as a convex one including all the constraints. Otherwise, the stability may not be guaranteed on account of the local convergence or the overconstrainted issue [38].

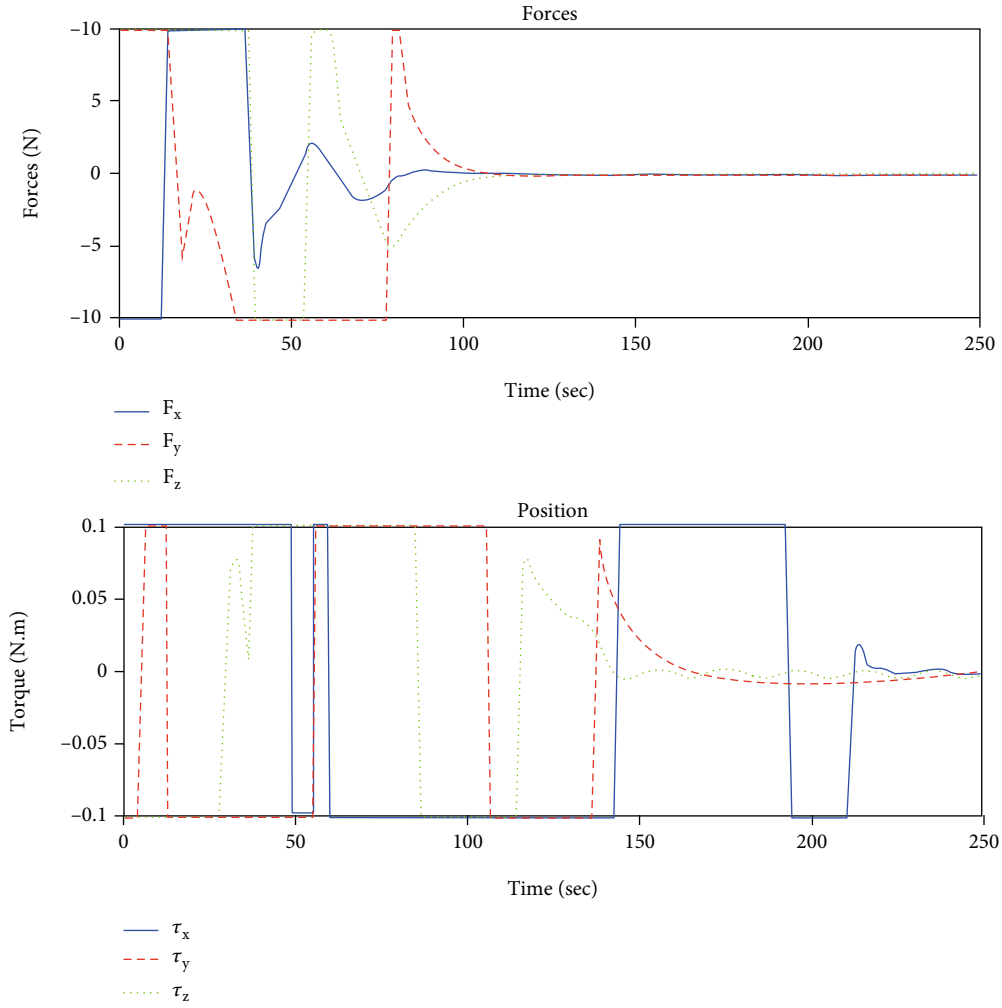

Figure 9: Time histories of control forces and torques expressed in the body-fixed frame with the prediction of 15 sampling instances.

4.2. Robustness Analysis. Robustness analysis requires the following assumptions:

Assumption 6. All the system states can be observed.

Assumption 7. The 2-norm of system disturbance is bounded, denoting as $\|d_k\|_2 \leq \bar{D}$.

Consider the discrete system with disturbance as:

$$x(k+1) = f(x(k), u_k, d_k). \tag{42}$$

According to equation (22) and Remark 1, the state $x(k+1)$ can be specified as a domain which is centered in the undisturbed state with a varying radius of the norm of disturbances, defined by:

$$\aleph_k = \left\{ \tilde{x}(k) \mid \tilde{x}(k)^T \rho_k^{-2} \tilde{x}(k) \leq 1 \right\}, \tag{43}$$

where ρ_k is a positive definite diagonal matrix representing the multidimensional radiuses. Take a single component of the input as an example illustrated in Figure 4, in the receding process the state space function can be rewritten based on equation (27) as:

$$\tilde{x}(k+1) = A\tilde{x}(k) + B\Delta v(k). \tag{44}$$

Then, this approach is similar to the stability proved. However, the system is not able to be stable on origin but converged into a neighborhood of origin, which satisfying the condition of robust control invariant set (RCIS): $\forall x \in \Omega, \exists u \in U$, if it makes $f(x,u) + d \in \Omega$ when $\forall d \in D$, both X and U are compact and convex.

Remark 8. The robustness analysis extremely relies on the Assumption 3 in the stability analysis. Except for the constraints, the condition for an optimal solution likewise depends on the prediction horizon when the origin system may not find a solution if the prediction horizon keeps maintaining, in which case the optimization has to reduce the predicting intervals [39].

Additionally, the robustness explanation points at the MPC in this work have the capability to resist disturbances to some extent, which is not targeting on a robust MPC for a higher order of magnitude of system interference.

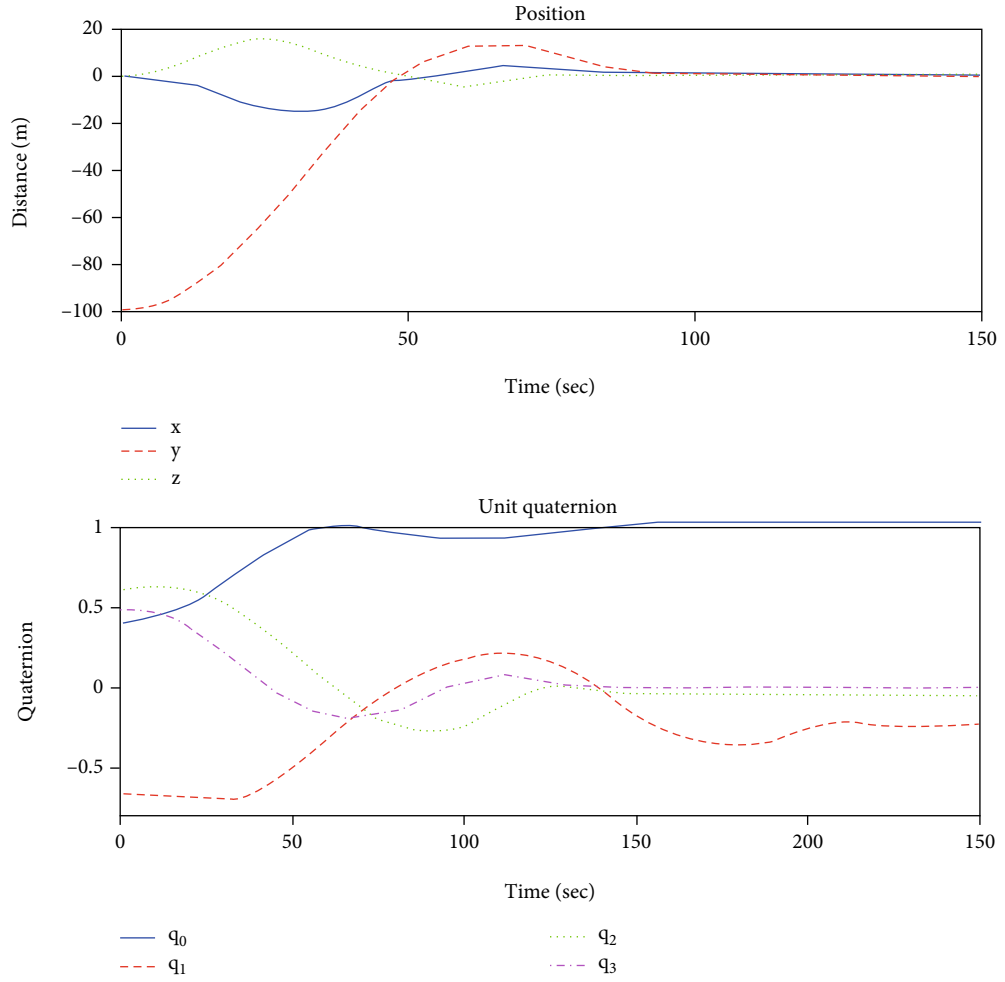

Figure 10: Time histories of control forces and torques expressed in the body-fixed frame with the prediction of 15 sampling instances.

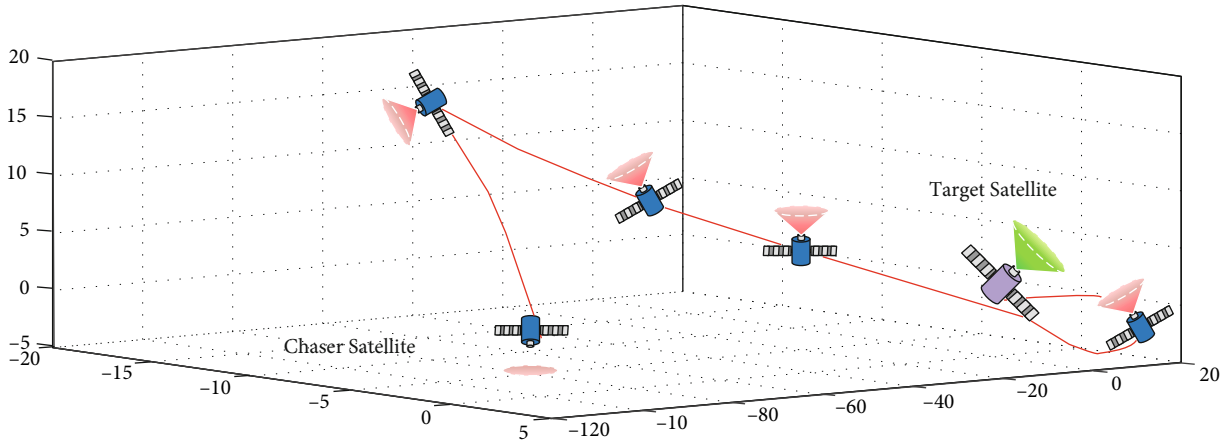

Figure 11: 3-D overall trajectory of close proximity maneuver via MPC with prediction horizon with the prediction of 15 sampling instances.

5. Simulation

In this section, we present a simulation example to demonstrate the effectiveness of the proposed approach for the 6-DOF close proximity problem. The simulations are carried out with Matlab R2021a software and modeled by Simulink. Although the simulations were not carried out using a custom solver for optimization, the execution time and the

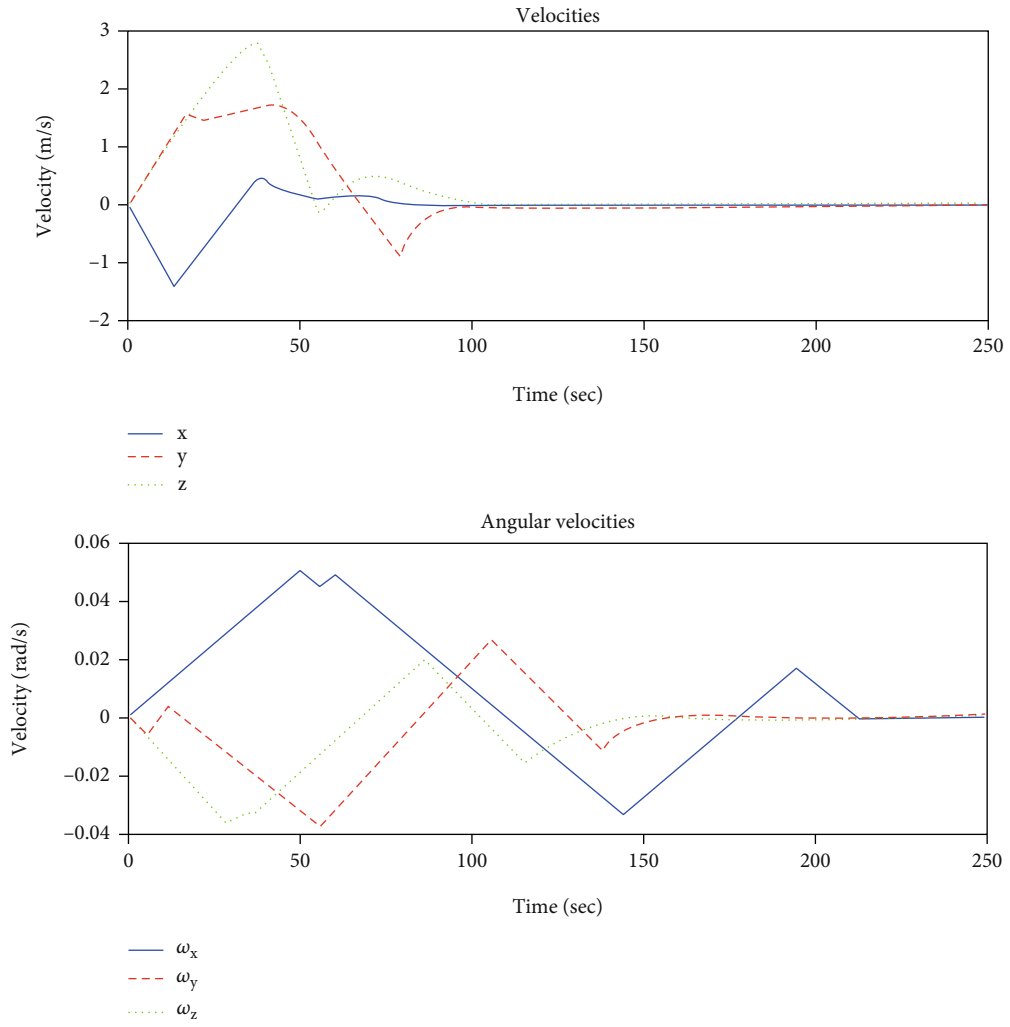

Figure 12: Time histories for the translational and rotational velocities in the body fixed frame with the prediction of 15 sampling instances.

convergence enable the proposed approach a viable candidate for guidance and control strategy for proximity maneuver. In the simulation, it is assumed the target body frame is always aligned with the orbit frame. The orbit parameters of chaser satellite are depicted in Table 1 in which we can obtain the target state information. The physical property and other initial state parameters are illustrated in Table 2. The desired state for attitude and position for chaser satellite is defined as the identity unit dual quaternion. The MPC system set is shown in Table 3. The disturbances exerted on chaser satellite are considered as

$$f_d = \begin{bmatrix} 0.06 + 0.01 \sin(0.5t) \\ 0.05 + 0.03 \sin(0.5t) \\ 0.04 + 0.02 \sin(0.5t) \end{bmatrix} (N),$$
$$\tau_d = \begin{bmatrix} 0.002 + 0.001 \sin\left(\frac{\pi}{10}t\right) \\ 0.003 - 0.001 \sin\left(\frac{\pi}{10}t\right) \\ 0.002 + 0.003 \sin\left(\frac{\pi}{10}t\right) \end{bmatrix} (N \cdot m). \quad (45)$$

In Figure 5, control input for the close proximity maneuver is depicted. Note that the control forces and torques never vanish for compensating the external disturbances. Figure 6 represents the time histories for the attitude and position in unit dual quaternion of the target satellite observed, whereas Figure 7 depicts the 3-D overall trajectory for the maneuver via MPC. Figure 8 represents the traces of velocities of translation and attitude. The results prove the effectiveness of our proposed approach as well as the stability and robustness. The controller could satisfy the actuator amplitude in the maneuver process.

Additionally, when dealing with the adjustment of controller parameters, we also find an important phenomenon related to the control horizon and prediction horizon. Generally, the increase of control period will reduce the controller performances such as response and stabilization time. Relative literatures have given detailed theory demonstrations, which we also verified during our research [40, 41]. Thus, we choose the minimum control horizon which is also an ideal situation to apply to our simulation. However, for the sake of fairness, considering the scenario of different prediction, we maintain other system parameters but change

the prediction horizon from 6 to 15 sampling instances for comparisons. Given the control output for translational and rotational motion, the 1-norm of the control optimized is used to demonstrate the fuel costume. As is shown in Table 4, when prediction horizon is set at $7 * Ts$, the required fuel is better optimized than other control groups. When the prediction horizon increases, the maneuver trends depict that the process requires more time and fuel costume. To provide an obvious contrast, the prediction with 15 sampling instances is given to indicate the impact of bigger prediction, which is illustrated in Figures 9–12. The optimized trajectory is planned requiring more distance to maneuver. In other words, the system requires more fuel cost and more time to drive the system to the set point for stabilization. This phenomenon indicates the significance of a proper prediction horizon to balance computing efficiency and cost.

6. Conclusion

In this paper, aiming at on-orbit service technology, we present an autonomous guidance and control strategy for 6-DOF close proximity operation. Dual quaternion is used to parameterize translational and rotational motion of rigid spacecraft. Based on the dual quaternion dynamics, a MPC-based pose control scheme is designed with considering actuator output constraints and external disturbances. The resulting approach is verified through numerical simulations. It is shown that it can provide a generic method for autonomous spacecraft operations. In addition, we discuss influences of different prediction horizons on MPC performance in the simulation via control variable method. The result depicts that prediction horizon could directly influence the optimization. Broader prediction horizon may cause more fuel consumption and more sensitive to the external disturbances, which may introduce new lead for further studies.

Data Availability

The numerical simulation data used to support the findings of this study are included within the article.

Conflicts of Interest

The authors declare that they have no conflicts of interest.

References

[1] E. Wang, S. Wu, G. Xun, Y. Liu, and Z. Wu, "Active vibration suppression for large space structure assembly: a distributed adaptive model predictive control approach," *Journal of Vibration and Control*, vol. 27, no. 5, 2020.

[2] W.-J. Li, D.-Y. Cheng, X.-G. Liu et al., "On-orbit service (OOS) of spacecraft: a review of engineering developments," *Progress in Aerospace Sciences*, vol. 108, pp. 32–120, 2019.

[3] J.-Y. Wang, H.-Z. Liang, Z.-W. Sun, S.-N. Wu, and S.-J. Zhang, "Relative motion coupled control based on dual quaternion," *Aerospace Science and Technology*, vol. 25, no. 1, pp. 102–113, 2013.

[4] X. Gao, C. Shang, D. Huang, and F. Yang, "A novel approach to monitoring and maintenance of industrial PID controllers," *Control Engineering Practice*, vol. 64, pp. 111–126, 2017.

[5] R. Singh, M. Ierapetritou, and R. Ramachandran, "System-wide hybrid MPC-PID control of a continuous pharmaceutical tablet manufacturing process via direct compaction," *European journal of pharmaceutics and biopharmaceutics: official journal of Arbeitsgemeinschaft fur Pharmazeutische Verfahrenstechnike*, vol. 85, no. 3, pp. 1164–1182, 2013.

[6] G. Etin, O. Zkaraca, and A. Keeba, "Development of PID based control strategy in maximum exergy efficiency of a geothermal power plant," *Renewable and Sustainable Energy Reviews*, vol. 137, p. 110623, 2021.

[7] H. L. Jay, "Model predictive control: review of the three decades of development," *International Journal of Control Automation & Systems*, vol. 9, no. 3, pp. 415–424, 2011.

[8] S. Chen, H. Chen, and N. Dan, "Implementation of MPC-based path tracking for autonomous vehicles considering three vehicle dynamics models with different fidelities," *Automotive Innovation*, vol. 3, no. 4, pp. 386–399, 2020.

[9] Y. Zhang, "MPC-based 3-D trajectory tracking for an autonomous underwater vehicle with constraints in complex ocean environments," *Ocean Engineering*, vol. 189, p. 106309, 2019.

[10] M. Allenspach and G. J. J. Ducard, "Nonlinear model predictive control and guidance for a propeller-tilting hybrid unmanned air vehicle," *Automatica*, vol. 132, p. 109790, 2021.

[11] H. Pan and V. Kapila, "Adaptive nonlinear control for spacecraft formation flying with coupled translation and attitude dynamics," in *Proceedings of the 40th IEEE Conference on Decision and Control*, pp. 2057–2062, Orlando, USA: IEEE Press, 2001.

[12] H. Wong, H. Pan, and V. Kapila, "Output feedback control for spacecraft formation flying with coupled translation and attitude dynamics," in *Proceedings of the 2005 American Control Conference*, pp. 2419–2426, Portland, USA: IEEE Press, 2005.

[13] L. Sun and Z. Zheng, "Adaptive relative pose control of spacecraft with model couplings and uncertainties," *Acta Astronautica*, vol. 143, pp. 29–36, 2018.

[14] L. Sun, W. Huo, and Z. Jiao, "Adaptive nonlinear robust relative pose control of spacecraft autonomous rendezvous and proximity operations," *ISA Transactions*, vol. 67, pp. 47–55, 2017.

[15] X. Kong and C. M. Gosselin, "Type synthesis of 3-DOF translational parallel manipulators based on screw theory," *Journal of Mechanical Design*, vol. 126, no. 1, pp. 83–92, 2004.

[16] H. Gui, Y. Wang, and W. Su, "Hybrid global finite-time dual-quaternion observer and controller for velocity-free spacecraft pose tracking," *IEEE Transactions on Control Systems Technology*, vol. 29, no. 5, pp. 2129–2141, 2021.

[17] J. Yang and E. Stoll, "Adaptive sliding mode control for spacecraft proximity operations based on dual quaternions," *Journal of Guidance, Control, and Dynamics*, vol. 42, no. 11, pp. 2356–2368, 2019.

[18] C. Xza, H. Zheng, and B. Jca, "Dual quaternion-based adaptive iterative learning control for flexible spacecraft rendezvous," *Acta Astronautica*, vol. 189, pp. 99–118, 2021.

[19] X. Sun, X. Wu, W. Chen, Y. Hao, K. A. Mantey, and H. Zhao, "Dual quaternion based dynamics modeling for electromagnetic collocated satellites of diffraction imaging on geostationary orbit," *Acta Astronautica*, vol. 166, pp. 52–58, 2020.

[20] J. Zhang, D. Ye, Z. Sun, and C. Liu, "Extended state observer based robust adaptive control on SE(3) for coupled spacecraft tracking maneuver with actuator saturation and misalignment," *Acta Astronautica*, vol. 143, pp. 221–233, 2018.

[21] X. Peng, Y. Zhou, J. Yu, K. Guo, and Z. Geng, "Predictor-based pose stabilization control for unmanned vehicles on _SE_ (3) with actuator delay and saturation," *Aerospace Science and Technology*, vol. 117, p. 106942, 2021.

[22] J. Wang, E. A. Butcher, and T. Yucelen, "Consensus estimation of rigid body motion using Lie algebra se(3) and the consensus extended Kalman filter," in *AIAA SPACE and Astronautics Forum and Exposition*, San Diego, California, 2019.

[23] U. Lee and M. Mesbahi, "Constrained autonomous precision landing via dual quaternions and model predictive control," *Journal of Guidance, Control, and Dynamics: A Publication of the American Institute of Aeronautics and Astronautics Devoted to the Technology of Dynamics and Control*, vol. 40, no. 2, pp. 292–308, 2017.

[24] X. Yan and Z. Yun, "Optimal quarantine and isolation control in SEQIJR SARS model," in *International Conference on Control*, IEEE, 2006.

[25] S. Berkani, F. Manseur, and A. Maidi, "Optimal control based on the variational iteration method," *Computers & Mathematics with Applications*, vol. 64, no. 4, pp. 604–610, 2012.

[26] W. Meng and J. Shi, "A global maximum principle for stochastic optimal control problems with delay and applications," *Systems & Control Letters*, vol. 150, p. 104909, 2021.

[27] R. Mitze and M. Mnnigmann, "A dynamic programming approach to solving constrained linear-quadratic optimal control problems," *Automatica*, vol. 120, p. 109132, 2020.

[28] R. Chai, A. Tsourdos, S. C. Al Savvaris, Y. Xia, and C. L. P. Chen, "Six-DOF spacecraft optimal trajectory planning and real-time attitude control: a deep neural network-based approach," *IEEE Transactions on Neural Networks and Learning Systems*, vol. 31, no. 11, pp. 5005–5013, 2020.

[29] Z. Peng, R. Luo, J. Hu, K. Shi, S. K. Nguang, and B. K. Ghosh, "Optimal tracking control of nonlinear multiagent systems using internal reinforce Q-learning," *IEEE Transactions on Neural Networks and Learning Systems*, pp. 1–13, 2021.

[30] A. S. M. Gilimalage and S. Kimura, "Model predictive control-based control algorithm for a target-chaser maneuvering situation," *Advanced Robotics*, vol. 103, pp. 1–12, 2021.

[31] H. Zeng, X. Fang, G. Chang, and R. Yang, "A dual quaternion algorithm of the Helmert transformation problem," *Earth Planets & Space*, vol. 70, no. 1, 2018.

[32] W. K. Clifford, "Preliminary sketch of bi-quaternions," *Proceedings of the London Mathematical Society*, vol. 4, 1873.

[33] Y. Liu, S. Wu, K. Zhang, and Z. Wu, "Gravitational orbit-attitude coupling dynamics of a large solar power satellite," *Aerospace Science and Technology*, vol. 62, pp. 46–54, 2017.

[34] J. Pluym and C. Damaren, "Second order relative motion model for spacecraft under J2 perturbations," in *AIAA/AAS Astrodynamics Specialist Conference and Exhibit*, Keystone, Colorado, 2006.

[35] B. Xiao, Q. Hu, W. Singhose, and X. Huo, "Reaction wheel fault compensation and disturbance rejection for spacecraft attitude tracking," *Journal of Guidance Control & Dynamics*, vol. 36, no. 6, pp. 1565–1575, 2013.

[36] C. Riano-Rios, R. Sun, R. Bevilacqua, and W. E. Dixon, "Aerodynamic and gravity gradient based attitude control for CubeSats in the presence of environmental and spacecraft uncertainties," *Acta Astronautica*, vol. 180, pp. 439–450, 2021.

[37] J. Lemos, "Nonlinear receding horizon control based on Pontryagin optimum principle," *IFAC Proceedings Volumes*, vol. 43, no. 14, pp. 1069–1074, 2010.

[38] D. Zhou, Y. Zhang, and S. Li, "Receding horizon guidance and control using sequential convex programming for spacecraft 6-DoF close proximity," *Aerospace Science and Technology*, vol. 87, pp. 459–477, 2019.

[39] V. Bachtiar, E. C. Kerrigan, W. H. Moase, and C. Manzie, "Continuity and monotonicity of the MPC value function with respect to sampling time and prediction horizon," *Automatica*, vol. 63, pp. 330–337, 2016.

[40] D. Seto, J. P. Lehoczky, L. Sha, and K. G. Shin, "On task schedulability in real-time control systems," in *17th IEEE Real-Time Systems Symposium*, Washington, DC, USA, 1996.

[41] X. Dai and A. Burns, "Period adaptation of real-time control tasks with fixed-priority scheduling in cyber-physical systems," *Journal of Systems Architecture*, vol. 103, p. 101691, 2020.

Hindawi
International Journal of Aerospace Engineering
Volume 2021, Article ID 4109118, 7 pages
https://doi.org/10.1155/2021/4109118

Research Article

Satellite Mission Instruction Sequence Generation Algorithm Using a Flexible Weighted Directed Graph

Zhang Yahang,[1,2] **Zhang Jiakai**,[3] **Yang Mengfei**,[1] **Yang Peiyao**,[2] **and Song Xiangshuai**[3]

[1]*College of Computer Science and Technology, Xidian University, Xi'an 710071, China*
[2]*Beijing Institute of Spacecraft System Engineering, Beijing 100094, China*
[3]*College of Aerospace and Civil Engineering, Harbin Engineering University, Harbin 150001, China*

Correspondence should be addressed to Zhang Yahang; zhangyahang@163.com

Received 9 August 2021; Accepted 16 September 2021; Published 20 October 2021

Academic Editor: Jiafu Liu

A satellite mission instruction generation algorithm based on a flexible weighted directed graph has been proposed. This algorithm can sort the instruction into sequence according to the instruction execution relationship with constraints, which can promote satellite operation performance of the ground station. Concepts like flexible edge, flexible zone, and implement zone were introduced, and the flexible weighted directed graph (FWDG) model was proposed. Based on this model, the satellite instruction sequence generation algorithm was designed. After practice and research, the result showed that according to the new algorithm, the instruction sequence can be consistent with all implement zones, consequently guaranteeing the correctness of the sequence.

1. Introduction

A low earth orbit remote sensing satellite with high resolution is the main channel to acquire ground information, which plays an increasingly important role in an earth optical and microwave survey [1]. A remote sensing satellite meets the users' needs through "task planning+instruction generation" [2]. The missions of a low earth orbit remote sensing satellite are intermittent, diverse, and uncertain, because of orbit revisit characteristics, weather conditions, onboard electronic constraints, and ground receiving resources. It is one of the most concerned problems for users and also a research hotspot in the academic field that a large space system takes advantage of a mission planning system to optimize the satellite-ground resources and accomplish the most imaging tasks with the least resources [3].

Lots of satellite task planning algorithms were presented based on artificial intelligence techniques [4]. Bensana et al. established the constraint satisfaction model and the integer programming model [5] and proposed the branch and bound algorithm and taboo search approximate algorithms to obtain the feasible solution. Hall and Magazine used a greedy algorithm and dynamic programming technique to solve a task programming model [6]. Vasquez and Hao map the SPOT5 satellite routine mission planning problem to a knapsack problem. Lin et al. use a Joseph-Louis Lagrange relaxation technique and tabu search algorithm to solve the imaging scheduling problem [7]. Mansour and Dessouky design the evolutionary algorithm and compare it with the traditional algorithm [8]. The main problem with these methods is that scheduling decisions cannot be changed dynamically. In References [9–11], the method of dynamically adjusting the results of planning such as task replanning is proposed, but the deviation between task planning and task execution cannot be considered.

On this basis, the satellite instruction sequence generation algorithm based on the weighted directed graph (WDG) presented in References [12, 13] can sort the satellite instruction sequence according to the constraint relation, and the operation efficiency of the ground control center to the spacecraft is greatly reduced. However, the interval between the instruction nodes of the noncritical path may

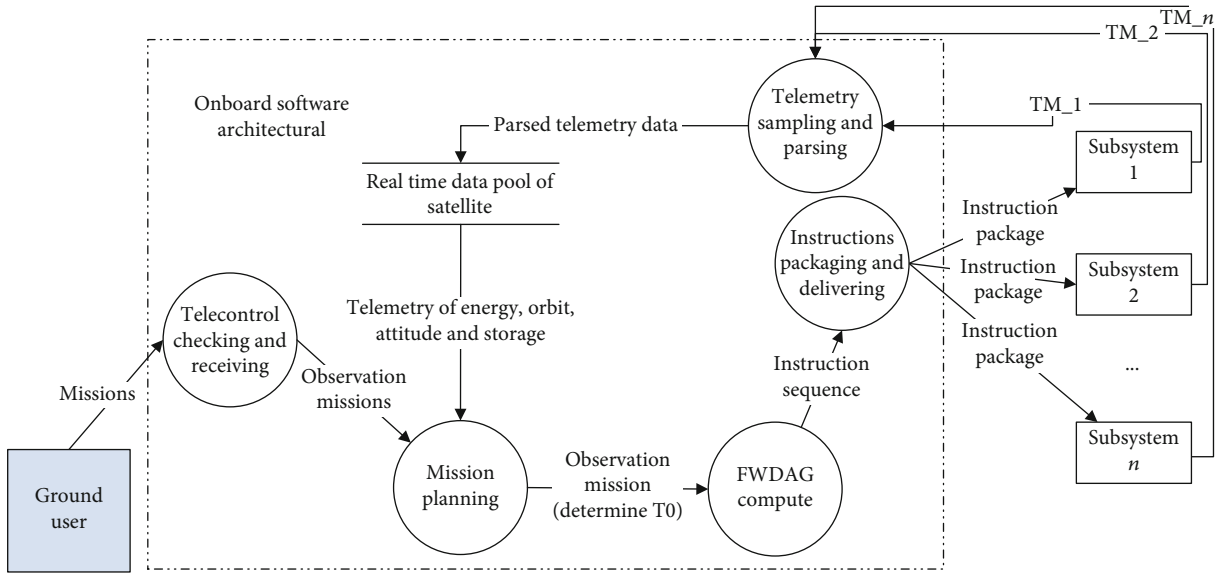

Figure 1: Relationship of the instruction module and onboard software modules.

be extended by default when the topological sorting algorithm is applied to generate the instruction sequence; it does not consider the need for strict protection of the execution interval of some spacecraft instructions.

In this paper, the concepts of directed acyclic flexible edge, flexible interval, and reasonable instruction execution interval of a directed acyclic graph are introduced, and a flexible weighted directed graph (FWDG) model is proposed to modify the instruction generation algorithm, and an instruction sequence generation algorithm based on the flexible weighted digraph is proposed. The FWDAG model is an essential module in onboard software, and it takes observation mission as input and instruction sequence as output, as shown in Figure 1. The example shows that the modified algorithm can satisfy the spacecraft instruction execution interval.

2. Satellite Instruction Sequence Generation Algorithm Based on the Directed Graph Model

2.1. Directed Graph Model. The satellite mission instruction sequence is transformed into a digraph model $G(V, E)$ consisting of instructions and their constraints. Among them,

(1) Graph $G = (V, E)$: source vertex represents the start of the task; sink vertex represents the end of the task

(2) $V = \{V_1, V_2, V_3, \cdots, V_N\}$ is the set of vertices of a directed graph; each vertex $V_j (j = 1, 2, \cdots, N)$ corresponds to an instruction. TIME(V_i) represents the execution time of the instruction

(3) $E = \{E_1, E_2, \cdots, E_M\}$ is the set of edges of a directed graph, edges $E_i = \{V_j \longrightarrow V_k\}$ $(i = 1, 2, \cdots, M; j, k = 1, 2, \cdots, N)$ represent instruction V_j preceding instruction V_k, V_j is the forward vertex of V_k, and V_k is the backward vertex of V_j; the length of the edge L_i represents the execution time interval between two instructions

In graph G, V is the set of vertices corresponding to all instructions contained in the task and E is the edge set corresponding to the instruction timing constraint that completes the task. In order to describe $G(V, E)$ in detail, more symbols are introduced; they are as follows:

N is the number of all vertices of a digraph $G(V, E)$.M is the number of all edges of a digraph $G(V, E)$.Source is the start of the instruction sequence for a task.

Sink is the end of the instruction sequence for a task.

$V(T_0)$ is the instructions at time T_0 (T_0 is the beginning time of imaging).

$V(T_1)$ is the instructions at time T_1 (T_1 is the beginning time of data transfer).

$X = \{S, X_l, X_m, \cdots\}$, where S is the start time of a mission and $\{X_l, X_m, \cdots\}$ is the interval between the instruction sequence $\{V_l, V_m \cdots\}$ and the first instruction.

2.2. Task Instruction Sequence Generation Algorithm Based on the Digraph Model. In this section, we introduce the directed graph-based task instruction sequence generation algorithm [12]:

A unified instruction topological sequence can be generated finally by Algorithm 1, after digraph modeling of a sensing task, according to the start time of the mission on the satellite, the interval of the basic instruction sequence, and the dependence of different instruction sequences.

However, in the second and fourth steps of the algorithm, when the earliest EST(V_i) and the latest LST(V_i) of each vertex are calculated, the default edge can be stretched [14, 15].

1. Hierarchizing the graph $G(V, E)$ according to the following definition.
   (i) Define *Source* as 0 – *layer* vertex;
   (ii) 1 – *layer* vertices only take the 0 – *layer* vertices as forward vertices;
   (iii) 2 – *layer* vertices only take the 1 – *layer* vertices or *Source* as forward vertices;
   (v) ...
   (vi) n – *layer* vertices take *Source*, 1 – *layer*, …, $n-1$ – *layer* vertices as forward vertices;
2. Start with *Source*, the earliest execution time interval $EST(V_i)$ of each vertex V_i relative to *Source* is computed by layer;
3. The earliest execution time interval of *Sink* relative to *Source* is the minimum execution time of the task instruction sequence;
4. Starting from *Sink*, the latest execution time interval $LST(V_i)$ of each vertex relative to *Source* is calculated in reverse step by step;
5. For instruction V_p like shutdown, the execution time delay X_p selects the earliest execution time interval relative to *Source*, and for instruction V_q like switch on, the execution time delay X_q selects the latest execution time interval relative to *Source*; Ensure that the command sequence satisfies the user's task, starting as late as possible and shutting down as early as possible;
6. The execution time of the *Source* vertices is the time T_0 subtracts the earliest execution time of the *Source* to T_0, which is also the start time S that the sequence starts to execute;
7. …

Algorithm 1: Instruction sequence generation algorithm based on the directed acyclic graph model.

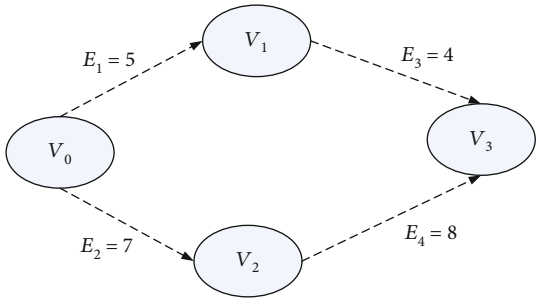

Figure 2: Instruction model of the general weighted directed acyclic graph.

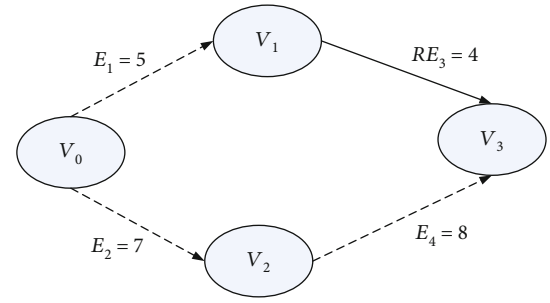

Figure 3: Instruction model of the general weighted RE acyclic graph.

According to the algorithm in [12, 13], for the model shown in Figure 2, if $T(V_0) = 0$, then

$$\begin{aligned} T(V_0) &= 0, \\ \mathrm{EST}(V_1) &= 5, \\ \mathrm{EST}(V_2) &= 7, \\ \mathrm{EST}(V_3) &= \max\{\mathrm{EST}(V_1) + E_3, \mathrm{EST}(V_2) + E_4\} = 15, \\ \mathrm{LST}(V_3) &= \mathrm{EST}(V_3) = 15, \\ \mathrm{LST}(V_1) &= \mathrm{LST}(V_3) - E_3 = 11, \\ \mathrm{LST}(V_2) &= \mathrm{LST}(V_3) - E_4 = 7, \\ \mathrm{LST}(V_0) &= \min\{\mathrm{LST}(V_1) - E_1, \mathrm{LST}(V_2) - E_2\} = 0. \end{aligned} \tag{1}$$

Obviously, for vertices V_2 and V_1, we have $\mathrm{EST}(V_1) \neq \mathrm{LST}(V_1)$ and $\mathrm{EST}(V_2) \neq \mathrm{LST}(V_2)$.

Algorithm 1 holds the execution time $T(V_1)$ and $T(V_1)$ for V_1 and V_2, respectively, which is reasonable, as long as $T(V_1) \in [\mathrm{EST}(V_1), \mathrm{LST}(V_1)]$ and $T(V_2) \in [\mathrm{EST}(V_2), \mathrm{LST}(V_2)]$. If V_1 is the shutdown instruction, according to Algorithm 1, $T(V_1) = \mathrm{EST}(V_1) = 5$. But consider an application scenario in which there are certain instructions and intervals between instructions that are fixed; that is, some edges E_x cannot be stretched and shortened. In this paper, we call this "rigid edge," denoted as RE.

As shown in Figure 3, the solid line RE_3 indicates that the edge can be neither shortened nor stretched, and the dash line indicates that the edge can be stretched but cannot be shortened. Obviously, $T(V_1)$ must be a fixed value; $T(V_1) = T(V_3) - 4 = 11$. However, Algorithm 1 cannot take into account this constraint, and the calculated results cannot meet this requirement.

3. Instruction Generation Algorithm Based on the FWDAG Instruction Model

In order to meet the more realistic and strict requirements of a satellite instruction transmission time slot, we propose an instruction generation algorithm based on a flexible weighted directed acyclic graph (FWDAG).

3.1. FWDAG Instruction Model. For the more general case, some instruction intervals can be within a set interval. For example, instruction V_1 must be executed after instruction V_0 is completed 3 ~ 4 s; then, obviously the interval [3, 4] is the variable interval of E_1. In this case, the concept of flexible interval edges is introduced into weighted directed acyclic graphs. The basic definitions are listed below:

Flexible Edge. In a directed acyclic graph, the edges with variable weights are called flexible edges and are denoted as FE.

Flexible Zone. The flexible interval of edge weight, which we call the flexible zone, is denoted as FZ. It is obvious that the rigid edge is a special flexible edge whose upper and lower limits of the flexible interval are equal.

Implement Zone. In a directed acyclic graph, the time of a node changes within a reasonable range, which becomes a reasonable range of execution, referred to as the implement zone, recorded as IZ.

Addition operation of IZ and FZ: the addition operation of the implement zone and the flexible zone is defined as follows:

$$\mathrm{IZ}^{'} = \mathrm{IZ} + \mathrm{FZ} = \left[\mathrm{IZ}_{\mathrm{down}} + \mathrm{FZ}_{\mathrm{down}}, \mathrm{LZ}_{\mathrm{up}} + \mathrm{FZ}_{\mathrm{up}}\right]. \quad (2)$$

Subtraction operation of IZ and FZ: the subtraction operation of the implement zone and the flexible zone is defined as follows:

$$\mathrm{IZ}^{'} = \mathrm{IZ} - \mathrm{FZ} = \left[\mathrm{IZ}_{\mathrm{down}} - \mathrm{FZ}_{\mathrm{up}}, \mathrm{LZ}_{\mathrm{up}} - \mathrm{FZ}_{\mathrm{down}}\right] I[0,+\infty). \quad (3)$$

Obviously, if $\mathrm{LZ}_{\mathrm{up}} < \mathrm{FZ}_{\mathrm{down}}$, $\mathrm{IZ}^{'} = \varnothing$.

In view of the above definition, the following theorem is proposed and proven.

Theorem 1. *Suppose that the node V_i in a directed acyclic graph has a precursor node V^{pre}, the corresponding flexible edge is FE^{pre}, and the flexible zone is $FZ(FE^{pre}) = [FZ(FE^{pre})_{down}, FZ(FE^{pre})_{up}]$. If $IZ(V^{pre}) = [IZ(V^{pre})_{down}, LZ(V^{pre})_{up}]$ has been determined, then $IZ(V_i) = [IZ(V^{pre})_{down} + FZ(FE^{pre})_{down}, LZ(V^{pre})_{up} + FZ(FE^{pre})_{up}]$.*

Proof. Let $x = T(V^{\mathrm{pre}})$, $y = T(\mathrm{FE}^{\mathrm{pre}})$, and $z = T(V_i)$. According to the flexible edge constraints of $\mathrm{FE}^{\mathrm{pre}}$, the objective function is $z = x + y$; here, $x \in [\mathrm{IZ}(V^{\mathrm{pre}})_{\mathrm{down}}, \mathrm{IZ}(V^{\mathrm{pre}})_{\mathrm{up}}]$ and $y \in [\mathrm{FZ}(\mathrm{FE}^{\mathrm{pre}})_{\mathrm{down}}, \mathrm{FZ}(\mathrm{FE}^{\mathrm{pre}})_{\mathrm{up}}]$. According to the property of the linear equations with two unknowns, the range of the objective function $z = x + y$ is $[\mathrm{IZ}(V^{\mathrm{pre}})_{\mathrm{down}} + \mathrm{FZ}(\mathrm{FE}^{\mathrm{pre}})_{\mathrm{down}}, \mathrm{LZ}(V^{\mathrm{pre}})_{\mathrm{up}} + \mathrm{FZ}(\mathrm{FE}^{\mathrm{pre}})_{\mathrm{up}}]$. And the range is continuous within its domain of definition $\mathrm{IZ}(V_i) = [\mathrm{IZ}(V^{\mathrm{pre}})_{\mathrm{down}} + \mathrm{FZ}(\mathrm{FE}^{\mathrm{pre}})_{\mathrm{down}}, \mathrm{LZ}(V^{\mathrm{pre}})_{\mathrm{up}} + \mathrm{FZ}(\mathrm{FE}^{\mathrm{pre}})_{\mathrm{up}}]$. □

Inference 2. Suppose that a node V_i in a directed acyclic graph has J precursor nodes V_j^{pre}, $j = 1, 2, \cdots, J$. One of the implement zones $\mathrm{IZ}(V_i)_j$ of node V_j^{pre} is determined by implement zone $\mathrm{IZ}(V_j^{\mathrm{pre}})$ of each precursor and flexible zone $\mathrm{FZ}(\mathrm{FE}_j)$ of FE_j. All entries of this node determine the intersection of the execution ranges of this node, which is equal to the execution ranges of this node. That is, $\mathrm{IZ}(V_i) = \bigcap_{j=0}^{J} (\mathrm{IZ}(V_j^{\mathrm{pre}}) + \mathrm{FZ}(\mathrm{FE}_j))$.

Theorem 3. *Suppose that the node V_i in a directed acyclic graph has a backward node V^{next}, the corresponding flexible edge is FE^{next}, and the flexible zone is $FZ(FE^{next}) = [FZ(FE^{next})_{down}, FZ(FE^{next})_{up}]$. If $IZ(V^{next}) = [IZ(V^{next})_{down}, LZ(V^{next})_{up}]$ has been determined, then $IZ(V_i) = [LZ(V^{next})_{down} - FZ(FE^{next})_{up}, IZ(V^{next})_{up} - FZ(FE^{next})_{down}]$.*

Proof. Let $x = T(V^{\mathrm{next}})$, $y = T(\mathrm{FE}^{\mathrm{next}})$, and $z = T(V_i)$. According to the flexible edge $\mathrm{FE}^{\mathrm{next}}$ constraints, it has objective function $z = x - y$, $x \in [\mathrm{IZ}(V^{\mathrm{next}})_{\mathrm{down}}, \mathrm{IZ}(V^{\mathrm{next}})_{\mathrm{up}}]$, and $y \in [\mathrm{FZ}(\mathrm{FE}^{\mathrm{next}})_{\mathrm{down}}, \mathrm{FZ}(\mathrm{FE}^{\mathrm{next}})_{\mathrm{up}}]$. According to the property of the linear equations with two unknowns, the range of the objective function $z = x - y$ is $[\mathrm{LZ}(V^{\mathrm{next}})_{\mathrm{down}} - \mathrm{FZ}(\mathrm{FE}^{\mathrm{next}})_{\mathrm{up}}, \mathrm{IZ}(V^{\mathrm{next}})_{\mathrm{up}} - \mathrm{FZ}(\mathrm{FE}^{\mathrm{next}})_{\mathrm{down}}]$, and the range is continuous within its domain of definition $\mathrm{IZ}(V_{\mathrm{i}}) = [\mathrm{LZ}(V^{\mathrm{next}})_{\mathrm{down}} - \mathrm{FZ}(\mathrm{FE}^{\mathrm{next}})_{\mathrm{up}}, \mathrm{IZ}(V^{\mathrm{next}})_{\mathrm{up}} - \mathrm{FZ}(\mathrm{FE}^{\mathrm{next}})_{\mathrm{down}}]$. □

Inference 4. Suppose a directed acyclic graph has a node V_i and J rear-driver nodes V_j^{next}, $j = 1, 2, \cdots, J$. Each rear-driver node V_j^{next} implement zone $\mathrm{IZ}(V_j^{\mathrm{next}})$ and the flexible zone $\mathrm{FZ}(\mathrm{FE}_j)$ of FE_j determine an implement zone $\mathrm{IZ}(V_i)_j$ of node V_i; all entries of this node determine the intersection of the execution ranges of this node, which is equal to the execution ranges of this node. That is, $\mathrm{IZ}(V_i) = \bigcap_{j=0}^{J} (\mathrm{IZ}(V_j^{\mathrm{next}}) - FZ(FE_j))$.

3.2. Instruction Generation Algorithm Based on FWDAG. In this paper, an instruction sequence generation algorithm based on the FWDAG model is proposed. A flexible edges FE are generated by the dependence of instructions with n nodes.

4. Application Example

Figure 4 is an instruction model of a satellite imaging task that is described by FWDAG. According to Algorithm 2, the procedure for calculating the graph above is

$$\begin{aligned}
&\mathrm{IZ}(V_0) = [0, 0], \mathrm{IZ}(V_1) = [0,+\infty], \mathrm{IZ}(V_2) = [0,+\infty], \mathrm{IZ}(V_3) = [0,+\infty],\\
&\mathrm{IZ}(V_{1.1}) = [0,+\infty], \mathrm{IZ}(V_{2.1}) = [0,+\infty], \mathrm{IZ}(V_{\mathrm{end}}) = [0,+\infty],\\
&\mathrm{IZ}(V_1) = \mathrm{IZ}(V_0) + \mathrm{FZ}(\mathrm{FE}_1) = [5, 7],\\
&\mathrm{IZ}(V_2) = \mathrm{IZ}(V_0) + \mathrm{FZ}(\mathrm{FE}_2) = [2, 3],\\
&\mathrm{IZ}(V_3) = \mathrm{IZ}(V_0) + \mathrm{FZ}(\mathrm{FE}_3) = [2, 3],\\
&\mathrm{IZ}(V_{1.1}) = \mathrm{IZ}(V_1) + \mathrm{FZ}(\mathrm{FE}_{1.1}) = [2, 3] + [5, 7] = [7, 10],\\
&\mathrm{IZ}(V_{2.1})' = \mathrm{IZ}(V_2) + \mathrm{FZ}(\mathrm{FE}_{2.1}) = [2, 3] + [2, 9] = [4, 12],\\
&\mathrm{IZ}(V_{2.1}) = (\mathrm{IZ}(V_3) + \mathrm{FZ}(\mathrm{FE}_{3.1})) \cap \mathrm{IZ}(V_{2.1})' = [9,+\infty) \cap [4, 12] = [9, 12],\\
&\mathrm{IZ}(V_{\mathrm{end}})' = \mathrm{IZ}(V_{1.1}) + \mathrm{FZ}(\mathrm{FE}_{1.1.1}) = [7, 10] + [120,145] = [127,155],\\
&\mathrm{IZ}(V_{\mathrm{end}}) = (\mathrm{IZ}(V_{2.1}) + \mathrm{FZ}(\mathrm{FE}_{2.1.1})) \cap \mathrm{IZ}(V_{\mathrm{end}})' = [14, 22] \cap [127, 155] = \varnothing.
\end{aligned} \quad (4)$$

There is no solution to the program break.

Obviously, according to the antenna path $V_0 \longrightarrow V_{1.1} \longrightarrow V_{\mathrm{end}}$, the earliest execution time of V_{end} is 127, and according to the camera path $V_0 \longrightarrow V_{2.1} \longrightarrow V_3$, the latest

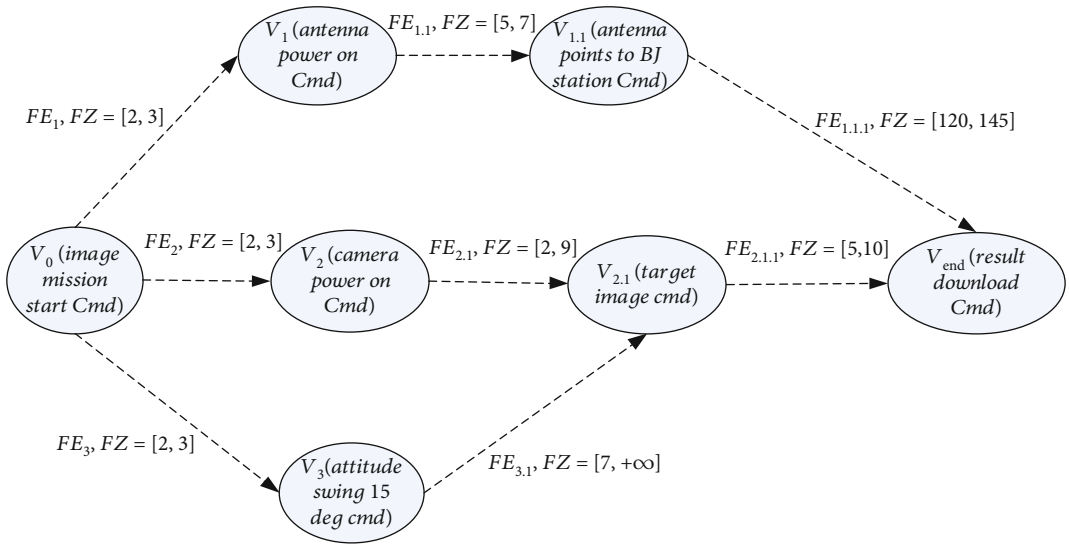

Figure 4: FWDAG instruction model.

1. The implement zone $IZ(V_0) = [0, 0]$ for the task starting node V_0, The implement zone for all other nodes is set to $IZ(V_i) = [0,+\infty)$;
2. Starting from V_0, select a node with degree 0 (no precursor node) from the digraph as the current node V_i. According to equation (2), calculate implement zone of all the backward nodes of the current node whose degree edges are connected.
3. According to Inference 2, the implement zone of the new node calculated by step 2 is updated by "And operation". If the result of "And operation" is "Empty", operation will be quit.
4. Deletes the current node and all flexible edges coming from this node.
5. Repeat steps 2 to step 4, until there are no more nodes in the directed graph.
6. Starting with V_N, select a node from the directed graph with an outdegree of 0 (without a trailing node) as the current node V_i, according to equation (3), select $T(V_i)$ from $IZ(V_i)$ according to the strategy of selecting node time (the last instruction is to select the earliest value, the start instruction is to be as late as possible, and the shutdown instruction is to be as early as possible), at the same time update the current node into all degrees edge connected to the precursor node implement zone;
7. According to Inference 4, the result of step 6 is updated by "And operation". The result of "And operation" should not be "Empty".
8. Deletes the current node and all flexible edges that enter this node.
9. Repeat steps 6 to step 8, until the node is no longer present in the directed graph.

Algorithm 2: An instruction sequence generation algorithm based on FWDAG.

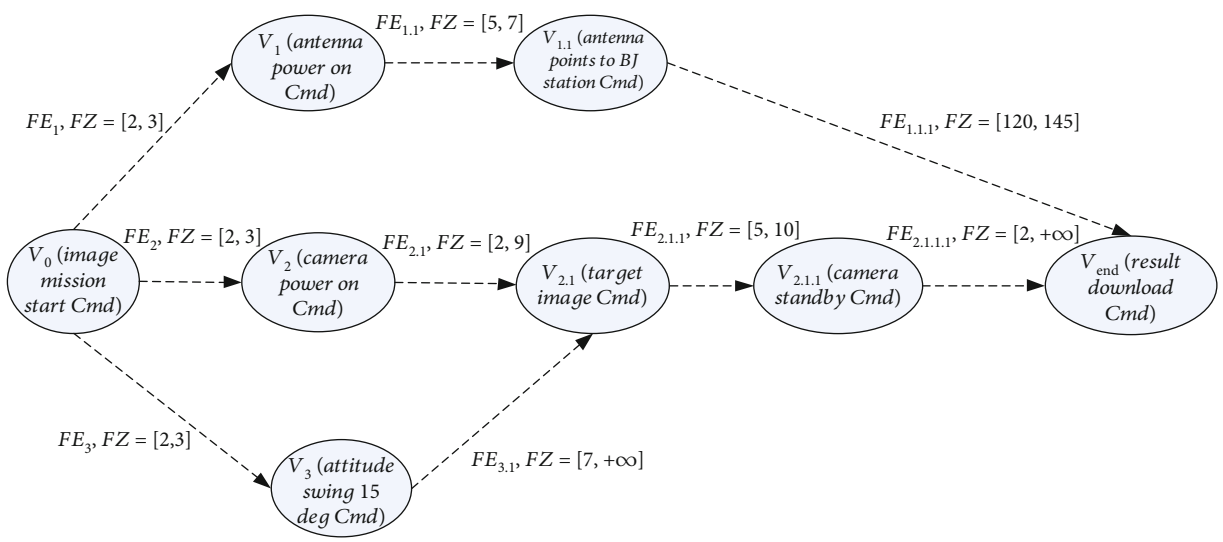

Figure 5: Adjusted FWDAG instruction model.

execution time of V_{end} is 22; obviously, there is no solution. This means that there are conflicts among camera payload, attitude executable trajectory, and antenna executable path constraint. The period of antenna execution is very long, while the time of camera payload powered on cannot be too long. Hence, the camera standby instruction is inserted into the onboard system, to prolong the camera instruction path $V_0 \longrightarrow V_{2.1} \longrightarrow V_3$ and then to match the antenna path, as shown in Figure 5.

By the updated instruction model, according to Algorithm 2, recalculated results are

$$\begin{aligned}
&\text{IZ}(V_0) = [0, 0], \text{IZ}(V_1) = [0,+\infty], \text{IZ}(V_2) \\
&\quad = [0,+\infty], \text{IZ}(V_3) = [0,+\infty], \\
&\text{IZ}(V_{1.1}) = [0,+\infty], \text{IZ}(V_{2.1}) = [0,+\infty], \text{IZ}(V_{\text{end}}) = [0,+\infty], \\
&\text{IZ}(V_1) = \text{IZ}(V_0) + \text{FZ}(\text{FE}_1) = [2, 3], \\
&\text{IZ}(V_2) = \text{IZ}(V_0) + \text{FZ}(\text{FE}_2) = [2, 3], \\
&\text{IZ}(V_3) = \text{IZ}(V_0) + \text{FZ}(\text{FE}_3) = [2, 3], \\
&\text{IZ}(V_{1.1}) = \text{IZ}(V_1) + \text{FZ}(\text{FE}_{1.1}) = [2, 3] + [5, 7] = [7, 10], \\
&\text{IZ}(V_{2.1})' = \text{IZ}(V_2) + \text{FZ}(\text{FE}_{2.1}) = [2, 3] + [2, 9] = [4, 12], \\
&\text{IZ}(V_{2.1}) = (\text{IZ}(V_3) + \text{FZ}(\text{FE}_{3.1})) \cap \text{IZ}(V_{2.1})' \\
&\quad = [9,+\infty) \cap [4, 12] = [9, 12], \\
&\text{IZ}(V_{2.1.1}) = \text{IZ}(V_{2.1}) + \text{FZ}(\text{FE}_{2.1.1}) \\
&\quad = [9, 12] + [5, 10] = [14, 22], \\
&\text{IZ}(V_{\text{end}})' = \text{IZ}(V_{1.1}) + \text{FZ}(\text{FE}_{1.1.1}) \\
&\quad = [7, 10] + [120,145] = [127,155], \\
&\text{IZ}(V_{\text{end}}) = (\text{IZ}(V_{2.1.1}) + \text{FZ}(\text{FE}_{2.1.1})) \cap \text{IZ}(V_{\text{end}})' \\
&\quad = [16,+\infty) \cap [127, 155] = [127, 155].
\end{aligned} \tag{5}$$

According to the end node selection of the earliest execution time principle, then

$$\begin{aligned}
&T(V_{\text{end}}) = 127, \text{LZ}(V_{\text{end}}) = [127,127], \\
&\text{IZ}(V_{1.1})'' = (\text{IZ}(V_{\text{end}}) - \text{FZ}(\text{FE}_{1.1.1})) \cap \text{IZ}(V_{1.1}) \\
&\quad = [0, 7] \cap [7, 10] = [7, 7], T(V_{1.1}) = 7, \\
&\text{IZ}(V_1)'' = \left(\text{IZ}(V_{1.1})'' - \text{FZ}(\text{FE}_{1.1})\right) \cap \text{IZ}(V_1) \\
&\quad = [0, 2] \cap [2, 3] = [2, 2], T(V_1) = 2, \\
&\text{IZ}(V_0)_1'' = \left(\text{IZ}(V_1)'' - \text{FZ}(\text{FE}_1)\right) \cap \text{IZ}(V_0) \\
&\quad = [0, 0] \cap [0, 0] = [0, 0], \\
&\text{IZ}(V_{2.1.1})'' = (\text{IZ}(V_{\text{end}}) - \text{FZ}(\text{FE}_{2.1.1.1})) \cap \text{IZ}(V_{2.1.1}) \\
&\quad = [0,125] \cap [14, 22] = [14, 22].
\end{aligned} \tag{6}$$

According to the end node selection of the earliest execution time principle, then

$$\begin{aligned}
&T(V_{2.1.1}) = 14, \text{LZ}(V_{2.1.1})'' = [14, 14], \\
&\text{IZ}(V_{2.1})'' = \left(\text{IZ}(V_{2.1.1})'' - \text{FZ}(\text{FE}_{2.1.1})\right) \cap \text{IZ}(V_{2.1}) \\
&\quad = [4, 9] \cap [9, 12] = [9, 9], T(V_{2.1}) = 9, \\
&\text{IZ}(V_2)'' = \left(\text{IZ}(V_{2.1})'' - \text{FZ}(\text{FE}_{2.1})\right) \cap \text{IZ}(V_1) \\
&\quad = [0, 7] \cap [2, 3] = [2, 3].
\end{aligned} \tag{7}$$

According to the end node selection of the earliest execution time principle, then

$$\begin{aligned}
&T(V_2) = 2, \text{LZ}(V_2)'' = [2, 2], \\
&\text{IZ}(V_0)_2'' = \left(\text{IZ}(V_2)'' - \text{FZ}(\text{FE}_2)\right) \cap \text{IZ}(V_0) \\
&\quad = [0, 0] \cap [0, 0] = [0, 0], \\
&\text{IZ}(V_3)'' = \left(\text{IZ}(V_{2.1})'' - \text{FZ}(\text{FE}_{3.1})\right) \cap \text{IZ}(V_3) \\
&\quad = [0, 2] \cap [2, 3] = [2, 2], T(V_3) = 2, \\
&\text{IZ}(V_0)_3'' = \left(\text{IZ}(V_2)'' - \text{FZ}(\text{FE}_2)\right) \cap \text{IZ}(V_0) \\
&\quad = [0, 0] \cap [0, 0] = [0, 0], \\
&\text{IZ}(V_0)'' = \text{IZ}(V_0)_1'' \cap \text{IZ}(V_0)_2'' \cap \text{IZ}(V_0)_3'' \\
&\quad = [0, 0], T(V_0) = 0.
\end{aligned} \tag{8}$$

At last, all the Ts were calculated:

$T(V_0) = 0$, $T(V_1) = 2$, $T(V_2) = 2$, $T(V_3) = 2$, $T(V_{1.1}) = 7$, $T(V_{2.1}) = 9$, $T(V_{2.1.1}) = 14$, and $T(V_{\text{end}}) = 127$, and we get the satellite imaging mission's command sequence.

The purposed scheme and algorithm are to model the existing constraints and find the feasible solution of the instruction sequence under this constraint model, which not only meets the constraint requirements but also improves the task execution energy efficiency as much as possible. If the feasible solution of the instruction sequence cannot be found under the current constraint model, the algorithm will alert the designer. As for how to modify the constraint model, such as the weight of edges or the number of vertices, designers need to adjust the design according to the actual situation of satellite missions and their own experience, so as to adjust the FWDAG model, and finally ensure that the instruction system can find a feasible solution under the adjusted constraint model.

5. Conclusion

An instruction generation algorithm based on the flexible weighted directed acyclic graph is proposed. By introducing the concept of a flexible edge into the directed acyclic graph, the problem that the time interval of instruction execution is fixed in a certain variable region is solved, ensuring that the execution interval of the dependent instruction is within the

preset range. The time complexity of the algorithm is $O(n) = O(n + 2e)$, where n is the number of nodes in the digraph model and e is the number of edges.

Data Availability

The data used to support the findings of this study are included within this paper.

Conflicts of Interest

The authors declare that there is no conflict of interest regarding the publication of this paper.

Acknowledgments

This work is supported in part by the National Natural Science Foundation of China (No. 11772185) and the project D020214.

References

[1] X. Wu, H. Zhao, B. Huang, J. Li, S. Song, and R. Liu, "Minimum-learning-parameter-based anti-unwinding attitude tracking control for spacecraft with unknown inertia parameters," *Acta Astronautica*, vol. 179, pp. 498–508, 2021.

[2] R. He, *Research on Imaging Reconnaissance Satellite Scheduling Problem, [Ph.D. thesis]*, National University of Defense Technology, 2004.

[3] J. S. Rodríguez, A. Y. Botero, D. Valle, J. G. Serna, and F. Botero, "Experimental approach for the evaluation of the performance of a satellite module in the CanSat form factor for in situ monitoring and remote sensing applications," *International Journal of Aerospace Engineering*, vol. 2021, Article ID 8868797, 28 pages, 2021.

[4] S. Mu, Y. Chen, and N. Zhang, "A rapid target searching scheme for a small satellite with device limits," *International Journal of Aerospace Engineering*, vol. 2021, Article ID 6627193, 9 pages, 2021.

[5] E. Bensana, M. Lemaitre, and G. Verfaillie, "Earth observation satellite management," *Constraints*, vol. 4, no. 3, pp. 293–299, 1999.

[6] N. G. Hall and M. J. Magazine, "Maximizing the value of a space mission," *European Journal of Operational Research*, vol. 78, no. 2, pp. 224–241, 1994.

[7] M. Vasquez and J. K. Hao, "A 'logic-constrained' knapsack formulation and a tabu algorithm for the daily photograph scheduling of an earth observation satellite," *Computational Optimization and Applications*, vol. 20, no. 2, pp. 137–157, 2001.

[8] M. A. A. Mansour and M. M. Dessouky, "A genetic algorithm approach for solving the daily photograph selection problem of the SPOT5 satellite," *Computers Industrial Engineering*, vol. 58, no. 3, pp. 509–520, 2010.

[9] X.-j. Huang, M.-h. Ma, D.-s. Qiu, and J.-h. Zhu, "Soving the cooperative reconnaissance of electronic reconnaissance satellite with a hybrid scheduling algorithm," *Journal of National University of Defense Technology*, vol. 33, no. 1, pp. 132–137, 2011.

[10] B.-f. Wu, Z.-g. Li, J.-y. Li, and J. Shi, "Design of mission-oriented autonomous commands for small satellite," *Spacecraft Engineering*, vol. 22, no. 4, pp. 68–71, 2013.

[11] C. Hao, L. Jun, J. Ning, X. G. Liu, and Y. Tang, "Scheduling model and algorithms for autonomous electromagnetic detection satellites," *Acta Aeronautica et Astronautica Sinica*, vol. 31, no. 5, pp. 1045–1053, 2010.

[12] T. Hai-Tao, W. Zhong-Guo, W. Da-Bao, and C. Jing, "Satellite utility improvement technique based on dynamic on-board command scheduling," *Journal of Astronautics*, vol. 35, no. 10, pp. 1105–1113, 2014.

[13] Z. Tian, D. Zhao, and H. Tang, "Satellite system performance improvement techniques based on key path optimization," in *The 1st China High Resolution Earth Observation Conference*, Beijing, 2012.

[14] S. Wang, *Graph Theory*, Science Press, Beijing, 2004.

[15] Y. Wang, *Discrete Mathematics*, Harbin Institute of Technology Press, 2007.

Hindawi
International Journal of Aerospace Engineering
Volume 2021, Article ID 6196556, 9 pages
https://doi.org/10.1155/2021/6196556

Research Article

Adaptive Control of Space Robot Despinning Tumbling Target Using Flexible Brushes

Shengxin Sun,[1] **Cheng Wei**,[1] **Zhuoran Huang**,[1] **Hao Wu**,[2] **Haibo Zhang**,[3] **Jianchun Lu**,[4] **and Yan Du**[5]

[1]*Harbin Institute of Technology, Harbin 150001, China*
[2]*KUKA Robotics Guangdong Co., Ltd., Foshan 528311, China*
[3]*Beijing Institute of Control Engineering, Beijing 100190, China*
[4]*China Academy of Space Technology, Beijing 100000, China*
[5]*Information Engineering University, Zhengzhou 450001, China*

Correspondence should be addressed to Shengxin Sun; 16b918086@stu.hit.edu.cn

Received 12 June 2021; Revised 9 July 2021; Accepted 28 July 2021; Published 26 September 2021

Academic Editor: Shunan Wu

A flexible brush mechanism is designed and mounted at the end of a seven-degree-of-freedom robotic arm to despin a tumbling target. The dynamics model of the flexible brush is established using the absolute nodal coordinate method (ANCF), and its contact collision with the solar wing of the tumbling target is analysed. The H_∞ optimal control is proposed for a seven-degree-of-freedom robotic arm during despinning of a tumbling target while ensuring the global robustness and stability. Simulations verify that the despinning strategy can successfully eliminate the rotation speed and is feasible and effective.

1. Introduction

With the development of space technology, the number of human space satellites has gradually increased and the resulting space debris removal has become a key topic in the space industry [1]. In order to control the growth of the space debris population and eliminate its threat to space-flight activities, active space debris removal techniques have become a current research hotspot [2]. Capture strategy for non-cooperative targets tumbling at high speed, applying resistance and reducing their angular speed of rotation to make capture less difficult [3]. In terms of contact despinning, Huang et al. [4, 5] proposed a method for attitude control of noncooperative targets based on a tether terminal, which stabilizes the attitude of the tumbling target by controlling the tether tension and damping force attached to it; Daneshjou and Alibakhshi [6] proposed a spring damper buffer device which is accomplished by contact collision during nozzle docking in the despinning process; Nishida and Kawamoto [7] designed a despinning device with a flexible brush as the end-effector, which uses the elastic contact force between the brush and the target for despinning. There are also space debris removal systems such as drag-increasing devices, which accelerate the target deconvolution process by increasing the surface-to-mass ratio of the target, thus increasing the air drag; methods include spraying foam on space debris [8, 9] and installing airbags for space debris [10].

For the stability of the deconvolution mechanism during the deconvolution process, the fast response and stability of the robotic arm are achieved by using sliding mode control. In terms of the sliding mode control, Oliveira et al. [11] proposed an adaptive sliding mode method based on the concept of extended equivalent control to deal with disturbances at unknown boundaries in nonlinear systems to avoid overestimation of controller gains and loss of sliding

motion. Kawamura et al. [12] proposed a sliding mode control design based on a disturbance observer using Lyapunov's stability theorem method, which reduces the gain of the switching term in the sliding mode controller and effectively eliminates jitter.

Veysi et al. [13] designed a fuzzy sliding mode controller for controlling the position of an end-effector in a space task. This controller uses a new heuristic algorithm, the adaptive improved BAT algorithm, to determine the coefficients of the fuzzy sliding-mode controller and verify its performance with a two-degree-of-freedom robotic arm. Mobayen et al. [14] investigated a second-order fast terminal sliding mode control technique based on linear matrix inequalities for a class of tracking problems with unmatched nonlinear uncertainty, which showed significant improvements in both control performance and tracking performance. Karimi et al. [15, 16] solved the control problem for a class of uncertain nonlinear systems using a generalized adaptive control. Sun and Hou [17] studied the control problem of a flexible linkage robotic arm with uncertainty and proposed a sliding mode control method with both a neural network and a disturbance observer for adaptive design. The update laws of the neural network and disturbance observer were designed on this basis, and the stability of the closed-loop system was proved by Lyapunov analysis. Mobayen et al. [18] designed an adaptive super-torsional global nonlinear sliding mode control rate for an N-linked robot, which ensured the elimination of the arrival phase and the presence of the sliding mode on the right side of the surface, while using the adaptive control law to eliminate external disturbances. Yang et al. [19, 20] designed an adaptive neural network for sliding mode control of flexible manipulators. Cao et al. [21, 22] use a robust fixed-time attitude stabilization control with spacecraft with actuator uncertainty. Zhang et al. [23–25], with regard to the issues of stability for hidden semi-Markov jump systems, designed a stabilizing controller dependent on both the observed mode, and the elapsed time it is constructed. In the sense of σ-error mean square stability (σ-MSS), numerically testable criteria on the basis of semi-Markov kernel (SMK) and emission probability of HS-MJLSs are obtained.

As a brand new research topic, despinning is still in the theoretical stage at home and abroad. This paper designs a robust optimal controller based on linear quadratic performance indicators for a seven-degree-of-freedom robotic arm with uncertainty and external disturbances. The essence of the control is to minimise the parametrization of the error transfer function under the condition that the disturbance is bounded, considering the maximum disturbance that the system may withstand. At the same time, the optimal control makes the system robustly optimal for a specified performance index. By analysing Lyapunov stability, it can be demonstrated that in the case of bounded disturbances, the robust state feedback control term in the controller can effectively compensate for the uncertainties in the system and external disturbances, allowing the robot arm to accurately track the desired trajectory, i.e., the closed-loop system achieves asymptotic stability, while the quadratic performance index is optimal.

2. Despin Dynamics

This paper designs a space robot with a flexible reduction brush at the end to deconvolve a tumbling target in space. The deconfliction mechanism is flexible and has soft contact characteristics for noncooperative targets in a free tumbling state, which can improve the safety of deconfliction. The model is shown in Figure 1.

Definition of the coordinate system and symbols: coordinate system Σ_{I} is the inertial coordinate system, coordinate system Σ_{b} is the base body coordinate system, coordinate system Σ_{t} is the target body coordinate system, $q = [q_1, q_2, q_3, q_4, q_5, q_6, q_7]$ are the robot arm joint variables, $q_{\boldsymbol{b}} = [q_{\boldsymbol{b1}}, q_{\boldsymbol{b2}}, q_{\boldsymbol{b3}}]$ is the attitude Euler angle of the base body, C_i is the mass center of the Kth rod of the robot arm, J_i is the joint connecting the $i-1$ and i rods, ${}^{I}r_i$ is the position of the mass center of the i rod of the robot arm in the inertial coordinate system, ${}^{I}r_0$ is the position vector of the mass center of the base spacecraft in the inertial coordinate system, ${}^{I}r_{\mathrm{g}}$ is the position vector of the mass center of the space robot system, ${}^{I}\omega_i$ is the angular velocity of the i rod of the arm, ${}^{I}\omega_0$ is the angular velocity of the base, ${}^{I}\omega_{\mathrm{t}}$ is the angular velocity of the target, and m_i is the mass of the i rod of the space robot. The top left corner I indicates the representation of the vector in the inertial coordinate system.

2.1. Modeling of Rope Dynamics Based on ANCF Cable-Beam Units. The flexible reduction brush at the end of the gyroscopic robot is modelled using rope dynamics based on the Absolute Nodal Coordinate Formulation (ANCF) cable-beam element.

2.1.1. Kinetic Energy of Cable Element. Since the shape function of the cable element is constant, the velocity vector at any point on the j cable element can be written as

$$ {}^{j}\dot{r} = S^{j}\dot{q}_{\mathrm{c}}, \tag{1} $$

where r is the global position vector at any point, S is the shape function, and q_{c} is the generalized coordinates.

Using equation (1), the kinetic energy of the flexible cable element can be written as

$$ {}^{j}T = \frac{1}{2}\int_0^L \rho \int_A {}^{j}\dot{q}_{\mathrm{c}}^{\mathrm{T}} S^{\mathrm{T}} S {}^{j}\dot{q}_{\mathrm{c}} \mathrm{d}A\mathrm{d}x = \frac{1}{2}{}^{j}\dot{q}_{\mathrm{c}}^{\mathrm{T}} \left(\int_0^L \rho \left(AS^{\mathrm{T}} S \right) \mathrm{d}x \right) {}^{j}\dot{q}_{\mathrm{c}} = \frac{1}{2}{}^{j}\dot{q}_{\mathrm{c}}^{\mathrm{T}} {}^{j}M {}^{j}\dot{q}_{\mathrm{c}}, \tag{2} $$

where ρ and A are the cable element density and cross-sectional area, respectively; L is the cable element length; and $M = \int_0^L \rho (AS^{\mathrm{T}} S)\mathrm{d}x$ represents the constant mass matrix of the cable element [19, 20].

2.1.2. Internal Energy of the Element. Using the Bernoulli-Euler beam equation, the flexible deceleration brush cable is subjected to preload and the element positive stress is

$$ \sigma = E\varepsilon + \sigma_1, \tag{3} $$

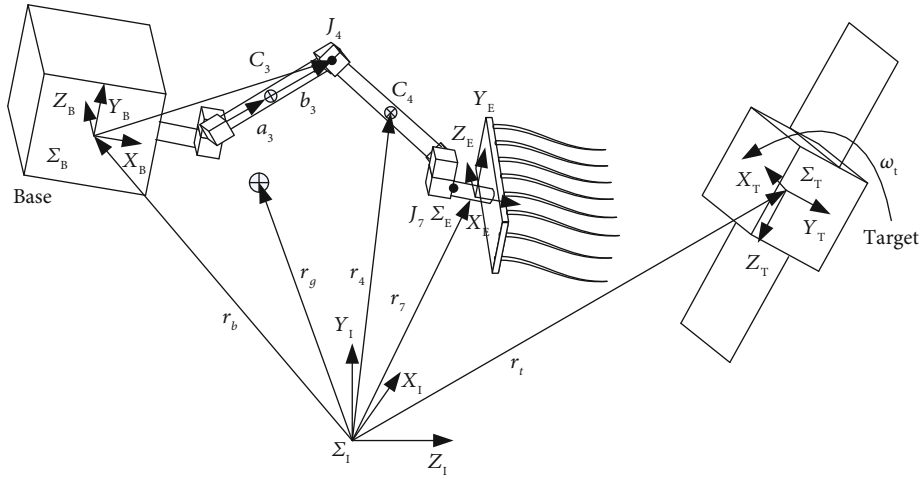

Figure 1: A model of seven-degree-of-freedom manipulator.

where σ_1 is the preload force, E is the modulus of elasticity, and ε is the axial strain. Then, the internal energy of the flexible cable element is expressed as

$$U = \int_V \left(\frac{1}{2}E\varepsilon^2 + \sigma_1\varepsilon\right)\mathrm{d}V = \mathrm{AL}\int_0^1 \left(\frac{1}{2}E\varepsilon^2 + \sigma_1\varepsilon\right)\mathrm{d}x, \quad (4)$$

where V is the volume of the flexible cable unit.

2.1.3. Kinetic Equations. The total kinetic energy and total strain energy of the flexible cable system are

$$\begin{cases} T = \sum_{j=1}^{3k} {}^jT = \frac{1}{2}\dot{q}_c^{\mathrm{T}} M \dot{q}_c, \\ U = \sum_{j=1}^{3k} {}^jU = \sum_{j=1}^{3k} \mathrm{AL}\int_0^1 \left(\frac{1}{2}E^j\varepsilon^2 + {}^j\sigma_1{}^j\varepsilon\right)\mathrm{d}x. \end{cases} \quad (5)$$

The kinetic equation for the flexible cable system is

$$\begin{cases} \frac{\mathrm{d}}{\mathrm{d}t}\left(\frac{\partial T}{\partial \dot{q}_c}\right)^{\mathrm{T}} - \left(\frac{\partial T}{\partial q_c}\right)^{\mathrm{T}} + \left(\frac{\partial U}{\partial q_c}\right)^{\mathrm{T}} + \left(\frac{\partial D}{\partial q_c}\right)^{\mathrm{T}}\lambda = Q_e, \\ D(q_c, t) = 0, \end{cases} \quad (6)$$

where D is the constraint equation, λ is the Rasch multiplier corresponding to the constraint equation, Q_e is the generalized force vector, and q_c and λ are both unknown quantities.

2.2. Contact Collision Dynamics Modelling. During the derotation process, the contact collision occurs mainly between the flexible reduction brush and the sail of the tumbling target. The contact collision between the flexible reduction brush and the target is modelled based on a nonlinear spring damping model. According to Hertz collision theory, the contact collision is represented as

$$\begin{cases} F = (F_K + F_C)B(\delta) = \left(K\delta^n + C\dot{\delta}\right)B(\delta), \\ B(\delta) = \begin{cases} 0 & \delta \geq 0, \\ 1 & \delta < 0. \end{cases} \end{cases} \quad (7)$$

F_K is the normal collision force, F_C is the normal damping force, K is the equivalent contact stiffness, C is the equivalent contact damping factor, δ is the normal penetration depth, $\dot{\delta}$ is the normal penetration velocity, n is the exponent ($n \geq 1$). $B(\delta)$ is a logistic function that determines whether contact is made based on the normal penetration δ.

2.3. Modelling the Dynamics of Free-Floating Space Robots. The equations for the dynamics of a free-floating space robot are

$$\begin{bmatrix} H_b & H_{bm} \\ H_{bm}^{\mathrm{T}} & H_m \end{bmatrix}\begin{bmatrix} \ddot{x}_b \\ \ddot{q}_m \end{bmatrix} + \begin{bmatrix} c_b \\ c_m \end{bmatrix} = \begin{bmatrix} F_b \\ \tau \end{bmatrix} + \begin{bmatrix} J_b^{\mathrm{T}} \\ J_m^{\mathrm{T}} \end{bmatrix} F_e, \quad (8)$$

where H_b is the base inertia matrix; H_m is the arm inertia matrix; H_{bm} is the space robot coupling inertia matrix; x_b is the base position; q_m is the arm joint angle; c_b is the nonlinear term of the base; c_m is the nonlinear term of the arm; F_b and F_e are the forces acting on the base and the end, respectively; τ is the arm joint moment; J_b is the end base Jacobi matrix; and J_m is the end joint Jacobi matrix.

2.4. Robust Control Dynamics Modelling. Dynamics modelling has been completed for space robots:

$$H\left(q_{tog}\right)\ddot{q}_{tog} + C\left(q_{tog}, \dot{q}_{tog}\right)\dot{q}_{tog} = \tau, \quad (9)$$

where $H(q_{tog})$ is the symmetric positive definite inertia matrix; $C(q_{tog}, \dot{q}_{tog})\dot{q}_{tog}$ is the nonlinear coupling term: $C($

Table 1: Kinetic parameters.

Parameter name	Matrix	Joint 1	Joint 2	Joint 3	Joint 4	Joint 5	Joint 6	Joint 7
Length a (m)	-	0	0	1	1	0	0	0
Angle α (°)	-	90	90	0	0	90	90	0
Joint distance d (m)	-	0	0.1	0	0	0.3	0.1	0
Joint angle θ (°)	-	$\theta 1$	$\theta 2$	$\theta 3$	$\theta 4$	$\theta 5$	$\theta 6$	$\theta 7$
Mass m (kg)	2811	2.8	2.8	25.39	25.39	2.8	2.8	10.6
Ix (kg·m^2)	473	0.005	0.005	2.76	2.76	0.005	0.005	1.33
Iy (kg·m^2)	473	0.005	0.005	2.76	2.76	0.005	0.005	1
Iz (kg·m^2)	467	0.005	0.005	0.03	0.03	0.005	0.005	1.5

Table 2: Spin target parameters.

m (kg)	Substrate volume (m^3)	Sail area (m^2)	Rolling speed (rad·s^{-1})	Ix (kg·m^2)	Iy (kg·m^2)	Iz (kg·m^2)
2000	$1 \times 1 \times 1$	1×5.113	1	200	300	200

$q_{\text{tog}}, \dot{q}_{\text{tog}})\dot{q}_{\text{tog}} = \dot{H}\dot{q}_{\text{tog}} - (\partial/\partial q_{\text{tog}})((1/2)\dot{q}_{\text{tog}}^{\text{T}} H \dot{q}_{\text{tog}})$; and τ is the forces and moments acting on the base and robotic arm joints.

The space ablative robot is in the complex microgravity environment of space and contains a flexible reduction brush at the end, so considering the uncertainties of external disturbances an friction and parameter errors, equation (9) can be expressed as

$$\begin{aligned} H\left(q_{\text{tog}}\right)\ddot{q}_{\text{tog}} + C\left(q_{\text{tog}}, \dot{q}_{tog}\right)\dot{q}_{\text{tog}} &= \tau, \\ H\left(q_{\text{tog}}\right) &= H_0\left(q_{\text{tog}}\right) + \Delta H\left(q_{\text{tog}}\right), \\ C\left(q_{\text{tog}}, \dot{q}_{\text{tog}}\right) &= C_0\left(q_{\text{tog}}, \dot{q}_{\text{tog}}\right) + \Delta C\left(q_{\text{tog}}, \dot{q}_{\text{tog}}\right), \end{aligned} \tag{10}$$

where $H_0(q_{\text{tog}})$ and $C_0(q_{\text{tog}}, \dot{q}_{\text{tog}})$ are the knowable nominal matrix and $\Delta H(q_{\text{tog}})$ and $\Delta C(q_{\text{tog}}, \dot{q}_{\text{tog}})$ are the unknowable nominal matrix.

$$H_0\left(q_{\text{tog}}\right)\ddot{q}_{\text{tog}} + C_0\left(q_{\text{tog}}, \dot{q}_{\text{tog}}\right)\dot{q}_{\text{tog}} = \tau - \Delta H\left(q_{\text{tog}}\right)\ddot{q}_{\text{tog}} - \Delta C\left(q_{\text{tog}}, \dot{q}_{\text{tog}}\right)\dot{q}_{\text{tog}}. \tag{11}$$

Dynamic compensation is as follows:

$$\tau = H_0\left(q_{\text{tog}}\right)u + C_0\left(q_{\text{tog}}, \dot{q}_{\text{tog}}\right)\dot{q}_{\text{tog}}, \tag{12}$$

$$\ddot{q}_{\text{tog}} = u - H_0^{-1}\Delta H\ddot{q}_{\text{tog}} - H_0^{-1}\Delta C\dot{q}_{\text{tog}}. \tag{13}$$

u is the control input vector, defining external disturbances τ_d:

$$\delta\left(q_{\text{tog}}, \dot{q}_{\text{tog}}, \ddot{q}_{\text{tog}}\right) = -\left(\Delta H\ddot{q}_{\text{tog}} + \Delta C\dot{q}_{\text{tog}} - \tau_d\right). \tag{14}$$

In order to make the space robot end track the desired trajectory with time variation, the state tracking error is defined as $e \in R^{13}$:

$$e = \begin{bmatrix} \dot{q}_{\text{tog}} - \dot{q}_{\text{tog}}^d \\ q_{\text{tog}} - q_{\text{tog}}^d \end{bmatrix} = \begin{bmatrix} \dot{\tilde{q}}_{\text{tog}} \\ \tilde{q}_{\text{tog}} \end{bmatrix}, \tag{15}$$

where q_{tog}^d is the expected arm joint angles and $\dot{q}_{\text{tog}}^d$ is the desired angular velocity of the joint of the manipulator.

The trajectory tracking error state equation of the space robot can be obtained as follows:

$$\dot{e} = A\left(q_{\text{tog}}, \dot{q}_{\text{tog}}\right)e + Bu + Bw. \tag{16}$$

Each parameter is specifically defined as

$$A\left(q_{\text{tog}}, \dot{q}_{\text{tog}}\right) = \begin{bmatrix} -H_0^{-1}C_0 & 0 \\ I_{13} & 0 \end{bmatrix}, \tag{17}$$

$$B = [I_{13}\ 0]^{\text{T}}, \tag{18}$$

$$w = -H_0^{-1}\delta\left(q_{\text{tog}}, \dot{q}_{\text{tog}}, \ddot{q}_{\text{tog}}\right), \tag{19}$$

$$u = H_0^{-1}\left(\tau - H_0\ddot{q}_{\text{tog}}^d - C_0\dot{q}_{\text{tog}}^d\right). \tag{20}$$

Therefore, the force and moment exerted on the space robot can be solved as

$$\tau = H_0\left(\ddot{q}_{\text{tog}}^d + u\right) + C_0\dot{q}_{\text{tog}}^d. \tag{21}$$

To track the desired trajectory and reach the desired point at the end, the design aid equation is as follows:

$$z = De = \begin{bmatrix} D_{11} & D_{12} \\ 0 & I \end{bmatrix}\begin{bmatrix} \dot{\tilde{q}}_{\text{tog}} \\ \tilde{q}_{\text{tog}} \end{bmatrix}, \tag{22}$$

where D_{11} and D_{12} are constant matrices.

Putting formula (16) to formula (10),

$$\dot{e} = A_N e + B_N u + B_N w. \tag{23}$$

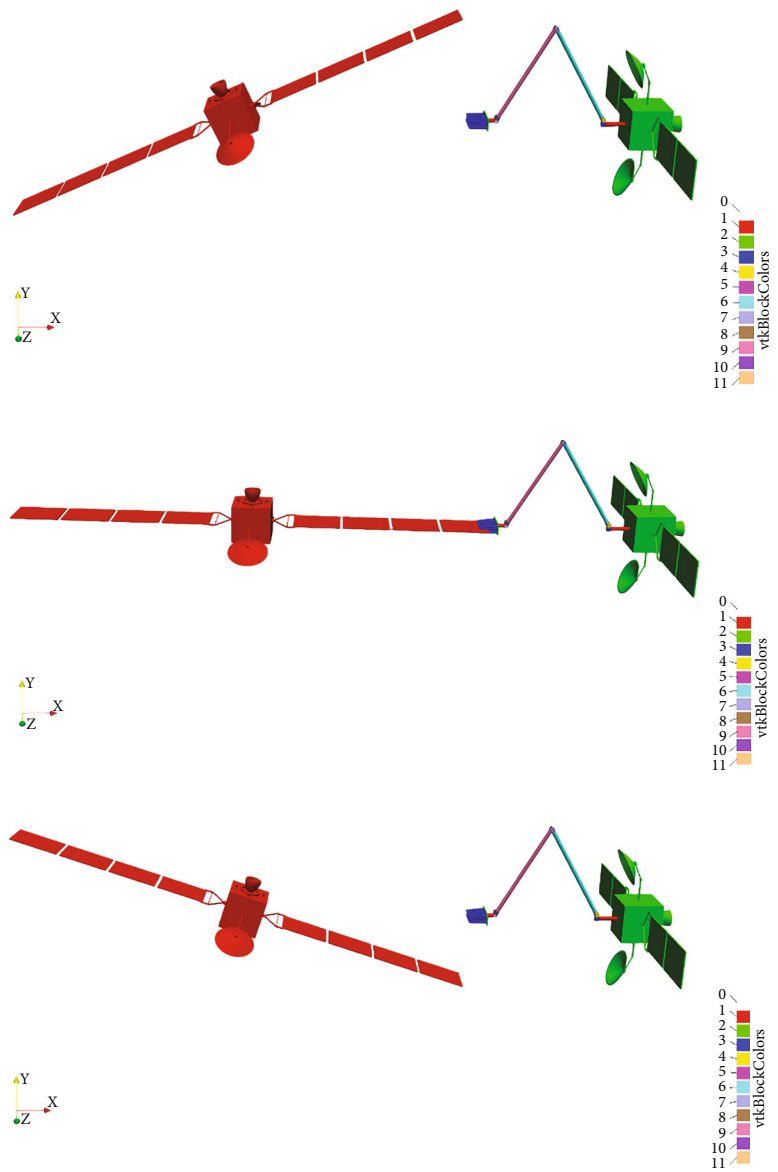

Figure 2: Spin satellite derotation effect.

In formula (17),

$$A_N = D^{-1}\begin{bmatrix} -H_0^{-1}C_0 & 0 \\ D_{11}^{-1} & -D_{11}^{-1}D_{12} \end{bmatrix} D, \tag{24}$$

$$B_N = D^{-1}\begin{bmatrix} H_0^{-1} \\ 0 \end{bmatrix}, \tag{25}$$

$$D_1 = [\, D_{11} \quad D_{12} \,], \tag{26}$$

$$u = H_0 D_1 \dot{e} + C_0 D_1 e, \tag{27}$$

$$w = H_0 D_{11} H_0^{-1} \delta\left(q_{\text{tog}}, \dot{q}_{\text{tog}}, \ddot{q}_{\text{tog}}\right). \tag{28}$$

Then, the control force and moment of the space robot can be expressed as

$$\tau = H_0 \ddot{q}_{\text{tog}} + C_0 \dot{q}_{\text{tog}}^d, \tag{29}$$

$$\begin{aligned} \ddot{q}_{\text{tog}} &= \ddot{q}_{\text{tog}}^d + \left(-D_{11}^{-1}H_0^{-1}C_0D_{11} - D_{11}^{-1}D_{12}\right)\dot{e} - D_{11}^{-1}H_0^{-1}C_0D_{12}e + D_{11}^{-1}H_0^{-1}u \\ &= \ddot{q}_{\text{tog}}^d - D_{11}^{-1}D_{12}\dot{e} - D_{11}^{-1}H_0^{-1}\left(C_0[\, D_{11} \quad D_{12} \,]\left[\dot{\tilde{q}}_{\text{tog}} \quad \tilde{q}_{\text{tog}}\right]^T - u\right) \\ &= \ddot{q}_{\text{tog}}^d - D_{11}^{-1}D_{12}\dot{\tilde{q}}_{\text{tog}} - D_{11}^{-1}H_0^{-1}(C_0D_1\dot{e} - u). \end{aligned} \tag{30}$$

Designing the control law $u = -Ke(t)$, the external disturbance w in the system is reduced. γ is any positive real number.

$$J = \min_{u \in L_2} \max_{0 \neq w \in L_2} \frac{\int_0^\infty \left((1/2)e^{\mathrm{T}}Qe + (1/2)u^{\mathrm{T}}Ru\right)dt}{\int_0^\infty \left((1/2)w^{\mathrm{T}}w\right)dt} \leq \gamma^2. \tag{31}$$

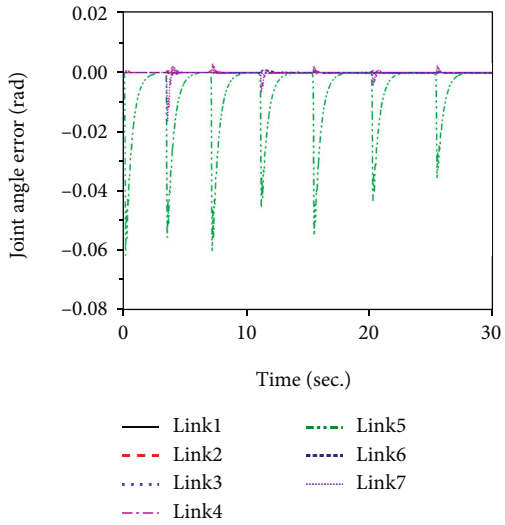

Figure 3: Joint angle error.

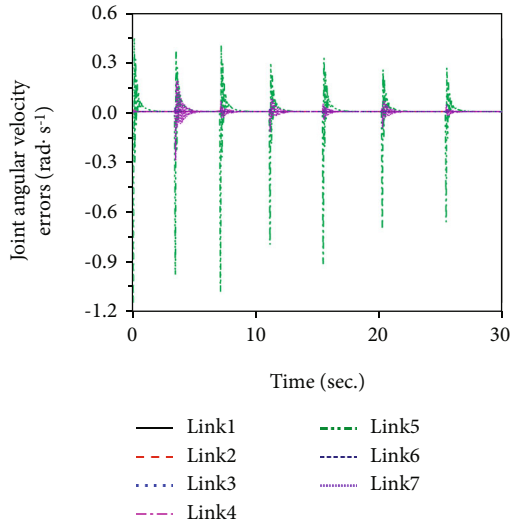

Figure 4: Joint angular velocity error.

Designing the Lyapunov function $V(x) = (1/2)x^{\mathrm{T}}Px$, the Riccati equation is solved as follows:

$$\dot{P} + PA_N + A_N P + PB_N\left(R^{-1} - \frac{1}{\gamma^2}I\right)B_N P + Q = 0. \quad (32)$$

By the skew symmetric matrix $C_0 - (1/2)M_0$, we design function P as follows:

$$P = D^T\begin{bmatrix} M_0 & 0 \\ 0 & N \end{bmatrix}D, \quad (33)$$

where N is a positive definite symmetric constant matrix.

Putting formula (27) in formula (26),

$$\begin{bmatrix} 0 & N \\ N & 0 \end{bmatrix} - D^{\mathrm{T}}B_N\left(R^{-1} - \frac{1}{\gamma^2}I\right)B_N^{\mathrm{T}}D + Q = 0. \quad (34)$$

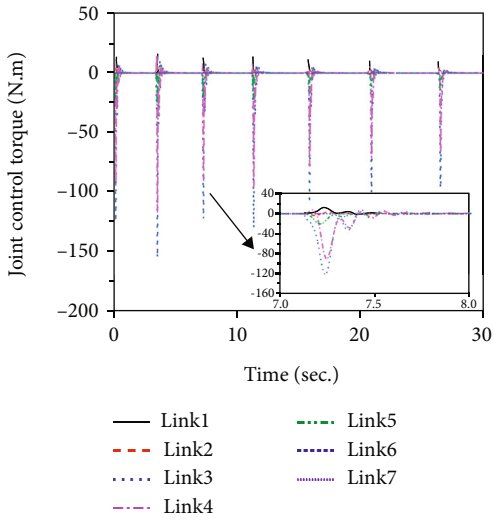

Figure 5: Joint control torque.

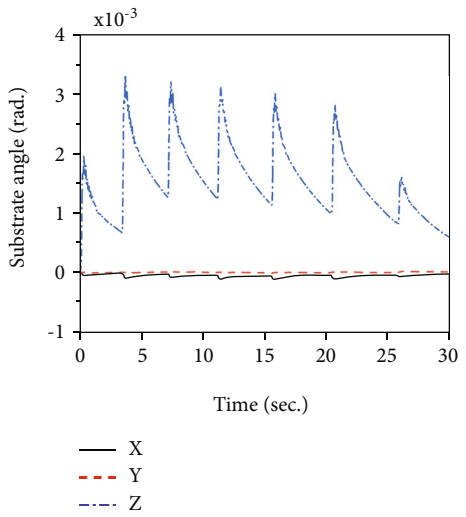

Figure 6: Substrate angle.

By Cholesky decomposition, we get R_1:

$$R_1^{\mathrm{T}}R_1 = \left(R^{-1} - \frac{1}{\gamma^2}I\right)^{-1}. \quad (35)$$

At the same time,

$$Q = \begin{bmatrix} Q_1^{\mathrm{T}}Q_1 & Q_{12} \\ Q_{12}^{\mathrm{T}} & Q_2^{\mathrm{T}}Q_2 \end{bmatrix}, \quad (36)$$

$$D = \begin{bmatrix} R_1^{\mathrm{T}}Q_1 & R_1^{\mathrm{T}}Q_2 \\ 0 & I \end{bmatrix}, \quad (37)$$

$$N = \frac{1}{2}\left(Q_1^T Q_2 + Q_2^T Q_1\right) - \frac{1}{2}\left(Q_{21}^T + Q_{12}\right). \quad (38)$$

So, H_∞ the state feedback control rate of the robust

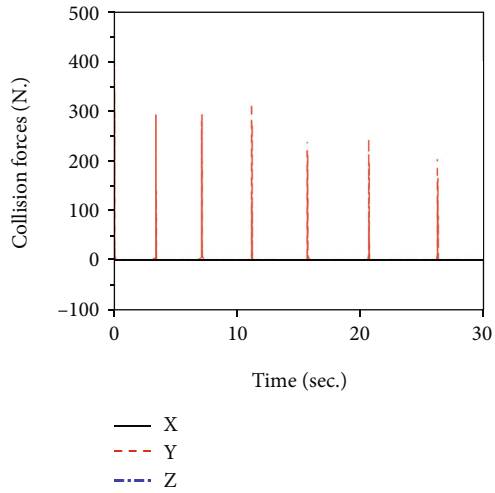

Figure 7: Collision forces.

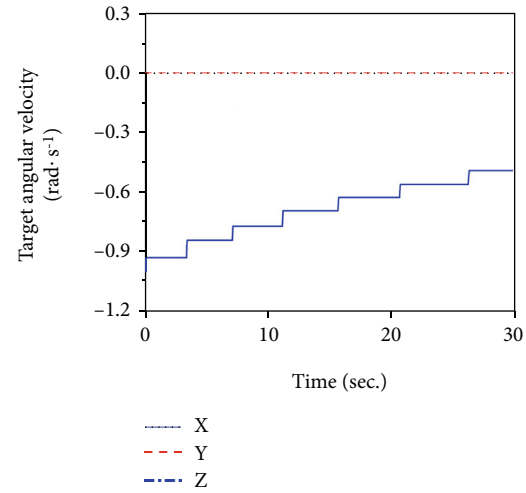

Figure 8: Target spin angular velocity.

optimal controller is

$$u = -R^{-1}B^{\mathrm{T}}De. \tag{39}$$

Remark 1. In [26], the authors mainly considered the stabilization problem of the flexible deceleration brush detumbling mechanism attached to a space robot arm, where an optimal adaptive control scheme and a backstepping control strategy with sliding mode differentiator are proposed. Different from [26], in this paper, we mainly discuss the stabilization issue of the manipulator under complex environmental conditions and we show that the developed despinning strategy can successfully eliminate the rotation speed.

3. Spin Target Decontrol Study

The redundant robotic arm has seven degrees of freedom, and the floating base has six degrees of freedom. The DH method was used to build the space robot structure with the dynamics parameters shown in Table 1. The parameters of the designed space spin target are shown in Table 2. The target is initially rotated around the axis with an angular velocity of the actual effect as shown in Figure 2.

A robust optimal controller is used to simulate the deconvolution of a spatial target in a spin state. The target mass center and the mass center of the space robot are located in the plane of deconvolution, and the initial position of the end flexible brush is set in this plane. Therefore, for the spin target deconvolution, once the deconvolution plane is determined, it is only necessary to maintain the initial joint angle of the robot arm to ensure that the end flexible reduction brush reaches the deconvolution position before the next deconvolution.

The arm's joint angle error and joint angular velocity error are shown in Figures 3 and 4, respectively. The joint angle error occurs during the contact collision process, where the instantaneous force causes a large deviation in the joint angle of the robot arm, which is then controlled by the controller to recover the initial position. The magnitude of the joint angle error is in the range of 0.06 rad, and the convergence time is approximately 3 s. The joint angle error due to the contact collision gradually decreases as the deconvolution progresses. The joint angular velocity error also decreases in magnitude.

The robot arm control torque is shown in Figure 5: the initial solving interval time is about 3.5 s and the initial joint control torque is in the range of 150 N. As the solving proceeds and the solving interval time increases, the solving torque gradually decreases. The simulation time for the spin target in this section is 30 s, in which a total of 7 spin cycles are performed. Later in the 30 s spin process, i.e., during the 6th and 7th spins, the spin interval has grown to 5.6 s and the joint control torque drops to within 100 N. Extracting the third deconvolution process for analysis shows that the initial joint moments are similarly large during the 7 to 8 s period when the contact collision causes a sudden increase in the robot arm joint error. At the end of the collision deconvolution, the control torque converges to zero within 0.8 s, completing the stable control of the system.

The substrate angle is shown in Figure 6. The motion of the robotic arm and the collision interference at the end affect the base angle of the space robot. The error accuracy of the base angle is 0.23°/s.

During the spin-up process, the spin target is subjected to contact collision forces, as shown in Figure 7. The collision forces occur mainly in the direction perpendicular to the spin plane, which in this case is the y-axis direction. The magnitude of the collision force is in the range of 400 N and decays with time. The collision force is applied at the deconfliction position at the edge of the target sail, with the point of action and the length of the sail at the mass center of the target acting as the deconfliction arm, both forming a despinning moment for despinning.

The change of the angular velocity of the spin target is shown in Figure 8. The angular velocity of the spin target decreases from 1 rad/s to 0.4944 rad/s within 30 s of deconvolution time, and the deconvolution effect is 49.44%.

Therefore, it can be proven that the deconvolution efficiency and H_∞ optimal controller designed in this paper can achieve the desired deconvolution effect. Due to the effectiveness and stability of the controller, the target has a good despinning effect and no large chapter motion in the other two axes. However, the spatial environment is complex and uncertain, and there is a high probability that the spin target will be converted into a chapter motion under the condition of unknown disturbance.

4. Conclusions

A H_∞ optimal controller is designed to address the external disturbances and uncertainties in the space robot deconvolution process. Using the Lyapunov stability theory, it is demonstrated that under the condition of bounded disturbances, the robust state feedback control term can be designed to compensate for uncertainties and unknown disturbances to achieve the purpose of deconvolution, thus ensuring the global asymptotic stability of the closed-loop system. It is also verified that the controller is able to demonstrate high accuracy and good convergence in both unknown disturbances and uncertain environments. The ability of the flexible reduction brush end designed in this paper to perform the deconvolution task also demonstrates the accuracy of the controller and the effectiveness of the deconvolution strategy. Simulations using the H_∞ optimal controller for autonomous deconvolution control show that the H_∞ optimal controller has high accuracy and good convergence.

Data Availability

The datasets generated and analysed during the current study are available from the corresponding author on reasonable request. The authors declare that the data supporting the findings of this study are available within the article.

Conflicts of Interest

The authors declare that they have no conflicts of interest.

Acknowledgments

The study was supported by the Science and Technology on Space Intelligent Control Laboratory (6142208180402).

References

[1] Y. LU, X. LIU, and Y. ZHOU, "Review of detumbling technologies for active removal of uncooperative targets," *Acta Aeronautica et Astronautica Sinica*, vol. 39, no. 1, pp. 38–50, 2018.

[2] X. ZHOU, *The simulation analysis of active debris removal of multiple targets in a single task*, Beijing: The University of Chinese Academy of Sciences, in Chinese, 2017.

[3] Y. GENG, W. LU, and X. CHEN, "Attitude synchronization control of on-orbit servicing spacecraft with respect to out-of-control target," *Journal of Harbin Institute of Technology*, vol. 44, no. 1, pp. 1–6, 2012.

[4] P. Huang, M. Wang, Z. Meng, F. Zhang, Z. Liu, and H. Chang, "Reconfigurable spacecraft attitude takeover control in post-capture of target by space manipulators," *Journal of the Franklin Institute*, vol. 353, no. 9, pp. 1985–2008, 2016.

[5] P. Huang, F. Zhang, Z. Meng, and Z. Liu, "Adaptive control for space debris removal with uncertain kinematics, dynamics and states," *Acta Astronautica*, vol. 128, pp. 416–430, 2016.

[6] K. Daneshjou and R. Alibakhshi, "Multibody dynamical modeling for spacecraft docking process with spring-damper buffering device: a new validation approach," *Advances in Space Research*, vol. 61, no. 1, pp. 497–512, 2018.

[7] S.-I. Nishida and S. Kawamoto, "Strategy for capturing of a tumbling space debris," *Acta Astronautica*, vol. 68, no. 1-2, pp. 113–120, 2011.

[8] A. NATARAJAN and H. SCHAUB, "Hybrid control of orbit normal and along-track two-craft Coulomb tethers," *Aerospace Science and Technology*, vol. 13, no. 4-5, pp. 183–191, 2009.

[9] P. PERGOLA and A. RUGGIERO, "Expanding foam application for active space debris removal systems," in *Proceedings of 62nd International Astronautical Congress (IAC11)*, 2011.

[10] L. LIN, "Status and removal of space debris," *Spacecraft Engineering*, vol. 21, no. 3, 2012.

[11] T. R. Oliveira, J. P. V. S. Cunha, and H. Liu, "Adaptive sliding mode control based on the extended equivalent control concept for disturbances with unknown bounds," *Studies in Systems, Decision and Control*, vol. 115, pp. 149–163, 2018.

[12] A. Kawamura, H. Ito, and K. Sakamoto, "Chattering reduction of disturbance observer based sliding mode control," *Transactions on industry applications*, vol. 30, no. 2, pp. 456–461, 1994.

[13] M. Veysi, M. R. Soltanpour, and M. H. Khooban, "A novel self-adaptive modified bat fuzzy sliding mode control of robot manipulator in presence of uncertainties in task space," *Robotica*, vol. 33, no. 10, pp. 2045–2064, 2015.

[14] S. Mobayen, D. Baleanu, and F. Tchier, "Second-order fast terminal sliding mode control design based on LMI for a class of non-linear uncertain systems and its application to chaotic systems," *Journal of Vibration and Control*, vol. 23, pp. 2912–2925, 2016.

[15] Z. Liu, H. R. Karimi, and J. Yu, "Passivity-based robust sliding mode synthesis for uncertain delayed stochastic systems via state observer," *Automatica*, vol. 111, p. 108596, 2020.

[16] J. Zhai and H. R. Karimi, "Universal adaptive control for uncertain nonlinear systems via output feedback," *Information Sciences*, vol. 500, pp. 140–155, 2019.

[17] H. B. Sun and L. L. Hou, "Composite anti-disturbance attitude and vibration control for flexible spacecraft," *IET Control Theory & Applications*, vol. 11, no. 14, pp. 2383–2390, 2017.

[18] S. Mobayen, F. Tchier, and L. Ragoub, "Design of an adaptive tracker for n-link rigid robotic manipulators based on super-twisting global nonlinear sliding mode control," *International Journal of Systems Science*, vol. 48, no. 9, pp. 1990–2002, 2017.

[19] H. Yang and M. Tan, "Sliding mode control for flexible-link manipulators based on adaptive neural networks," *International Journal of Automation and Computing*, vol. 15, no. 2, pp. 239–248, 2018.

[20] H. Yang and J. Liu, "An adaptive RBF neural network control method for a class of nonlinear systems," *IEEE/CAA Journal of Automatica Sinica*, vol. 5, no. 2, pp. 457–462, 2018.

[21] L. Cao, B. Xiao, and M. Golestani, "Robust fixed-time attitude stabilization control of flexible spacecraft with actuator uncertainty," *Nonlinear Dynamics*, vol. 100, no. 3, pp. 2505–2519, 2020.

[22] B. Xiao, L. Cao, and S. Y. Xu, "Robust tracking control of robot manipulators with actuator faults and joint velocity measurement uncertainty," *IEEE/ASME Transactions on Mechatronics*, vol. 25, no. 3, pp. 1354–1365, 2020.

[23] L. X. Zhang, B. Cai, and Y. Shi, "Stabilization of hidden semi-Markov jump systems: emission probability approach," *Automatica*, vol. 101, pp. 87–95, 2019.

[24] B. Cai, L. X. Zhang, and Y. Shi, "Observed-mode-dependent state estimation of hidden semi-Markov jump linear systems," *IEEE Transactions on Automatic Control*, vol. 65, no. 1, pp. 442–449, 2019.

[25] L. X. Zhang, B. Cai, T. Tan, and Y. Shi, "Stabilization of non-homogeneous hidden semi-Markov jump systems with limited sojourn-time information," *Automatica*, vol. 101, no. 7–8, pp. 87–95, 2020.

[26] S. Sun, Y. Zhao, and H. Wu, "Optimal adaptive control and backstepping control method with sliding mode differentiator," *Complexity*, vol. 2021, 15 pages, 2021.